



**HAL**  
open science

# Numerical schemes for anisotropic PDEs on cartesian grid domains

Jean-Marie Mirebeau

► **To cite this version:**

Jean-Marie Mirebeau. Numerical schemes for anisotropic PDEs on cartesian grid domains. Numerical Analysis [math.NA]. Université Paris-Sud XI, 2018. tel-01811841

**HAL Id: tel-01811841**

**<https://theses.hal.science/tel-01811841>**

Submitted on 10 Jun 2018

**HAL** is a multi-disciplinary open access archive for the deposit and dissemination of scientific research documents, whether they are published or not. The documents may come from teaching and research institutions in France or abroad, or from public or private research centers.

L'archive ouverte pluridisciplinaire **HAL**, est destinée au dépôt et à la diffusion de documents scientifiques de niveau recherche, publiés ou non, émanant des établissements d'enseignement et de recherche français ou étrangers, des laboratoires publics ou privés.

UNIVERSITÉ PARIS-SUD

École doctorale de mathématiques Hadamard (ED 574)

Laboratoire de mathématique d'Orsay (UMR 8628 CNRS)

Mémoire présenté pour l'obtention du

**Diplôme d'habilitation à diriger les recherches**

Discipline : Mathématiques

*par*

**Jean-Marie Mirebeau**

Schémas numériques pour les EDPs anisotropes sur grille cartésienne  
*Numerical schemes for anisotropic PDEs on cartesian grid domains*

Rapporteurs :

MAURY BERTRAND

UGO BOSCAIN

JAMES A. SETHIAN

Date de soutenance : 18 Mai 2018

Composition du jury :

MAURY BERTRAND (Rapporteur)

UGO BOSCAIN (Rapporteur)

J. FREDERIC BONNANS (Examinateur)

RON KIMMEL (Examinateur)

SIMON MASNOU (Examinateur)

GABRIEL PEYRÉ (Examinateur)

*A Rachel et Ariane*

# Contents

List of publications . . . . .	4
Main notations . . . . .	7
<b>1 Introduction</b>	<b>8</b>
1.1 Version française . . . . .	9
1.2 English version . . . . .	31
<b>I Anisotropic Eikonal equations</b>	<b>46</b>
<b>2 Semi-Lagrangian schemes</b>	<b>52</b>
2.1 Riemannian metrics . . . . .	54
2.2 Finsler metrics . . . . .	58
<b>3 Eulerian schemes</b>	<b>63</b>
3.1 Quadratic Hamiltonians . . . . .	65
3.2 Curvature penalized models . . . . .	71
<b>4 Applications</b>	<b>78</b>
4.1 Tubular structure segmentation . . . . .	78
4.2 Region segmentation using Rander metrics . . . . .	88
4.3 Motion planning and surveillance . . . . .	91
<b>II Second order equations</b>	<b>97</b>
<b>5 Anisotropic diffusion</b>	<b>99</b>
5.1 Non-Divergence form diffusion . . . . .	99
5.2 Divergence form diffusion . . . . .	102
<b>6 The Monge-Ampere operator</b>	<b>105</b>
6.1 Discretization of general Pucci operators . . . . .	106
6.2 The MA-LBR numerical scheme . . . . .	111
<b>7 The constraint of convexity</b>	<b>113</b>
7.1 Discrete analogues of convexity. . . . .	114
7.2 Convexity constraints on the cartesian grid. . . . .	116

7.3	Hierarchical cones of discrete convex functions . . . . .	119
7.4	Cardinality of the minimal stencils . . . . .	121

**III Appendix 123**

**A Geometry of lattices 124**

A.1	Basis reduction methods . . . . .	125
A.2	Voronoi reductions of quadratic forms . . . . .	129

**B The fast marching algorithm 134**

B.1	Fixed point formulation . . . . .	136
B.2	Systems of equations . . . . .	137

## List of publications

The following papers and preprints were written after my PhD [Mir11]. Articles [A4] and [A8] will not be presented here, so as to keep the document consistent. The reference numbers throughout the document do not refer to this page, but to the bibliography located in the end.

## International refereed journals

### Published

- [A1] Jean-Marie Mirebeau. *Efficient fast marching with Finsler metrics*. Numerische Mathematik, vol. 126, no. 3, pp. 515-557, 2013.
- [A2] Jérôme Fehrenbach and Jean-Marie Mirebeau. *Sparse Non-negative Stencils for Anisotropic Diffusion*. Journal of Mathematical Imaging and Vision, vol. 49, no. 1, pp. 123-147, 2014.
- [A3] Jean-Marie Mirebeau. *Anisotropic Fast-Marching on cartesian grids using Lattice Basis Reduction*. SIAM Journal on Numerical Analysis, vol. 52, no. 4, pp. 1573-1599, Jan. 2014.
- [A4] Jérémy Bleyer, Guillaume Carlier, Vincent Duval, Jean-Marie Mirebeau, and Gabriel Peyré. *A  $\Gamma$ -Convergence Result for the Upper Bound Limit Analysis of Plates*. ESAIM: Mathematical Modelling and Numerical Analysis (M2AN), vol. 50, no. 1, pp. 215-235, 2016.
- [A5] Jean-David Benamou, Francis Collino, and Jean-Marie Mirebeau. *Monotone and Consistent discretization of the Monge-Ampere operator*. Mathematics of Computation, vol. 85, no. 302, pp. 2743-2775, 2016.
- [A6] Jean-Marie Mirebeau. *Discretization of the 3D Monge-Ampere operator, between Wide Stencils and Power Diagrams*. Mathematical Modeling and Numerical Analysis (M2AN), vol. 49, no. 5, pp. 1511-1523, 2015.
- [A7] Jean-Marie Mirebeau. *Adaptive, Anisotropic and Hierarchical Cones of Convex functions*. Numerische Mathematik, vol. 132, no. 4, pp. 807-853, 2016.
- [A8] Quentin Merigot and J.-M. Mirebeau. *Minimal geodesics along volume preserving maps, through semi-discrete optimal transport*, SIAM journal on Numerical Analysis, vol. 54, no. 6, pp. 3465-3492, 2016.
- [A9] J.-M. Mirebeau. *Minimal Stencils for Monotony or Causality Preserving Discretizations of Anisotropic PDEs*, SIAM journal on Numerical Analysis, vol. 54, no. 3, pp. 1582-1611, 2016.

## Published in journals specialized in image processing

- [A10] Da Chen, Jean-Marie Mirebeau, and Laurent Cohen, *Global Minimum For A Finsler Elastic Minimal Path Approach*, International Journal of Computer Vision, vol. 122, no. 3, pp. 458-483, 2017.
- [A11] Da Chen, Jean-Marie Mirebeau, and Laurent Cohen, *Vessel Tree Extraction using Radius-Lifted Keypoints Searching Scheme and Anisotropic Fast Marching Method*, Journal of Algorithms and Computational Technology, vol. 10, no. 4, pp. 224-234, Jul. 2016.

## Submitted

- [A12] J.-M. Mirebeau, *Anisotropic fast-marching on cartesian grids using Voronoi's first reduction of quadratic forms*, 2017
- [A13] J.-M. Mirebeau, *Fast Marching Methods for Curvature Penalized Shortest Paths*, 2017
- [A14] Remco Duits, Stephan P.L. Meesters, J.-M. Mirebeau, Jorg M. Portegies, *Optimal Paths for Variants of the 2D and 3D Reeds-Shepp Car with Applications in Image Analysis*, 2017

## Conference proceedings

### Peer reviewed

- [P1] Da Chen, Laurent D. Cohen, and Jean-Marie Mirebeau, *Vessel Extraction Using Anisotropic Minimal Paths and Path Score*, IEEE International Conference on Image Processing (ICIP), pp. 1570-1574, 2014.
- [P2] Gonzalo Sanguinetti, Erik Bekkers, Remco Duits, Michiel Janssen, Alexey Mash-takov, and Jean-Marie Mirebeau, *Sub-Riemannian Fast Marching in  $SE(2)$* , Ibero-american Congress on Pattern Recognition (CIARP), vol. 9423, no. 44, pp. 366-374, 2015.
- [P3] Da Chen, Jean-Marie Mirebeau, and Laurent D. Cohen, *Global Minimum for Curvature Penalized Minimal Path Method*, British Machine Vision Conference (BMVC), pp 81-86, 2015.
- [P4] Da Chen, Jean-Marie Mirebeau, and Laurent D. Cohen, *A New Finsler Minimal Path Model with Curvature Penalization for Image Segmentation and Closed Contour Detection*, IEEE Conference on Computer Vision and Pattern Recognition (CVPR), pp. 355-363, Jun. 2016.
- [P5] Da Chen, Jean-Marie Mirebeau, and Laurent D. Cohen, *Finsler Geodesic Evolution Model for Region based Active Contours*, British Machine Vision Conference (BMVC), 2016.

- [P6] Jean-Marie Mirebeau, Johann Dreo, *Automatic differentiation of non-holonomic fast marching for computing most threatening trajectories under sensors surveillance*, Geometric Science of Information (GSI), 2017

### **Without peer review**

- [P7] J.-M. Mirebeau, *Adaptive, hierarchical cones of convex functions*. Workshop *Multi-scale and High Dimensional Problems*, Oberwolfach, 2013
- [P8] J.-M. Mirebeau, *Numerical resolution of Euler equations, through semi-discrete optimal transport*, Journées équations aux dérivées partielles de Roscoff, 2015

### **Reproducible research with distribution of C++ codes**

- [R1] Jean-Marie Mirebeau, Jérôme Fehrenbach, Laurent Risser, and Shaza Tobji. *Anisotropic Diffusion in ITK*. The Insight Journal, 2015.
- [R2] Jean-Marie Mirebeau. *Anisotropic Fast-Marching in ITK*. The Insight Journal, 2015.

# Main notations

## Geometrical objects

- $d \geq 1$  is the ambient space dimension. All considered vector spaces are over the field  $\mathbb{R}$  of reals.
- $\mathbb{E}_d := \mathbb{R}^d$  denotes the  $d$ -dimensional *euclidean* space. The euclidean norm is denoted  $\|\cdot\|$ , and the euclidean scalar product  $\langle \cdot, \cdot \rangle$ .
- $\mathbb{L}_d := \mathbb{Z}^d$  is the  $d$ -dimensional *lattice* of integer points.
- Points are denoted e.g.  $\mathbf{p}, \mathbf{q}$ . Vectors are generally distinguished with a “dot” e.g.  $\dot{\mathbf{p}}, \dot{\mathbf{q}} \in \mathbb{E}_d$ , and co-vectors with a “hat” e.g.  $\hat{\mathbf{p}}, \hat{\mathbf{q}} \in \mathbb{E}_d^*$ , especially in part I which has a strong geometric content.
- Lattice elements are distinguished with the use of specific letters, usually  $\dot{\mathbf{e}}, \dot{\mathbf{f}} \in \mathbb{L}_d$ .

## Quadratic forms

- $L(\mathbb{E}, \mathbb{F})$  denotes the set of linear maps from a vector space  $\mathbb{E}$  to another  $\mathbb{F}$ .
- $S(\mathbb{E}) \supseteq S^+(\mathbb{E}) \supseteq S^{++}(\mathbb{E})$  denote respectively the sets of symmetric linear maps, of semi-definite ones, and of positive definite ones, on a vector space  $\mathbb{E}$ . Note that  $S(\mathbb{E}) \subseteq L(\mathbb{E}, \mathbb{E}^*)$ . Symmetric linear maps are often identified with quadratic forms.
- $\|\dot{\mathbf{p}}\|_M := \sqrt{\langle M\dot{\mathbf{p}}, \dot{\mathbf{p}} \rangle}$  denotes the norm of a vector  $\dot{\mathbf{p}} \in \mathbb{E}$  induced by a positive quadratic form  $M \in S^{++}(\mathbb{E})$ .
- $\hat{\mathbf{p}} \otimes \hat{\mathbf{p}} \in S^+(\mathbb{E})$  is the outer product of a co-vector  $\hat{\mathbf{p}} \in \mathbb{E}^*$  with itself.
- $\text{Cond}(M) := \sqrt{\|M\| \|M^{-1}\|}$  denotes the condition number, or anisotropy ratio, of a positive quadratic form.

## Miscellaneous

- $\llbracket m, n \rrbracket$  denotes the range of all integers from  $m$  to  $n$ , bounds inclusive.

# Chapter 1

## Introduction

### Contents

---

<b>1.1</b>	<b>Version française . . . . .</b>	<b>9</b>
1.1.1	Outils géométriques . . . . .	10
1.1.2	Equations eikonales . . . . .	14
1.1.3	Equations du second ordre. . . . .	24
1.1.4	Faits marquants sur la période 2012-2017 . . . . .	29
<b>1.2</b>	<b>English version . . . . .</b>	<b>31</b>
1.2.1	Geometric tools . . . . .	32
1.2.2	Eikonal equations . . . . .	34
1.2.3	Second order equations. . . . .	41
1.2.4	Highlights of the period 2012-2017 . . . . .	44

---

*Tu ne sais plus de quel côté de la grille est le rêve.* (Erin Morgenstern<sup>1</sup>)

## 1.1 Introduction (Version française)

Ce mémoire présente mes recherches dans le domaine de la discrétisation des Equations aux Dérivées Partielles (EDPs), en se focalisant sur les difficultés liées à l'anisotropie, et en se limitant délibérément à l'utilisation de grilles cartésiennes. L'interaction de ces deux contraintes mène à l'utilisation d'outils géométriques originaux. Les EDPs considérées sont très variées, allant des équations de Hamilton-Jacobi-Bellman à celle de Monge-Ampère, en passant par la diffusion anisotrope, et l'optimisation de fonctionnelles sur l'ensemble des fonctions convexes. Ma contribution majeure, en termes d'impact sur la communauté du traitement de l'image notamment, est la conception de nouvelles variantes de l'algorithme du Fast-Marching. Celles-ci permettent la résolution numérique efficace d'équations eikoniales anisotropes, et ainsi le calcul de distances riemanniennes, finsleriennes, voire pour des systèmes de contrôle non-holonomes.

L'analyse numérique, domaine principal de ce mémoire, consiste à construire et étudier des schémas de discrétisation pour les EDPs. Ceux-ci doivent respecter au mieux la structure de l'EDP originale, par exemple un principe du maximum, ou de causalité, et être suffisamment robustes pour en extraire des solutions faibles, en un sens approprié. Satisfaire ces propriétés représente un véritable challenge dans le cas de problèmes fortement anisotropes, qui présentent des directions privilégiées non-uniformes sur le domaine de résolution, et non alignées avec les axes de coordonnées. Une réponse possible, pour laquelle je réfère à ma thèse [Mir11] et aux références qu'elle contient, est d'utiliser un maillage du domaine adapté à la géométrie de l'EDP choisie, par la taille, la forme et l'orientation de ses éléments. Nous prenons dans ce mémoire un parti pris opposé : la représentation discrète du domaine utilise toujours une grille cartésienne - par simplicité et car c'est le contexte naturel du traitement de l'image - dont l'alignement périodique des

---

<sup>1</sup>Ecrivain et artiste peintre américain. 1978-

points semble en conflit évident avec la géométrie anisotrope et arbitraire des problèmes étudiés.

La spécificité et la cohérence de ce travail se trouvent du côté des outils, issus de la géométrie discrète, utilisés pour résoudre ce conflit<sup>2</sup>. Il s'agit principalement de deux constructions géométriques dues à Voronoi, liées aux diagrammes de Voronoi et aux empilements compacts de sphères respectivement, ainsi que de deux objets spécifiques des basses dimensions  $d \in \{2, 3\}$ , que sont l'arbre de Stern-Brocot et l'algorithme de Selling. Certains de ces outils sont loin d'être récents, et sont bien connus pour leurs applications en génération de maillage, en cryptographie ou encore en arithmétique. Étudier leur interaction avec des opérateurs différentiels représente cependant une réelle nouveauté, l'unique travail antérieur en ce sens étant à notre connaissance dû à Bonnans et al [BOZ04]. Les thématiques de ce mémoire, EDPs et géométrie différentielle sur la grille cartésienne, suggèrent un rapprochement avec la *géométrie digitale* [KR04]; un examen plus approfondi révèle pourtant, en l'état, peu de techniques et de problèmes communs.

Nous évoquons dans la suite de cette introduction les principaux résultats de ces recherches. Elle met également en avant plusieurs projets et perspectives, qui seront l'objet de futurs travaux. Nous renvoyons au corps du texte pour le cadre formel, le détail des applications, et des illustrations numériques supplémentaires. Les articles originaux contiennent les preuves mathématiques, qui ne sont pas reproduites ici.

**Organisation du mémoire.** Ce mémoire est organisé en deux parties, largement indépendantes, regroupant les chapitres §2-4 et §5-7 respectivement. La première partie porte sur la discrétisation des équations eikonales anisotropes, à l'aide de schémas semi-lagrangiens §2, ou Eulériens fondés sur une représentation particulière du hamiltonien §3, et sur l'application de ces méthodes au traitement de l'image principalement §4. La seconde partie décrit la discrétisation d'équations du second ordre : la diffusion anisotrope §5, l'équation de Monge-Ampère §6, et la question liée de la contrainte de convexité §7. Deux appendices servent de référence pour des outils revenant fréquemment au fil des chapitres. L'un §A est dédié à la description des techniques de géométrie discrète utilisés. Le second §B donne deux formulations utiles de l'algorithme du fast marching.

### 1.1.1 Outils géométriques

Les schémas numériques développés dans ce mémoire sont, pour l'essentiel, fondés sur deux constructions du mathématicien Voronoi, appelées première et seconde réduction d'une forme quadratique, toujours supposée *définie positive*. Celle-ci est définie sur un espace vectoriel réel de dimension finie, contenant un réseau additif. Dans les deux cas, Voronoi associe à la forme quadratique un objet de nature *discrète*, d'une manière *invariante* sous l'action des transformations linéaires stabilisant le réseau. Les Réductions de Voronoi ont été introduites à des fins de classification des formes quadratiques [Sch09], mais nous utilisons surtout des sous-produits de ces constructions géométriques.

---

<sup>2</sup> Dans un souci de cohérence du mémoire, mes travaux sur les modèles de plaque mince [BCD<sup>+</sup>16], et sur les équations d'Euler des fluides incompressibles [MM16], ne seront pas évoqués en détail. En effet, leur discrétisation ne n'utilise pas de grille cartésienne, et est fondée sur des outils distincts.

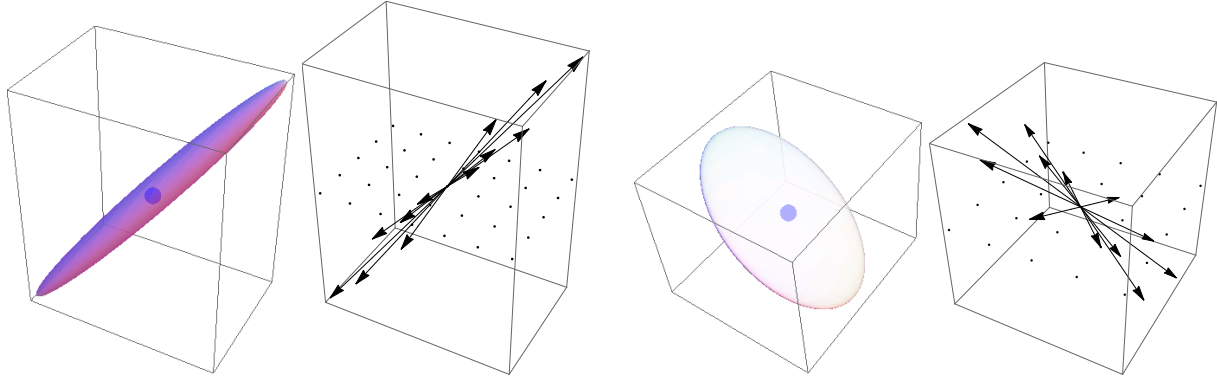


FIGURE 1.1 – Ellipsoïde  $\{\dot{\mathbf{p}} \in \mathbb{E}_2; \|\dot{\mathbf{p}}\|_M \leq 1\}$ , et vecteurs apparaissant dans la décomposition (1.2) de  $D := M^{-1}$ , où  $M \in S^{++}(\mathbb{R}^3)$  a pour valeurs propres  $1, 10^2, 10^2$  (aiguille, à gauche) ou  $1, 1, 10^2$  (assiette, à droite) respectivement.

*Ellipsoid  $\{\dot{\mathbf{p}} \in \mathbb{E}_2; \|\dot{\mathbf{p}}\|_M \leq 1\}$ , and offsets appearing in the decomposition (1.17) of  $D := M^{-1}$ , for some  $M \in S^{++}(\mathbb{R}^3)$  of eigenvalues  $1, 10^2, 10^2$  (needle-like, left) and  $1, 1, 10^2$  (plate-like, right) respectively.*

On note  $S^{++}(\mathbb{E})$  l'ensemble des applications bilinéaires symétriques définies positives sur un espace vectoriel  $\mathbb{E}$ , qui est isomorphe à l'ensemble des formes quadratiques d'intérêt. Sans nuire à la généralité, l'espace vectoriel est usuellement  $\mathbb{E}_d := \mathbb{R}^d$  euclidien, ou son dual, et le réseau est l'ensemble  $\mathbb{L}_d := \mathbb{Z}^d$  des points à coordonnées entières.

La première réduction de Voronoi associée à  $D \in S^{++}(\mathbb{E}_d^*)$  la solution d'un problème d'optimisation linéaire  $\mathcal{L}(D)$ , défini comme suit :

$$\mathcal{L}(D) := \inf_{M \in \mathfrak{M}} \text{Tr}(MD), \quad \text{où } \mathfrak{M} := \{M \in S^{++}(\mathbb{E}_d); \forall \dot{\mathbf{e}} \in \mathbb{L}_d \setminus \{0\}, \|\dot{\mathbf{e}}\|_M \geq 1\}. \quad (1.1)$$

On a noté  $\|\cdot\|_M$  la norme définie par  $\|\dot{\mathbf{e}}\|_M^2 = \langle M\dot{\mathbf{e}}, \dot{\mathbf{e}} \rangle = \text{Tr}(M\dot{\mathbf{e}} \otimes \dot{\mathbf{e}})$ , et cette dernière identité montre que les contraintes portant sur la matrice  $M$ , dans la définition de  $\mathfrak{M}$ , sont linéaires<sup>3</sup>. Le problème (1.1) est bien posé dans le sens où il admet un ensemble compact de solutions, génériquement une seule [Sch09]. En dimension  $d \in \{2, 3\}$ , l'algorithme du simplexe appliqué à ce problème prend une forme simple et intéressante d'un point de vue géométrique, appelée algorithme de Selling [Sel74], voir §A.1.2. Pour la construction de schémas numériques pour les EDPs, du premier et second ordre, l'intérêt principal de (1.1) est son *certificat d'optimalité*. Les conditions de Karush-Kuhn-Tucker, affirment en effet qu'il existe  $(\rho_i, \dot{\mathbf{e}}_i)_{i=1}^{d'} \in (\mathbb{R}_+ \times \mathbb{L}_d)^{d'}$ , multiplicateurs de Lagrange et vecteurs associés aux contraintes actives, tels que

$$D = \sum_{1 \leq i \leq d'} \rho_i \dot{\mathbf{e}}_i \otimes \dot{\mathbf{e}}_i. \quad (1.2)$$

On a noté  $d' := d(d+1)/2$  la dimension de l'espace des formes quadratiques. Voir la Figure 1.1. Cette décomposition matricielle rappelle l'écriture  $D = \sum_{i=1}^d \mu_i \dot{\mathbf{v}}_i \otimes \dot{\mathbf{v}}_i$  en termes des

<sup>3</sup> La contrainte implicite de définie positivité  $M \succ 0$  peut être omise, car elle est conséquence de la famille de contraintes  $\langle M\dot{\mathbf{e}}, \dot{\mathbf{e}} \rangle > 0, \dot{\mathbf{e}} \in \mathbb{L}_d \setminus \{0\}$ .

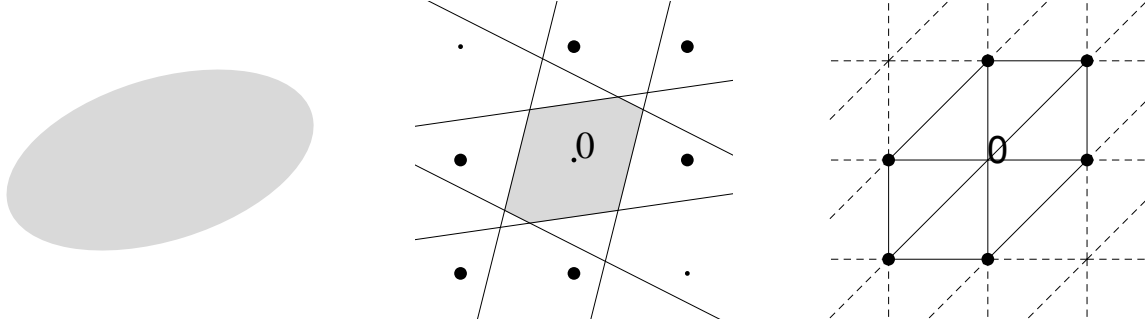


FIGURE 1.2 – Gauche : Ellipse  $\{\mathbf{p} \in \mathbb{E}_2; \|\mathbf{p}\|_M \leq 1\}$ , où  $M \in \mathbb{S}^{++}(\mathbb{E}_2)$ . Centre : Région de Voronoi  $\text{Vor}_M^Z(0)$ , où  $Z := \mathbb{Z}^2$  est la grille cartésienne. Droite : triangulation de Delaunay  $\text{Del}_M^Z$ , le voisinage de l’origine étant mis en avant.

*Left : Ellipsoid  $\{\mathbf{p} \in \mathbb{E}_2; \|\mathbf{p}\|_M \leq 1\}$ , where  $M \in \mathbb{S}^{++}(\mathbb{E}_2)$ . Center : Voronoi region  $\text{Vor}(M)$ , where  $Z := \mathbb{Z}^2$  is the cartesian grid. Right : Delaunay triangulation  $\text{Del}(M)$ , with a highlight on the origin’s neighborhood.*

valeurs propres et vecteurs propres  $(\mu_i, \dot{\mathbf{v}}_i)_{i=1}^d \in (\mathbb{R} \times \mathbb{S}^{d-1})^d$  de la matrice. L’avantage crucial de (1.2) est cependant que les vecteurs  $\dot{\mathbf{e}}_i \in \mathbb{L}_d$  sont à coordonnées entières, et peuvent donc être utilisés dans la construction de schémas numériques aux différences finies sur grille cartésienne, pour des équations eikonales §3, de diffusion §5, et de Monge-Ampere §6. La norme  $\max_{i=1}^d \|\dot{\mathbf{e}}_i\|$  des vecteurs apparaissant dans (1.2) détermine la *localité* de ces schémas, qui est liée à leur précision, coût numérique, potentiel de parallélisation, et à la difficulté d’implémenter les conditions au bord. Son estimation, et l’optimalité de cette construction, sont l’objet de plusieurs résultats : voir les Theorèmes 2.1.5 et 2.1.6, et les Propositions 3.2.3 et 5.1.2.

La seconde réduction de Voronoi fait intervenir le concept de diagramme de Voronoi. Etant donné  $Z \subseteq \mathbb{E}_d$  un ensemble discret de points, et  $M \in \mathbb{S}^{++}(\mathbb{E}_d)$ , on pose

$$\text{Vor}_M^Z(\mathbf{p}) := \{\mathbf{x} \in \mathbb{E}_d; \mathbf{p} \in \underset{\mathbf{q} \in Z}{\text{argmin}} \|\mathbf{x} - \mathbf{q}\|_M^2\}.$$

La triangulation de Delaunay<sup>4</sup>  $\text{Del}_M^Z$ , est définie comme duale de la partition de l’espace par le diagramme de Voronoi  $(\text{Vor}_M^Z(\mathbf{p}))_{\mathbf{p} \in X}$ . Voir la Figure 1.2. La triangulation de Delaunay est un objet fondamental en géométrie algorithmique [LS80, ES86]. Nous nous limitons ici au cas de sites périodiques, qui possède une propriété géométrique exceptionnelle : ses angles internes sont aigus, pour le produit scalaire  $\langle M \cdot, \cdot \rangle$ , voir le Lemme 2.1.2. Sa construction est aussi facilitée, voir §A.2.2. Ceci permet de l’utiliser pour développer des schémas semi-lagrangiens causaux pour les équations eikonales riemanniennes, suivant un principe dû à Sethian et al [SV03], voir §2.1.

Un dernier objet géométrique nous sera utile, appelé arbre Stern-Brocot [Bro62] et limité à la dimension  $d = 2$ , voir la Figure 1.3. Il s’agit d’un arbre binaire complet infini,

<sup>4</sup>La généralisation présentée, par l’introduction d’une norme anisotrope  $\|\cdot\|_M$ , n’en est pas vraiment une car on peut se ramener au cas classique  $M = \text{Id}$  par un changement de variables linéaire.

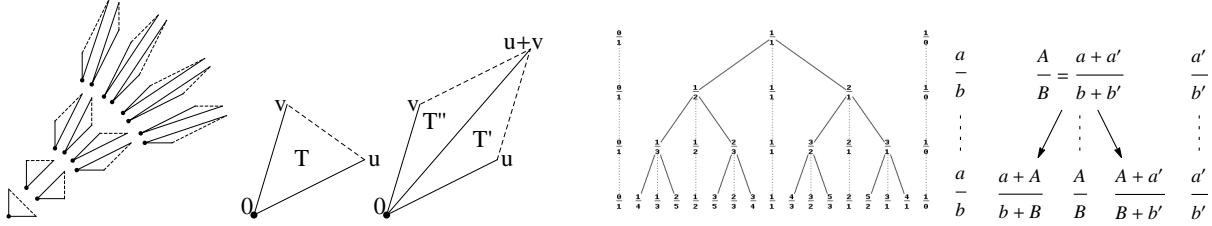


FIGURE 1.3 – Deux représentations de l’arbre (binaire infini complet) de Stern-Brocot, avec la procédure de raffinement associée. Gauche : Les noeuds sont des paires de vecteurs, vus comme des triangles. Droite : Les noeuds sont des rationnels (représentation classique).

*Two representations of the (complete infinite binary) Stern-Brocot tree, with the associated refinement procedure. Left : Nodes are pairs of vectors, displayed as triangles. Right : Nodes are rational numbers (classical representation).*

dont les noeuds sont les paires de vecteurs<sup>5</sup> entiers  $(\mathbf{e}, \mathbf{f}) \in \mathbb{L}_2^2$  appartenant au premier quadrant  $\mathbb{R}_+^2$  et tels que  $\det(\mathbf{e}, \mathbf{f}) = 1$ . Les enfants du noeud  $(\mathbf{e}, \mathbf{f})$  sont  $(\mathbf{e}, \mathbf{e} + \mathbf{f})$  et  $(\mathbf{e} + \mathbf{f}, \mathbf{f})$ . Explorer l’arbre de Stern-Brocot permet de raffiner des secteurs angulaires, d’une manière compatible avec la grille cartésienne. Cet arbre intervient dans la discrétisation des équations eikonales finlériennes §2.2, et de la contrainte de convexité §7. Sa première utilisation en EDP est due à Bonnans et al [BOZ04].

**Projets et perspectives** (*Court terme*. Réductions de Voronoi en dimension 4 et 5). *Les réductions de Voronoi se calculent de manière particulièrement simple et efficace en dimension  $d \in \{2, 3\}$  grâce à l’algorithme de Selling, voir §A.1.2. C’est ce cas particulier qui est utilisé dans tous nos codes informatiques, et dans l’intégralité des résultats numériques présentés. Les équations eikonales sous-riemanniennes considérées en dimension 5, voir §4.1.4, sont possibles grâce à la structure diagonale par blocs de la métrique.*

*A court terme, nous souhaitons produire une implémentation C++ rapide et robuste de la première réduction de Voronoi en dimension 4 et 5, en nous fondant sur les résultats de classification [CS88]. Les schémas numériques résultats seront mis en oeuvre sur des applications pertinentes en ces dimensions, notamment en géométrie sous-riemannienne et pour des problèmes de contrôle stochastique.*

**Projets et perspectives** (Généralisation de la première réduction de Voronoi aux nuages de points). *Il est tentant de généraliser le programme linéaire (1.1) en remplaçant la grille cartésienne  $\mathbb{L}_d$  par un nuage de points  $L \subseteq \mathbb{R}^d$  quelconque. On obtient alors une décomposition similaire à (1.2), a priori applicable à la discrétisation des EDPs sur un milieu non-structuré.*

*Nous étudions cette possibilité, en gardant toutefois à l’esprit certaines réserves : (i) Cette approche est inapplicable à la discrétisation des équations eikonales riemanniennes (1.9), car celle ci utilise de manière cruciale la symétrie de l’ensemble d’offsets :  $\mathbf{e} \in L \Leftrightarrow -\mathbf{e} \in L$ . (ii) Pour la discrétisation des équations de diffusion, des contraintes*

<sup>5</sup>Une autre représentation, plus classique, utilise des étiquettes rationnelles [Niq07]. Au noeud  $(\mathbf{e}, \mathbf{f})$ , où  $\mathbf{e} = (a, b)$  et  $\mathbf{f} = (a', b')$ , est associée l’étiquette  $(a + a')/(b + b')$ .

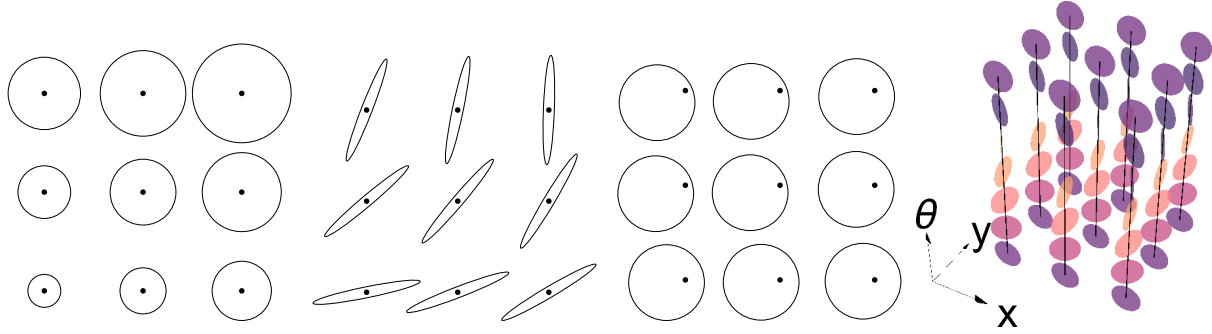


FIGURE 1.4 – Une métrique associée à chaque point une gauge, c.a.d. une norme généralisée pouvant potentiellement être asymétrique et prendre des valeurs infinies. On en représente ici la boule unité (indicatrice de Tissot). De gauche à droite : Métrique isotrope, riemannienne, et finslerienne (asymétrique) sur  $\mathbb{R}^2$ . Puis métrique sous-riemannienne, ici celle du modèle de Reeds-Shepp posé sur  $\mathbb{R}^2 \times \mathbb{S}^1$ .

*A metric associates to each point a gauge, i.e. a generalized norm which may be non-symmetrical and may take infinite values. We display here the gauge's unit balls (Tissot's indicatrix). From left to right : Isotropic, Riemannian, and Finslerian metric on  $\mathbb{R}^2$ . Rightmost : a sub-Riemannian metric, here associated to the Reeds-Shepp model on  $\mathbb{R}^2 \times \mathbb{S}^1$ .*

supplémentaires doivent être ajoutées afin de garantir que  $\sum_{i=1}^{d'} \rho_i \dot{\mathbf{e}}_i = 0$ , autrement un terme indésirable du premier ordre est introduit. (iii) Le problème (1.1) ainsi généralisé est en général mal posé, par exemple en dimension  $d = 2$  si  $L = (\mathbb{Z} \setminus \{0\}) \times \mathbb{Z}$  et  $D$  est la matrice identité.

## 1.1.2 Equations eikonales

Les équations eikonales sont des équations aux dérivées partielles, de type Hamilton-Jacobi-Bellman, statiques et du premier ordre, caractérisant les solutions de problèmes de contrôle optimal déterministes. Nous nous focalisons sur le cas le plus simple, où il s'agit de trouver la longueur minimale des chemins allant du bord d'un domaine  $\Omega \subseteq \mathbb{E}_d$  à un point  $\mathbf{p} \in \Omega$  donné

$$u(\mathbf{p}) := \inf\{\text{length}_{\mathcal{F}}(\gamma); \gamma : [0, 1] \rightarrow \bar{\Omega}, \gamma(0) \in \partial\Omega, \gamma(1) = \mathbf{p}\}. \quad (1.3)$$

Le chemin  $\gamma : [0, 1] \rightarrow \bar{\Omega}$  est supposé localement Lipschitzien. Sa longueur est mesurée via une métrique  $\mathcal{F} : \bar{\Omega} \times \mathbb{E}_d \rightarrow [0, \infty]$  donnée, convexe et 1-homogène en sa seconde variable :

$$\text{length}_{\mathcal{F}}(\gamma) := \int_0^1 \mathcal{F}_{\gamma(t)}(\dot{\gamma}(t)) dt. \quad (1.4)$$

Nos travaux vont bien au delà des classiques métriques conformes [Tsi95, Set96, RT92], localement proportionnelles à la norme euclidienne, qui sont de la forme  $\mathcal{F}_{\mathbf{p}}(\dot{\mathbf{p}}) = \|\dot{\mathbf{p}}\|/s(\mathbf{p})$  où  $s : \bar{\Omega} \rightarrow ]0, \infty[$  est une fonction vitesse donnée. Nous traitons en effet le cas de métriques riemanniennes §2.1, finsleriennes (asymétriques) §2.2, voire dégénérées de forme sous-riemannienne §3.1 ou associée à des problèmes de contrôle optimal non-holonyme §3.2.

L'équation eikonale est, comme annoncé, une EDP satisfaite par la fonction temps d'arrivée  $u : \overline{\Omega} \rightarrow [0, \infty]$ , au sens des solutions de viscosité [BCD08]. Elle s'écrit

$$\mathcal{F}_{\mathbf{p}}^*(du(\mathbf{p})) = 1, \quad \text{où } \mathcal{F}_{\mathbf{p}}^*(\hat{\mathbf{p}}) := \sup\{\langle \hat{\mathbf{p}}, \dot{\mathbf{p}} \rangle; \mathcal{F}_{\mathbf{p}}(\dot{\mathbf{p}}) \leq 1\}, \quad (1.5)$$

pour tout  $\mathbf{p} \in \Omega$ , avec la condition au bord  $u(\mathbf{p}) = 0$  pour tout  $\mathbf{p} \in \partial\Omega$ . Cette formulation EDP est l'outil principal pour établir la convergence des schémas numériques. Une estimation de la vitesse de convergence peut être obtenue dans le cas de problèmes localement contrôlables §3.1, grâce à la méthode du dédoublement des variables [SMK16, Mir17a]. Dans le cas contraire, nous établissons la convergence en un sens faible, grâce à la notion de solution de viscosité discontinue d'une équation eikonale [BCD08], voir §3.2 issu de [Mir17b].

Deux paradigmes s'opposent pour la discrétisation de l'EDP (1.5), fondés sur les approches semi-lagrangienne et eulerienne respectivement. Avant de rentrer dans leurs détails, je souhaite mettre en avant une seconde distinction, entre schémas *causaux* et *non-causaux*. La causalité, définie dans §B, traduit la préservation au sein du problème discret du caractère déterministe du problème de contrôle optimal sous-jacent. Elle équivaut, dans le cadre des problèmes posés sur des graphes, à la positivité des longueurs des arêtes. Cette hypothèse permet l'extraction rapide de chemins minimaux par l'algorithme de Dijkstra, au lieu de la méthode générale plus lente de Bellman-Ford [Dij71]. Nous faisons systématiquement le choix de schémas numériques causaux, résolus par l'algorithme du Fast-marching qui généralise Dijkstra, pour plusieurs raisons : garantie d'un court temps de calcul, pas de critère d'arrêt à définir, extraction plus robuste des géodésiques<sup>6</sup>, possibilité de différentiation automatique §4.3.2, ... L'avantage en coût de calcul est particulièrement marqué pour les métriques fortement anisotropes et spatialement hétérogènes, qui interviennent souvent dans les applications en traitement de l'image [BC10, Mir14a]. Les algorithmes alternatifs au Fast-Marching ont d'autres avantages, notamment un traitement plus simple des géométries complexes (pour lesquelles la causalité est difficile à satisfaire) [BR06, TCO04, Zha05], ou des possibilités de parallélisation [CV15, Tug08] y compris sur les architectures GPU [WDB<sup>+</sup>08, JW08], voir aussi la discussion dans §B.

**Projets et perspectives** (Algorithmes massivement parallèles compatibles avec nos schémas adaptatifs). *Le calcul de chemins minimaux pour des modèles non-holonomes, implémentant par exemple une pénalisation de la courbure §3.2, nécessite de résoudre des équations eikonales dégénérées sur des espaces de dimension assez élevée, tels que  $\mathbb{R}^d \times \mathbb{S}^{d-1}$  où  $d \in \{2, 3\}$ . La réduction d'un ordre de grandeur des temps de calcul, actuellement d'environ 1 seconde pour les cas-test intéressants, permettrait d'envisager le contrôle de systèmes (véhicules, robots, ...) en temps réel.*

*Les méthodes numériques parallèles semblent être une solution à ce problème, et elles ont déjà été étudiées pour les équations eikonales, y compris sur GPU comme discuté plus haut. Cependant, toutes ces méthodes requièrent actuellement d'utiliser le stencil de discrétisation canonique de la grille cartésienne, et ne sont donc pas appropriées pour gérer les fortes anisotropies. Pour y remédier, nous recherchons des structures de données compatibles avec ces architectures mais aussi avec nos stencils de discrétisation anisotropes.*

---

<sup>6</sup>Grâce au champ de vitesses upwind obtenu.

**Projets et perspectives** (Quantification de la non-causalité des discrétisations d'équations eikonales). *Les méthodes numériques pour la résolution des équations eikonales se divisent actuellement en deux groupes : (I) les discrétisations causales, numériquement résolues par des algorithmes en une passe de type Dijkstra, et (II) les discrétisations non-causales, résolues par des méthodes itératives génériques. Nous souhaitons remplacer cette dichotomie par une gradation, en quantifiant au sein du second groupe dans quelle mesure une discrétisation donnée est non-causale, et en exploitant cette propriété au sein de l'algorithme de résolution. Des résultats préliminaires ont été obtenus sur des modèles jouets en dimension 1, où nous remplaçons par exemple la différence finie amont  $h\partial_x u \approx u(x) - u(x-h)$  par*

$$h\partial_x u \approx (1 + 2\gamma)u(x) - (1 + \gamma)u(x-h) - \gamma u(x+h),$$

où la constante  $\gamma \geq 0$  quantifie le caractère non-amont. Les contextes visés concrètement sont les métriques de Rander sur grille cartésienne, voir §3.1.3, et les métriques riemanniennes sur nuage de points en prenant pour point de départ le travail [RL16], voir la perspective de recherche ci-dessous.

### Schémas numériques semi-lagrangiens.

Les méthodes *semi-lagrangiennes* de calcul des temps d'arrivée (1.3) sont fondées sur une propriété de consistance interne de la fonction valeur  $u : \bar{\Omega} \rightarrow [0, \infty]$ , appelée principe d'optimalité de Bellman. Elle exprime qu'un chemin minimal de  $\partial\Omega$  à  $\mathbf{p} \in \Omega$  peut se décomposer en la concaténation de deux chemins minimaux, de  $\partial\Omega$  à un certain  $\mathbf{q} \in \partial V(\mathbf{p})$  et de  $\mathbf{q}$  à  $\mathbf{p}$  respectivement, où  $V(\mathbf{p}) \subseteq \Omega$  est un voisinage arbitraire de  $\mathbf{p}$ . Ainsi, en notant  $d_{\mathcal{F}}$  la quasi-distance<sup>7</sup> associée à  $\mathcal{F}$ ,

$$u(\mathbf{p}) = \inf_{\mathbf{q} \in \partial V(\mathbf{p})} d_{\mathcal{F}}(\mathbf{q}, \mathbf{p}) + u(\mathbf{q}). \quad (1.6)$$

Les schémas numériques semi-lagrangiens miment, dans le domaine discret, cette propriété. Soient  $X$  et  $\partial X$  des parties discrètes de  $\mathbb{E}_d$  destinées à approcher  $\Omega$  et  $\partial\Omega$ , et pour tout  $\mathbf{p} \in X$  soit  $V(\mathbf{p})$  un polytope contenant  $\mathbf{p}$  et dont les sommets appartiennent à  $X \cup \partial X$ . Trouver  $U : X \cup \partial X \rightarrow [0, \infty]$  tel que pour tout  $\mathbf{p} \in X$

$$U(\mathbf{p}) = \inf_{\mathbf{q} \in \partial V(\mathbf{p})} \mathcal{F}_{\mathbf{p}}(\mathbf{p} - \mathbf{q}) + I_{V(\mathbf{q})} U(\mathbf{q}), \quad (1.7)$$

et  $U(\mathbf{p}) = 0$  pour tout  $\mathbf{p} \in \partial X$ . En comparaison avec (1.6), la distance  $d_{\mathcal{F}}(\mathbf{q}, \mathbf{p})$  est approchée à l'aide de la métrique locale  $\mathcal{F}_{\mathbf{p}}(\mathbf{p} - \mathbf{q})$ , et les valeurs de  $U$  aux points  $\mathbf{q} \in \partial V(\mathbf{p})$  qui ne sont pas des sommets sont approchées par l'interpolation linéaire  $I_{V(\mathbf{p})} U(\mathbf{q})$ .

Sethian et al [SV03, Vla08], ont identifié une propriété géométrique dite d'*angle aigu*, portant sur les couples  $(V(\mathbf{p}), \mathcal{F}_{\mathbf{p}})_{\mathbf{p} \in X}$  de stencil et métrique locale, impliquant la propriété *causalité* du système (1.7), voir §B.

Notre contribution est la construction de stencils respectant la propriété d'angle aigu, donc définissant des schémas numériques causaux, appelés Fast Marching using Lattice

---

<sup>7</sup>Une quasi-distance obéit aux axiomes de séparation et à l'inégalité triangulaire, mais n'est pas forcément symétrique et peut prendre des valeurs infinies.

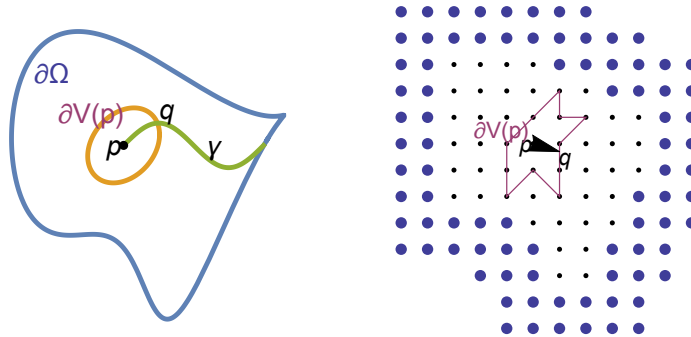


FIGURE 1.5 – Gauche : Illustration du principe d’optimalité de Bellman. Droite : Sa discrétisation, qui est à la fondation des schémas semi-lagrangiens.

*Left : Illustration of Bellman’s optimality principle. Right : Discretization of this principle, which is a the foundation of semi-Lagrangian numerical schemes for eikonal PDEs.*

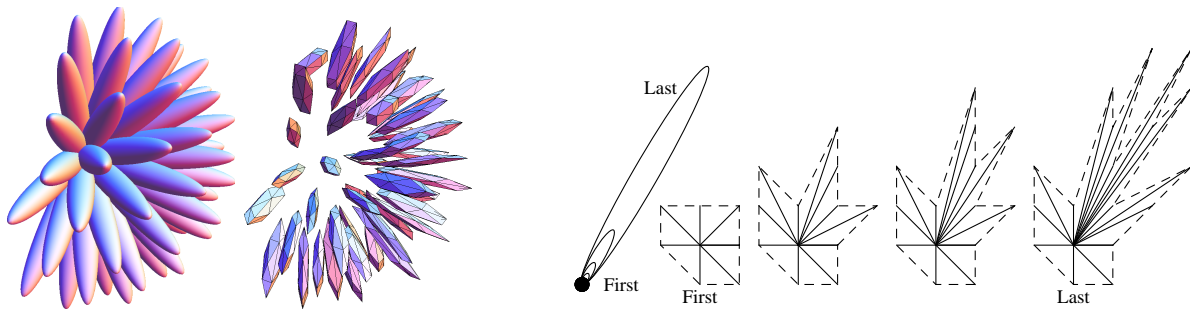


FIGURE 1.6 – Boule unité et stencil associé dans nos schémas semi-lagrangien. Gauche : Cas d’une norme  $\|\cdot\|_M$ ,  $M \in S^{++}(\mathbb{E}_3)$ , et du schéma FM-LBR. Droite : Cas d’une norme finslerienne asymétrique sur  $\mathbb{E}_2$ , et du schéma FM-ASR.

*Unit ball of a norm, and corresponding stencil in our semi-Lagrangian schemes. Left : Case of a norm  $\|\cdot\|_M$ , where  $M \in S^{++}(\mathbb{E}_3)$ , and of the FM-LBR scheme §2.1. Right : Case of a non-symmetrical norm on  $\mathbb{E}_2$ , and of the FM-ASR scheme §2.2.*

Basis Reduction (FM-LBR) et Fast Marching using Anisotropic Stencil Refinement (FM-ASR), voir respectivement §2.1 issu de [Mir14a], et §2.2 issu de [Mir14b]. Pour les métriques riemanniennes nous utilisons le concept de triangulation de Delaunay, et dans le cas de métriques finsleriennes bidimensionnelles nous utilisons l'arbre de Stern-Brocot, voir la Figure 1.6. Notre approche requiert que l'ensemble discret  $X \cup \partial X$  soit une grille cartésienne. Des constructions antérieures existaient [SV03, AM11, KS98, SK04], mais elles étaient bien moins efficaces à cause de la grande taille et du grand nombre de sommets des polytopes obtenus. Nos gains ont rendu possibles les applications [CCM14, BDMS15, CMC16c, DMMP16] et [CMC16a, CMC16b, CC17a, CC17b] notamment, et ont été distribués au sein du code open source [Mir15a].

**Projets et perspectives** (Extension de l'algorithme FM-ASR aux nuages de points bi-dimensionnels quelconques). *Nous étudions une généralisation de cet algorithme, dédié aux équations eikonales finsleriennes en dimension deux, voir §2.2, aux géométries représentées par un ensemble discret quelconque de points  $L \subseteq \mathbb{E}_2$  du plan au lieu d'une grille cartésienne. Ceci est motivé par les applications, qui demandent une meilleure résolution numérique dans certaines zones que d'autres (e.g. port et pleine mer dans le cadre maritime considéré avec J. Dreo).*

*Ce travail requiert de généraliser l'arbre de Stern-Brocot, en remplaçant la somme arithmétique  $\mathbf{t} = \mathbf{q} + \mathbf{r} - \mathbf{p} \in \mathbb{L}_2$  d'éléments du réseau  $\mathbf{p}, \mathbf{q}, \mathbf{r} \in \mathbb{L}_2$  par une construction géométrique, comme "le point de discrétisation  $\mathbf{t} \in L$  appartenant aux cônes engendrés par  $\overrightarrow{\mathbf{p}\mathbf{q}}$  et  $\overrightarrow{\mathbf{p}\mathbf{r}}$ , et le plus proche de son sommet  $\mathbf{p}$ , où  $\mathbf{p}, \mathbf{q}, \mathbf{r} \in L$ ."*

**Projets et perspectives** (Généralisation de l'algorithme FM-LBR fondée sur les étoiles de Delaunay). *Etant donné un nuage de points  $L \subseteq \mathbb{E}_d$  discret, et une famille de tenseurs  $\mathcal{M} : L \rightarrow \mathbb{S}^{++}(\mathbb{E}_d)$ , on appelle étoile de Delaunay en  $\mathbf{p} \in L$  l'union  $V(\mathbf{p})$  des simplexes contenant  $\mathbf{p}$  dans la triangulation de Delaunay de  $L$  associée à la norme  $\|\cdot\|_{\mathcal{M}(\mathbf{p})}$ . Lorsque  $L$  est le réseau  $\mathbb{L}_d$ , et seulement dans ce cas, ces étoiles vérifient la propriété d'angle aigu [SV03], peuvent être calculées rapidement indépendamment les unes des autres, et sont à la fondation de l'algorithme FM-LBR de résolution des équations eikonales riemanniennes, voir §2.1.*

*Un algorithme efficace de construction des étoiles de Delaunay, dans le cadre d'un nuage arbitraire de points, est introduit dans [RL16], et utilisé pour l'amélioration d'une méthode heuristique [CHK13] de calcul de géodésiques riemanniennes. Nous étudions leur utilisation au sein d'un schéma numérique semi-lagrangien.*

## Schémas numériques Eulériens.

L'équation eikonale (1.5) peut également être discrétisée directement, de manière eulérienne, permettant de nouveau le calcul des temps d'arrivée (1.3). Cette discretization prend la forme

$$\mathfrak{F}_{\mathbf{p}}(U(\mathbf{p}), (U(\mathbf{p}) - U(\mathbf{q}))_{\mathbf{q} \in X}) = 1, \quad (1.8)$$

pour tout  $\mathbf{p} \in X$ , avec la condition au bord  $U = 0$  sur  $\partial X$ . De nouveau  $X$  et  $\partial X$  sont des ensembles discrets dédiés à l'approximation du domaine  $\Omega$  et de son bord  $\partial\Omega$ . La résolution stable du système (1.8) est possible pourvu que  $\mathfrak{F}_{\mathbf{p}} : \mathbb{R} \times \mathbb{R}^X \rightarrow \mathbb{R}$  soit *monotone*, c'est à dire croissante en chacune de ses variables. Si de plus  $\mathfrak{F}_{\mathbf{p}}$  est *causale*, c'est à dire dépend

seulement des parties positives des différences  $(U(\mathbf{p}) - U(\mathbf{q}))_{\mathbf{q} \in X}$ , alors la résolution peut être effectuée en une seule passe par l’algorithme du Fast-Marching, donc très rapidement en pratique, voir §B.2.

Notre contribution est l’introduction d’un schéma numérique *monotone et causal* dans le cas d’une métrique riemannienne et d’une discrétisation sur grille cartésienne, appelé FM-VR1 (Fast Marching using Voronoi’s First Reduction), voir §3.1 issu de [Mir17a]. Il repose sur l’approximation au premier ordre

$$\|du(\mathbf{p})\|_D^2 \approx h^{-2} \sum_{1 \leq i \leq d'} \rho_i \max\{0, u(\mathbf{p}) - u(\mathbf{p} - h\dot{\mathbf{e}}_i), u(\mathbf{p}) - u(\mathbf{p} + h\dot{\mathbf{e}}_i)\}^2, \quad (1.9)$$

où  $D \in S^{++}(\mathbb{E}_d^*)$  est décomposée à sous la forme (1.2) à l’aide de la première réduction de Voronoi. Nous avons également étendu cette approche (avec perte de causalité) aux métriques finsleriennes asymétriques de type Rander §3.1.3. Plusieurs cas intéressants de métriques singulières, définissant des normes “infinies” pour certains vecteurs tangents, sont aussi traités. Ceux-ci correspondent à des systèmes de contrôle non-holonomes, où certaines directions de mouvement sont localement interdites.

Les métriques sous-riemanniennes sont un premier exemple de métrique singulière. On peut les voir comme des métriques riemanniennes dont certaines valeurs propres sont infinies, mais pour lesquelles des propriétés de contrôlabilité locale sont néanmoins satisfaites [Mon06]. Nous approchons ces valeurs infinies par de grandes valeurs, et établissons des taux de convergence pour le schéma numérique résultant, voir §3.1. Avec Duits et al [SBD<sup>+</sup>15, DMMP16], nous avons en particulier implémenté le modèle de Reeds-Shepp, une métrique sous-riemannienne sur  $\mathbb{R}^2 \times \mathbb{S}^1$  décrivant le déplacement de véhicules de type “chaise roulante”, voir la Figure 1.7. Des variantes de ce modèle, posées sur le domaine  $\mathbb{R}^3 \times \mathbb{S}^2$  de dimension  $d = 5$ , sont étudiées §4.1.4.

Nous avons également étudié des métriques conçues pour implémenter une pénalisation de la courbure d’un chemin planaire. Associons à  $\gamma : [0, L] \rightarrow \mathbb{R}^2$ , supposé paramétré à vitesse unité, l’énergie

$$\int_0^L \alpha(\gamma(t), \dot{\gamma}(t)) \mathcal{C}(\xi |\ddot{\gamma}(t)|) dt, \quad (1.10)$$

voir §3.2. L’application visée dicte le coût scalaire  $\alpha$ , le paramètre  $\xi$  homogène à un rayon de courbure, et la fonction  $\mathcal{C}$  convexe et croissante, tous supposés positifs. La courbure locale  $\kappa(t) = \|\ddot{\gamma}(t)\|$  intervenant dans (1.10) est une quantité d’ordre 2, ne pouvant pas apparaître directement dans l’expression d’une métrique  $\mathcal{F}_{\gamma(t)}(\dot{\gamma}(t))$ . Pour palier à cette difficulté, nous introduisons le domaine tri-dimensionnel  $\mathbb{M} := \mathbb{R}^2 \times \mathbb{S}^1$ , dont les éléments  $\mathbf{p} = (\mathbf{x}, \theta)$  sont des paires déterminant une position spatiale et une orientation angulaire. Les vecteurs tangents à cette variété  $\dot{\mathbf{p}} = (\dot{\mathbf{x}}, \dot{\theta}) \in \mathbb{R}^2 \times \mathbb{R}$  contiennent donc une information de vitesse spatiale et angulaire. Munissons  $\mathbb{M}$  de la métrique dégénérée définie lorsque  $\|\dot{\mathbf{x}}\| = 1$  par

$$\mathcal{F}_{\mathbf{p}}(\dot{\mathbf{p}}) = \mathcal{F}_{(\mathbf{x}, \theta)}(\dot{\mathbf{x}}, \dot{\theta}) = \begin{cases} \alpha(\mathbf{x}, \theta) \mathcal{C}(\xi |\dot{\theta}|) & \text{si } \dot{\mathbf{x}} = \mathbf{n}(\theta), \\ +\infty & \text{sinon,} \end{cases}$$

et étendue par homogénéité  $\mathcal{F}_{\mathbf{p}}(\lambda \dot{\mathbf{p}}) = \lambda \mathcal{F}_{\mathbf{p}}(\dot{\mathbf{p}})$  pour tout  $\lambda > 0$ . Par construction, tout chemin  $\eta : [0, L] \rightarrow \mathbb{M}$  de longueur finie vis à vis de la métrique  $\mathcal{F}$  est à une reparamétrisation

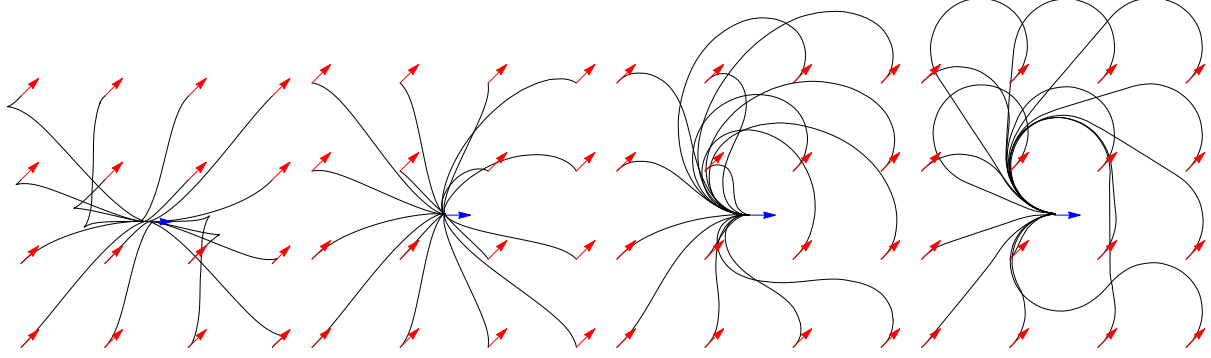


FIGURE 1.7 – Chemins planaires minimisant globalement une énergie dépendant de la courbure, obtenus par la résolution d'équations eikonales dégénérées sur  $\mathbb{R}^2 \times \mathbb{S}^1$ , voir §3.2. De gauche à droite : modèle de Reeds-Shepp réversible, Reeds-Shepp non-réversible, Euler-Mumford, et Dubins. Paramètres du modèle :  $\alpha \equiv 1$ ,  $\xi = 0.3$  (Reeds-Shepp) ou  $\xi = 0.2$  (autres). Point source  $(1/2, 1/2, 0) \in \mathbb{R}^2 \times \mathbb{S}^1$ . Points cible  $(k/3, l/3, \pi/4)$ ,  $k, l \in \{0, \dots, 3\}$ . *Planar paths globally minimizing a curvature dependent energy, obtained by solving a degenerate eikonal PDE on  $\mathbb{R}^2 \times \mathbb{S}^1$ , see §3.2. From left to right : Reeds-Shepp reversible, Reeds-Shepp forward, Euler-Mumford, and Dubins models. Model parameters :  $\alpha \equiv 1$ ,  $\xi = 0.3$  (Reeds-Shepp) or  $\xi = 0.2$  (other). Source point  $(1/2, 1/2, 0) \in \mathbb{R}^2 \times \mathbb{S}^1$ . Target points  $(k/3, l/3, \pi/4)_{k,l=0}^3$ .*

sation près le relevé  $\eta = (\gamma, \dot{\gamma})$  d'un chemin planaire  $\gamma : [0, L] \rightarrow \mathbb{R}^2$  paramétré à vitesse unité<sup>8</sup>. De plus la longueur  $\text{length}_{\mathcal{F}}(\eta)$ , définie par (1.4), égale (1.10) comme souhaité.

Nous nous sommes intéressés aux coûts classiques associés aux modèles de Reeds-Shepp [RS90, DMMP16], de Euler-Mumford [Mum94], et de Dubins [Dub57], qui pénalisent de manière croissante les fortes courbures et dont l'expression est la suivante :

$$\mathcal{C}^{\text{RS}}(\kappa) := \sqrt{1 + \kappa^2}, \quad \mathcal{C}^{\text{EM}}(\kappa) := 1 + \kappa^2, \quad \mathcal{C}^{\text{D}}(\kappa) := \begin{cases} 1 & \text{si } \kappa \leq 1, \\ +\infty & \text{sinon.} \end{cases}$$

Notre contribution est la conception de schémas numériques pour les métriques (dégénérées) correspondant à ces coûts. Les premiers essais étant semi-lagrangiens *non-causaux* [BDMS15, CMC17], puis des schémas Euleriens causaux ont été établis, voir §3.2 issu de [Mir17b, DMMP16].

**Projets et perspectives** (*Court terme. Modèles dissymétriques*). Avec *L. Cohen et Da Chen*, nous nous intéressons à des modèles de chemins davantage paramétrables et notamment dissymétriques, dont la métrique prend la forme

$$\mathcal{F}_{(\mathbf{x}, \theta)}(\dot{\mathbf{x}}, \dot{\theta}) := \alpha(\mathbf{x}, \theta) \mathcal{C} \left( \xi(\mathbf{x}, \theta) (\dot{\theta} - \kappa(\mathbf{x}, \theta)) \right) \quad \text{si } \dot{\mathbf{x}} = \mathbf{n}(\theta),$$

avec l'extension usuelle par 1-homogénéité positive, et par  $+\infty$  sinon. Le champ scalaire  $\kappa : \mathbb{M} \rightarrow \mathbb{R}$  définit une courbure de référence, par rapport à laquelle on pénalise la courbure du chemin. En choisissant par exemple un champ constant non nul  $\kappa \equiv \kappa_0 \in \mathbb{R}$ , on

<sup>8</sup>Cette interprétation heuristique doit être légèrement modifiée pour les modèles autorisant la *rotation sur place*, comme le modèle de Reeds-Shepp sans marche arrière.

*implémente un véhicule de Dubins ayant un plus petit rayon de braquage d'un côté que de l'autre, ou encore des elasticæ d'Euler pour un matériau élastique ayant une configuration de repos tordue et non droite. De premiers résultats numériques ont déjà été obtenus, et leur application au traitement de l'image est en cours d'investigation.*

**Projets et perspectives** (Utilisation d'approximations nilpotentes de distances sous-riemanniennes). *Considérons le modèle de Reeds-Shepp sous-riemannien, décrivant typiquement une chaise roulante, initialement aux position et orientation  $(x_0, y_0, \theta_0) = (0, 0, 0)$ . Le coût du chemin menant à la configuration  $(x, y, \theta) \in \mathbb{M}$  peut être localement approché de plusieurs manières, comme*

$$\sqrt{x^2 + \varepsilon^{-2}y^2 + \theta^2}, \quad \sqrt[4]{(x^2 + \theta^2)^2 + y^2}. \quad (1.11)$$

*L'approximation (1.11, gauche), faisant intervenir un petit paramètre  $\varepsilon > 0$ , est une relaxation riemannienne, actuellement utilisée dans nos schémas numériques pour ce modèle et ses variantes [SBD<sup>+</sup>15, DMMP16]. Nous souhaitons développer des méthodes fondées sur l'approximation locale (1.11, droite), qui est bien plus fidèle [BCP17]. Des principes similaires sont susceptibles de s'appliquer aux autres systèmes non-holonomes étudiés, par exemple les Elasticæ de Euler-Mumford.*

### Applications, notamment en segmentation d'images.

Le traitement des images médicales est une motivation majeure des mes travaux sur la résolution numérique des équations eikonales anisotropes. Les applications dans ce domaine présentées ci-dessous sont développées en collaboration avec L. Cohen<sup>9</sup> [CMC16a, CMC16b, CC17a, CC17b, CCM14, CMC16c] et plus récemment avec R. Duits<sup>10</sup> [SBD<sup>+</sup>15, DMMP16]. Des applications indépendantes, dans le domaine de la planification de mouvement et de la surveillance, sont développées avec J. Dreo<sup>11</sup> et discutées §4.3.

L'utilisation de chemins minimaux, issus de la résolutions d'équations eikonales, pour la segmentation de contours d'objets ou de structures tubulaires dans des images a été introduite par Cohen et Kimmel [CK97], voir l'introduction historique §4.1.1. Le choix de métriques anisotropes est naturel dans ce contexte, pour mieux guider ces chemins le long des structures d'intérêt, et éviter les problèmes dits de "cours-circuits" et de "fuites". Cet enrichissement était rendu difficile en pratique par la mauvaise performance des algorithmes connus [BC10] dans le cas de fortes anisotropies, mais cette limitation a été essentiellement levée grâce aux contributions de ce mémoire. Des améliorations de temps de calcul pouvant atteindre quatre (!) ordres de grandeur ont été obtenues dans les cas tests du domaine [Mir14a], et de nombreuses applications ont été rendues possibles, voir la Figure 1.8 et les références ci-dessus.

Je souhaite mettre en avant deux développements, initialement inattendus, qui n'auraient pu être envisagés sans des algorithmes efficaces pour la résolution des équations eikonales anisotropes. Le premier est lié à la minimisation d'énergies de segmentation, de

---

<sup>9</sup>Directeur de Recherches CNRS, Laboratoire Ceremade, Université Paris-Dauphine

<sup>10</sup>Professeur à l'Université TU/e d'Eindhoven

<sup>11</sup>PhD, Thales Research and Technology

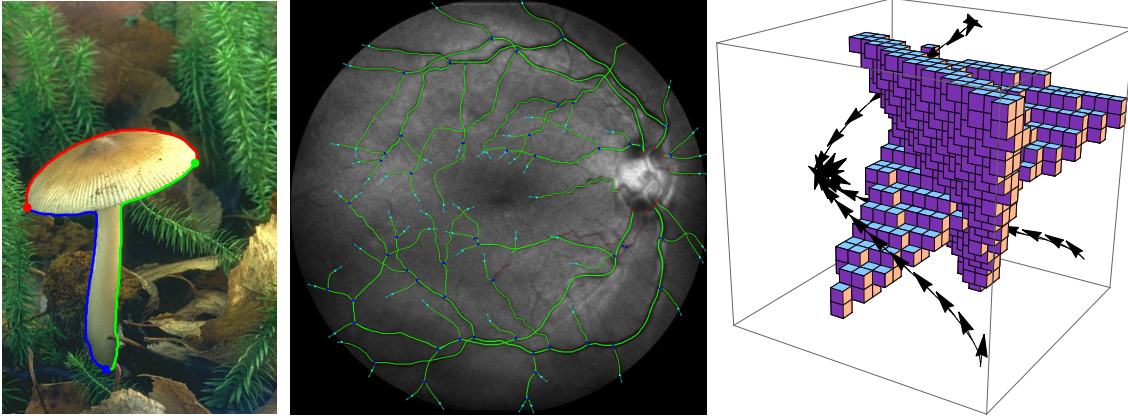


FIGURE 1.8 – Gauche : Segmentation fondée sur la minimisation une énergie (1.12) de type Chan-Vese. Notre méthode numérique extrait le bord en tant que géodésique minimisante pour une métrique asymétrique, voir §4.2 issu de [CMC16b]. Centre : Segmentation du réseau vasculaire rétinien, utilisant des chemins minimaux pour le modèle de Reeds-Shepp [SBD<sup>+</sup>15]. Droite : Chemins minimaux pour le modèle de Reeds-Shepp sans marche arrière, posé sur  $\mathbb{R}^3 \times \mathbb{S}^2$ , avec obstacles.

*Left : Region segmentation based on the minimization of an energy (1.28) of Chan-Vese type, extracting the boundary as a minimal geodesic w.r.t. an asymmetric metric, see §4.2 from [CMC16b]. Center : Segmentation of the retinal vascular tree, based on minimal paths for a data-driven Reeds-Shepp model [SBD<sup>+</sup>15]. Right : Minimal paths for the Reeds-Shepp forward model, defined on  $\mathbb{R}^3 \times \mathbb{S}^2$ , with obstacles.*

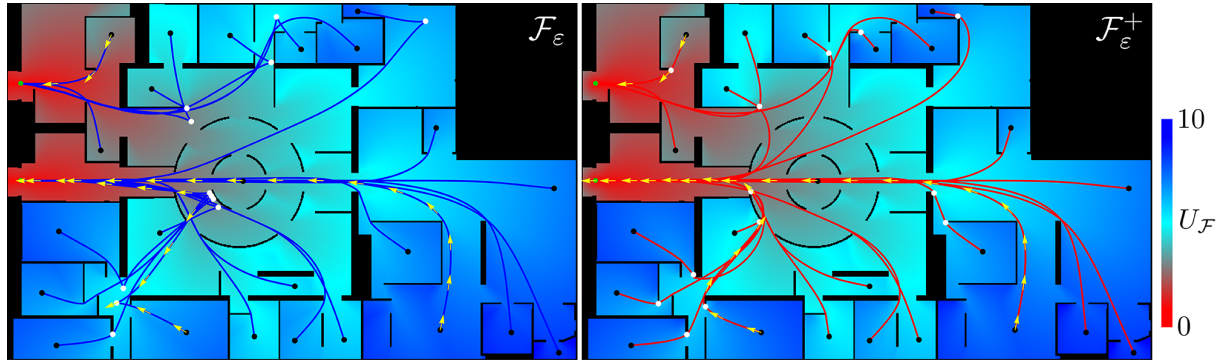


FIGURE 1.9 – Comparaison des plus courts chemins des points (noirs) au sorties (vertes) du centre Pompidou, pour le modèle de Reeds-Shepp avec (gauche) ou sans (droite) marche arrière. En blanc apparaissent les points singuliers des différents modèles : points de rebroussement (gauche), ou de rotation sur place (droite).

*Comparison between the shortest paths from some points (black) to the exits (green), in a map of Centre Pompidou, for cars with (left, blue lines) or without (right, red lines) reverse gear. The yellow arrows indicate the orientation of the curve. The background colors show the distances at each position, minimized over the orientation. White points indicate the curve singularities : cusps (left), or in-place rotations (right).*

type Chan-Vese [CV01] : associons à toute partie de bord rectifiable  $U$  d'un domaine  $\Omega$  l'énergie

$$\mathcal{E}(U) = \int_U f + \int_{\partial U} g, \quad (1.12)$$

où  $f, g : \Omega \rightarrow \mathbb{R}$  sont données,  $g$  étant positive. L'approche classique pour minimiser (1.12) consiste à introduire une fonction  $\psi : \Omega \rightarrow \mathbb{R}$  dont la région d'intérêt est un ensemble de niveau :  $U = \{\mathbf{p} \in \Omega; \psi(\mathbf{p}) < 0\}$ . La mise en oeuvre de ces méthodes, dites level set, pose cependant plusieurs difficultés, comme la sensibilité à l'initialisation, la création fréquente de petites composantes connexes indésirables, et le coût numérique. Nous avons observé, en dimension  $d = 2$  et en utilisant le théorème de la divergence, que le bord  $\partial U$  de l'ensemble minimal était une géodésique pour une métrique de Rander, à savoir

$$\mathcal{F}_{\mathbf{p}}(\dot{\mathbf{p}}) = g(\mathbf{p})\|\dot{\mathbf{p}}\| + \langle \omega(\mathbf{p})^\perp, \dot{\mathbf{p}} \rangle.$$

où le champ de vecteurs  $\omega : \overline{\Omega} \rightarrow \mathbb{E}_2$  satisfait  $\operatorname{div} \omega = f$  et  $\|\omega^\perp\| < 1$  au voisinage de  $\partial U$ . Cette reformulation permet de minimiser (1.12) en calculant, par la résolution d'une équation eikonale, le chemin minimal pour la métrique anisotrope et asymétrique ci-dessus. Voir §4.2, issu de [CMC16b].

Le second développement concerne la segmentation du réseau vasculaire rétinien. L'approche de classique [CK97] pour la segmentation d'une structure tubulaire est d'introduire une métrique isotrope  $\mathcal{F}_{\mathbf{p}}(\dot{\mathbf{p}}) := \|\dot{\mathbf{p}}\|/s(\mathbf{p})$ , déterminée par un champ scalaire de vitesses  $s : \Omega \rightarrow ]0, \infty[$  prenant de petites valeurs sur la structure d'intérêt et de grandes valeurs sur le fond. On extrait ensuite les chemins minimaux reliant les extrémités de la structure, qui sont déterminées par l'utilisateur ou par un autre algorithme. Cette méthode est malheureusement rendue inopérante par l'intrication et les nombreuses intersections des vaisseaux visibles dans les images de fonds rétinien<sup>12</sup>, voir la Figure 1.8 (centre). En effet, les chemins minimaux obtenus sont la concaténation de branches de plusieurs vaisseaux sanguins. Pour résoudre ce problème, nous enrichissons le modèle de chemin par une pénalisation de la courbure, de type Reeds-Shepp ou Euler-Mumford [SBD<sup>+</sup>15, DMMP16, CMC17], implémentée comme ci-dessus, améliorant une proposition de Duits et al [BDMS15]. Ce nouveau modèle élimine les courts-circuits, en rendant trop coûteux les changements brutaux de direction qui avaient lieu au niveau des intersections, voir §4.1.

**Projets et perspectives** (*Court terme*. Publication des codes informatiques de résolution d'équations eikonales non-holonomes). *Avec J. Portegies, nous clarifions, documentons, et assortissons d'exemples, les codes C++ développés pour le calcul de chemins minimaux avec pénalisation de courbure. Ceci en vue de leur soumission à une revue de recherche reproductible, et leur mise à disposition open-source à la communauté du traitement de l'image.*

**Projets et perspectives** (Planification de mouvements de véhicules). *Avec J. Dreo, nous étudions les applications industrielles des solveurs d'équations eikonales anisotropes développés dans le cadre de mes recherches. Nous nous intéressons en particulier au calcul de trajectoires furtives et à leur détection par des dispositifs de surveillance [MD17].*

---

<sup>12</sup>Précisément, les vaisseaux sont disjoints dans l'espace tri-dimensionnel, mais leurs projections sur l'image se superposent.

Nous souhaitons également les coupler avec les algorithmes de planification multi-agent développés dans le cadre du projet européen SWARM. La pénalisation de la courbure des chemins, permise par les méthodes numériques présentées dans ce mémoire, est un réel plus dans ce cadre compte tenu des contraintes mécaniques des véhicules considérés.

### 1.1.3 Equations du second ordre.

Nous avons étudié la discrétisation des EDPs d'ordre deux, à l'aide d'outils de géométrie algorithmique mêlant anisotropie et structure de réseau - première réduction de Voronoi, et arbre de Stern-Brocot -, déjà appliqués aux équations eikonales dans la section précédent. Nos résultats concernent notamment les EDPs de diffusion anisotrope, l'équation de Monge-Ampère, et la contrainte de convexité. Voir §5 issu de [FM06], §6 issu de [BCM16], et §7 issu de [Mir16a] respectivement.

#### Equation de diffusion anisotrope.

Le domaine de l'imagerie a été moteur, un temps au moins, dans la proposition et l'étude d'EDPs de diffusion très générales, non-linéaires, anisotropes, et typiquement sous forme divergence. Elles prennent la forme

$$\partial_t u(\mathbf{x}, t) = \operatorname{div}(\mathcal{D}_u(\mathbf{x}, t) \nabla u(\mathbf{x}, t)) \quad (1.13)$$

en tout point  $(\mathbf{x}, t) \in \Omega \times ]0, \infty[$ , où  $\Omega \subseteq \mathbb{E}_d$  est le domaine de l'image. Pour compléter le problème, une condition initiale est nécessaire sur  $\Omega \times \{0\}$ , et des conditions au bord sur  $\partial\Omega \times ]0, \infty[$ , par exemple de Neumann.

Par un choix judicieux des tenseurs non-linéaires  $\mathcal{D}_u$ , ce type d'équations permet d'éliminer du bruit<sup>13</sup>, de rehausser les contours, ou d'appliquer des effets artistiques à une image donnée. Voir [Wei98] et la Figure 1.10. Il convient de distinguer les tenseurs non-linéaires mais *isotropes*, comme celui  $\mathcal{D}_u(\mathbf{x}, t) = \operatorname{Id} / \|\nabla u(\mathbf{x}, t)\|$  de Perona et Malik<sup>14</sup> [PM90], des constructions *anisotropes* plus sophistiquées dues par exemple à Weickert [Wei98] et dont les vecteurs propres sont alignés avec les directions localement privilégiées de l'image.

Fehrenbach et l'auteur [FM14] ont introduit un schéma numérique pour l'EDP (1.13), avec des tenseurs de diffusion anisotropes (leur non-linéarité ne posant pas de difficultés dans les applications étudiées). Il est fondé sur l'approximation au premier ordre

$$\|\nabla u(\mathbf{p})\|_D^2 \approx \sum_{1 \leq i \leq d'} \rho_i \frac{(u(\mathbf{p}) - u(\mathbf{p} - h\mathbf{e}_i))^2 + (u(\mathbf{p}) - u(\mathbf{p} + h\mathbf{e}_i))^2}{2h^2}, \quad (1.14)$$

où les poids et offsets  $(\rho_i, \mathbf{e}_i)_{i=1}^{d'}$  sont issus de la première réduction de Voronoi (1.2). L'approximation (1.14) permet d'approcher des énergies elliptiques définies par des champs de tenseurs anisotropes, et donc de résoudre les EDPs de diffusion anisotrope qui sont leurs flots gradients pour la métrique  $L^2$ . Ce schéma préserve le principe du maximum, et utilise un stencil plus compact que les constructions alternatives, voir §5.

<sup>13</sup>Effet de moutonnement présent dans e.g. les prises de vues en basse lumière.

<sup>14</sup> Le modèle de Perona et Malik, introduit sous forme *divergence et isotrope*, et implémenté numéri-

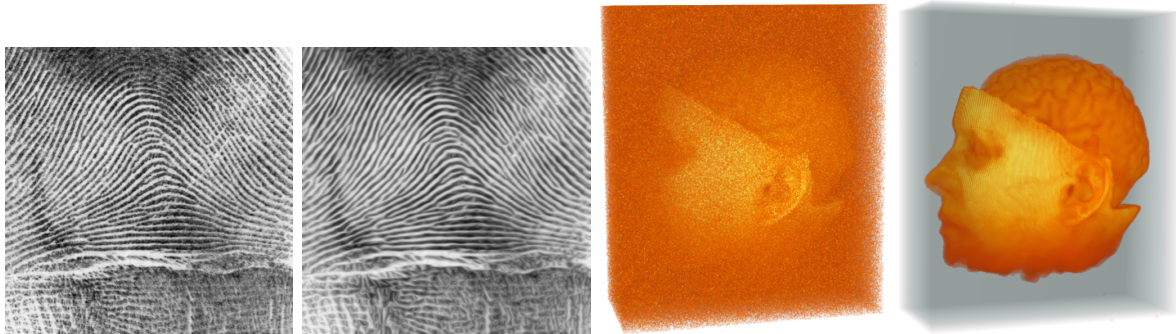


FIGURE 1.10 – Débruitage par diffusion anisotrope, images issues [Mir15a]. Gauche : Empreinte digitale traitée par Coherence Enhancing Diffusion (CED). Droite : Scan IRM (avec bruit artificiel) traité par Edge Enhancing Diffusion (EED). EDPs proposées dans [Wei98], implémentation de [Mir15a].

*Image denoising by anisotropic diffusion. Left : Coherence Enhancing Diffusion applied to a fingerprint image. Right : Edge Enhancing Diffusion applied to IRM data (with artificial noise). PDEs introduced in [Wei98], implementation from [Mir15a].*

Notre approche permet également de traiter les équations de diffusion sous forme non-divergence, grâce à l'approximation au second ordre

$$\text{Tr}(D\nabla^2 u(\mathbf{p})) \approx \sum_{1 \leq i \leq d'} \rho_i \frac{u(\mathbf{p} - h\mathbf{e}_i) - 2u(\mathbf{p}) + u(\mathbf{p} + h\mathbf{e}_i)}{h^2},$$

où les poids et offsets  $(\rho_i, \mathbf{e}_i)_{i=1}^{d'}$  sont de nouveau issus de la première réduction de Voronoi (1.2). Dans le cas particulier de la dimension  $d = 2$ , une construction équivalente avait été proposée antérieurement [BOZ04].

**Projets et perspectives** (Généralisation de la formule de Varadhan aux métriques de Rander). *La formule de Varadhan lie les solutions de l'équation de diffusion en temps court, et de l'équation eikonale, sur une variété riemannienne [Var67]. Elle est à la base de méthodes numériques originales pour le calcul de plus courts chemins riemanniens [CWW12], particulièrement efficaces en dimension  $d = 2$ . Avec D. Prandi, L. Cohen et sont étudiante F. Yang, nous étudions un lien similaire entre les équations de dérive diffusion, et les équations eikonales vis à vis de métriques de Rander non-symétriques.*

### Equation de Monge-Ampère.

L'opérateur de Monge-Ampère fait partie de la classe des opérateurs différentiels *monotones* du second ordre, voir [CIL92] ou la Définition §B.1.1. Sous de faibles hypothèses, ceux-ci peuvent s'exprimer en termes d'opérateurs de diffusion sous forme non-divergence ; toute discrétisation des seconds permet donc de s'attaquer aux premiers, suivant la stratégie [KT92]. Dans le cas de Monge-Ampère, ceci découle de l'identité

$$d(\det M)^{\frac{1}{d}} = \inf\{\text{Tr}(DM); D \in S^{++}(\mathbb{E}), \det D = 1\}$$

quement comme tel, est parfois artificiellement reformulé sous forme *non-divergence et non-isotrope*, ce qui a entraîné une malheureuse confusion terminologique [Wei98].

valable pour tout  $M \in S^+(\mathbb{E})$ . Plus précisément, en dimension  $d = 2$  et en regroupant les matrices  $D \in S^{++}(\mathbb{E}_2)$  suivant le support de leur décomposition associée à la première réduction de Voronoi (1.2), nous aboutissons à une discrétisation monotone et consistante de l'opérateur de Monge-Ampère, voir §6 issu de [BCM16]. Elle s'écrit, pour  $u$  convexe et régulière

$$\det(\nabla^2 u(\mathbf{p})) \approx \min_{(\hat{\mathbf{e}}_0, \hat{\mathbf{e}}_1, \hat{\mathbf{e}}_2) \in \mathcal{B}} H(\Delta_{\hat{\mathbf{e}}_0}^+ u(\mathbf{p}), \Delta_{\hat{\mathbf{e}}_1}^+ u(\mathbf{p}), \Delta_{\hat{\mathbf{e}}_2}^+ u(\mathbf{p})) \quad (1.15)$$

où  $\mathcal{B} \subseteq (\mathbb{L}_2)^3$  désigne l'ensemble des superbases de  $\mathbb{L}_2$ , et où  $H$  est une fonction explicite et croissante en ses trois variables. On a noté  $\Delta_{\hat{\mathbf{e}}}^+ u(\mathbf{p}) := \max\{0, u(\mathbf{p} - h\hat{\mathbf{e}}) - 2u(\mathbf{p}) + u(\mathbf{p} + h\hat{\mathbf{e}})\}/h^2$  la partie positive de la différence finie seconde de  $u$  dans la direction  $\hat{\mathbf{e}}$ , sur une grille cartésienne d'échelle  $h > 0$ . Cette approche améliore les résultats [FO11b], en éliminant l'erreur de consistance.

Dans le cadre de ces recherches, nous avons également établi la convergence d'un Algorithme de Newton amorti [Mir15b] appliqué à la discrétisation de l'équation de Monge-Ampère en dimension  $d = 3$ . Cette technique fut reprise par Mérigot et al [KMT16] pour établir la convergence de schémas de transport optimal semi-discrets sous les hypothèses géométriques générales de Loeper et Ma-Trudinger-Wang [MTW05].

Mérigot et l'auteur ont également introduit une nouvelle discrétisation des équations d'Euler des fluides incompressibles, avec conditions au bord de Dirichlet [MM16], en utilisant les méthodes du transport optimal semi-discret [OP89, AHA98], qui sont liées bien que distinctes. Nous nous intéressons au problème de reconstruction des états intermédiaires du fluide, avec données au bord, et non au problème de Cauchy considéré dans [dGWH<sup>+</sup>15] avec des techniques liées. Nous avons publié les premiers résultats numériques en dimension deux pour ce problème, voir la Figure 1.11, et mis en lumière des comportements paradoxaux étudiés par Brenier [Bre08]. Cette thématique a ensuite été développée au sein de l'équipe Mokaplan/MAGA, avec un schéma pour le problème de Cauchy par Gallouet et al [GV16], et une approche numérique différente due à Benamou et al [BCC<sup>+</sup>15].

**Projets et perspectives** (Discrétisations monotones et consistantes d'opérateurs de type Hamilton-Jacobi-Bellman du second ordre). *Dans ce travail, entrepris avec J.-D. Benamou et V. Duval, nous développons des schémas numériques robustes, précis, et respectant la monotonie en un sens discret pour des EDPs de HJB associées à des opérateurs extrémaux au sens de Pucci, voir §5. Notre approche, dont le principe est présenté §6.1, généralise nos résultats sur l'équation de Monge-Ampère. Elle donne des schémas consistants, donc bien plus précis que les schémas classiquement considérés dans la littérature [FO11a] qui dépendent d'un paramètre de relaxation et sont seulement asymptotiquement consistants. Nous nous intéressons notamment au cas du 2-laplacien, un opérateur intermédiaire entre le laplacien et celui de Monge-Ampère.*

**Projets et perspectives** (Schémas numériques pour la mécanique des fluides). *Notre travail, avec Q. Merigot [MM16], sur la résolution des équations d'Euler des fluides incompressibles, se prête à des généralisations. Par exemple dans le cadre des équations de Camassa-Holm [GM16], ou des équations d'Euler avec borne supérieure sur la densité [MP15]. Plusieurs schémas de discrétisation sont à l'étude.*

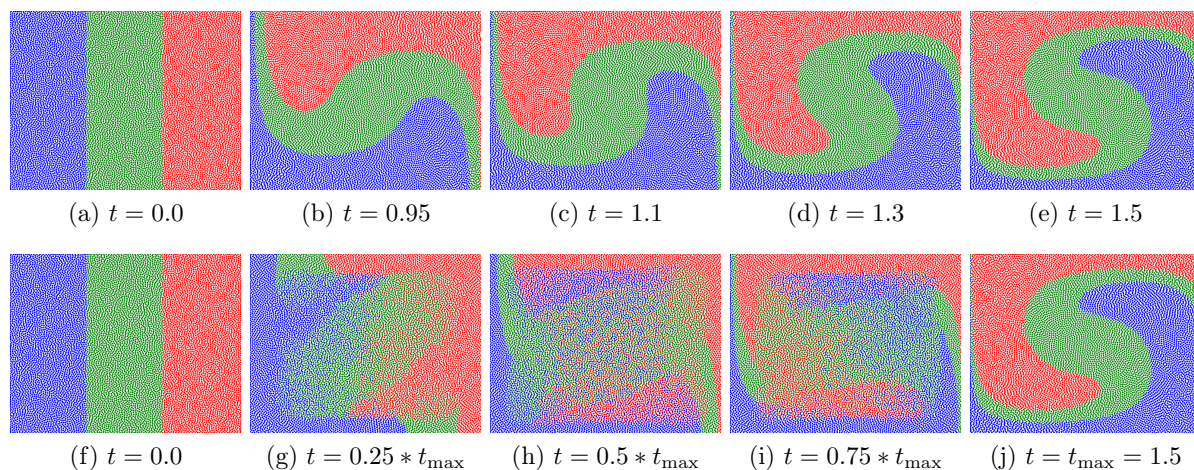


FIGURE 1.11 – Haut : Particules transportées par le flot de Beltrami, qui est solution des équations d’Euler, donc définit une géodésique dans l’espace l’espace des difféomorphismes préservant le volume [Arn66]. Bas : Géodésique minimisante au sens relaxé de Brenier [Bre89], calculée numériquement dans [MM16]. La géodésique minimisante est ici strictement plus courte, et fait apparaître un phénomène a priori paradoxal de mélange.

*Top : Particles transported along the Beltrami flow, which obeys Euler’s equations of incompressible fluids, hence is a geodesic in the space of volume preserving diffeomorphisms [Arn66]. Bottom : Minimizing geodesic, in the relaxed sense of Brenier [Bre89], numerically computed in [MM16]. The minimizing geodesic is here strictly shorter, and displays the paradoxical mixing behavior.*

## Contrainte de convexité.

Le problème du monopoliste, aussi appelé modèle de l’agent principal, fut proposé en économie théorique par Rochet et al [RC98]. Un fabricant de produits, sans concurrence sur son marché, décide librement du catalogue de ses prix et le propose à une population. Ses membres choisissent individuellement le produit du catalogue qui leur est d’utilité maximale, le prix en étant soustrait, ou n’achètent rien si les prix proposés sont excessifs. Connaissant ce comportement général, ainsi que le type et la distribution des fonctions d’utilité au sein de la population, le monopoliste ajuste ses prix pour maximiser son profit.

D’un point de vue mathématique, ce problème est équivalent à la minimisation d’une énergie elliptique dans l’ensemble des fonctions *convexes* sur un domaine. Son instance la plus simple et la plus étudiée est la suivante :

$$\min\left\{\int_{[1,2]^2}\left(\frac{1}{2}|\nabla u(\mathbf{p})|^2 - \langle \nabla u(\mathbf{p}), \mathbf{p} \rangle + u(\mathbf{p})\right) d\mathbf{p}; u \geq 0, u \text{ convexe}\right\}.$$

L’existence d’un minimiseur découle facilement des propriétés de compacité de l’ensemble des fonctions convexes. Lors de la discrétisation, la contrainte de convexité crée cependant de sérieuses difficultés, identifiées dans [CLM06]. Ceci a conduit au développement d’une variété de méthodes numériques [CLRM01, AM08, AM09, EMB10, Obe13, MO14, Wac17, Mir16a]. Pour s’en convaincre, donnons nous un convexe borné  $\Omega \subseteq \mathbb{E}_2$  de dimension deux, posons  $X := \Omega \cap h\mathbb{L}_2$ , où  $h > 0$  est l’échelle de discrétisation, et considérons

$$\text{Conv}(X) := \{u|_X; u : \Omega \rightarrow \mathbb{R} \text{ est convexe}\}.$$

L’ensemble  $\text{Conv}(X) \subseteq \mathbb{R}^X$  est un cône convexe caractérisé par  $\mathcal{O}(N^2)$  inégalités linéaires non-redondantes, où  $N = \#(X)$ , que nous avons identifiées, corrigeant [CLRM01]. Ce grand nombre de contraintes, quadratique en la dimension du problème, rend excessivement coûteuses les discrétisations naïves, fondées sur leur énumération. Notons cependant qu’au plus  $N = \dim(\mathbb{R}^X)$  contraintes non-redondantes peuvent être actives simultanément.

Notre contribution a été d’organiser les contraintes linéaires définissant  $\text{Conv}(X)$  en une structure hiérarchique, fondée sur l’arbre de Stern-Brocot, défini en §A.1.3. Ceci a permis de définir des sur- et sous-cones de  $\text{Conv}(X)$ , définis par un nombre moindre d’inégalités linéaires, et de développer des stratégies adaptatives d’implémentation de la contrainte de convexité. Nous avons ainsi pu améliorer substantiellement l’état de l’art pour ce problème, et comme sous produit estimer (dans certains cas) la complexité moyenne d’une procédure très utilisée en géométrie algorithmique, appelée Edge-Flipping [HOS96], voir §7 et [Mir16a].

**Projets et perspectives** (*Court terme*. Implémentation de la contrainte de convexité par les techniques du transport optimal semi-discret). *Avec Q. Mérigot, nous étudions une nouvelle approche, fondée sur la pénalisation de l’entropie de la mesure image du gradient, pour la minimisation d’énergies dans l’espace des fonctions convexes et des corps convexes. Des résultats préliminaires sont présentés §7, portant sur la conjecture de Meissner et le problème de l’agent principal en dimension 3.*

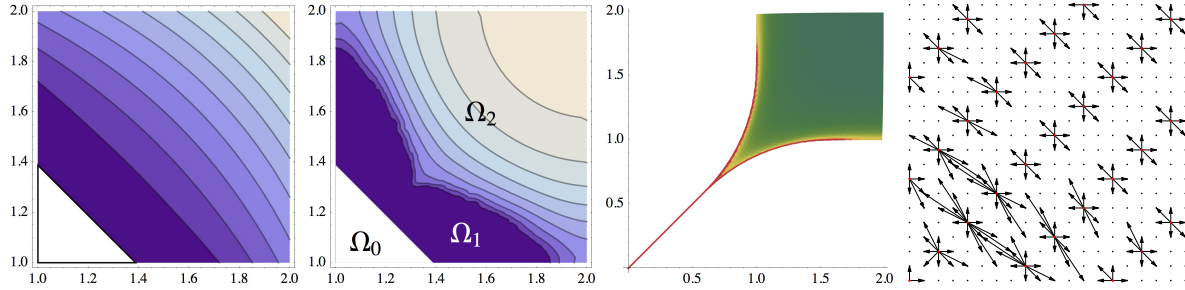


FIGURE 1.12 – Gauche : Solution  $u$  de (1.1.3). Centre-gauche : Régions définies par le rang de  $d^2u$ , et lignes de niveau de  $\det(d^2u)$ . Centre droit : Densité des produits achetés selon ce modèle. Droite : Stencils adaptatifs utilisés pour la discrétisation de la contrainte de convexité, sur grille  $20 \times 20$ .

*Left : Solution  $u$  of (1.2.3). Center-left : Regions defined by the rank of  $d^2u$ , and level lines of  $\det(d^2u)$ . Center-right : Density of products bought according to this model. Right : Adaptive stencils used for the discretization of the convexity constraint, on a  $20 \times 20$  grid.*

### 1.1.4 Faits marquants sur la période 2012-2017

**Distinction.** *Prix Vasil A. Popov*, remis lors de l’International Conference on Approximation Theory, San-Antonio, 22-25 mai 2016. Ce prix international est remis tous les trois ans, depuis 1995, à des chercheurs ayant soutenu leur thèse depuis moins de six ans et ayant apporté des “contributions exceptionnelles à la théorie de l’approximation”.

**Management.** *Porteur de l’ANR NS-LBR, JCJC*, Numerical Schemes using Lattice Basis Reduction, ayant pour objet la conception, l’analyse, et la distribution de schémas numériques pour des EDPs anisotropes sur grille cartésienne (thème de ce mémoire également). Les autres membres de l’équipe sont Laurent Cohen, Jérôme Fehrenbach, et Laurent Risser. Dario Prandi puis Da Chen sont recrutés en tant que post-doctorants en 2016 et 2017.

**Open source.** *Distribution sous forme de code Open-Source des schémas numériques* issus de mes recherches, pour la diffusion anisotrope et les équations eikonales anisotropes<sup>15</sup>, dans l’Insight Journal [MFRT15, Mir15a]. Suite à leur succès, avec 18000 et 25000 téléchargements selon la plateforme, le premier module est repris par la société Kitware (France et USA) et intégré à la librairie pour l’imagerie médicale Insight Toolkit.

**Encadrement.** *Co-encadrement à 25% de Da Chen*, en thèse sous la direction de Laurent Cohen sur la segmentation d’images médicales via des plus courts chemins [Che16], soutenue en septembre 2016. J’ai également participé à l’encadrement de Vijaya Ghorpade, en stage niveau M2 sous la direction de Laurent Cohen, et de Shaza Tobji, en stage niveau M1 sous la direction de Jérôme Fehrenbach et de Laurent Risser.

<sup>15</sup>Schémas semi-lagrangiens seulement. Les schémas hamiltoniens et les techniques de pénalisation de courbure, sont en 2017 encore distribués de manière informelle sur [Github.com/Mirebeau/](https://github.com/Mirebeau/).

**Industrie.** *Collaboration avec Johann Dreo, ingénieur de recherche chez Thalès, sur la thématique du routage de drones [MD17]. Les étudiants Meryem El Yamani et Allan Rakotoarivony ont effectué un stage niveau M2 co-encadré en 2016 et 2017 sur un semestre.*

**International.** *Collaboration avec R. Duits de l'Université d'Eindhoven, autour des algorithmes de type programmation dynamique pour le calcul de distances sous-riemanniennes, et leurs applications à l'imagerie médicale [SBD<sup>+</sup>15, DMMP16].*

**Intégration.** *Au sein de l'équipe Inria Mokaplan, et de l'ANR MAGA, portées par J.-D. Benamou et Q. Merigot, avec lesquelles de fructueuses collaborations sont menées [BCM16, MM16].*

**Naissance.** *Naissance de mes deux filles Rachel et Ariane, pour le bonheur de leurs parents et de leur grand frère Nathanaël, le 16 juin 2013 et le 26 février 2016.*

You don't know on which side of the grid is the dream. (Erin Morgenstern)

## 1.2 Introduction (English version)

This dissertation presents my research in the field of the discretization of Partial Differential Equations (PDEs), focusing on the difficulties associated with anisotropy, and deliberately limiting myself to discretizations on Cartesian grids. The combination of these two choices leads to the use of original geometric tools. The considered PDEs are very diverse, ranging from the Hamilton-Jacobi-Bellman equations to that of Monge-Ampere, as well as anisotropic diffusion, and energy minimization among the set of convex functions. My major contribution, in view of its impact on the image processing community, is the design of variants of the Fast Marching algorithm. These allow the efficient numerical resolution of anisotropic eikonal equations and thus the computation of distances w.r.t Riemannian and Finslerian metrics, and even some non-holonomic models.

Numerical analysis, which is the main domain of this dissertation, consists in constructing and studying discretization schemes for PDEs. These should respect the structural properties of the original PDE, for example a maximum principle, or a property of causality, and be robust enough to extract weak solutions. Satisfying these properties is challenging in the case of anisotropic problems, which feature preferential directions, not aligned with the coordinate axes and non-uniform over the domain. A possible approach, for which I refer to my thesis [Mir11] and references therein, is to design a mesh of the domain which takes into account the geometry of the chosen PDE, by using triangles of appropriately chosen size, shape and orientation. An opposite approach is taken in this dissertation: the discrete representation of the domain uses, systematically, a basic Cartesian grid - for simplicity and because it is natural in the context of image processing - whose regular structure seems to be in obvious conflict with the anisotropic geometry of the problems studied.

The specificity and the coherence of this work are found in the tools, derived from the discrete geometry, used to solve this conflict<sup>16</sup>. We rely on two general constructions of Voronoi, and on two objects of low dimension named the Stern-Brocot tree and Selling’s algorithm. Some of these tools are far from recent, and are well known for their applications in mesh generation, cryptography or arithmetic [Sch09]. To our knowledge, and with the sole the exception of Bonnans and al [BOZ04], their interaction with anisotropic differential operators however had never been studied. The themes of this memoir, PDEs and differential geometry on the Cartesian grid, are reminiscent of *digital geometry* [KR04]; however a closer examination reveals, as it stands, only few common techniques and problems.

The main results of this research are discussed below. We refer to the body of the text for the formal framework, the details of the applications, and additional illustrations. The original articles contain the mathematical proofs, which are not reproduced here. This introduction also highlights several projects and perspectives, that will be the object of future research. The (numerous) figures illustrating this introduction are located in the french version of it, and feature english captions.

**Organization of the dissertation.** This dissertation is organized in two parts, largely independent, regrouping chapters §2-4 and §5-7 respectively. The first part deals with the discretization of anisotropic eikonal equations, using semi-Lagrangian schemes §2, or Eulerian schemes involving a particular representation of the Hamiltonian §3. Applications of these methods to image processing and motion planning are presented in §4. The second part describes the discretization of second-order equations: anisotropic diffusion §5, the Monge-Ampere equation §6, and the constraint of convexity §7. Two appendices serve as a reference for tools used within several chapters. The first §A describes a series of techniques from discrete geometry. The second §B presents two general and abstract formulations of the fast marching algorithm.

### 1.2.1 Geometric tools

Two constructions of Voronoi, referred to as Voronoi’s first and second reductions of a quadratic form, serve as a foundation for many of the numerical schemes presented in this dissertation. These quadratic forms are always assumed to be *positive definite*, and are defined over a vector space  $\mathbb{E}$  of finite dimension containing a lattice  $\mathbb{L}$ . In both cases, Voronoi associates a *discrete* object to the quadratic form, in a way that is *invariant* under the action of the linear transformations stabilizing the lattice.

We denote  $S^{++}(\mathbb{E})$  the set of symmetric positive definite bilinear maps defined on a vector space  $\mathbb{E}$ , which is isomorphic to the set of quadratic forms of interest. Without loss of generality, the vector space is usually  $\mathbb{E}_d := \mathbb{R}^d$  equipped with the canonical euclidean structure, or its dual, and the additive lattice is the set  $\mathbb{L}_d := \mathbb{Z}^d$  of points with integer coordinates.

---

<sup>16</sup> For the sake of consistency, my work on the thin plate models [BCD<sup>+</sup>16] and the Euler equations of incompressible fluids [MM16], will not be discussed in detail. Indeed, the PDE discretizations involved do not use a Cartesian grid, and are based on distinct tools.

Voronoi's first reduction attaches to each  $D \in \mathbb{S}^{++}(\mathbb{E}_d^*)$  the solution to a linear optimization problem  $\mathcal{L}(D)$ , defined as follows:

$$\mathcal{L}(D) := \inf_{M \in \mathfrak{M}} \text{Tr}(MD), \quad \text{where } \mathfrak{M} := \{M \in \mathbb{S}^{++}(\mathbb{E}_d); \forall \dot{\mathbf{e}} \in \mathbb{L}_d \setminus \{0\}, \|\dot{\mathbf{e}}\|_M \geq 1\}. \quad (1.16)$$

We denoted  $\|\cdot\|_M$  the norm defined by  $\|\dot{\mathbf{e}}\|_M^2 = \langle M\dot{\mathbf{e}}, \dot{\mathbf{e}} \rangle = \text{Tr}(M\dot{\mathbf{e}} \otimes \dot{\mathbf{e}})$ , and the latter equality shows that the matrix  $M$  is indeed only subject to linear constraints<sup>17</sup>. Voronoi's first reduction is a well posed optimization problem, in the sense that it has a compact set of solutions, generically a single one [Sch09]. In dimension  $d \in \{2, 3\}$ , the simplex algorithm applied to this problem takes a simple form, which is interesting from a geometrical point of view, and called Selling's algorithm [Sel74], see §A.1.2. For the design of PDE numerical schemes, of first and second order, the main interest of problem (1.16) lies in its *optimality certificate*. The Karush-Kuhn-Tucker conditions indeed state that there exists  $(\rho_i, \dot{\mathbf{e}}_i)_{i=1}^{d'} \in (\mathbb{R}_+ \times \mathbb{L}_d)^{d'}$ , respectively Lagrange multipliers and vectors associated to the active constraints, where  $d' := d(d+1)/2$  is the vector dimension of the space of quadratic forms, such that

$$D = \sum_{1 \leq i \leq d'} \rho_i \dot{\mathbf{e}}_i \otimes \dot{\mathbf{e}}_i. \quad (1.17)$$

See Figure 1.1. This is reminiscent of the expression  $D = \sum_{1 \leq i \leq d} \mu_i \dot{\mathbf{v}}_i \otimes \dot{\mathbf{v}}_i$  of a matrix in terms of its eigenvalues and eigenvectors  $(\mu_i, \dot{\mathbf{v}}_i)_{i=1}^d \in (\mathbb{R} \times \mathbb{S}^{d-1})^d$ . The fundamental advantage of (1.17) is however that the vectors  $\dot{\mathbf{e}}_i \in \mathbb{L}_d$  have integer coordinates, and can thus be used for the design of finite differences schemes on Cartesian grids, for eikonal §3, diffusion §5, or Monge-Ampere §6 PDEs. The norm  $\max_{i=1}^{d'} \|\dot{\mathbf{e}}_i\|$  of the vectors appearing in (1.17) dictates the *stencil width* of these PDE schemes, which is related to their accuracy, numerical cost, parallelization potential, and to the difficulty of implementing boundary conditions. Estimating this norm, and establishing the optimality of this construction, is the subject of Theorems 2.1.5 and 2.1.6, and of Propositions 3.2.3 and 5.1.2.

Voronoi's second reduction involves the Voronoi cell of  $M \in \mathbb{S}^{++}(\mathbb{E}_d)$ , defined as the polytope containing all points closer to the origin 0 than to any other point with integer coordinates

$$\text{Vor}(M) := \{\mathbf{p} \in \mathbb{E}_d; \forall \mathbf{e} \in \mathbb{L}_d, \|\mathbf{p}\|_M \leq \|\mathbf{e} - \mathbf{p}\|_M\}. \quad (1.18)$$

Voronoi's second reduction attaches to  $M$  the Delaunay triangulation  $\text{Del}(M)$ , defined as the dual to the tiling of  $\mathbb{E}_d$  by the region  $\text{Vor}(M)$  and its translates by vectors  $\mathbf{e} \in \mathbb{L}_d$ . The Delaunay triangulation is a fundamental object in algorithmic geometry, usually defined with  $M = \text{Id}$  and an arbitrary set of sites instead of  $\mathbb{L}_d$  in (1.18). See [ES86] and Figure 1.2. The case of periodic sites, considered here, however has an exceptional geometrical property: the internal angles of the triangulation are acute, hence it can be used for the design of semi-Lagrangian schemes for Riemannian eikonal equations, following Sethian et al [SV03], see §2.1.

---

<sup>17</sup>The implicit constraint of positive definiteness  $M \succ 0$  can be omitted, since it is implied by the family of constraints  $\langle M\dot{\mathbf{e}}, \dot{\mathbf{e}} \rangle > 0, \dot{\mathbf{e}} \in \mathbb{L}_d \setminus \{0\}$ .

A last geometrical object will be useful, called the Stern-Brocot tree and defined in dimension  $d = 2$  only. The original description of the Stern-Brocot tree involves rational scalar labels, see [Bro62, Niq07] and Figure 1.3, but we choose here an alternative construction that is more suitable for our application, see §A.1.3 for details. The Stern-Brocot tree is an infinite complete binary tree whose nodes are (here) labeled with pairs of integer vectors  $(\mathbf{e}, \mathbf{f}) \in \mathbb{L}_2^2$  belonging to the first quadrant  $\mathbb{R}_+^2$  and such that  $\det(\mathbf{e}, \mathbf{f}) = 1$ . The children of node labeled  $(\mathbf{e}, \mathbf{f})$  are labeled  $(\mathbf{e}, \mathbf{e} + \mathbf{f})$  and  $(\mathbf{e} + \mathbf{f}, \mathbf{f})$ . Descending into the Stern-Brocot tree allows to refine angular sectors, in a way compatible with the Cartesian grid. This tree intervenes in the discretization of Finslerian eikonal equations §2.2, and of the constraint of convexity §7. In the context of the numerical analysis of PDEs, the Stern-Brocot tree was first used in [BOZ04].

**Projects and perspectives** (*Short term.* Voronoi reductions in dimension 4 and 5). *Voronoi reductions are particularly simple to implement in dimension  $d \in \{2, 3\}$ , thanks to Selling’ algorithm, see §A.1.2. This particular case is used in all our computer programs, and in all the numerical results presented. The experiments involving 5-dimensional sub-Riemannian eikonal equations, see §4.1.4, are made possible by the block-diagonal structure of the metric.*

*In the short term, we intend to produce a fast and robust C++ implementation of Voronoi’s first reduction in dimension 4 and 5, based on the classification results [CS88]. The resulting numerical schemes will be used for applications which are relevant in these dimensions, especially in sub-Riemannian geometry and for stochastic control problems.*

**Projects and perspectives** (Extension of Voronoi’s first reduction to point clouds). *It is tempting to generalize the linear program (1.16) by replacing the Cartesian grid  $\mathbb{L}_d$  with an arbitrary set of points  $L \subseteq \mathbb{R}^d$ . This yields a decomposition similar to (1.2), in principle applicable to the discretization of PDEs in an unstructured environment.*

*We study this possibility, but keep in mind certain issues: (i) This approach is not applicable to the discretization of Riemannian eikonal equations (1.9), because they crucially use the symmetry of the set of offsets:  $\dot{\mathbf{e}} \in L \Leftrightarrow -\dot{\mathbf{e}} \in L$ . (ii) For the discretization of diffusion equations, additional constraints must be added to ensure that  $\sum_{i=1}^d \rho_i \dot{\mathbf{e}}_i = 0$ , otherwise an undesirable first-order term is introduced. (iii) The generalized problem (1.16) is often ill posed, for example in dimension  $d = 2$  if  $L = (\mathbb{Z} \setminus \{0\}) \times \mathbb{Z}$  and  $D$  is the identity matrix.*

## 1.2.2 Eikonal equations

Eikonal equations are static, first order partial differential equations of Hamilton-Jacobi-Bellman type, which characterize solutions of deterministic optimal control problems [BCD08]. We focus on the simplest case, where the objective is to find the shortest path from the boundary of a domain  $\Omega \subseteq \mathbb{E}_d$  to a given point  $\mathbf{p} \in \Omega$

$$u(\mathbf{p}) := \inf\{\text{length}_{\mathcal{F}}(\gamma); \gamma : [0, 1] \rightarrow \bar{\Omega}, \gamma(0) \in \partial\Omega, \gamma(1) = \mathbf{p}\}. \quad (1.19)$$

The considered paths  $\gamma : [0, 1] \rightarrow \bar{\Omega}$  are implicitly assumed to be locally Lipschitz. Path length is measured using a given metric  $\mathcal{F} : \bar{\Omega} \times \mathbb{E}_d \rightarrow [0, \infty]$ , assumed to be convex and

1-homogenous in its second argument:

$$\text{length}_{\mathcal{F}}(\gamma) := \int_0^1 \mathcal{F}_{\gamma(t)}(\dot{\gamma}(t)) dt. \quad (1.20)$$

Our results encompass a variety of models, going much beyond the classical case of conformal metrics [Tsi95, Set96, RT92], which are locally proportional to the euclidean metric and thus take the form  $\mathcal{F}_{\mathbf{p}}(\dot{\mathbf{p}}) = \|\dot{\mathbf{p}}\|/s(\mathbf{p})$  where  $s : \bar{\Omega} \rightarrow ]0, \infty[$  is a given speed function. We indeed address Riemannian metrics in §2.1, Finslerian metrics in §2.2, as well as degenerate metrics associated with non-holonomic optimal control problems in §3. These metric structures are illustrated on Figure 1.4.

The eikonal equation is, as announced, a PDE obeyed by the front arrival time function  $u : \bar{\Omega} \rightarrow [0, \infty]$ , in the sense of viscosity solutions [BCD08]. It reads

$$\mathcal{F}_{\mathbf{p}}^*(du(\mathbf{p})) = 1, \quad \text{where } \mathcal{F}_{\mathbf{p}}^*(\dot{\mathbf{p}}) := \sup\{\langle \dot{\mathbf{p}}, \mathbf{p} \rangle; \mathcal{F}_{\mathbf{p}}(\dot{\mathbf{p}}) \leq 1\}, \quad (1.21)$$

for all  $\mathbf{p} \in \Omega$ , with the boundary condition  $u(\mathbf{p}) = 0$  for all  $\mathbf{p} \in \partial\Omega$ . This formalism is the main tool for establishing the convergence of numerical schemes. Convergence rates can be obtained for locally controllable models, see §3.1 and [SMK16, Mir17a]. Otherwise, convergence is established in a weak sense using the notion of discontinuous viscosity solution to a PDE [BCD08], see §3.2 from [Mir17b].

Two approaches can be distinguished for the discretization of the PDE (1.5), based on the semi-Lagrangian and the Eulerian paradigms respectively. Before going into details, I emphasize a second distinction, between *causal* and *non-causal* schemes. Causality, defined in §B, reflects the deterministic nature of the underlying optimal control problem. It is equivalent, in the context of the problems posed on graphs, to the positivity of the lengths of the edges, which enables the rapid extraction of minimal paths using Dijkstra's algorithm instead of the slower method of Bellman-Ford [Dij71]. We make systematically the choice of causal numerical schemes, solved using the Fast-marching algorithm, which generalizes Dijkstra, for several reasons: the guarantee of short computation times, the absence of stopping criteria, a more robust extraction of the geodesics<sup>18</sup>, the possibility of automatic differentiation §4.3.2, ... The computational cost advantage is particularly strong for highly anisotropic and spatially heterogeneous metrics, which are often involved in image processing applications [BC10, Mir14a]. Alternatives to the Fast-Marching algorithm have other advantages, such as a simpler processing of complex geometries (for which causality is difficult to satisfy) [BR06, TCO04, Zha05], or possibilities of parallelization [CV15, Tug08] including on GPU architectures [WDB<sup>+</sup>08, JW08], see also the discussion in §B.

**Projects and perspectives** (Massively parallel algorithms compatible with our adaptive numerical schemes). *Computing minimal paths for non-holonomic models, such as those used to implement curvature penalization in §3.2, requires solving degenerate eikonal equations on spaces which are of quite high dimension, such as  $\mathbb{R}^d \times \mathbb{S}^{d-1}$  where  $d \in \{2, 3\}$ . Reducing computation times, currently about 1 second for interesting test cases, by an order of magnitude would may allow the real time control of some systems (vehicles, robots, ...).*

---

<sup>18</sup>Thanks to the upwind vector field obtained for the velocities.

Parallel numerical methods are an appealing solution, and they do already exist for eikonal equations, including on GPU as discussed above. However all existing methods require using the canonical discretization stencil of the Cartesian grid, which is not suitable for handling strong anisotropies. We are thus looking for algorithms and data structures compatible with these architectures and also with our anisotropic discretization stencils.

**Projects and perspectives** (Intermediate classes between causal and non-causal discretizations of eikonal equations). Numerical methods for the resolution of eikonal equations are currently divided into two groups: (i) causal discretizations, numerically solved by single-pass algorithms of Dijkstra type, and (II) non-causal discretizations, addressed using generic iterative methods. We want to replace this dichotomy with a gradation, by quantifying within the second group to what extent a given discretization is non-causal, and by exploiting this property within the numerical solver. Preliminary results have been obtained for toy models in dimension 1, in which we replace the upwind finite difference  $h\partial_x u \approx u(x) - u(x - h)$  with

$$h\partial_x u \approx (1 + 2\gamma)u(x) - (1 + \gamma)u(x - h) - \gamma u(x + h),$$

where the constant  $\gamma \geq 0$  quantifies the non-upwind character. In practice, we are concerned with Rander metrics on Cartesian grids, see §3.1.3, and with Riemannian metrics on unstructured point sets, see the perspective below.

### Semi-Lagrangian numerical schemes.

Semi-Lagrangian methods for computing the arrival time function (1.19) are based on Bellman's optimality principle, described below and illustrated on Figure 1.5. This principle reflects the fact that a minimal path from  $\partial\Omega$  to a given  $\mathbf{p} \in \Omega$  can be regarded as the concatenation of two minimal paths, from  $\partial\Omega$  to some  $\mathbf{q} \in \partial V(\mathbf{p})$  and from  $\mathbf{q}$  to  $\mathbf{p}$  respectively, where  $V(\mathbf{p}) \subseteq \Omega$  is an arbitrary but fixed neighborhood of  $\mathbf{p}$ . Hence, denoting by  $d_{\mathcal{F}}$  the path length quasi-distance<sup>19</sup> defined from (1.20),

$$u(\mathbf{p}) = \inf_{\mathbf{q} \in \partial V(\mathbf{p})} d_{\mathcal{F}}(\mathbf{q}, \mathbf{p}) + u(\mathbf{q}). \quad (1.22)$$

Semi-Lagrangian numerical schemes mimic, in the discrete setting, this principle. Let  $X$  and  $\partial X$  be finite disjoint subsets of  $\mathbb{E}_d$  devoted to the approximation of  $\Omega$  and  $\partial\Omega$ , and for all  $\mathbf{p} \in X$  let  $V(\mathbf{p})$  be a polytope enclosing  $\mathbf{p}$  and which vertices belong to  $X \cup \partial X$ . Find  $U : X \cup \partial X \rightarrow [0, \infty]$  such that for all  $\mathbf{p} \in X$

$$U(\mathbf{p}) = \min_{\mathbf{q} \in \partial V(\mathbf{p})} \mathcal{F}_{\mathbf{p}}(\mathbf{q} - \mathbf{p}) + I_{V(\mathbf{p})} U(\mathbf{q}), \quad (1.23)$$

and  $U(\mathbf{p}) = 0$  and for all  $\mathbf{p} \in \partial X$ . In comparison with (1.22), the distance  $d_{\mathcal{F}}(\mathbf{p}, \cdot)$  is here approximated using the local metric  $\mathcal{F}_{\mathbf{p}}(\cdot - \mathbf{p})$ , and the values of  $U$  at the points  $\mathbf{q} \in \partial V(\mathbf{p})$  which are not vertices are approximated using the linear interpolation operator  $I_{V(\mathbf{p})} U(\mathbf{q})$ .

---

<sup>19</sup>A quasi-distance obeys the positive definiteness and triangular inequality axioms, but may be asymmetric and may take infinite values.

Sethian et al [SV03, Vla08] discovered a geometrical *acuteness* property, involving the pairs  $(V(\mathbf{p}), \mathcal{F}_{\mathbf{p}})_{\mathbf{p} \in X}$  of a local stencil and metric. It implies the *causality* of the system (1.23), which can thus be solved efficiently using the Fast-Marching algorithm.

The author's contribution is the design of stencils obeying the acuteness property. We use for Riemannian metrics the concept of Delaunay triangulation, see the numerical method referred to as Fast Marching using Lattice Basis Reduction (FM-LBR), described in §2.1 from [Mir14a]. For two dimensional Finslerian metrics we rely on the Stern-Brocot tree, see Fast Marching using Anisotropic Stencil Refinement (FM-ASR), described in §2.2 from [Mir14b]. Our approach requires the discrete set  $X \cup \partial X$  to be a Cartesian grid. Previous constructions [SV03, AM11, KS98, SK04] were much less effective due to the large size and the large number of vertices of the obtained stencils. Our improved methods are an essential ingredient of the application papers [CCM14, BDMS15, CMC16c] and [CMC16a, CMC16b, CC17a, CC17b] respectively. They are distributed within open source codes [Mir15a].

**Projects and perspectives** (Extension of the FM-ASR algorithm to arbitrary two-dimensional point sets). *We study a generalization of this algorithm, devoted to two-dimensional Finslerian eikonal equations, see §2.2, to unstructured point sets  $L \subseteq \mathbb{E}_2$  instead of the Cartesian grid  $\mathbb{L}_2$ . We are motivated by some applications which require a higher numerical resolution in some areas than others (e.g. harbor and open sea in the maritime framework considered with J. Dreo).*

*This work requires generalizing the Stern-Brocot tree structure, by replacing the arithmetic sum  $\mathbf{t} = \mathbf{q} + \mathbf{r} - \mathbf{p} \in \mathbb{L}_2$  of some lattice elements  $\mathbf{p}, \mathbf{q}, \mathbf{r} \in \mathbb{L}_2$  with a geometrical construction, such as the point  $\mathbf{t} \in L$  within the cone generated by  $\mathbf{p}\mathbf{q}$  and  $\mathbf{p}\mathbf{r}$  which is closest to  $\mathbf{p}$ , where  $\mathbf{p}, \mathbf{q}, \mathbf{r} \in \mathbb{L}$ .*

**Projects and perspectives** (Generalization of the FM-LBR algorithm based on Delaunay stars). *Given a point cloud  $L \subseteq \mathbb{E}_d$  and a family of tensors  $\mathcal{M} : L \rightarrow \mathbb{S}^{++}(\mathbb{E}_d)$ , the Delaunay star at  $\mathbf{p} \in L$  is the union of the simplices containing  $\mathbf{p}$  in the Delaunay triangulation of  $L$  defined w.r.t. the norm  $\|\cdot\|_{\mathcal{M}(\mathbf{p})}$ . If  $L$  is the lattice  $\mathbb{L}_d$ , and in this case only, then these stars obey the acuteness property defined in [SV03], can be computed quickly and independently of each other, and are at the foundation of the FM-LBR algorithm for solving Riemannian eikonal equations, see §2.1.*

*An efficient algorithm for the construction of Delaunay stars of general point sets is introduced in [RL16], where it is used to improve an heuristic method [CHK13] for geodesic computation. We consider using them in a semi-Lagrangian numerical scheme.*

### Eulerian numerical schemes.

The eikonal equation (1.21) can also be discretized directly, in an Eulerian way, which yields a distinct numerical method for computing the arrival times (1.3). This discretization takes the form

$$\mathfrak{F}_{\mathbf{p}}(U(\mathbf{p}), (U(\mathbf{p}) - U(\mathbf{q}))_{\mathbf{q} \in X}) = 1, \quad (1.24)$$

for all  $\mathbf{p} \in X$ , with the boundary condition  $U = 0$  on  $\partial X$ . We require  $\mathfrak{F}_{\mathbf{p}} : \mathbb{R} \times \mathbb{R}^X \rightarrow \mathbb{R}$  to be *monotonous*, in other words non-decreasing w.r.t. each entry, since this implies comparison principles and stability properties for solutions of the system (1.24). If in

addition  $\mathfrak{F}_{\mathbf{p}}$  is *causal*, i.e. only depends on the positive parts of the differences  $(U(\mathbf{p}) - U(\mathbf{q}))_{\mathbf{q} \in X}$ , then the system can be solved in a single pass and for a quasi-linear numerical cost using the Fast-Marching algorithm, see §B.2.

Our contribution is the design of a *monotone and causal* numerical scheme, in the case of a Riemannian metric and of a Cartesian discretization grid, based on the first order approximation

$$\|du(\mathbf{p})\|_D^2 \approx h^{-2} \sum_{1 \leq i \leq d'} \rho_i \max\{0, u(\mathbf{p}) - u(\mathbf{p} - h\mathbf{e}_i), u(\mathbf{p}) - u(\mathbf{p} + h\mathbf{e}_i)\}^2, \quad (1.25)$$

where  $D \in S^{++}(\mathbb{E}_d^*)$  is expressed in the form (1.17) using Voronoi's first reduction, see [Mir17a] and §3.1. This approach is extended in §3.1.3 to Rander metrics, a family of non-symmetric Finsler metrics, with the loss of causality. We also address a variety of singular metrics, which associate “infinite” norms to some tangent vectors. They correspond to non-holonomic control systems, in which some directions of motion are inaccessible at some points.

Sub-Riemannian metrics are the simplest instance of such singular metrics. They can be regarded as Riemannian metrics which tensors have some infinite eigenvalues, but for which some local controllability properties are nevertheless satisfied [Mon06]. We relax these infinite eigenvalues into large values, and establish convergence rates for the resulting numerical scheme, see §3.1. With Duits et al [SBD<sup>+</sup>15, DMMP16] We implemented in particular the Reeds-Shepp model, which is a sub-Riemannian metric on  $\mathbb{R}^2 \times \mathbb{S}^1$  appropriate for wheelchair-like vehicles, see Figure 1.7. Several higher dimensional variants, posed on the 5-dimensional domain  $\mathbb{R}^3 \times \mathbb{S}^2$ , are also discussed in §4.1.4.

Some singular metrics, combined with a dimension lifting technique, can be used to encode a penalization of path curvature, see §3.2 from [Mir17b]. Define the energy of a path  $\gamma : [0, L] \rightarrow \mathbb{E}_2$ , parametrized at unit euclidean speed, as

$$\int_0^L \alpha(\gamma(t), \dot{\gamma}(t)) \mathcal{C}(\xi |\ddot{\gamma}(t)|) dt. \quad (1.26)$$

The scalar cost  $\alpha : \mathbb{R}^2 \rightarrow \mathbb{S}^1 \rightarrow \mathbb{R}$ , the parameter  $\xi > 0$  which is homogeneous to a turning radius, and the convex non-decreasing function  $\mathcal{C} : \mathbb{R}_+ \rightarrow \mathbb{R}$ , are positive and dictated by the intended application. Clearly, the path curvature  $\kappa(t) = \|\ddot{\gamma}(t)\|$  is expressed in terms of the second order path derivative, and thus cannot appear as is in the expression  $\mathcal{F}_{\gamma(t)}(\dot{\gamma}(t))$  of a metric. To overcome this difficulty, we introduce the three-dimensional domain  $\mathbb{M} := \mathbb{R}^2 \times \mathbb{S}^1$ , which elements  $\mathbf{p} = (\mathbf{x}, \theta)$  are pairs characterizing a spatial position and an angular orientation. The tangent vectors  $\dot{\mathbf{p}} = (\dot{\mathbf{x}}, \dot{\theta}) \in \mathbb{R}^2 \times \mathbb{R}$  to this manifold therefore contain both spatial and angular velocity information. Let us equip  $\mathbb{M}$  with the degenerate metric defined when  $\|\dot{\mathbf{x}}\| = 1$  by

$$\mathcal{F}_{\mathbf{p}}(\dot{\mathbf{p}}) = \mathcal{F}_{(\mathbf{x}, \theta)}(\dot{\mathbf{x}}, \dot{\theta}) = \begin{cases} \alpha(\mathbf{x}, \theta) \mathcal{C}(\xi |\dot{\theta}|) & \text{if } \dot{\mathbf{x}} = \mathbf{n}(\theta), \\ +\infty & \text{otherwise,} \end{cases}$$

and 1-homogeneously extended  $\mathcal{F}_{\mathbf{p}}(\lambda \dot{\mathbf{p}}) = \lambda \mathcal{F}_{\mathbf{p}}(\dot{\mathbf{p}})$  for all  $\lambda > 0$ . By design, any path  $\eta : [0, L] \rightarrow \mathbb{M}$  of finite length w.r.t. the metric  $\mathcal{F}$  is up to re-parametrization the lift

$\eta = (\gamma, \dot{\gamma})$  of a planar path  $\gamma : [0, L] \rightarrow \mathbb{R}^2$  parameterized at unit euclidean speed<sup>20</sup>. In addition  $\text{length}_{\mathcal{F}}(\eta)$ , defined by (1.20), equals (1.26) as desired.

We focused on three classical curvature costs named by Reeds-Shepp [RS90, DMMP16], Euler-Mumford [Mum94], and Dubins [Dub57], with the following expressions:

$$\mathcal{C}^{\text{RS}}(\kappa) := \sqrt{1 + \kappa^2}, \quad \mathcal{C}^{\text{EM}}(\kappa) := 1 + \kappa^2, \quad \mathcal{C}^{\text{D}}(\kappa) := \begin{cases} 1 & \text{si } \kappa \leq 1, \\ +\infty & \text{sinon.} \end{cases}$$

Our contribution is the design of numerical schemes for the eikonal equations associated with (degenerate) metrics on  $\mathbb{R}^2 \times \mathbb{S}^1$  corresponding to this costs. Our first experiments used non-causal semi-Lagrangian schemes [CMC17, DMMP16], but we eventually managed to design *causal* Eulerian schemes [Mir17b], see §3.2. See Figure 1.7 for some globally minimal paths obtained with the latter method.

**Projects and perspectives** (*Short term. Unsymmetrical models*). *With L. Cohen and Da Chen, we are interested in more configurable path models and in particular in asymmetric models, which metric takes the form*

$$\mathcal{F}_{(\mathbf{x}, \theta)}(\dot{\mathbf{x}}, \dot{\theta}) := \alpha(\mathbf{x}, \theta) \mathcal{C} \left( \xi(\mathbf{x}, \theta) (\dot{\theta} - \kappa(\mathbf{x}, \theta)) \right) \quad \text{si } \dot{\mathbf{x}} = \mathbf{n}(\theta).$$

*As before  $\mathcal{F}$  is extended positively 1-homogeneously, and set to  $+\infty$  otherwise. The scalar field  $\kappa : \mathbb{M} \rightarrow \mathbb{R}$  defines a reference curvature, with respect to which the path curvature is penalized. If this field is defined as a non-zero constant  $\kappa \equiv \kappa_0 \in \mathbb{R}$ , then we obtain a Dubins car with a distinct turning radius on the right and left sides, or Euler elastica curves w.r.t. a material which rest position is distorted instead of straight.*

*We already obtained preliminary numerical results, and are investigating their applications to image processing.*

**Projects and perspectives** (Using nilpotent approximations of sub-Riemannian distance functions). *Consider the Reeds-Shepp model, used to describe wheelchair-like vehicles, with an initial configuration  $(x_0, y_0, \theta_0) = (0, 0, 0)$  of position an orientation. The cost of motion to the configuration  $(x, y, \theta) \in \mathbb{M}$  can be locally approximated in several ways, such as*

$$\sqrt{x^2 + \varepsilon^{-2}y^2 + \theta^2}, \quad \sqrt[4]{(x^2 + \theta^2)^2 + y^2}. \quad (1.27)$$

*The expression (1.27, left), involving a small parameter  $\varepsilon > 0$ , is a Riemannian relaxation of the sub-Riemannian model, currently used in our numerical schemes. We want to develop numerical methods based on the approximation (1.11, right), which is much more accurate [BCP17]. Similar techniques may apply to the other non-holonomic systems studied, for instance the Euler-Mumford Elasticae.*

---

<sup>20</sup>A slight modification of this argument is required for models allowing *in place rotations* such as the Reeds-Shepp model without reverse gear.

## Applications, mainly to image segmentation.

Medical image processing is one of the main motivation for our works on the discretization of anisotropic eikonal equations. Applications to this field are developed in collaboration with L. Cohen [CMC16a, CMC16b, CC17a, CC17b, CCM14, CMC16c] and more recently with R. Duits [SBD<sup>+</sup>15, DMMP16], see §4. Independent applications, in the field of motion planning and surveillance, are developed with J. Drezo, see §4.3 from [MD17]. Some of our results are illustrated on Figure 1.8.

Cohen and Kimmel [CK97] were first to consider the use of globally minimal paths, computed by solving eikonal equations, for the segmentation of contours or of tubular structures, see §4.1.1 for a brief historical discussion. Considering anisotropic metrics is natural in this context, so as to better guide these paths along the structures of interest, and to avoid segmentation artifacts known as “short-circuits” and “leaks”. This enhancement was initially difficult to put into practice, due to the poor performance of the classical eikonal equation solvers when applied to strongly anisotropic problems [BC10, Mir14a]. The contributions of this dissertation yield computation time reductions by several up to four (!) orders of magnitude in some test cases of the field, see [Mir14a], and made possible numerous new applications.

I wish to highlight two realizations, unexpected at first and that could not be envisioned without efficient algorithms for solving anisotropic eikonal equations. The first is a new procedure for minimizing Chan-Vese-like energies [CV01] involved the segmentation of image regions. To each subset  $U$  of a domain  $\Omega$ , with rectifiable boundary, associate the energy

$$\mathcal{E}(U) = \int_U f + \int_{\partial U} g, \quad (1.28)$$

where  $f, g : \Omega \rightarrow \mathbb{R}$  are given, and  $g$  is positive. The usual method for minimizing (1.28) relies on the introduction of a map  $\psi : \Omega \rightarrow \mathbb{R}$ , of which the region of interest is a level set  $U = \{\mathbf{p} \in \Omega; \psi(\mathbf{p}) < 0\}$ . Numerical implementations of this approach unfortunately suffer from several issues, such as the excessive sensitivity to initialization, the lack of control on the topology of the region  $U$ , and the numerical cost. We observed, in dimension  $d = 2$  and using the divergence theorem, that the boundary  $\partial U$  of the optimal set is a geodesic for a Rander metric, namely

$$\mathcal{F}_{\mathbf{p}}(\dot{\mathbf{p}}) = g(\mathbf{p})\|\dot{\mathbf{p}}\| + \langle \omega(\mathbf{p})^\perp, \dot{\mathbf{p}} \rangle.$$

where the vector field  $\omega : \bar{\Omega} \rightarrow \mathbb{E}_2$  obeys  $\operatorname{div} \omega = f$  and  $\|\omega^\perp\| < 1$  in the neighborhood of  $\partial U$ . We can thus optimize (1.28) by computing a minimal path for the above anisotropic and asymmetric metric, using our eikonal equation solvers, see §4.2 from [CMC16b].

Our second highlight deals with the segmentation of the retinal vascular network. The classical approach [CK97] for segmentating a tubular structure is to introduce a metric taking small values on the structure and large values in the image background. Minimal paths are then extracted between the structure endpoints, which are provided by the user or found by another algorithm. Retinal background images however display so many entangled and superposed<sup>21</sup> vessels that this approach is impractical. Indeed, the

---

<sup>21</sup>The vessels are disjoint in three dimensional physical space, but the input medical image only shows their two dimensional projections, which intersect.

obtained minimal paths feature short circuits, engaging from one blood vessel to another at the places of their intersections. To solve this problem, we augment the path model with a Reeds-Shepp or Euler-Mumford curvature penalty [SBD<sup>+</sup>15, DMMP16, CMC17], implemented as above, improving on an idea of Duits and al [BDMS15]. This eliminates short circuits, by increasing the cost of sudden changes in orientation, which occurred at vessel intersections, see §4.1.

**Projects and perspectives** (*Short term.* Publication of the computer codes for solving non-holonomic eikonal equations). *With J. Portegies, we clean up the C++ codes developed for the computation of minimal paths with a curvature penalty, and add documentation and examples. Our objective is to submit them to a reproducible research journal, and distribute them open-sourced to the image processing community.*

**Projects and perspectives** (Motion planning for vehicles). *With J. Dreo, we study the industrial applications of the numerical solvers of anisotropic eikonal equations here presented. We are particularly interested in the computation of threatening trajectories, and in their detection by surveillance systems [MD17]. We also want to couple these solvers with the multi-agent planning algorithms developed as part of the European project SWARM. The penalization of path curvature, made possible by the numerical methods presented in this memoir, is fully relevant in this context given the mechanical constraints of the controlled vehicles.*

### 1.2.3 Second order equations.

We studied second-order PDEs, using the same tools from lattice geometry that are applied to eikonal equations in the previous section. Our results on anisotropic diffusion, the Monge-Ampere equation, and the constraint of convexity, are presented below. See also §5 from [FM06], §6 from [BCM16], and §7 from [Mir16a] respectively.

#### Anisotropic diffusion.

Image processing has fueled, for some time, the study of very general diffusion PDEs, simultaneously non-linear and anisotropic, and usually in divergence form. They take the form

$$\partial_t u(\mathbf{x}, t) = \operatorname{div}(\mathcal{D}_u(\mathbf{x}, t) \nabla u(\mathbf{x}, t)) \quad (1.29)$$

for all  $(\mathbf{x}, t) \in \Omega \times ]0, \infty[$ , where  $\Omega \subseteq \mathbb{E}_d$  is the image domain. In addition, an initial state is chosen on  $\Omega \times \{0\}$ , and boundary conditions on  $\partial\Omega \times ]0, \infty[$ , often of Neumann type.

This class of PDEs allows, by a careful choice of the non-linear tensors  $\mathcal{D}_u$ , to remove noise, enhance object contours, or imitate the style of artists. See Figure 1.10 and [Wei98]. One must distinguish the use of non-linear but *isotropic* tensor fields, such as Perona and Malik [PM90] filtering defined by  $\mathcal{D}_u(\mathbf{x}, t) = \operatorname{Id} / \|\nabla u(\mathbf{x}, t)\|^{22}$ , from genuinely *anisotropic* tensor designs due in particular to Weickert [Wei98] and which eigenvectors are aligned with the locally preferred image directions.

---

<sup>22</sup> The Perona and Malik model, which is best described as (non-linear) *divergence form diffusion with isotropic tensors*, is often artificially reformulated as *non-divergence form diffusion with anisotropic tensors*, which led to an unfortunate terminological confusion [Wei98].

Fehrenbach and the author [FM14] introduced a numerical scheme for the PDE (1.29), associated with an arbitrary given anisotropic tensor field  $\mathcal{D} : \overline{\Omega} \rightarrow \mathbb{S}^{++}(\mathbb{E}_d)$  (non-linearity and time dependency are not the difficulty in this context). Our approach is based on the first order approximation

$$\|\nabla u(\mathbf{p})\|_D^2 \approx \sum_{1 \leq i \leq d'} \rho_i \frac{(u(\mathbf{p}) - u(\mathbf{p} - h\dot{\mathbf{e}}_i))^2 + (u(\mathbf{p}) - u(\mathbf{p} + h\dot{\mathbf{e}}_i))^2}{2h^2}, \quad (1.30)$$

where the weights and offsets  $(\rho_i, \dot{\mathbf{e}}_i)_{i=1}^{d'}$  are obtained from Voronoi's first reduction (1.17). Using (1.30) and a Riemann sum one can approximate the elliptic energy defined by an anisotropic tensor field, and thus solve the anisotropic diffusion PDE which is its gradient flow w.r.t. the  $L^2$  metric. This numerical scheme obeys the maximum principle, and uses a more compact stencil than alternative methods, see §5.

Non-divergence form diffusion equations can also be discretized using our techniques, using the second order approximation

$$\text{Tr}(D\nabla^2 u(\mathbf{p})) \approx \sum_{1 \leq i \leq d'} \rho_i \frac{u(\mathbf{p} - h\dot{\mathbf{e}}_i) - 2u(\mathbf{p}) + u(\mathbf{p} + h\dot{\mathbf{e}}_i)}{h^2}$$

where the weights and offsets  $(\rho_i, \dot{\mathbf{e}}_i)_{i=1}^{d'}$  are again obtained from Voronoi's first reduction (1.17). In the two dimensional case, an equivalent construction was earlier proposed [BOZ04].

**Projects and perspectives** (Extension of Varadhan's formula to Rander metrics). *The Varadhan formula relates the solution in short time of the equation of diffusion, with the solution of the eikonal equation, on a Riemannian manifold [Var67]. It is the basis of an original numerical method for the computation of Riemannian minimal paths [CWW12], which is particularly competitive in dimension  $d = 2$ . With D. Prandi, L. Cohen and F. Yang, we study a similar link between drift and diffusion equations, and eikonal equations with respect to non-symmetric Rander metrics.*

### Monge-Ampere equations.

The Monge-Ampere operator belongs to the class of second-order *monotone* differential operators, see [CIL92] or Definition B.1.1. Under weak assumptions, they can be expressed in terms of non-divergence form diffusion operators; hence any discretization of the latter can be used to address the former [KT92]. In the case of the Monge-Ampere operator, this follows from the property

$$d(\det M)^{\frac{1}{d}} = \inf\{\text{Tr}(DM); D \in \mathbb{S}^{++}(\mathbb{E}), \det D = 1\},$$

which holds for any  $M \in \mathbb{S}^+(\mathbb{E}_d)$ . More precisely, in dimension  $d = 2$  and by grouping matrices  $D \in \mathbb{S}^{++}(\mathbb{E}_2)$  according to the support  $\{\pm\dot{\mathbf{e}}_i; 1 \leq i \leq d'\}$  of their decomposition (1.2), we obtain a monotone and consistent discretization of the Monge-Ampere operator, see §6 from [BCM16]. For any smooth convex map  $u$ ,

$$\det(\nabla^2 u(\mathbf{p})) \approx \min_{(\dot{\mathbf{e}}_0, \dot{\mathbf{e}}_1, \dot{\mathbf{e}}_2) \in \mathcal{B}} H(\Delta_{\dot{\mathbf{e}}_0}^+ u(\mathbf{p}), \Delta_{\dot{\mathbf{e}}_1}^+ u(\mathbf{p}), \Delta_{\dot{\mathbf{e}}_2}^+ u(\mathbf{p})) \quad (1.31)$$

where  $\mathcal{B} \subseteq (\mathbb{L}_2)^3$  stands for the set of all obtuse superbases of  $\mathbb{L}_2$ , where  $H$  is an explicit and non-decreasing function, and where  $\Delta_{\mathbf{e}}^+ u(\mathbf{p}) := \max\{0, u(\mathbf{p} - h\mathbf{e}) - 2u(\mathbf{p}) + u(\mathbf{p} - h\mathbf{e})\}/h^2$  denotes the positive part of the second order finite difference of  $u$  with offset  $\mathbf{e}$ .

This research also led us to establish the convergence of a damped Newton algorithm [Mir15b] applied to the discretization of the three dimensional Monge-Ampere equation. This technique was later applied by Mériqot et al. [KMT16] to semi-discrete optimal transport schemes with a transport cost obeying the general geometric assumptions of Loeper and Ma-Trudinger-Wang [MTW05].

Merigot and the author also introduced a numerical method for solving the Euler equations of incompressible fluids [MM16], relying on efficient discretizations of optimal transport problems. Note that we are interested in the reconstruction of the intermediate states of the fluid, given the initial and final states, and not in the Cauchy problem addressed in [dGWH<sup>+</sup>15] with related techniques. We published the first two dimensional numerical results for this problem, illustrating paradoxical behaviors studied by Brenier [Bre08], see Figure 1.11. This thematic was then developed within the Mokaplan/MAGA team: our numerical scheme was adapted to the Cauchy problem by Gallouet et al. [GV16], and a distinct numerical method was introduced by Benamou et al. [BCC<sup>+</sup>15].

**Projects and perspectives** (Monotonous and consistent discretizations of second-order Hamilton-Jacobi-Bellman operators). *In this work, undertaken with J.-D. Benamou and V. Duval, we develop robust, precise, and monotonous numerical schemes for HJB EDPs associated with Pucci extremal operators, see §5. Our approach, whose principle is presented in §6.1, generalizes our results on the Monge-Ampere equation. The resulting numerical schemes are consistent, hence much more accurate than the schemes classically considered in the literature [FO11a] which depend on a relaxation parameter and are only asymptotically consistent. We are particularly interested in the case of the 2-Laplacian, an intermediate operator between the Laplacian and Monge-Ampere.*

**Projects and perspectives** (Numerical schemes for fluid mechanics). *Our work on the numerical solution of the Euler equations of incompressible fluids, with Q. Merigot [MM16], lends itself to generalizations. For example, in the framework of the Camassa-Holm equations [GM16], or of the Euler equations subject to an upper bound on the density [MP15]. Several discretization schemes are under study.*

### **The constraint of convexity.**

The monopolist problem, also called the principal agent model, belongs to the field of theoretical economy and was introduced by Rochet et al [RC98]. A manufacturer of products, without competition in his market, freely decides of his catalog of prices and proposes it to a population. The population members individually select the product from the catalog which maximizes their personal utility, taking price into account, or reject the offer if the proposed prices are excessive. Knowing this general behavior, as well the type and distribution of the utility functions within the population, the monopolist adjusts his prices so as to maximize profit.

From a mathematical point of view, the monopolist problem is equivalent to minimizing an elliptic functional over the set of all *convex* functions on a domain. The simplest

and most studied instance is the following:

$$\min\left\{\int_{[1,2]^2}\left(\frac{1}{2}|\nabla u(\mathbf{p})|^2 - \langle \nabla u(\mathbf{p}), \mathbf{p} \rangle + u(\mathbf{p})\right) d\mathbf{p}; u \geq 0, u \text{ convex}\right\},$$

see Figure 1.12 for a numerical solution. Existence theory is particularly simple, thanks to the compactness properties of the set of convex functions. When discretizing this problem, serious difficulties however arise from the constraint of convexity, as discovered in [CLM06]. A variety of numerical methods have been developed in the attempt to address them [CLRM01, AM08, AM09, EMB10, Obe13, MO14, Wac17, Mir16a]. Indeed consider a two dimensional convex bounded domain  $\Omega \subseteq \mathbb{E}_2$ , denote  $X := \Omega \cap h\mathbb{L}_2$  where  $h > 0$  is the gridscale, and introduce the cone of all restrictions to  $X$  of convex functions

$$\text{Conv}(X) := \{u|_X; u : \Omega \rightarrow \mathbb{R} \text{ is convex}\}.$$

The set  $\text{Conv}(X) \subseteq \mathbb{R}^X$  is a convex cone, which can be equivalently defined via  $\mathcal{O}(N^2)$  non-redundant linear inequalities, where  $N = \#(X)$ , which we classified, correcting [CLRM01]. This huge number of linear constraints, quadratic in the problem dimension, makes naive discretizations excessively costly.

Our contribution is to organize the linear constraints defining  $\text{Conv}(X)$  within a hierarchical structure, based on the Stern-Brocot tree. This enables the design of adaptive strategies for implementing the constraint of convexity, based on super- and sub-cones of  $\text{Conv}(X)$ . Our numerical results substantially improve on the state of the art for the problem (1.2.3) and variants, and as a byproduct we obtain an average complexity estimate of a procedure frequently used in algorithmic geometry and referred to as Edge-Flipping, see §7 and [Mir16a].

**Projects and perspectives** (*Short term.* Implementation of the constraint of convexity using semi-discrete optimal transport techniques). *With Q. Mérigot, we study a new approach for the minimization of energy functionals in the space of convex functions, or of convex bodies. More precisely, we regard the gradient of such a map as a transport plan, and penalize the entropy of the image measure. Preliminary results, applied to the Meissner conjecture and to the three dimensional principal agent problem, are presented in §7.*

## 1.2.4 Highlights of the period 2012-2017

**Distinction.** *Vasil A. Popov prize* awarded at the International Conference on Approximation Theory, San-Antonio, May 22-25 2016. This international prize is awarded every three years, since 1995, to a mathematician who defended his PhD at most six years before, for “exceptional contributions to approximation theory”.

**Management.** *Leader of the NS-LBR young researcher grant*, from the french National Research Agency, where the acronym stands for Numerical Schemes using Lattice Basis Reduction. This project is devoted to the design, analysis, and distribution within open source numerical codes, of numerical schemes for anisotropic PDEs on Cartesian grids

(which incidentally is also the topic of this report). Team members are Laurent Cohen, Jérôme Fehrenbach, and Laurent Risser. Dario Prandi and Da Chen are recruited as post-doctoral researchers in 2016 and 2017.

**Open source.** *Distribution of C++ implementations of the numerical schemes* from my research, for anisotropic diffusion §5, and eikonal equations<sup>23</sup> §2, in the insight journal [MFRT15, Mir15a]. In view of their success, with 18000 and 25000 downloads respectively according to the platform, the first module was incorporated within the Insight Toolkit software by the Kitware team (based in France and the US).

**Supervision.** *Co-supervision of Da Chen, PhD student* of Laurent Cohen, working on medical image segmentation methods using minimal paths [Che16]. He defended in September 2016. I was also involved in the supervision of Vijaya Ghorpade, in internship (M2 level) under the direction of Laurent Cohen, and of Shaza Tobji, in internship (M1 level) under the direction of Jérôme Fehrenbach and Laurent Risser.

**Industry.** *Collaboration with Johann Dreo, from Thales Research and Technology*, on the topic of drone routing and surveillance [MD17]. Co-supervision of Meryem El Yamani and Allan Rakotoarivony, who did an internship (M2 level) in 2016 and 2017 respectively.

**International.** *Collaboration with R. Duits from Eindhoven university*, on the topic of efficient algorithms for the computation of sub-Riemannian distances, and of their applications to medical imaging [SBD<sup>+</sup>15, DMMP16].

**Integration.** *Within the Mokaplan INRIA team, and the MAGA ANR research grant*, led by J.-D. Benamou and Q. Merigot, see the joint publications [BCM16, MM16].

**Birth.** *Birth of my two girls Rachel and Ariane*, for the delight of their parents and of their brother Nathanaël, on June 16th 2013 and February 26th 2016.

---

<sup>23</sup>This publication features the semi-Lagrangian schemes only. As of 2017, Eulerian numerical schemes are still informally distributed at [Github.com/Mirebeau/](https://github.com/Mirebeau/).

# Part I

## Anisotropic Eikonal equations

This chapter describes efficient numerical methods for computing globally optimal solutions to deterministic, time-optimal control problems, by solving an eikonal PDE, following a line of research begun in the 1990’s [RT92, Tsi95, Set99]. In contrast with these early works, we focus on anisotropic models, in the sense that the addressed control problem features some privileged directions of motion. Numerical methods for such problems can be separated into two classes, either based on the Semi-Lagrangian paradigm, see §2 in the spirit of [SV03, AM11, KS98], or the Eulerian discretization of the underlying HJB PDE using finite differences and a special representation of the Hamiltonian, see §3 in the spirit of [RT92]. Some applications of our methods to medical image processing and motion planning are presented §4.

As mentioned in the general introduction, we limit our attention to causal numerical methods<sup>24</sup> both for the semi-Lagrangian and the Eulerian paradigms, which enables us to solve all the discretized problems using the Fast-Marching algorithm, §B. There exists alternative approaches to distance computation w.r.t. anisotropic metrics, the most obvious one being non-causal discretizations of the eikonal PDE. More exotic approaches include the Short Term Vector Dijkstra method [CHK13, RL16], or the “geodesics in heat” method based on the short time asymptotics of the diffusion equation [Var67, CWW12]. They latter two methods have advantages but also significant flaws, such as respectively the lack of a convergence proof, and the excessive numerical cost in dimension<sup>25</sup>  $d \geq 3$ . We will not discuss them further in this dissertation.

In order to present our results, we need to introduce some basic (although not entirely conventional) geometrical notation, following [Che16, DMMP16]. The concept of metric, next defined, is illustrated on Figure 1.4.

**Definition 1.2.1.** *Let  $\mathbb{E}$  be a finite dimensional vector space<sup>26</sup>, and let  $\Omega \subseteq \mathbb{E}$  be open.*

- *A gauge is a 1-homogeneous, convex and lower-semi-continuous map  $F : \mathbb{E} \rightarrow [0, \infty]$*

---

<sup>24</sup>With the exception of §3.1.3, on Rander metrics.

<sup>25</sup>The method [CWW12] requires solving an elliptic PDE, which sparse matrix  $M$  is in practice Cholevsky factored:  $M = LL^T$  where  $L$  is lower triangular. The factor  $L$  happens to be remarkably sparse when  $d \leq 2$ , but this miracle ceases in dimension  $d \geq 3$ , strongly increasing the numerical cost.

<sup>26</sup>The definition of a metric easily extends to subdomains of manifolds, see [DMMP16]

vanishing at the origin only. The gauge's unit ball is the compact and convex set  $B := \{\dot{\mathbf{p}} \in \mathbb{E}; F(\dot{\mathbf{p}}) \leq 1\}$ .

- A metric on  $\Omega$  is a map  $\mathcal{F} : \bar{\Omega} \times \mathbb{E} \rightarrow [0, \infty]$  such that  $\mathcal{F}_{\mathbf{p}}$  is a gauge for each  $\mathbf{p} \in \bar{\Omega}$ , and the unit balls depend continuously on  $\mathbf{p}$  w.r.t. the Hausdorff distance.

A gauge, or a metric, which takes infinite values is said singular (otherwise said finite).

In contrast with usual norms, gauges can be non-symmetric (i.e.  $F(\dot{\mathbf{x}}) \neq F(-\dot{\mathbf{x}})$  for some  $\dot{\mathbf{x}} \in \mathbb{E}$ ), and non-finite (i.e.  $F(\dot{\mathbf{x}}) = \infty$  for some  $\dot{\mathbf{x}} \in \mathbb{E}$ ). Note that any compact and convex set  $B \subseteq \mathbb{E}$  containing the origin conversely defines the gauge  $F(\dot{\mathbf{p}}) := \min\{r \in [0, \infty]; \dot{\mathbf{p}} \in rB\}$ , and is its unit ball. The purpose of metrics is to measure the length of Lipschitz paths  $\gamma : [0, 1] \rightarrow \bar{\Omega}$ , thus defining a quasi-distance<sup>27</sup>  $d_{\mathcal{F}}$  on the domain  $\bar{\Omega}$ :

$$\text{length}_{\mathcal{F}}(\gamma) := \int_0^1 \mathcal{F}_{\gamma(t)}(\dot{\gamma}(t)) dt, \quad d_{\mathcal{F}}(\mathbf{p}, \mathbf{q}) := \inf_{\substack{\gamma: [0,1] \rightarrow \bar{\Omega}, \\ \gamma(0)=\mathbf{p}, \gamma(1)=\mathbf{q}}} \text{length}_{\mathcal{F}}(\gamma).$$

Depending on the particular choice of metric  $\mathcal{F}$ , the following properties may or may not hold:  $d_{\mathcal{F}}(\mathbf{p}, \mathbf{q}) = d_{\mathcal{F}}(\mathbf{q}, \mathbf{p})$  (symmetry),  $d_{\mathcal{F}}(\mathbf{p}, \mathbf{q}) = \infty$  (global controllability), and  $d_{\mathcal{F}}(\mathbf{p}, \mathbf{q}) \rightarrow 0$  as  $\mathbf{p} \rightarrow \mathbf{q}$  (local controllability), where  $\mathbf{p}, \mathbf{q} \in \bar{\Omega}$ .

This first two chapters of this part are devoted to the description and numerical analysis of methods for computing the map  $u : \bar{\Omega} \rightarrow [0, \infty]$  defined as the distance from the domain boundary

$$u(\mathbf{p}) = \inf_{\mathbf{q} \in \partial\Omega} d_{\mathcal{F}}(\mathbf{q}, \mathbf{p}). \quad (1.32)$$

The value  $u(\mathbf{p})$  can be regarded at the arrival time at  $\mathbf{p} \in \Omega$  of a front originating from  $\partial\Omega$  at time 0, and propagating at unit speed w.r.t. the local metric  $\mathcal{F}$ . In applications, it is often convenient<sup>28</sup> to introduce a position dependent initial delay  $\mu : \partial\Omega \rightarrow ]-\infty, \infty]$ , but for simplicity we limit our theoretical analysis to the case of a null boundary condition<sup>29</sup>.

The value map  $u$  obeys a PDE, and the minimal paths  $\gamma$  an ODE, both involving the dual metric; recall that the dual of a gauge is defined as

$$F^*(\dot{\mathbf{p}}) := \sup\{\langle \dot{\mathbf{p}}, \dot{\mathbf{p}} \rangle; \dot{\mathbf{p}} \in \mathbb{E}, F(\dot{\mathbf{p}}) \leq 1\}.$$

More precisely,  $u$  is under weak assumptions a viscosity solution [BCD08] to a generalized eikonal equation, as already mentioned in the general introduction.

$$\forall \mathbf{p} \in \Omega, \mathcal{F}_{\mathbf{p}}^*(du(\mathbf{p})) = 1, \quad \forall \mathbf{p} \in \partial\Omega, u(\mathbf{p}) = 0. \quad (1.33)$$

<sup>27</sup>A quasi-distance obeys the positive definiteness and the triangular inequality axioms, but may be asymmetric and may take infinite values.

<sup>28</sup>In applications, outflow boundary conditions are obtained by setting  $\mu = \infty$  on part of  $\partial\Omega$ .

<sup>29</sup>Non-constant boundary conditions must indeed be interpreted in a weak sense in the PDE formulation (1.33), which complicates the proofs and the statements of convergence, see [BCD08]. These technicalities can only be avoided if the boundary data  $\mu$  varies very slowly [BR06].

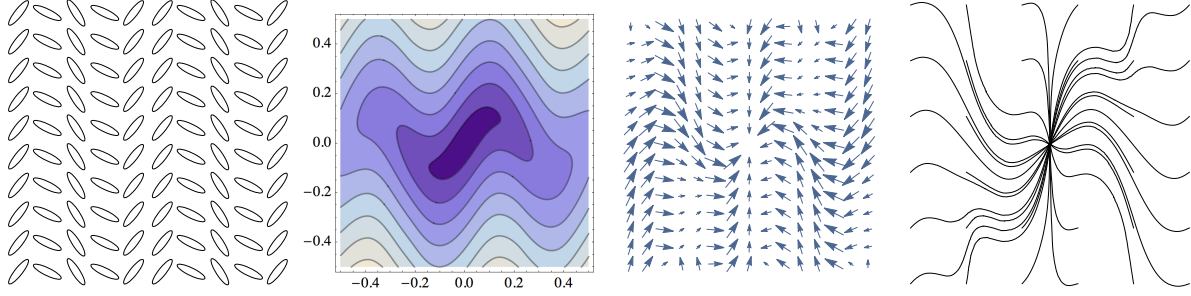


Figure 1.13 – From left to right: (I) a Riemannian metric, proposed as a test case in [SV03], and inspired by seismic imaging, (II) level lines of the distance map  $u$  from the center point, (III) geodesic flow direction  $\mathbf{p} \mapsto d\mathcal{F}_{\mathbf{p}}^*(du(\mathbf{p}))$ , (iv) minimal geodesics, backtraced to the center point.

As announced our numerical schemes for this PDE assume and exploit a specific form of the discretization sets, denoted  $X$  and  $\partial X$  and which must be part of an additive lattice  $\mathbb{L} \subseteq \mathbb{E}$ .

$$X = \Omega \cap \mathbb{L}, \quad \partial X := (\mathbb{E} \setminus \Omega) \cap \mathbb{L}. \quad (1.34)$$

In practice,  $\mathbb{E} = \mathbb{E}_d := \mathbb{R}^d$  is the Euclidean space, and  $\mathbb{L} = h\mathbb{L}_d := h\mathbb{Z}^d$  is the lattice of integers scaled by a parameter  $h > 0$ . Once  $u$  is computed, the minimal paths for (1.32) are extracted for a negligible cost by solving, backwards in time, the following ODE:

$$\dot{\gamma}(t) = d\mathcal{F}_{\gamma(t)}^*(du(\gamma(t))), \quad (1.35)$$

see [DMMP16] appendix C for the (weak) required assumptions and a proof. The ODE integration is non-trivial in practice, especially in the cases where (i) the metric is singular, (ii) the arrival times map  $u$  is discontinuous, (iii) discretization stencils are wide, and/or (iv) obstacles are present in the domain. We choose however not to discuss this point in detail in this dissertation, and focus instead on the computation of  $u$  which is more interesting from the mathematical point of view. Let us only say that our latest software<sup>30</sup> offers two backtracing methods. The first method relies on a second order Euler scheme for the ODE (1.35), where the geodesic flow direction  $\mathbf{p} \mapsto d\mathcal{F}_{\mathbf{p}}^*(du(\mathbf{p}))$  is obtained in an upwind manner as a byproduct of solving the PDE, see [Mir17a]. The second method is based on the diffuse geodesics obtained by automatic differentiation of the PDE scheme, in the spirit of [BCPS10].

The metric  $\mathcal{F} : \overline{\Omega} \times \mathbb{E} \rightarrow [0, \infty]$  encodes the geometry of  $\Omega$ , and is usually data-driven in applications, see §4. The specific form of  $\mathcal{F}$  plays a crucial role, both for the applications and for the discretization strategy, and in our works it may be Riemannian §2.1, Finslerian §2.2, sub-Riemannian §3.1, or related to more complex non-holonomic control models §3.2. In addition to these structural properties, the condition number of the metric also determines the difficulty of the numerical implementation. This parameter describes how much a gauge  $F$ , or a metric  $\mathcal{F}$ , distorts length w.r.t. some reference norm

<sup>30</sup>HamiltonFastMarching project on [GitHub.com/Mirebeau/](https://github.com/Mirebeau/)

$\|\cdot\|$ , which in practice is the Euclidean norm on  $\mathbb{E}_d$ . It is defined as

$$\text{Cond}(F) := \sup_{\|\dot{\mathbf{p}}\|=\|\dot{\mathbf{q}}\|=1} \frac{F(\dot{\mathbf{p}})}{F(\dot{\mathbf{q}})}, \quad \text{Cond}(\mathcal{F}) := \sup_{\mathbf{p} \in \bar{\Omega}} \text{Cond}(\mathcal{F}_{\mathbf{p}}). \quad (1.36)$$

For instance, a Riemannian metric  $\mathcal{F}$  on  $\Omega \subseteq \mathbb{E}_d$  is defined via a continuous field of positive definite matrices  $\mathcal{M} : \bar{\Omega} \rightarrow S^{++}(\mathbb{E}_d)$ , and for any  $\mathbf{p} \in \bar{\Omega}$  and any  $\dot{\mathbf{p}} \in \mathbb{E}_d$

$$\mathcal{F}_{\mathbf{p}}(\dot{\mathbf{p}}) := \|\dot{\mathbf{p}}\|_{\mathcal{M}(\mathbf{p})}, \quad \text{Cond}(\mathcal{F}_{\mathbf{p}}) := \sqrt{\|\mathcal{M}(\mathbf{p})\| \|\mathcal{M}(\mathbf{p})^{-1}\|}. \quad (1.37)$$

Our numerical methods are tailored to robustly handle strongly anisotropic metrics, typically obeying  $\text{Cond}(\mathcal{F}) \lesssim 10$ , which is common in applications to image segmentation [BC10]. Extreme anisotropy  $\text{Cond}(\mathcal{F}) \approx 100$  is also considered in some test cases, with rather convincing results [Mir14a, Mir14b, Mir17a]. We also address degenerate models, obeying  $\text{Cond}(\mathcal{F}) = \infty$ , but for that purpose we rely on a relaxed metric, see §3.1.2 and §3.2.

The rest of this part's introduction is devoted to a short discussion of differences between Semi-Lagrangian and Eulerian based numerical schemes for eikonal equations. For each point, we indicate the best class of methods, in the author's experience. This paragraph is purely informal, and is open to discussion.

- *Soundness of the discretization principle:* advantage to semi-Lagrangian schemes. These schemes are based on Bellman's optimality principle, which is intuitive and geometrical. Eulerian schemes rely on a wide stencil finite differences discretization of the eikonal PDE, which is hardly interpretable.
- *Obeying the causality property:* equality. In both cases, causality can be related to a simple and interpretable property of the discretization scheme. However there is no general recipe, independent of the metric structure and dimension, for designing small stencils obeying this property, and whose construction has a low numerical cost. At the time of writing, this remains an open question for many classes of metrics, except of course for those addressed in this dissertation.
- *Ease of the numerical implementation:* advantage to Eulerian schemes. Semi-Lagrangian schemes require rather complex geometrical computations, involving the enumeration of all facets and sub-facets of a  $d$ -dimensional polytope. Eulerian schemes use basic finite differences, which implementation is straightforward.
- *Extension to meshed domains:* advantage to semi-Lagrangian schemes. The semi-Lagrangian paradigm trivially extends to meshed domains, whereas our Eulerian discretization intrinsically requires a cartesian grid<sup>31</sup>.
- *Numerical cost:* advantage to Eulerian schemes in dimension  $d \geq 4$ . In lower dimension, the  $\mathcal{O}(N \ln N)$  cost of maintaining the priority queue dominates the

---

<sup>31</sup>Specifically, we use symmetric upwind finite differences  $\max\{0, u(\mathbf{x}) - u(\mathbf{x} - \dot{\mathbf{e}}), u(\mathbf{x}) - u(\mathbf{x} + \dot{\mathbf{e}})\}$ . They only make sense provided one has the following symmetry property:  $\mathbf{x} + \dot{\mathbf{e}} \in X \Rightarrow \mathbf{x} - \dot{\mathbf{e}} \in X$ , for any discretization point  $\mathbf{x} \in X$  and any offset  $\dot{\mathbf{e}} \in \mathbb{E}_d$ . This implies that  $X$  is an additive lattice.

computation time in both cases. In dimension  $d \geq 4$  however, the complexity of the geometrical computations involved in Semi-Lagrangian schemes starts to explode. For instance the semi-Lagrangian implementation of the generalized Reeds-Shepp model considered in [DMMP16], sub-Riemannian on  $\mathbb{R}^3 \times \mathbb{S}^2$ , uses 5 dimensional polytopes each having 20 vertices, 126 edges, 324 faces, 360 three dimensional facets, and 144 four dimensional facets. Computation times for the Eulerian discretization of the same model [Mir17a] are up to 6 times faster.

- *Accuracy:* advantage to Eulerian schemes. Eulerian schemes can trivially be made second order accurate, at least formally, which substantially increases their accuracy in practice. Second order semi-Lagrangian schemes are in contrast more difficult to implement, in particular when the metric is non-constant.

# Chapter 2

## Semi-Lagrangian schemes

### Contents

---

<b>2.1 Riemannian metrics</b> . . . . .	<b>54</b>
<b>2.2 Finsler metrics</b> . . . . .	<b>58</b>

---

This section describes the design of Semi-Lagrangian schemes for eikonal equations associated with Riemannian metrics, in arbitrary dimension, and Finsler metrics, in dimension  $d = 2$ . Our approach is based, respectively, on a specific property of Delaunay triangulations of periodic sets, see §2.1 from [Mir14a], and on a two dimensional structure named the Stern-Brocot tree, see §2.1 from [Mir14b]. Here and below, the letter  $\mathbb{E}$  denotes a finite dimensional real vector space.

Semi-Lagrangian discretization schemes for eikonal equations are based on a characterization of the distance to the boundary (1.32) by Bellman’s optimality principle. More precisely, let  $\Omega \subseteq \mathbb{E}$  be a bounded domain, and let  $\mathcal{F} : \Omega \times \mathbb{E}$  be a *finite* metric. Let also  $V(\mathbf{p}) \subseteq \bar{\Omega}$  be a neighborhood of each  $\mathbf{p} \in \Omega$ . Then one easily checks that  $u : \Omega \rightarrow [0, \infty[$  is the unique continuous map obeying

$$\forall \mathbf{p} \in \Omega, u(\mathbf{p}) = \min_{\mathbf{q} \in \partial V(\mathbf{p})} d_{\mathcal{F}}(\mathbf{q}, \mathbf{p}) + u(\mathbf{q}), \quad \forall \mathbf{p} \in \partial\Omega, u(\mathbf{p}) = 0. \quad (2.1)$$

Numerically, as described in the introduction, finite sets  $X$  and  $\partial X$  are introduced, devoted to the discretization of  $\Omega$  and  $\partial\Omega$ . For each  $\mathbf{p} \in X$ , a polytope  $V(\mathbf{p})$  is constructed, enclosing  $\mathbf{p}$  and with its vertices within  $X \cup \partial X$ . See Figure 2.1 for classical examples. The characterization (2.1) is approximated as

$$\forall \mathbf{p} \in X, U(\mathbf{p}) = \inf_{\mathbf{q} \in \partial V(\mathbf{p})} \mathcal{F}_{\mathbf{p}}(\mathbf{p} - \mathbf{q}) + I_{V(\mathbf{p})} U(\mathbf{q}), \quad \forall \mathbf{p} \in \partial X, U(\mathbf{p}) = 0. \quad (2.2)$$

Within the domain interior, the system (2.2) approximates (2.1) by replacing the distance function with the local gauge of the metric, and substituting the exact value of the function  $u(\mathbf{q})$  at  $\mathbf{q} \in \partial V$  with the piecewise linear interpolation  $I_{V(\mathbf{p})} U(\mathbf{q})$  of its approximation  $U$ .

The r.h.s. of the discrete system of non-linear equations (2.2) is denoted by  $\Lambda : \mathbb{R}^{X \cup \partial X} \rightarrow \mathbb{R}^{X \cup \partial X}$  and referred to as the Hopf-Lax operator, following [BE84]. This operator is by construction *monotone*, in the sense that  $U \leq V \Rightarrow \Lambda U \leq \Lambda V$ , where

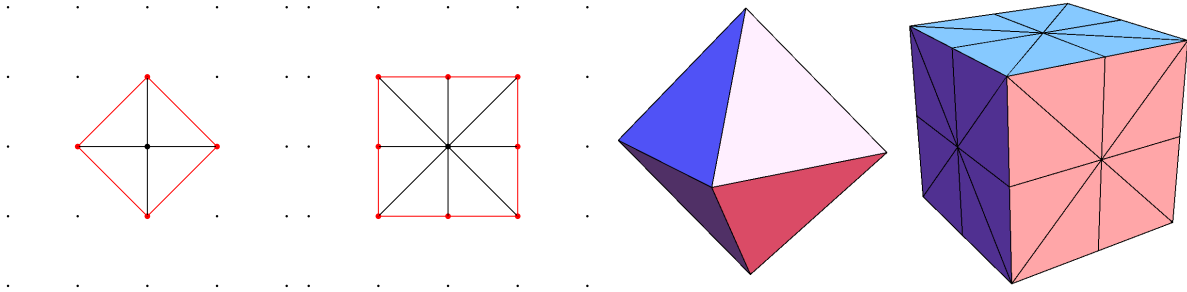


Figure 2.1 – Some classical stencils used in semi-Lagrangian discretizations of two dimensional (left) or three dimensional (right) eikonal equations. They are  $\|\cdot\|_M$ -acute, where  $M \in S^{++}(\mathbb{E}_d)$ , see Definition 2.0.1, provided the condition number  $\text{Cond}(M) := \sqrt{\|M\| \|M^{-1}\|}$  is bounded by respectively 1,  $1 + \sqrt{2}$ , 1,  $(\sqrt{3} + 1)/2$  (from left to right). In the following, we refer by FM-8 to the two dimensional Fast-Marching algorithm using with the stencil (center-left).

$U, V : X \cup \partial X \rightarrow \mathbb{E}$  and inequalities are understood pointwise on  $X \cup \partial X$ . This property, along with mild assumptions, implies comparison principles, and thus stability properties and the convergence of iterative schemes for solving the system of equations (2.2), see §B.1. We choose to postpone to §3 the discussion of convergence, of the discrete solutions of this system towards the actual distance to boundary as the discretization set  $X \cup \partial X$  is refined. Indeed these matters become more interesting there, due to additional difficulties related with the non-holonomy of the considered models. Let us only mention that the papers [Mir14b, Mir14a] from which this chapter is adapted establish convergence without rates, by relying on compactness arguments similarly to [BR06], but that the doubling of variables technique used in [SMK16] could easily be adapted to establish a  $\mathcal{O}(\sqrt{h})$  convergence rate, where  $h$  is the grid scale.

An additional property of the operator  $\Lambda$ , referred to as *causality* and defined in §B.1, is required for being able to solve (2.2) via the efficient and single pass Fast-Marching algorithm. Within the Semi-Lagrangian paradigm, as mentioned in the general introduction, causality turns out to be equivalent to a geometrical property of the stencils, referred to as *acuteness* and defined below, see [SV03, Vla08, Mir14b].

**Definition 2.0.1** (Generalized acuteness property). *Let  $\mathbf{p} \in \mathbb{E}$ , let  $V$  be a polytope<sup>1</sup> containing  $\mathbf{p}$  in its interior, and let  $F$  be a finite gauge on  $\mathbb{E}$ . We say that  $(V, \mathbf{p})$  is  $F$ -acute iff for any points  $\mathbf{q} = \mathbf{p} + \dot{\mathbf{q}}$  and  $\mathbf{r} = \mathbf{p} + \dot{\mathbf{r}}$  of a common facet of  $\partial V$  one has*

$$\forall t \geq 0, F(\dot{\mathbf{q}} + t\dot{\mathbf{r}}) \geq F(\dot{\mathbf{q}}). \quad (2.3)$$

The point  $\mathbf{p}$  in Definition 2.0.1 is not mentioned when it is obvious from context. One can show that it suffices to check (2.3) for points  $\mathbf{q}, \mathbf{r}$  belonging to the *boundary of a common facet* of  $V(\mathbf{p})$ . In particular, in dimension  $d = 2$ , it suffices to check (2.3) for consecutive vertices of  $V(\mathbf{p})$ , a property used in §2.2. In the case of a gauge of Riemannian type (in arbitrary dimension  $d$ ), the condition (2.3) becomes bi-linear w.r.t.  $\dot{\mathbf{q}}$  and  $\dot{\mathbf{r}}$ , see

<sup>1</sup>A polytope is defined here a bounded set which boundary is a triangulated surface.

the next proposition, and thus it suffices again to satisfy it for any vertices  $\dot{\mathbf{q}}$  and  $\dot{\mathbf{r}}$  of a common face of  $V(\mathbf{p})$ .

The name *acuteness* given to property (2.3) is justified by the simpler equivalent form that it takes when the metric is Riemannian or isotropic, as shown in the next proposition, proved in [Mir14b]. The acuteness property defined above was first described under these specialized forms [SV03, Vla08].

**Proposition 2.0.2.** *Under the assumptions of Definition 2.0.1.*

- If  $F$  is differentiable at  $\dot{\mathbf{q}}$ , then (2.3) is equivalent to

$$\langle dF(\dot{\mathbf{q}}), \dot{\mathbf{r}} \rangle \geq 0.$$

- If  $F$  is of Riemannian type, that is if there exists  $M \in S^{++}(\mathbb{E}_d)$  such that  $F(\dot{\mathbf{p}}) = \|\dot{\mathbf{p}}\|_M$  for all  $\dot{\mathbf{p}} \in \mathbb{E}_d$ , then (2.3) is equivalent to

$$\langle M\dot{\mathbf{r}}, \dot{\mathbf{q}} \rangle \geq 0. \tag{2.4}$$

- If  $F$  is isotropic, that is if there exists  $m > 0$  such that  $F(\dot{\mathbf{p}}) = m\|\dot{\mathbf{p}}\|$  for all  $\dot{\mathbf{p}} \in \mathbb{E}_d$ , then (2.3) is equivalent to

$$\langle \dot{\mathbf{r}}, \dot{\mathbf{q}} \rangle \geq 0.$$

In addition, if the dimension is  $d = 2$ , or if the metric is Riemannian, then it suffices to check (2.3) when  $\mathbf{p} + \dot{\mathbf{q}}$  and  $\mathbf{p} + \dot{\mathbf{r}}$  are vertices of a common facet of  $V$ .

If the metric  $F$  is Euclidean or has a small condition number, then a reasonably small isotropic stencil based of the immediate neighbors on the grid may be acute, see Figure 2.1. In contrast, the construction of acute stencils w.r.t. metrics of arbitrarily strong anisotropy is non-trivial and has been the subject of a continued line of research [SV03, AM11, KS98]. The next two chapters present the contributions of the author in this direction, published in [Mir14a, Mir14b]. Theoretical guarantees and numerical experiments illustrate their superior efficiency, when they are applicable.

## 2.1 Riemannian metrics

This subsection is devoted to Fast-Marching using Lattice Basis Reduction (FM-LBR) [Mir14a], a causal semi-Lagrangian numerical scheme for eikonal equations involving Riemannian metrics (1.37), discretized on Cartesian grids of arbitrary dimension (1.34). Open source implementations in dimension  $d \leq 3$  are distributed [Mir15a]. Our stencil construction is based on the concept of Delaunay triangulation, and obeys the required acuteness property (2.4). In two dimensions, we can describe the dependency of the stencil size on the metric condition number in the worst case and in the average case, see Theorem 2.1.6, and establish that it is minimal among causal semi-lagrangian schemes, see Theorem 2.1.5.

For that purpose, we briefly recall the concept of Delaunay triangulation, which is a fundamental tool in discrete geometry [ES86]. See also A.2.2.

**Definition 2.1.1.** Let  $Z \subseteq \mathbb{E}$  be a discrete point set, and let  $M \in S^{++}(\mathbb{E})$ . The Voronoi cell  $\text{Vor}_M^Z(\mathbf{p}) \subseteq \mathbb{E}$  of a site  $\mathbf{p} \in Z$  is defined as

$$\text{Vor}_M^Z(\mathbf{p}) := \{\mathbf{x} \in \mathbb{E}_d; \mathbf{p} \in \underset{\mathbf{q} \in Z}{\text{argmin}} \|\mathbf{x} - \mathbf{q}\|_M^2\}.$$

One denotes by  $\text{Del}_M^Z$  the collection of simplices, of any dimension, such that the Voronoi cells associated to their vertices intersect

$$\{\mathbf{p}_0, \dots, \mathbf{p}_k\} \in \text{Del}_M^Z \quad \Leftrightarrow \quad \text{Vor}_M^Z(\mathbf{p}_0) \cap \dots \cap \text{Vor}_M^Z(\mathbf{p}_k) \neq \emptyset.$$

If the point set  $Z$  and the matrix  $M$  are generic, then it is known that  $\text{Del}_M^Z$  is indeed a triangulation<sup>2</sup> of  $\text{Hull}(Z)$ , referred to as the Delaunay triangulation. Note that Definition 2.1.1 slightly generalizes (up to a linear changes of variables) the classical one [LS80], which requires that  $M = \text{Id}$ . More complex generalizations exist [BGM97, LS03, BWY15, RL16, Mir11], defined w.r.t. a non-constant Riemannian metric  $\mathcal{M} : \mathbb{E} \rightarrow S^{++}(\mathbb{E})$  instead of a single tensor  $M$ . However, and despite their relevancy for the discretization of anisotropic PDEs, they will not be further discussed here.

The key ingredient of the FM-LBR numerical scheme is a geometrical property of Delaunay triangulations, which holds when the collection of sites obeys an additive stability property, thus in particular when it is a lattice.

**Lemma 2.1.2.** Let  $\mathbf{p}, \mathbf{q} = \mathbf{p} + \dot{\mathbf{q}}$  and  $\mathbf{r} = \mathbf{p} + \dot{\mathbf{r}}$  be the vertices of a common simplex of a Delaunay triangulation  $\text{Del}_M^Z$ . If  $\mathbf{p} + \dot{\mathbf{q}} + \dot{\mathbf{r}} \in Z$  then  $\langle M\dot{\mathbf{r}}, \dot{\mathbf{q}} \rangle \geq 0$ .

*Proof.* Let  $\mathbf{x} \in \text{Vor}_M^Z(\mathbf{p}) \cap \text{Vor}_M^Z(\mathbf{q}) \cap \text{Vor}_M^Z(\mathbf{r})$ . Then denoting  $\mathbf{z} := \mathbf{p} + \dot{\mathbf{q}} + \dot{\mathbf{r}} = \mathbf{q} + \mathbf{r} - \mathbf{p}$  one obtains

$$\|\mathbf{z} - \mathbf{x}\|_M = \|(\mathbf{q} + \mathbf{r} - \mathbf{p}) - \mathbf{x}\|_M \geq \delta := \|\mathbf{p} - \mathbf{x}\|_M = \|\mathbf{q} - \mathbf{x}\|_M = \|\mathbf{r} - \mathbf{x}\|_M.$$

Therefore, denoting  $\dot{\mathbf{x}} := \mathbf{x} - \mathbf{p}$

$$\begin{aligned} 0 &\leq \|(\mathbf{q} + \mathbf{r} - \mathbf{p}) - \mathbf{x}\|_M^2 - \|\mathbf{q} - \mathbf{x}\|_M^2 - \|\mathbf{r} - \mathbf{x}\|_M^2 + \|\mathbf{p} - \mathbf{x}\|_M^2 \\ &= \|\dot{\mathbf{q}} + \dot{\mathbf{r}} - \dot{\mathbf{x}}\|_M^2 - \|\dot{\mathbf{q}} - \dot{\mathbf{x}}\|_M^2 - \|\dot{\mathbf{r}} - \dot{\mathbf{x}}\|_M^2 + \|\dot{\mathbf{x}}\|_M^2 \\ &= 2\langle M\dot{\mathbf{r}}, \dot{\mathbf{q}} \rangle \end{aligned} \quad \square$$

We next deduce from Lemma 2.1.2 that the germ of a Delaunay triangulation  $\text{Del}_M^Z$  at a point of an additive lattice  $Z$ , referred to as the Delaunay star [BWY15], obeys the acuteness property of Definition 2.0.1 w.r.t. the norm defined by  $M$ .

**Definition 2.1.3** (Delaunay star). The Delaunay star  $\text{Star}_M^Z(\mathbf{p})$  collects all simplices of a Delaunay triangulation  $\text{Del}_M^Z$  containing a given vertex  $\mathbf{p} \in Z$ .

**Proposition 2.1.4.** Let  $M \in S^{++}(\mathbb{E})$ , let  $Z$  be an additive lattice of  $\mathbb{E}$ , and let  $\mathbf{p} \in Z$ . Then  $V(\mathbf{p}) := \text{Star}_M^Z(\mathbf{p})$  is  $F$ -acute, in the sense of Definition 2.0.1, where  $F(\dot{\mathbf{p}}) := \|\dot{\mathbf{p}}\|_M$ .

---

<sup>2</sup>A triangulation is a collection of simplices which is stable under intersection.

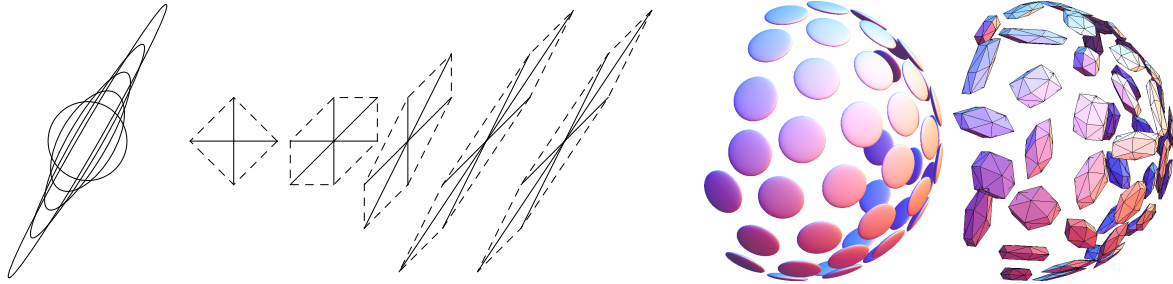


Figure 2.2 – Unit ball  $\{\mathbf{p} \in \mathbb{E}_d; \|\mathbf{p}\|_M \leq 1\}$  and FM-LBR stencil  $V(M)$  defined in (2.6), for some  $M \in \mathbb{S}^{++}(\mathbb{E}_d)$  of varying orientation and condition number. The three dimensional matrices are plate-like, with eigenvalues  $1, 10^2, 10^2$ . See Figure 1.6 for the needle-like case.

Consider a Riemannian metric  $\mathcal{M} : \bar{\Omega} \rightarrow \mathbb{S}^{++}(\mathbb{E})$ , and a discretization set  $X \cup \partial X$  based on a Cartesian grid  $Z$ , see (1.34). The stencils of the FM-LBR semi-Lagrangian scheme are defined, at each discretization point  $\mathbf{p} \in X$ , as the local star of the Delaunay triangulation of  $Z$ , *defined w.r.t. the geometry encoded in the local tensor  $\mathcal{M}(\mathbf{p})$ .*

$$V(\mathbf{p}) := \text{Star}_{\mathcal{M}(\mathbf{p})}^Z(\mathbf{p}). \quad (2.5)$$

The acuteness property follows from Proposition 2.1.4, and thus the guarantee that the FM-LBR scheme can be solved in a single pass and with quasi-linear complexity. The stencil (2.5) can be efficiently constructed in dimension  $d \leq 3$  using Selling’s algorithm and the concept of obtuse superbase, rather than actually computing the Voronoi diagram, see §A.2.2 or [CS92]. In contrast, causality does not hold if the collection  $Z$  of sites is not an additive lattice. In that case, the stencils (2.5) nevertheless remain “nicely shaped” typically, and have been used to solve Riemannian eikonal equations [RL16], improving on the (partly heuristic) approach [CHK13].

Let us emphasize that that the stars (2.5) are typically inconsistent with each other, in other words they cannot be glued into a global triangulation, since the matrix  $\mathcal{M}(\mathbf{p})$  changes from point to point. Consistent stars are only obtained if the metric varies very slowly and if the point set obeys a quantitative non-degeneracy property [BWY15], which is not satisfied by Cartesian grids. A much weaker consistency property of these Delaunay stars is nevertheless proved in Proposition 1.8 of [Mir14a]: in dimension  $d \leq 4$ , if  $Z$  is an additive lattice and if  $M, M' \in \mathbb{S}^{++}(\mathbb{E}_d)$  are sufficiently close, then  $\text{Star}_M^Z$  and  $\text{Star}_{M'}^Z$  contain the elements of a common basis of  $Z$ , and their opposites. This property implies that the discrete solution  $U$  of (2.2) obeys a Lipschitz property, and thus does not suffer from the chessboard artifacts which are commonly observed with (badly designed) adaptive PDE schemes on Cartesian grids.

In the rest of this subsection, we show evidence that the FM-LBR is better than alternative semi-Lagrangian schemes, for Riemannian eikonal equations on Cartesian grids. We present theoretical arguments as well as numerical test cases. We say that a stencil  $V$  is  $M$ -acute iff it is  $F$ -acute, where  $F = \|\cdot\|_M$  and where the reference point is  $\mathbf{p} = 0$ . We also use the following shorthand for the FM-LBR stencils, i.e. Delaunay stars of the canonical lattice  $\mathbb{L}_d \subseteq \mathbb{E}_d$

$$V(M) := \text{Star}_{M}^{\mathbb{L}_d}(0). \quad (2.6)$$

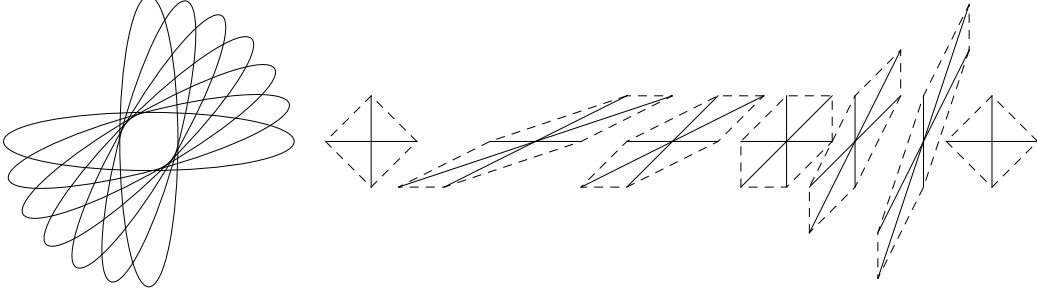


Figure 2.3 – Unit ball  $\{\dot{\mathbf{p}} \in \mathbb{E}_2; \|\dot{\mathbf{p}}\|_M \leq 1\}$  and stencil  $V(M)$  defined in (2.6), for some  $M \in S^{++}(\mathbb{E}_2)$ .

A first argument in favor of the FM-LBR is numerical cost, which is under control since the scheme is causal and uses stencils with few vertices. More precisely, the number of vertices of  $V(M)$  is independent of the specific tensor  $M \in S^{++}(\mathbb{E}_d)$  considered, but is bounded in terms of the dimension  $d$  alone. In dimension  $d = 2$  there are 6 vertices, and in dimension  $d = 3$  there are 14 vertices, for almost every  $M \in S^{++}(\mathbb{E}_d)$ , see [Mir14a]. In arbitrary dimension, boundedness follows from a result of Voronoi stating that there are only finitely many classes of Delaunay triangulations  $\mathcal{T}_M^{\mathbb{L}_d}$ , where  $M \in S^{++}(\mathbb{E}_d)$ , up to linear changes of coordinates in  $GL(\mathbb{L}_d)$ , see §A.2.2 or [Sch09]. In contrast, alternative constructions of  $M$ -acute stencils typically yield a number of vertices growing polynomially with the condition number  $\text{Cond}(M)$ , see [SV03, AM11, KS98]. The main exception is the FM-ASR scheme, presented in the next section, for which growth is poly-logarithmic w.r.t.  $\text{Cond}(M)$  in average, see §2.2. However, the FM-ASR is only applicable in dimension  $d = 2$ , contrary to the FM-LBR.

A second argument in favor of the FM-LBR is numerical accuracy, which is tied to the diameter of the stencils, since the metric  $\mathcal{M}$  is approximated with a constant tensor  $\mathcal{M}(\mathbf{p})$  over the stencil  $V(\mathbf{p})$ . The FM-LBR stencils are optimal in this regard, in dimension  $d = 2$ , as shows the following result proved in [Mir16b]. See also the discussion in Appendix B of [Mir14a].

**Theorem 2.1.5** (Minimality of the FM-LBR stencils). *Let  $M \in S^{++}(\mathbb{E}_2)$  be generic<sup>3</sup>, and let  $V$  be an  $M$ -acute stencil with vertices in  $\mathbb{L}_d$ . Then  $\text{Hull}(V) \supseteq \text{Hull}(V(M))$ .*

The final result of this section provides sharp quantitative asymptotic estimates of the FM-LBR stencil radius, in dimension  $d = 2$ , in both the average case and the worst case. The proof, presented in [Mir16b], is based on a careful study of the Minkowski reduced bases, see Definition A.1.2, associated with the following family of matrices. For all  $\kappa \in [1, \infty[$  and all  $\theta \in \mathbb{R}$ ,

$$M_\kappa(\theta) := \kappa^{-1} \mathbf{n}(\theta) \otimes \mathbf{n}(\theta) + \kappa \mathbf{n}(\theta)^\perp \otimes \mathbf{n}(\theta)^\perp, \quad \text{where } \mathbf{n}(\theta) := (\cos \theta, \sin \theta).$$

The eigenvalues of  $M_\kappa^\theta$  are  $\kappa$  and  $\kappa^{-1}$ , thus the related metric condition number is  $\kappa$  in the sense of (1.37). We denote  $V_\kappa(\theta) := V(M_\kappa^\theta)$ , and measure the radius of this stencil

<sup>3</sup>It suffices that  $V(M)$  is uniquely defined, which is the case for every  $M \in S^{++}(\mathbb{E}_d)$  except on a set of co-dimension 1.

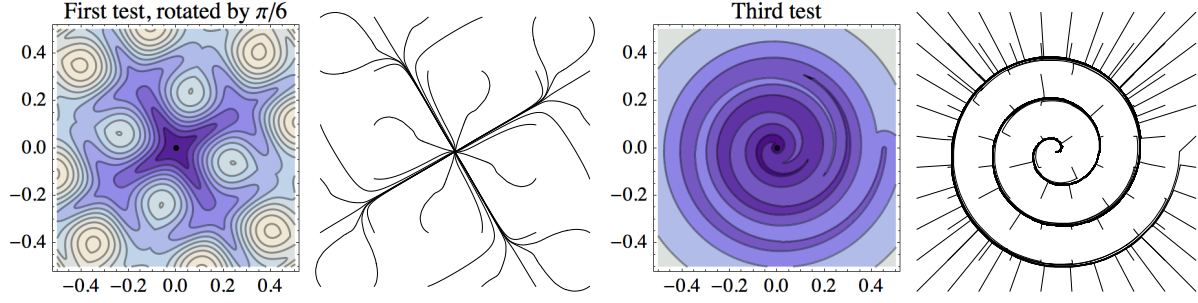


Figure 2.4 – Distance to the center point w.r.t. to anisotropic Riemannian metrics, computed by the FM-LBR, and backtraced minimal paths, see [Mir14a]. Left: Distance computation on an embedded manifold, considered in [SV03] and with maximal condition number  $\text{Cond}(\mathcal{M}) \approx 5.1$ . Right: Test inspired by tubular structure segmentation, considered in [BC10]. The metric is in this second case Euclidean, except along a thin spiraling tube where it is extremely anisotropic, with  $\text{Cond}(\mathcal{M}) \approx 100$ .

w.r.t. both the Euclidean norm and the intrinsic Riemannian norm.

$$R_\kappa(\theta) := \max_{\dot{\mathbf{q}} \in V_\kappa(\theta)} \|\dot{\mathbf{q}}\|, \quad S_\kappa(\theta) := \max_{\dot{\mathbf{q}} \in V_\kappa(\theta)} \|\dot{\mathbf{q}}\|_{M_\kappa(\theta)}.$$

**Theorem 2.1.6** (Worst and average size of the FM-LBR stencils). *For any  $\mathbf{p} \in [1, \infty]$  one has*

$$\|R_\kappa\|_{L^p} \approx \kappa^{\frac{1}{2}} \|S_\kappa\|_{L^p}, \quad \|S_\kappa\|_{L^p} \approx \begin{cases} 1 & \text{if } p < 2 \\ \sqrt{\ln \kappa} & \text{if } p = 2 \\ \kappa^{\frac{1}{2} - \frac{1}{p}} & \text{if } p > 2. \end{cases}$$

The  $L^p$  norms are over the interval  $[0, 2\pi]$ , and the  $\approx$  sign means that the ratio of the l.h.s. and r.h.s. is bounded above and below by positive constants as  $\kappa \rightarrow \infty$ .

In summary, the stencil size grows linearly  $\|R_\kappa\|_{L^\infty} \approx \kappa$ , when measured using the Euclidean metric and in the worst case. However, stencil size  $\|S_\kappa\|_{L^\infty} \approx \sqrt{\kappa}$  is much smaller when measured in the intrinsic metric, which is often more relevant for the numerical error, see Appendix B of [Mir14a]. In addition, stencil size is also much smaller in average, e.g.  $\|R_\kappa\|_{L^2} \approx \sqrt{\kappa \ln \kappa}$  and  $\|S_\kappa\|_{L^2} \approx \sqrt{\ln \kappa}$ , which we believe has a favorable impact on the effective numerical error. See §A.1.1 or [Mir16b] for more on this topic.

## 2.2 Finsler metrics

We describe in this section a numerical scheme referred to as Fast-Marching using Anisotropic Stencil Refinement (FM-ASR), which applies to eikonal equations associated with Finsler metrics, discretized on two dimensional Cartesian grids. In applications to image processing and segmentation, the main interest of Finsler metrics is that they can be asymmetric, in contrast with Riemannian metrics, which allows for a variety of new applications, see §4.2 or [MPAT08, ZSN09, CMC16a, CMC16b, CC17a, CC17b]. The

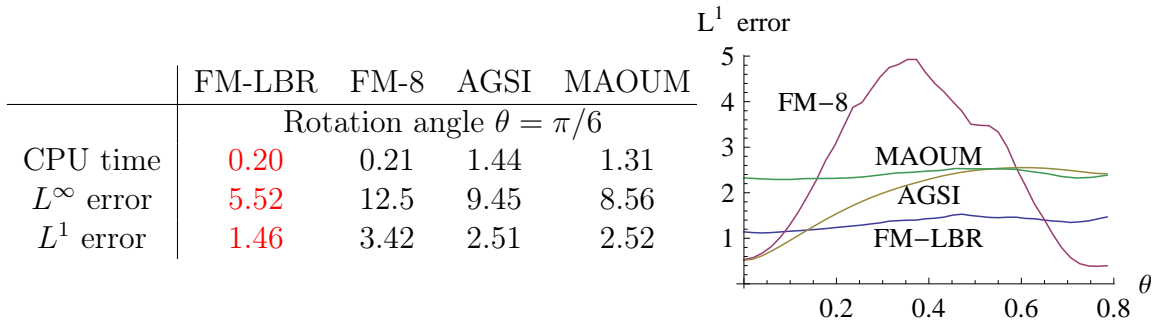


Figure 2.5 – Left: Comparison, on the test case of Figure 2.4 (left), of different numerical methods. Grid size is  $193 \times 193$ , CPU time is in seconds on a 2.7Ghz laptop, and numerical errors are multiplied by 100 for convenience. Discretization schemes are (i) The FM FM-LBR, presented here, (ii) FM-8, Fast marching using the 8-point stencil of Figure 2.1 (center left) - this stencil is not acute w.r.t. the metric at all points, hence convergence does not hold asymptotically. (iii) AGSI, a non-causal, iterative method [BR06], instantiated with a 6-point stencil. (iv) MAOUM, a causal method with a very wide stencil [AM11]. Right: Comparison of the error for different angles of rotation the test case (lower is better). The coordinate bias of the FM-8 and AGSI methods is apparent.

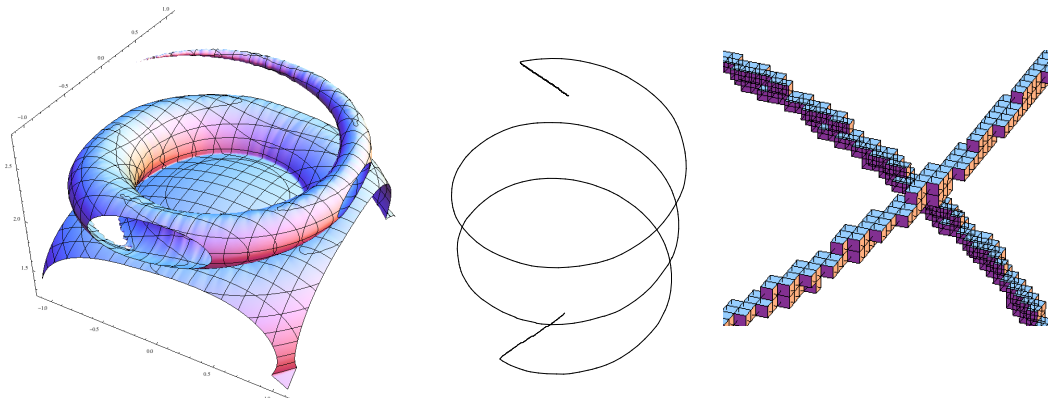


Figure 2.6 – Results of the FM-LBR in a 3D test case, inspired by applications to tubular structure segmentation, see [Mir14a]. The metric is Euclidean, except in a tube along a curve  $\Gamma$ , where it is highly anisotropic with condition number equal to 50. Iso-surface  $\{u(z) = 2\}$  (left), and shortest path joining the points  $(0, 0, 0)$  and  $(3, 0, 0)$  (center). Detail of the discrete points (represented by small cubes), in the neighborhood of the curve  $\Gamma(t) = (\cos \omega_0 t, \sin \omega_0 t, t)$ , for which the Riemannian metric is not Euclidean (right).

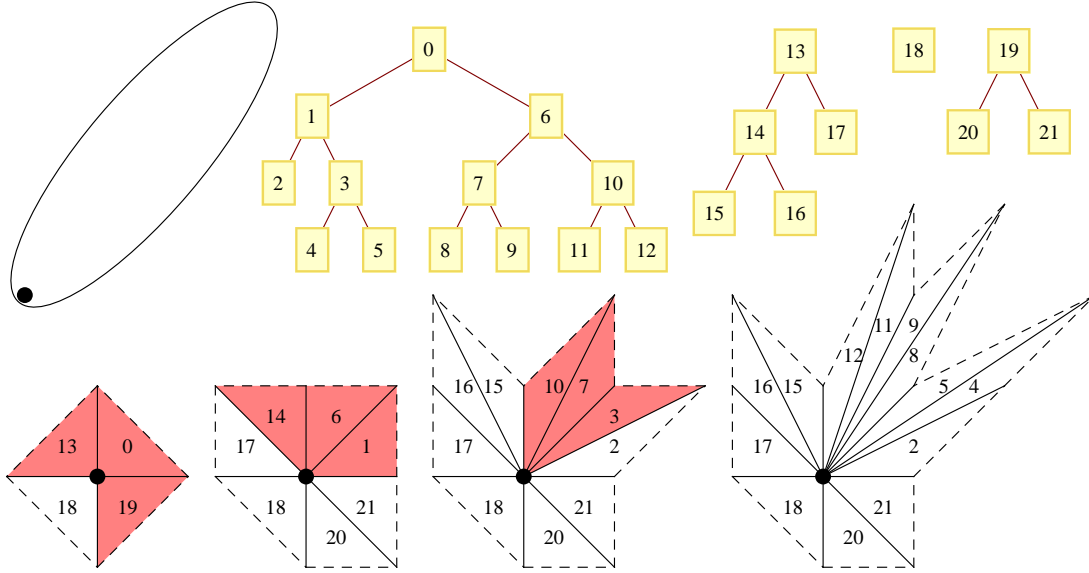


Figure 2.7 – Top left: Unit ball of an asymmetric gauge  $F$  of condition number  $\text{Cond}(F) = 20$ . Bottom: Construction of  $V(F)$  by recursive refinement (bottom, left to right). The triangles which non-zero vertices for not do not form an  $F$ -acute angle are shown in color, and are refined in the next step. Top right: The four binary trees corresponding to this refinement procedure.

FM-ASR stencil construction is based on an arithmetic structure named the Stern-Brocot tree, which is mostly known for its applications in the study of rational approximations of reals, see §A.1.3 or [Niq07] and references therein.

**Definition 2.2.1.** Let  $F$  be a finite gauge on  $\mathbb{E}_2$ . We say that  $\mathbf{p}, \mathbf{q} \in \mathbb{E}_2$  form an  $F$ -acute angle, iff  $F(\mathbf{p} + t\mathbf{q}) \geq F(\mathbf{p})$  and  $F(t\mathbf{p} + \mathbf{q}) \geq F(\mathbf{q})$  for all  $t \geq 0$ .

See Proposition 2.0.2 for equivalent but simpler forms of this condition when the gauge  $F$  has additional structure, e.g. is differentiable or is of Riemannian type. As its name indicates, the FM-ASR numerical scheme builds its stencils using an iterative refinement procedure, ending when all the external angles are acute w.r.t. the metric. See Figure 2.7.

**Definition 2.2.2.** To each asymmetric gauge  $F$  on  $\mathbb{E}_2$  we associate a family  $(V_n)_{n \geq 0}$  of triangulations defined as follows:

- $V_0$  consists of the four triangles of vertices  $\{(0, 0), (\pm 1, 0), (0, \pm 1)\}$ .
- $V_{n+1}$  is obtained by replacing any triangle  $\{0, \mathbf{p}, \mathbf{q}\}$  of  $V_n$  such that  $\mathbf{p}, \mathbf{q}$  do not form an  $F$ -acute angle, with its two children  $\{0, \mathbf{p}, \mathbf{p} + \mathbf{q}\}$  and  $\{0, \mathbf{p} + \mathbf{q}, \mathbf{q}\}$ .

The four triangles of  $V_0$  can be regarded as the roots of four copies of the Stern-Brocot tree, one for each quadrant. The algorithm main loop, described in the second point of this definition, inductively defines four finite subtrees. Each node is replaced with its two children, until a stopping criterion is met, which is based on the notion of  $F$ -acute angle.

**Proposition 2.2.3.** *The refinement procedure of Definition 2.2.2 stabilizes<sup>4</sup> to a stencil denoted  $V(F)$ , which by construction is  $F$ -acute.*

Let  $\Omega \subseteq \mathbb{E}_2$  be a bounded two-dimensional domain, equipped with a finite metric  $\mathcal{F} : \bar{\Omega} \times \mathbb{E}_2 \rightarrow [0, \infty[$ . Let  $h > 0$  be a gridscale, and let  $X := \Omega \cap h\mathbb{L}_2$  and  $\partial X := (\mathbb{E}_2 \setminus \Omega) \cap h\mathbb{L}_2$  be the discrete domain and discrete boundary. For each  $\mathbf{p} \in X$ , the FM-ASR  $\mathcal{F}_{\mathbf{p}}$ -acute stencil  $V(\mathbf{p})$  is defined by choosing the local gauge  $F := \mathcal{F}_{\mathbf{p}}$  in Definition 2.2.2, and adequately translating and scaling the result

$$V(\mathbf{p}) := \mathbf{p} + hV(\mathcal{F}_{\mathbf{p}}).$$

The resulting semi-Lagrangian discretization is causal, since its stencils by construction obey the acuteness property, see Definition 2.0.1. It can thus be solved in a single pass using the fast marching algorithm, and is referred to as the FM-ASR. The complexity<sup>5</sup> of this algorithm is  $\mathcal{O}(M \ln N)$ , where  $N := \#(X)$  is the cardinality of the discrete domain, and  $M := \sum_{\mathbf{p} \in X} \#(V(\mathbf{p}))$  is the total number of elements of the stencils (triangles or vertices equivalently). Our main result shows that the FM-ASR stencils cardinality  $\#(V(F))$  grows quasi-linearly in the worst case and poly-logarithmically in the average case (under random rotations of the discretization grid), w.r.t. the condition number of the gauge  $F$ , defined by (1.34).

**Theorem 2.2.4.** *Let  $F$  be an finite gauge on  $\mathbb{E}_2$ , with condition number  $\kappa := \text{Cond}(F)$ . Then  $\#V(F) \leq C\kappa(1 + \ln \kappa)$ , and*

$$\int_0^{2\pi} \#(V(F \circ R_\theta)) \, d\theta \leq C(1 + \ln^3 \kappa), \quad (2.7)$$

where  $R_\theta$  denotes the rotation of angle  $\theta \in \mathbb{R}$ , and  $C$  is an absolute constant.

The proof of the average case estimate (2.7), presented in [Mir14b], proceeds by successive generalizations. Riemannian norms are addressed first, since in that case the stencil construction of Definition 2.2.2 only explores a single branch of the Stern-Brocot tree, and can be related to the continued fraction approximation of  $\tan \theta$ . A similar behavior is observed in [BOZ04] in the context of anisotropic non-divergence form diffusion. Arguments of convex analysis and of approximation theory are then used to extend the result to arbitrary non-symmetric finite gauges.

---

<sup>4</sup>In other words there exists  $N \geq 0$  such that  $V_n = V(F)$  for all  $n \geq N$ .

<sup>5</sup>The complexity is given assuming a standard heap structure for the the sorted list of points, such as red-black trees. Theoretical complexity drops to  $\mathcal{M}(M + N \ln N)$  when using the Fibonacci heap data structure, but computation time empirically increases, due to the larger hidden constant.

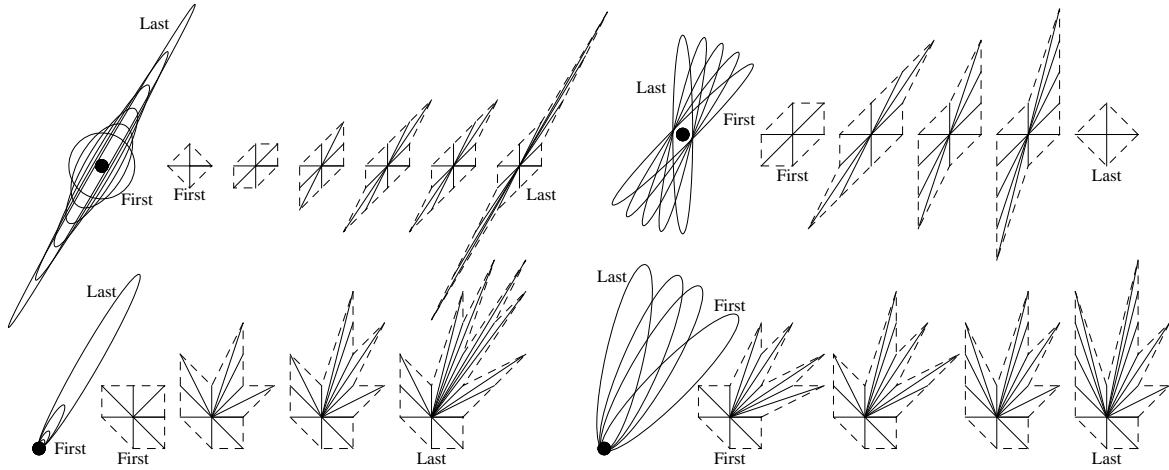


Figure 2.8 – Unit balls and stencils generated by the FM-ASR, for some symmetric (top) and asymmetric (bottom) norms.

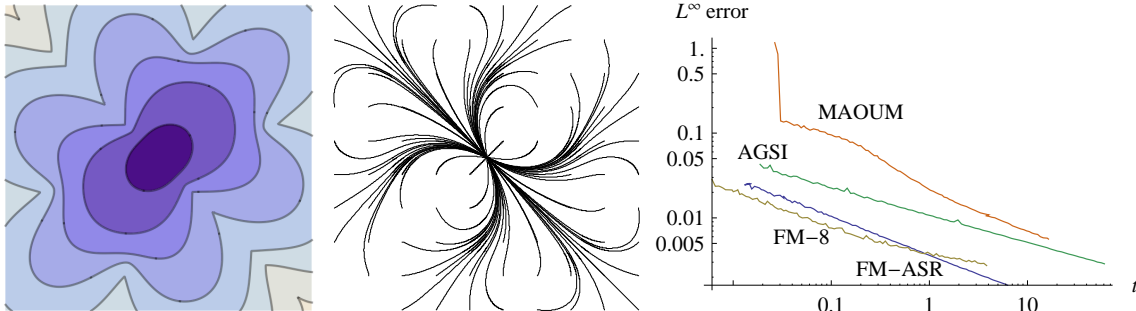


Figure 2.9 – An instance of Zermelo's problem, considered in [SV03]. The unit ball of the metric  $\mathcal{F}_{(x,y)}$  is the Euclidean unit ball translated by  $-\gamma \sin(4\pi x) \sin(4\pi y) \frac{(x,y)}{\|(x,y)\|}$ , where  $\gamma := 0.9$ . Left: Distance to the center. Center: Minimal geodesics backtraced. Right: Error vs CPU time plot (lower is better), for the FM-ASR presented here, the AGSI [BR06], the MAOUM [AM11], and the FM-8 see Figure 2.1. The latter is fast and gives good results at low resolutions, but is non-convergent asymptotically due to the lack of acuteness.

# Chapter 3

## Eulerian schemes

### Contents

---

<b>3.1 Quadratic Hamiltonians . . . . .</b>	<b>65</b>
3.1.1 Riemannian metrics . . . . .	65
3.1.2 Sub-Riemannian metrics . . . . .	66
3.1.3 Rander metrics . . . . .	69
<b>3.2 Curvature penalized models . . . . .</b>	<b>71</b>
3.2.1 The Reeds-Shepp forward model. . . . .	74
3.2.2 The Euler-Mumford elastica model. . . . .	76
3.2.3 The Dubins car model. . . . .	76

---

This section describes Eulerian numerical schemes for generalized eikonal PDEs, associated with Riemannian metrics, sub-Riemannian metrics, and more general non-holonomic models. Contrary to the semi-Lagrangian schemes discussed in §2, which can be interpreted in geometrical terms, the numerical schemes presented in this section directly discretize the eikonal PDE using upwind finite differences. For that purpose, let us introduce the Lagrangian and Hamiltonian associated to a metric  $\mathcal{F}$ , which are defined for any point  $\mathbf{p} \in \Omega$ , any vector  $\dot{\mathbf{p}} \in \mathbb{E}$ , and any co-vector  $\hat{\mathbf{p}} \in \mathbb{E}_d^*$  by

$$\mathcal{L}_{\mathbf{p}}(\dot{\mathbf{p}}) := \frac{1}{2} \mathcal{F}_{\mathbf{p}}(\dot{\mathbf{p}})^2, \quad \mathcal{H}_{\mathbf{p}}(\hat{\mathbf{p}}) := \sup_{\dot{\mathbf{p}} \in \mathbb{E}_d} \langle \hat{\mathbf{p}}, \dot{\mathbf{p}} \rangle - \mathcal{L}_{\mathbf{p}}(\dot{\mathbf{p}}).$$

One easily checks that the Hamiltonian is the half squared dual metric:  $\mathcal{H}_{\mathbf{p}} = \frac{1}{2}(\mathcal{F}_{\mathbf{p}}^*)^2$ . The eikonal equation (1.33) can thus be rewritten in terms of the Hamiltonian

$$\forall \mathbf{p} \in \Omega, \quad 2\mathcal{H}_{\mathbf{p}}(du(\mathbf{p})) = 1, \quad \forall \mathbf{p} \in \partial\Omega, \quad u(\mathbf{p}) = 0. \quad (3.1)$$

Note that the distance map  $u$  associated with the non-locally controllable models considered in §3.2 has discontinuities, both on  $\partial\Omega$  and within  $\Omega$ . The PDE (3.1), and its boundary conditions, thus need to be understood in the relaxed sense of discontinuous viscosity solutions [BCD08]. Our discretizations of the PDE (3.1) rely on a special representation or approximation of the Hamiltonian  $H_{\mathbf{p}}(\hat{\mathbf{p}}) \approx \mathcal{H}_{\mathbf{p}}(\hat{\mathbf{p}})$ , of the following form

$$2H_{\mathbf{p}}(\hat{\mathbf{p}}) = \max_{i \in I} \sum_{j \in J} \rho_{ij}(\mathbf{p}) \langle \hat{\mathbf{p}}, \dot{\mathbf{e}}_{ij}(\mathbf{p}) \rangle_+^2, \quad (3.2)$$

where  $a_+ := \max\{a, 0\}$ , and where  $I$  and  $J$  are finite sets. The choice of the weights  $\rho_{ij}(\mathbf{p}) \geq 0$  and offsets  $\dot{\mathbf{e}}_{ij}(\mathbf{p}) \in \mathbb{L}_d$  is non-trivial and depends on the structure of the metric, see §3.1 and §3.2. In the following, for readability, we omit to write the dependency of the offsets  $\mathbf{e}_{ij} = \mathbf{e}_{ij}(\mathbf{p})$  on the base point  $\mathbf{p} \in \bar{\Omega}$ .

The discrete domain samples, as usual, the PDE domain  $\Omega \subseteq \mathbb{E}_d$  on the canonical cartesian grid of scale  $h > 0$

$$X_h := \Omega \cap h\mathbb{L}_d, \quad \partial X_h := (\mathbb{E}_d \setminus \Omega) \cap h\mathbb{L}_d. \quad (3.3)$$

The generalized eikonal PDE (3.1) is discretized using (3.2) as follows: find  $U : X_h \cup \partial X_h \rightarrow \mathbb{R}$  obeying

$$\forall \mathbf{p} \in X_h, \max_{i \in I} \sum_{j \in J} \rho_{ij}(\mathbf{p}) (U(\mathbf{p}) - U(\mathbf{p} - h\dot{\mathbf{e}}_{ij}))_+^2 = h^2, \quad \forall \mathbf{p} \in \partial X_h, U(\mathbf{p}) = 0. \quad (3.4)$$

The l.h.s. of the numerical scheme (3.4, left) is a *non-decreasing* function of the *positive parts* of the finite differences  $(U(\mathbf{p}) - U(\mathbf{q}))_{\mathbf{q} \in X_h}$ . Our discretization is therefore *monotone* and *causal*, in the sense of Definition B.2.1, thus the system can be solved in a single pass and with quasi-linear complexity using the Fast-Marching algorithm, see §B.2.

For several models, it is interesting to introduce symmetric terms in (3.2), which yield symmetric upwind finite differences after discretization in (3.4), as follows

$$\mu_{ij}(\mathbf{p}) \langle \hat{\mathbf{p}}, \dot{\mathbf{f}}_{ij}(\mathbf{p}) \rangle^2, \quad \mu_{ij}(\mathbf{p}) \max\{0, U(\mathbf{p}) - U(\mathbf{p} - h\dot{\mathbf{f}}_{ij}), U(\mathbf{p}) - U(\mathbf{p} + h\dot{\mathbf{f}}_{ij})\}^2. \quad (3.5)$$

Note that this type of finite differences cannot be envisioned if the discretization set  $X_h \cup \partial X_h$  is not an additive grid, since it relies on the assumption that  $\mathbf{p} + \dot{\mathbf{e}} \in X_h \cup \partial X_h$  iff  $\mathbf{p} - \dot{\mathbf{e}} \in X_h \cup \partial X_h$ , with  $\dot{\mathbf{e}} = h\dot{\mathbf{f}}_{ij}$ . In the next two subsections, we introduce numerical schemes for various models, using representations of their Hamiltonians in the form (3.2). We also state convergence results, with convergence rates for the models which are locally controllable, and in a weak sense otherwise.

Before turning to these complex models, we recall the classical case of an isotropic metric, first addressed in [Set96, RT92]. Denoting by  $c : \bar{\Omega} \rightarrow ]0, \infty[$  the cost function, the metric and hamiltonian read

$$\mathcal{F}_{\mathbf{p}}(\dot{\mathbf{p}}) := c(\mathbf{p}) \|\dot{\mathbf{p}}\|, \quad 2\mathcal{H}_{\mathbf{p}}(\hat{\mathbf{p}}) = c(\mathbf{p})^{-2} \|\hat{\mathbf{p}}\|^2 = c(\mathbf{p})^{-2} \sum_{1 \leq j \leq d} \langle \hat{\mathbf{p}}, \dot{\mathbf{e}}_j \rangle^2,$$

for any  $\mathbf{p} \in \bar{\Omega}$ , any vector  $\dot{\mathbf{p}} \in \mathbb{E}_d$ , and any co-vector  $\hat{\mathbf{p}} \in \mathbb{E}_d^*$ . We denoted by  $(\mathbf{e}_j)_{j=1}^d$  the canonical basis of  $\mathbb{E}_d$ . This leads to the eikonal PDE discretization

$$\forall \mathbf{p} \in X_h, c(\mathbf{p})^{-2} \sum_{1 \leq j \leq d} \max\{0, U(\mathbf{p}) - U(\mathbf{p} - h\dot{\mathbf{e}}_j), U(\mathbf{p}) - U(\mathbf{p} + h\dot{\mathbf{e}}_j)\}^2 = h^2,$$

and  $\forall \mathbf{p} \in \partial X_h, U(\mathbf{p}) = 0$ . Surprisingly, this formulation is mathematically equivalent to a common semi-Lagrangian scheme, in the sense that the discrete solutions are identical. The corresponding scheme is based on the stencil which is the convex hull of  $\{\mathbf{p} \pm h\dot{\mathbf{e}}_j\}_{j=1}^d$ , as illustrated on Figure 2.1 (left and center right). In contrast the discretizations of Riemannian eikonal equations described in §2.1 and §3.1.1 are genuinely distinct.

## 3.1 Quadratic Hamiltonians

This subsection is devoted to Fast-Marching using Voronoi's First Reduction, abbreviated FM-VR1, which applies primarily to Riemannian metrics. Adaptations are provided for singular sub-Riemannian metrics (via Riemannian approximations), and non-symmetric Rander metrics (with the loss of causality). The results of this section are from [Mir17a].

### 3.1.1 Riemannian metrics

A Riemannian metric is determined by a field of positive definite tensors  $\mathcal{M} : \bar{\Omega} \rightarrow \mathbb{S}^{++}(\mathbb{E}_d)$ . The metric, dual metric, Lagrangian and Hamiltonian read as follows. For any point  $\mathbf{p} \in \bar{\Omega}$ , any vector  $\dot{\mathbf{p}} \in \mathbb{E}_d$  and any co-vector  $\hat{\mathbf{p}} \in \mathbb{E}_d^*$

$$\begin{aligned} \mathcal{F}_{\mathbf{p}}(\dot{\mathbf{p}}) &= \|\dot{\mathbf{p}}\|_{\mathcal{M}(\mathbf{p})}, & \mathcal{F}_{\mathbf{p}}^*(\hat{\mathbf{p}}) &= \|\hat{\mathbf{p}}\|_{\mathcal{D}(\mathbf{p})}, \\ 2\mathcal{L}_{\mathbf{p}}(\dot{\mathbf{p}}) &= \|\dot{\mathbf{p}}\|_{\mathcal{M}(\mathbf{p})}^2, & 2\mathcal{H}_{\mathbf{p}}(\hat{\mathbf{p}}) &= \|\hat{\mathbf{p}}\|_{\mathcal{D}(\mathbf{p})}^2, \end{aligned}$$

where  $\mathcal{D}(\mathbf{p}) := \mathcal{M}(\mathbf{p})^{-1}$ . Voronoi's first reduction, applied to the matrix  $\mathcal{D}(\mathbf{p})$ , provides a decomposition of the Hamiltonian

$$\mathcal{D}(\mathbf{p}) = \sum_{1 \leq i \leq d'} \rho_i(\mathbf{p}) \dot{\mathbf{e}}_i \otimes \dot{\mathbf{e}}_i, \quad \mathcal{H}_{\mathbf{p}}(\hat{\mathbf{p}}) = \frac{1}{2} \sum_{1 \leq i \leq d'} \rho_i(\mathbf{p}) \langle \hat{\mathbf{p}}, \dot{\mathbf{e}}_i \rangle^2, \quad (3.6)$$

where  $d' := d(d+1)/2$ ,  $\rho_i(\mathbf{p}) \geq 0$ , and  $\dot{\mathbf{e}}_i = \dot{\mathbf{e}}_i(\mathbf{p}) \in \mathbb{E}_d$  for all  $1 \leq i \leq d'$ . We recognize the general form (3.2), except that there is no need of a maximum over a finite set  $I$ , and that the terms do not feature the positive part, hence they are discretized using symmetric upwind finite differences as in (3.5). See Figure 1.1 for examples of the decomposition (3.6, left).

A convergence analysis of this numerical scheme is presented in [Mir17a], with convergence rates, obtained using the doubling of variables technique [Eva10]. This technique is also applicable to adaptive semi-lagrangian schemes [SMK16].

**Theorem 3.1.1.** *Let  $\Omega \subseteq \mathbb{E}_d$  be open and bounded, and let  $\mathcal{M} : \bar{\Omega} \rightarrow \mathbb{S}^{++}(\mathbb{E}_d)$  be Lipschitz. Then the discretized<sup>1</sup> system (3.4) admits for each  $h > 0$  a unique solution, denoted  $U_h$ . Furthermore, denoting by  $u : \bar{\Omega} \rightarrow \mathbb{R}$  the solution of the continuous problem (3.1), one has*

$$\max_{\mathbf{p} \in X_h} |U_h(\mathbf{p}) - u(\mathbf{p})| \leq C\sqrt{h},$$

where the constant  $C$  depends on  $\Omega$  and  $\mathcal{M}$ .

In our experiments, first order convergence  $\mathcal{O}(h)$  is typically observed [Mir17a], but the announced slower rate  $\mathcal{O}(\sqrt{h})$  does hold in some pathological cases [SMK16]. In favorable cases and with a careful initialization, second order convergence  $\mathcal{O}(h^2)$  can be achieved in the  $L^1$  norm, provided the scheme is modified in the spirit of the High Accuracy Fast Marching Method (HAFMM) [Set99]. More precisely, the first order upwind finite differences appearing in (3.4) are replaced when possible with the following formally second

<sup>1</sup>Instantiated with symmetric upwind finite differences (3.5) in this case.

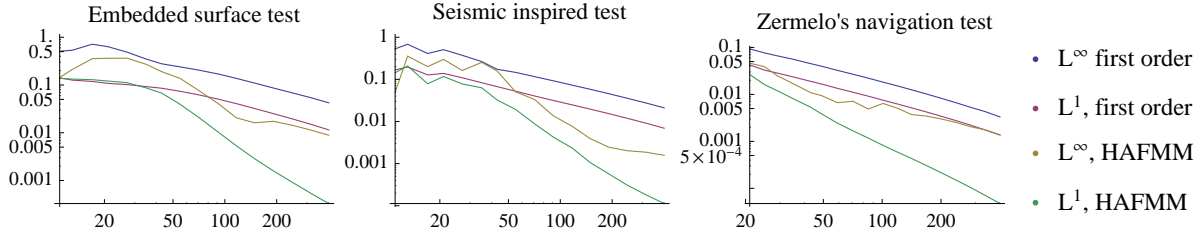


Figure 3.1 – Numerical error of the FM-VR1 as a function of gridsize for some two dimensional test cases, illustrated respectively on Figure 1.13, Figure 2.4, and Figure 2.9 (with the adequate modification for Rander metrics in the latter case, see §3.1.3). Second order convergence is achieved in the  $L^1$  norm, but not in the  $L^\infty$  norm (despite the removal of a 5 pixel layer along the boundary), which is not surprising since solutions to eikonal equations are not smooth, but typically feature a gradient discontinuity along a  $(d - 1)$ -dimensional interface called the cut locus.

order counterparts. For any smooth  $U : \Omega \rightarrow \mathbb{R}$ , any point  $\mathbf{p} \in \Omega$ , any offset  $\dot{\mathbf{e}} \in \mathbb{E}_d$ , and any small grid scale  $h > 0$

$$\langle dU(\mathbf{p}), \dot{\mathbf{e}} \rangle = \frac{1}{h}(U(\mathbf{p} + h\dot{\mathbf{e}}) - U(\mathbf{p})) - \frac{1}{2h}(U(\mathbf{p}) - 2U(\mathbf{p} + h\dot{\mathbf{e}}) + U(\mathbf{p} + 2h\dot{\mathbf{e}})) + \mathcal{O}(h^2). \quad (3.7)$$

Second order convergence however cannot be expected in the  $L^p$  norm for any  $p > 1$ . Indeed, numerical error is at best  $\mathcal{O}(h^2)$  in regions where the distance map solution  $u$  is smooth, but is also  $\mathcal{O}(h)$  along a surface of co-dimension 1 where  $u$  is non-differentiable. This singular set, where minimal geodesics of equal length meet, is an important object of study for several communities, and may be called the cut locus, the Maxwell set, or the medial axis.

### 3.1.2 Sub-Riemannian metrics

Sub-Riemannian metrics are the simplest class of singular metrics: their gauges attach infinite values to some vectors, thus forbidding direct motion in some directions, a property also referred to as non-holonomy. One of their simplest instances, due to Reeds and Shepp [RS90] describes the motion of a wheelchair, which can move forward and backward, rotate left and right, but cannot translate sideways. This model is considered in §3.2 and §4.1.3, and higher dimensional extensions are considered in §4.1.4. See also Figure 3.2.

A sub-Riemannian metric  $\mathcal{F} : \overline{\Omega} \times \mathbb{E} \rightarrow [0, \infty]$  can be regarded as degenerate Riemannian metric, which gauges  $\mathcal{F}_{\mathbf{p}}$  take infinite values outside of a subspace  $\Delta(\mathbf{p}) \subseteq \mathbb{E}$  of the tangent space, depending on the current point  $\mathbf{p} \in \overline{\Omega}$ . We denote by  $\mathbb{E}$  a finite dimensional real vector space, and by  $\Omega \subseteq \mathbb{E}$  a subdomain. In addition, it is assumed that vector fields within the subspace distribution  $\Delta$  and their Lie brackets up to a finite depth span the tangent space  $\mathbb{E}$ , which implies the local controllability of the model [Mon06]. This latter point turns out to be irrelevant for the design of our discretization scheme and its convergence analysis, hence it is not discussed here. Instead of sub-Riemannian geometry, we actually consider the simpler class of pre-Riemannian models, defined below, and introduce alternative controllability assumptions, also considered in [BCD08].

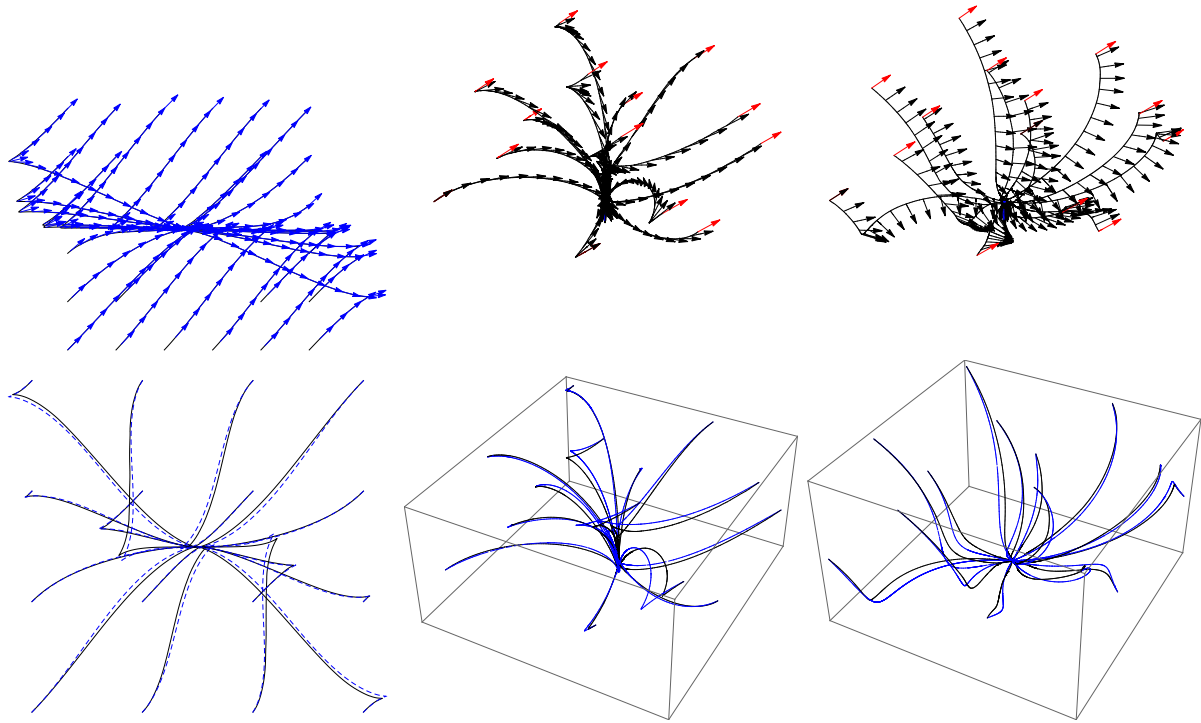


Figure 3.2 – Minimal paths for the Reeds-Shepp sub-riemannian model on  $\mathbb{R}^2 \times \mathbb{S}^1$  (left), its generalization to  $\mathbb{R}^3 \times \mathbb{S}^2$  (center), and the dual model (right), see §4.1.4. A point  $(\mathbf{x}, \mathbf{n}) \in \mathbb{R}^d \times \mathbb{S}^{d-1}$  is shown as an arrow originating from  $\mathbf{x}$  and with direction  $\mathbf{n}$ . Top: The backtraced paths do (approximately) obey the sub-riemannian constraint of parallelism  $\dot{\mathbf{x}} \parallel \mathbf{n} = 0$  (left and center) or orthogonality  $\dot{\mathbf{x}} \perp \mathbf{n} = 0$  (right) of the physical velocity  $\dot{\mathbf{x}}$  with the angular coordinate  $\mathbf{n}$ . Bottom: Comparison of the backtraced paths obtained from the numerical solution to the eikonal equation, with paths obtained using an ODE shooting method based on Hamilton’s equations of geodesics.

**Definition 3.1.2.** A pre-riemannian model is the data of Lipschitz vector fields  $\dot{\omega}_1, \dots, \dot{\omega}_n : \bar{\Omega} \rightarrow \mathbb{E}$ . We let  $\Delta(\mathbf{p}) := \text{Span}\{\omega_i(\mathbf{p}); 1 \leq i \leq n\}$ , and say that the model is:

- Globally Controllable to the Boundary (GCB) iff for each  $\mathbf{p} \in \Omega$  there exists a smooth path  $\gamma : [0, 1] \rightarrow \bar{\Omega}$  obeying  $\gamma(0) = \mathbf{p}$ ,  $\gamma(1) \in \partial\Omega$ , and  $\gamma(t) \in \Delta(\mathbf{p})$  for all  $t \in [0, 1]$ .
- Short Time Locally Controllable to the Boundary (STLCB) iff  $\partial\Omega$  admits unit normals  $\mathbf{n} : \partial\Omega \rightarrow \mathbb{E}_d$  with Lipschitz regularity, obeying  $\mathbf{n}(\mathbf{p}) \notin \Delta(\mathbf{p})^\perp$  for each  $\mathbf{p} \in \partial\Omega$ .

Each pre-Riemannian model comes with a singular metric, defined *dually* as follows. For any point  $\mathbf{p} \in \bar{\Omega}$ , and any co-vector  $\hat{\mathbf{p}} \in \mathbb{E}^*$

$$\mathcal{F}_{\mathbf{p}}^*(\hat{\mathbf{p}}) := \|\hat{\mathbf{p}}\|_{\mathcal{D}(\mathbf{p})}, \quad \text{where } \mathcal{D}(\mathbf{p}) := \sum_{1 \leq i \leq n} \omega_i(\mathbf{p}) \otimes \omega_i(\mathbf{p}).$$

Note that  $\mathcal{D}(\mathbf{p})$  is only positive *semi*-definite in general, thus admits no inverse tensor in the sense of linear algebra. The primal metric itself  $\mathcal{F}_{\mathbf{p}}(\hat{\mathbf{p}})$ , determined by the above expression of  $\mathcal{F}^*$ , therefore equals  $+\infty$  unless the vector  $\hat{\mathbf{p}}$  belongs to the range  $\Delta(\mathbf{p})$  of  $\mathcal{D}(\mathbf{p})$ . Property GCB nevertheless implies that the distance  $u : \bar{\Omega} \rightarrow \mathbb{R}_+$  to the domain boundary, as measured by the metric  $\mathcal{F}$ , only takes finite values. The additional property STLCB implies that  $u$  has Lipschitz regularity, see [Mir17a], and thus is a standard viscosity solution of the eikonal equation (1.33).

A relaxation strategy is used to compute the distance map w.r.t. a sub-Riemannian metric, based on an approximating family  $(\mathcal{M}_\varepsilon)_{\varepsilon>0}$  of Riemannian metrics, increasingly degenerate as  $\varepsilon \rightarrow 0$ .

**Definition 3.1.3.** A completion of a pre-riemannian model  $\dot{\omega}_1, \dots, \dot{\omega}_n$  is the data of an additional family of Lipschitz vector fields  $\dot{\omega}_1^*, \dots, \dot{\omega}_{n^*}^* : \bar{\Omega} \rightarrow \mathbb{E}$  which, together with the former, span  $\mathbb{E}_d$  at each point of  $\bar{\Omega}$ . For each  $\mathbf{p} \in \bar{\Omega}$  and each  $\varepsilon > 0$ , we let

$$\mathcal{D}^*(\mathbf{p}) := \sum_{1 \leq i \leq n^*} \omega_i^*(\mathbf{p}) \otimes \omega_i^*(\mathbf{p}), \quad \mathcal{D}_\varepsilon(\mathbf{p}) := \mathcal{D}(\mathbf{p}) + \varepsilon^2 \mathcal{D}^*(\mathbf{p}), \quad \mathcal{M}_\varepsilon(\mathbf{p}) := \mathcal{D}_\varepsilon(\mathbf{p})^{-1}.$$

**Theorem 3.1.4.** Consider a pre-riemannian model  $(\omega_i)_{i=1}^n$  obeying GCB and STLCB, and a completion  $(\omega_i^*)_{i=1}^{n^*}$ . Let  $u : \bar{\Omega}$  be the pre-Riemannian distance to the domain boundary  $\partial\Omega$ , and for each  $\varepsilon \in ]0, 1]$  denote by  $u_\varepsilon : \bar{\Omega} \rightarrow \mathbb{R}_+$  the distance w.r.t. the Riemannian metric defined by  $\mathcal{M}_\varepsilon$ . Let also  $U_{h,\varepsilon} : X_h \rightarrow \mathbb{R}_+$  be the discrete solution of the FM-VR1 numerical scheme applied to the metric  $\mathcal{M}_\varepsilon$  with the grid scale  $h > 0$ . Then

$$\max_{\mathbf{p} \in \bar{\Omega}} |u(\mathbf{p}) - u_\varepsilon(\mathbf{p})| \leq C\varepsilon, \quad \max_{\mathbf{p} \in X_h} |u_\varepsilon(\mathbf{p}) - U_{\varepsilon,h}(\mathbf{p})| \leq C\sqrt{r_\varepsilon h},$$

where  $r_\varepsilon$  denotes the maximal stencil radius (measured in pixels) used for  $\mathcal{M}_\varepsilon$ , and  $C$  only depends on  $\Omega, (\omega_i)_{i=1}^n, (\omega_i^*)_{i=1}^{n^*}$ . In particular  $U_{h,\varepsilon} \rightarrow u$  uniformly as  $\varepsilon \rightarrow 0$  and  $h r_\varepsilon \rightarrow 0$ .

By construction, the condition number of the tensors  $\mathcal{M}_\varepsilon$  is  $\mathcal{O}(\varepsilon^{-1})$ , hence  $r_\varepsilon \leq C\varepsilon^{-\alpha}$  with  $\alpha = 1$  if  $d \in \{2, 3\}$ , and  $\alpha = d - 1$  otherwise<sup>2</sup>, see Proposition A.2.2. The convergence

---

<sup>2</sup>We conjecture that this estimate is sub-optimal when  $d \geq 4$ , but this is the best that we have presently.

rate  $\max_{\Omega_h} |U_{h,\varepsilon} - u| \leq Ch^{\frac{1}{\alpha+2}}$  is thus ensured by choosing  $\varepsilon = h^{\frac{1}{\alpha+2}}$ . We must however admit that these rates are hard to measure in practice, and that a convenient small fixed value of the relaxation parameter is used in our applications, such as  $\varepsilon = 0.1$  typically.

### 3.1.3 Rander metrics

Rander metrics are among the simplest examples of non-symmetric metrics [Ran41]. They are encountered in Zermelo's motion planning problem, which involves a vehicle moving a unit speed but subject to a drift term, see the end of this subsection. They also appear in the reformulation of some region based energies appearing in image segmentation, see §4.2, and in the study of the Euler elastica model, see [CMC17]. Rander metrics are a generalization of Riemannian metrics, taking the form

$$\mathcal{F}_{\mathbf{p}}(\dot{\mathbf{p}}) = \|\dot{\mathbf{p}}\|_{\mathcal{M}(\mathbf{p})} + \langle \hat{\eta}(\mathbf{p}), \dot{\mathbf{p}} \rangle,$$

for any point  $\mathbf{p} \in \Omega$  and any vector  $\dot{\mathbf{p}} \in \mathbb{E}$ . Rander metrics are thus parametrized by a field of positive definite tensors  $\mathcal{M} : \bar{\Omega} \rightarrow \mathbb{S}^{++}(\mathbb{E}_d)$  and a field of co-vectors  $\hat{\eta} : \bar{\Omega} \rightarrow \mathbb{E}_d^*$ , which must obey following compatibility relation so as to ensure the positiveness  $\mathcal{F}_{\mathbf{p}}(\dot{\mathbf{p}}) > 0$  of the gauges on any non-zero vector  $\dot{\mathbf{p}} \in \mathbb{E} \setminus \{0\}$ . For any point  $\mathbf{p} \in \bar{\Omega}$

$$\|\hat{\eta}(\mathbf{p})\|_{\mathcal{D}(\mathbf{p})} < 1, \quad \text{where } \mathcal{D}(\mathbf{p}) := \mathcal{M}(\mathbf{p})^{-1}. \quad (3.8)$$

The eikonal equation satisfied by the distance map w.r.t. to a Rander metric can be stated in several equivalent forms, such as the natural one  $\mathcal{F}_{\mathbf{p}}^*(du(\mathbf{p})) = 1$ . The following inhomogeneous one however turns out to be more easily amenable to discretization

$$\forall \mathbf{p} \in \Omega, \quad \|du(\mathbf{p}) - \hat{\eta}(\mathbf{p})\|_{\mathcal{D}(\mathbf{p})}^2 = 1, \quad \forall \mathbf{p} \in \partial\Omega, \quad u(\mathbf{p}) = 0. \quad (3.9)$$

Similarly to the Riemannian case (3.6), we use Voronoi's first reduction of quadratic forms to obtain a decomposition  $\mathcal{D}(\mathbf{p}) = \sum_{i=1}^{d'} \rho_i(\mathbf{p}) \dot{\mathbf{e}}_i(\mathbf{p}) \otimes \dot{\mathbf{e}}_i(\mathbf{p})$  of the tensors. We discretize the HJB PDE (3.9, left) as follows: find  $U : X_h \cup \partial X_h \rightarrow \mathbb{R}$ , such that for all  $\mathbf{p} \in X_h$

$$\sum_{i \leq i \leq d'} \rho_i(\mathbf{p}) \max\{0, U(\mathbf{p}) - U(\mathbf{p} + h\dot{\mathbf{e}}_i) + h\langle \hat{\eta}(\mathbf{p}), \dot{\mathbf{e}}_i \rangle, U(\mathbf{p}) - U(\mathbf{p} - h\dot{\mathbf{e}}_i) - h\langle \hat{\eta}(\mathbf{p}), \dot{\mathbf{e}}_i \rangle\}^2 = h^2,$$

and  $U(\mathbf{p}) = 0$  for all  $\mathbf{p} \in \partial X_h$ . This numerical scheme is monotone, i.e. the above expression is a non-decreasing function of the finite differences  $(U_h(\mathbf{p}) - U_h(\mathbf{q}))_{\mathbf{q} \in X}$ , but unfortunately it is *not* causal, i.e. a function of their positive parts only. As a result, the fast marching algorithm is not applicable, and this PDE discretization *cannot* be solved in a single pass. We rely instead on iterative solvers, such as [BR06], which provide good performance provided the metric anisotropy and non-homogeneity are moderate.

It is natural to compare the present approach with the semi-Lagrangian FM-ASR scheme, see §2.2 or [Mir14b]. The latter has the advantage of being *causal*, and applies not only to Rander metrics, see Figure 2.9, but also to arbitrary Finsler metrics. However, the present approach applies in arbitrary dimension, see e.g. the three dimensional instance on Figure 3.3, in contrast with the FM-ASR which is limited to planar problems  $d = 2$ .

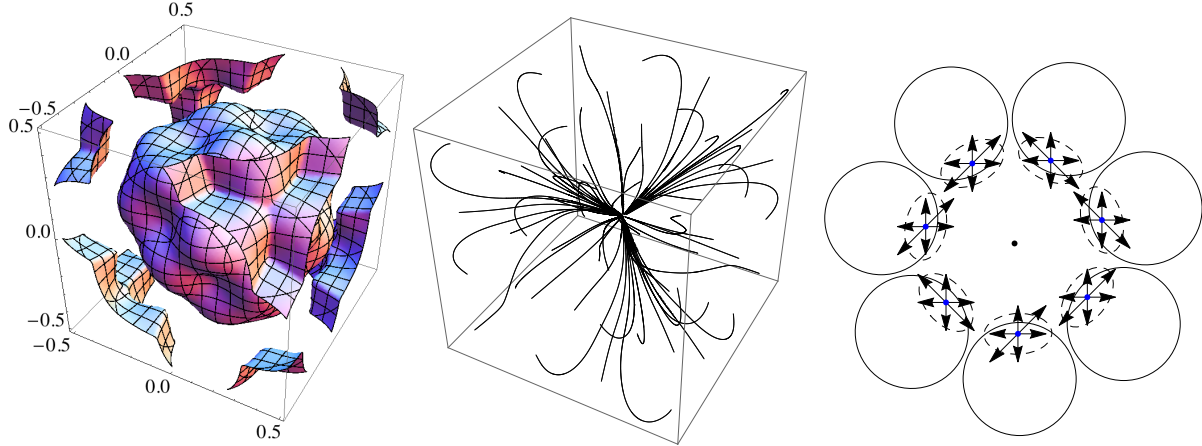


Figure 3.3 – Left and center: Level sets and minimal geodesics for a three dimensional instance of Zermelo’s problem, see [Mir17a]. Right: Illustration of the numerical scheme in dimension  $d = 2$ . Current point (blue), discretization stencil (arrows), unit ball for the local non-symmetric gauge  $\mathcal{F}_{\mathbf{p}}$  (black circle), unit ball for  $\mathcal{M}(\mathbf{p})$  (dashed ellipse).

The discretized PDE (3.9) admits a unique solution, converging uniformly as  $h \rightarrow 0$  to the distance  $u$  from the boundary  $\partial\Omega$  w.r.t. the Rander metric [Mir17a]. The guaranteed convergence rate  $\mathcal{O}(\sqrt{h})$  is similar to the Riemannian case, see Theorem 3.1.1, provided the tensors  $\mathcal{M}$  and co-vectors  $\hat{\eta}$  have Lipschitz regularity. The proofs are similar to the Riemannian case, since they only use the *monotony* of the discretization scheme, see [Mir17a]. (The lack of *causality* solely raises difficulties of algorithmic nature.) In practice, similarly again to the Riemannian case, the observed convergence rate is usually  $\mathcal{O}(h)$ , and convergence can be further accelerated by using the formally second order HAFMM finite differences (3.7). Second order  $\mathcal{O}(h^2)$  convergence is then observed in the  $L^1$  norm, in favorable cases and with a careful initialization, see Figure 3.1.

We conclude this section with a brief description of Zermelo’s navigation problem [BCD08], a classical optimal control problem involving Rander metrics, also illustrated on Figure 2.9. Consider a drift velocity on a domain  $\Omega \subseteq \mathbb{E}_d$ , encoded in a vector field  $\dot{\eta} : \bar{\Omega} \rightarrow \mathbb{E}_d$ . Define  $u : \bar{\Omega} \rightarrow \mathbb{R}_+$  as the minimal time needed to reach  $\partial\Omega$  for a vehicle subject to a unit speed constraint *relative* to the drift  $\dot{\eta}$ . In other words,  $T = u(\mathbf{p})$  is the smallest time for which there exists a Lipschitz path  $\gamma : [0, T] \rightarrow \bar{\Omega}$  satisfying  $u(0) = \mathbf{p}$ ,  $u(T) \in \partial\Omega$ , and for all  $t \in [0, T]$

$$\|\dot{\gamma}(t) - \dot{\eta}(\gamma(t))\| \leq 1.$$

We assume the strict bound  $\|\dot{\eta}(\mathbf{p})\| < 1$  for all  $\mathbf{p} \in \bar{\Omega}$ , so that local controllability holds. The exit time  $u$  then obeys the HJB PDE (3.9), with null boundary conditions, where the tensor field  $\mathcal{D}$  and *co-vector* field  $\hat{\eta}$  are defined as follows, see [Mir17a]

$$\mathcal{D}(\mathbf{p}) := (1 - \|\dot{\eta}(\mathbf{p})\|^2)(1 - \dot{\eta}(\mathbf{p}) \otimes \dot{\eta}(\mathbf{p})), \quad \hat{\eta}(\mathbf{p}) = \frac{-\dot{\eta}(\mathbf{p})}{1 - \|\dot{\eta}(\mathbf{p})\|^2}.$$

## 3.2 Curvature penalized models

The numerical schemes presented in this section are designed to extract planar paths, with prescribed endpoints and tangents, minimizing an integral energy defined in terms of their local position, tangent, and *curvature*. The results of this section are from [Mir17b]. At the risk of introducing a slight redundancy with the general introduction, we first recall the models of interest.

Define the cost of a smooth path  $\mathbf{x} : [0, T] \rightarrow \mathbb{R}^2$ , parametrized at unit euclidean speed, as

$$\int_0^T \alpha(\mathbf{x}(t), \dot{\mathbf{x}}(t)) \mathcal{C}(\xi |\ddot{\mathbf{x}}(t)|) dt.$$

The parameter  $\xi > 0$  is homogeneous to a radius of curvature. It is fixed in the following, but could equally well depend on the local path position and orientation. The cost  $\alpha : \mathbb{R}^2 \times \mathbb{S}^1 \rightarrow ]0, \infty[$ , depending on the path position and orientation, is typically application dependent and data driven. The curvature penalization  $\mathcal{C}$ , on the other hand, is so far chosen within a limited number of models, for we which have developed efficient numerical schemes. The three available choices implement increasingly strong penalizations of large curvatures, and are related to classical optimal control problems referred to as the Reeds-Shepp car [RS90, DMMP16], the Euler-Mumford elastica [Mum94], and the Dubins car [Dub57] respectively.

$$\mathcal{C}^{\text{RS}}(\kappa) := \sqrt{1 + |\kappa|^2}, \quad \mathcal{C}^{\text{EM}}(\kappa) := 1 + |\kappa|^2, \quad \mathcal{C}^{\text{D}}(\kappa) := \begin{cases} 1 & \text{if } |\kappa| \leq 1, \\ +\infty & \text{otherwise.} \end{cases} \quad (3.10)$$

Note, importantly, that we address in this section the discretization of the Reeds-Shepp *forward* model, without reverse gear, see [DMMP16]. This models differs from the Reeds-Shepp *reversible* model, able to shift into reverse gear instantly and at no cost, which is sub-Riemannian and is considered in §3.1.2. Figure 3.5 (left and center left) clearly illustrates the difference. Qualitatively, physical projections of minimal paths feature *cusps* in the reversible case, and *in place rotations* in the forward only case, see Figure 1.7 page 20.

Our numerical strategy requires to lift the planar paths of interest into the three dimensional manifold  $\mathbb{M} := \mathbb{R}^2 \times \mathbb{S}^1$  of positions and orientations, where  $\mathbb{S}^1 := \mathbb{R}/(2\pi\mathbb{Z})$ . It is equipped with a singular metric, designed to appropriately penalize changes in direction, and to forbid physical motions (sideways or reverse) which are not positively collinear with the current orientation. More precisely, given a point  $\mathbf{p} = (\mathbf{x}, \theta) \in \mathbb{M}$  and a tangent vector  $\dot{\mathbf{p}} = (\dot{\mathbf{x}}, \dot{\theta}) \in T_{(\mathbf{x}, \theta)}\mathbb{M}$  such that  $\|\dot{\mathbf{x}}\| = 1$ , we let

$$\mathcal{F}_{\mathbf{p}}(\dot{\mathbf{p}}) = \mathcal{F}_{(\mathbf{x}, \theta)}(\dot{\mathbf{x}}, \dot{\theta}) := \begin{cases} \alpha(\mathbf{x}, \theta) \mathcal{C}(\xi |\dot{\theta}|) & \text{if } \dot{\mathbf{x}} = \mathbf{n}(\theta), \\ +\infty & \text{otherwise,} \end{cases} \quad (3.11)$$

where  $\mathbf{n}(\theta) := (\cos \theta, \sin \theta)$ . The metric (3.11) is extended by positive 1-homogeneity to velocities  $(\dot{\mathbf{x}}, \dot{\theta})$  which physical component is not unit:  $\|\dot{\mathbf{x}}\| \neq 1$ . In other words  $\mathcal{F}_{\mathbf{p}}(\lambda \dot{\mathbf{p}}) := \lambda \mathcal{F}_{\mathbf{p}}(\dot{\mathbf{p}})$  for any  $\lambda > 0$ . The gauge (3.11) is singular by construction, and is convex provided the cost  $\mathcal{C}$  is non-decreasing and convex, see [Mir17b]. The unit balls of

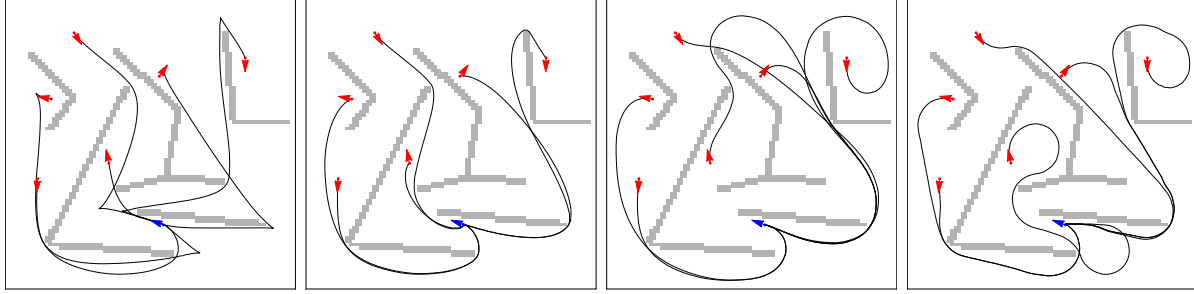


Figure 3.4 – Minimal paths in the presence of obstacles, w.r.t. the Reeds-Shepp reversible, Reeds-Shepp forward, Euler-Mumford, and Dubins models. Parameters  $\alpha \equiv 1$ ,  $\xi = 0.2$  or  $\xi = 0.1$  in the Dubins case. CPU time, on a single core, from 0.2s to 1.2s depending on the model.

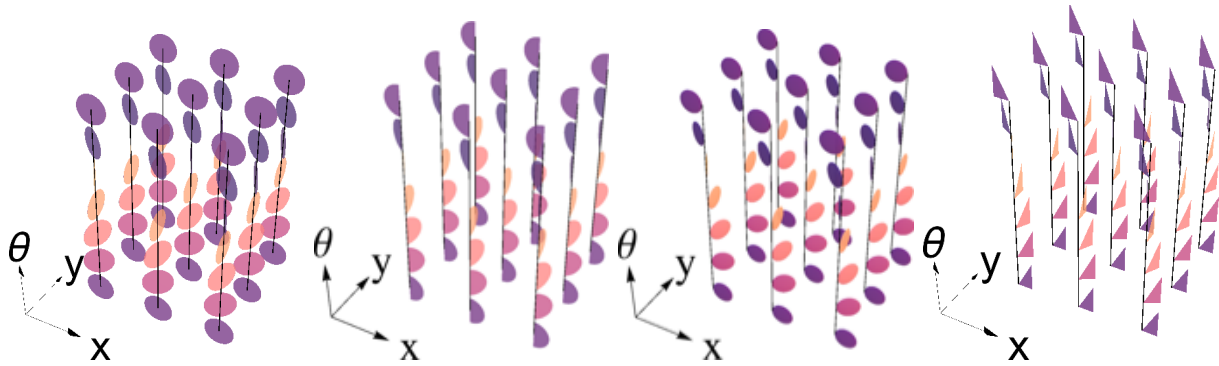


Figure 3.5 – Unit balls of the gauges of the Reeds-Shepp reversible, Reeds-Shepp forward, Euler-Mumford and Dubins models, see (3.10). Model parameters  $\xi = 1$  and  $\alpha \equiv 1$ . All have empty interior, reflecting the non-holonomy of the models.

(3.11) are illustrated on Figure 3.5, and some minimal paths are presented on Figure 1.7 and Figure 3.4.

The models considered in this section are not locally controllable, as illustrated on Figure 3.6. For instance Dubins paths have a positively lower bounded radius of curvature (and no cusps), therefore large maneuvers are required for e.g. moving to a close position sideways. For this reason, following [BCD08], two variants of the distance to the boundary must be considered. Given a bounded domain  $\Omega \subseteq \mathbb{M}$ , we define two maps  $u, \hat{u} : \bar{\Omega} \rightarrow \mathbb{R}_+$  as follows

$$\begin{aligned} u(\mathbf{p}) &:= \inf\{\text{length}_{\mathcal{F}}(\gamma); \gamma(0) \in \partial\Omega, \quad \gamma(1) = \mathbf{p}\}, \\ \hat{u}(\mathbf{p}) &:= \inf\{\text{length}_{\mathcal{F}}(\gamma); \gamma(0) \in \mathbb{M} \setminus \Omega, \gamma(1) = \mathbf{p}\}. \end{aligned}$$

The functions  $u$  and  $\hat{u}$  may be discontinuous, both in the interior of  $\Omega$  and on its boundary, see Proposition 3.2.2 below. They are respectively the smallest super-solution, and the largest sub-solution, to the eikonal PDE (1.33), with boundary conditions understood in a weak sense [BCD08].

Our discretization schemes for this degenerate HJB PDE involve both a scale parameter  $h > 0$ , and a relaxation parameter  $\varepsilon > 0$ . Before entering their details, we state a

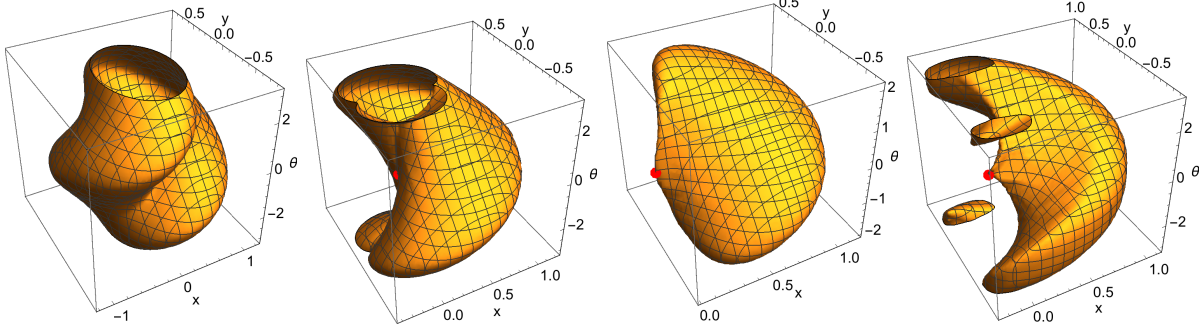


Figure 3.6 – Level set  $\{\mathbf{p} \in \mathbb{R}^2 \times \mathbb{S}^1; d_{\mathcal{F}}(\mathbf{p}, 0) = 0.6\}$  of the distance map associated to the Reeds-Shepp reversible, Reeds-Shepp forward, Euler-Mumford and Dubins models. Parameters  $\xi = 0.14$ ,  $\alpha \equiv 1$ . Origin shown as a red point. The origin lies on the boundary of the level set on pictures (II, III, IV), illustrating the lack of local controllability of these models. (In contrast, the Reeds-Shepp reversible model (I) is sub-Riemannian hence locally controllable.)

convergence result common to the three models. Given  $h > 0$ , we denote by  $\mathbb{M}_h \subseteq \mathbb{M}$  the three dimensional, semi-periodic cartesian grid  $\mathbb{M}_h := (h\mathbb{L}_2) \times (h\mathbb{Z})/(2\pi\mathbb{Z})$ , with the implicit assumption that  $2\pi/h$  must be a positive integer.

**Theorem 3.2.1.** *Let  $\Omega \subseteq \mathbb{M}$  be an open and bounded domain, and let  $\alpha : \overline{\Omega} \rightarrow ]0, \infty[$  have Lipschitz regularity. Let  $X_h := \Omega \cap \mathbb{M}_h$ ,  $\partial X_h := (\mathbb{M} \setminus \Omega) \cap \mathbb{M}_h$ , and let  $H_{\varepsilon, h}$  be the discretization scheme presented in this section for the Reeds-Shepp forward model, or the Dubins model. Then for any  $h > 0$  and any  $\varepsilon \in ]0, 1]$  the system*

$$\forall \mathbf{p} \in X_h, H_h^\varepsilon U(\mathbf{p}) = 1/2, \quad \forall \mathbf{p} \in \partial X_h, U(\mathbf{p}) = 0, \quad (3.12)$$

admits a unique solution denoted  $U_{\varepsilon, h} : \mathbb{M}_h \rightarrow \mathbb{R}$ . This solution can be computed using the fast marching algorithm with complexity  $\mathcal{O}(N_h \ln N_h)$ , where  $N_h := \#(\Omega_h)$ .

Let  $U_n := U_{\varepsilon_n, h_n}$ , where  $\varepsilon_n \rightarrow 0$  and  $h_n/\varepsilon_n \rightarrow 0$  as  $n \rightarrow \infty$ . Define for all  $\mathbf{p} \in \overline{\Omega}$

$$\underline{u}(\mathbf{p}) := \lim_{r \rightarrow 0} \liminf_{n \rightarrow \infty} \inf_{\mathbb{M}_h \cap B(\mathbf{p}, r)} U_n, \quad \overline{u}(\mathbf{p}) := \lim_{r \rightarrow 0} \limsup_{n \rightarrow \infty} \sup_{\mathbb{M}_h \cap B(\mathbf{p}, r)} U_n.$$

Then  $u \leq \underline{u} \leq \overline{u} \leq \hat{u}$  on  $\overline{\Omega}$ .

Our discretization schemes, denoted by  $H_h^\varepsilon$  in the above result, are based on sparse and adaptive stencils of radius  $\mathcal{O}(h/\varepsilon)$ , where  $h > 0$  is the gridscale and  $\varepsilon > 0$  is a relaxation parameter. See Figure 3.7. In order to achieve convergence, the relaxation parameter  $\varepsilon$  needs to tend to zero, for consistency with the continuous model, but slower than the grid scale so that the effective discretization scale  $h/\varepsilon$  also tends to zero. Indeed, our discretization uses stencils of radius  $\mathcal{O}(1/\varepsilon)$ , measured in pixels, which are each of width  $h$ . In the absence of quantitative error estimates, due to the discontinuity of the problem solution  $u$ , we have no clear rule on how to optimally set the relative magnitude of  $\varepsilon$  and  $h$  asymptotically. In numerical applications one typically chooses  $\varepsilon = 1/10$ , independently of the other parameters. The discretization of the Euler-Mumford elastica

Hamiltonian involves a third parameter, which is an integer  $K \geq 1$ , affecting the number of points in the discretization stencil but not its radius,  $K = 5$  typically in applications. Theorem 3.2.1 also holds for this model, but the complexity becomes  $\mathcal{O}(KN_h \ln N_h)$ , and convergence requires the extra assumption that  $K_n \rightarrow \infty$  as  $n \rightarrow \infty$ .

The proof of Theorem 3.2.1 proceeds by first showing that the discrete maps  $U_n$  are uniformly bounded independently of  $n \geq 0$ , using a comparison principle. Their lower and upper limits  $\underline{u}$  and  $\bar{u}$  are respectively super- and sub-solutions to the eikonal PDE (1.33), with the appropriate boundary conditions. The minimality and maximality of  $u$  and  $\hat{u}$  allows to conclude.

The conclusion  $u \leq \underline{u} \leq \bar{u} \leq \hat{u}$  of Theorem 3.2.1 is not a proper convergence result unless one can show that  $u = \hat{u}$  on a sufficiently large set. Our knowledge on this subject is gathered in the next proposition, proved in [Mir17b]. Surprisingly, the qualitative continuity properties of the distance(s) to the boundary are distinct for each of the considered models. The Reeds-Shepp reversible model is included for completeness, see §3.2.1 for a discussion.

**Proposition 3.2.2.** *Under the assumptions of Theorem 3.2.1, and in addition that the interior of  $\bar{\Omega}$  equals  $\Omega$ . The value functions  $u, \hat{u} : \bar{\Omega} \rightarrow \mathbb{R}$  are equal in the following cases:*

- (Reeds-Shepp reversible model)  $u = \hat{u}$  on  $\bar{\Omega}$ .
- (Reeds-Shepp forward model)  $u = \hat{u}$  on  $\Omega$ , if this domain has the form  $\Omega = \Omega_0 \times \mathbb{S}^1$ .
- (Euler-Mumford model)  $u = \hat{u}$  on  $\Omega$ .
- (Dubins model)  $u = \hat{u}$  on a dense subset of  $\Omega$ .

Furthermore, in each case,  $u$  and  $\hat{u}$  are continuous at each point  $\mathbf{p} \in \bar{\Omega}$  such that  $u(\mathbf{p}) = \hat{u}(\mathbf{p})$ .

In the rest of this subsection, we provide the expression of the Hamiltonians of the three considered models, see [Mir17b] for a proof, and we approximate them in the form (3.2). This which naturally defines a monotone and causal finite differences scheme (3.4), see Figure 3.7. For notational simplicity, we assume that the cost  $\alpha : \bar{\Omega} \rightarrow ]0, \infty[$  is identically equal to 1. Otherwise the Hamiltonians simply need to be multiplied by the scalar factor  $\alpha(\mathbf{x}, \theta)^{-2}$ .

### 3.2.1 The Reeds-Shepp forward model.

We focus on the *forward only* variant of the Reeds-Shepp model, without reverse gear. More precisely, the distinction between the forward and the reversible Reeds-Shepp models lies in the collinearity constraint imposed in the metric expression (3.11), respectively  $\dot{\mathbf{x}} = \mathbf{n}(\theta)$  and  $\dot{\mathbf{x}} = \pm \mathbf{n}(\theta)$ . The (more classical) reversible Reeds-Shepp model benefits from a sub-Riemannian structure (4.5), which makes it locally controllable and allows it to be addressed using a Riemannian relaxation, see §3.1.2 for details.

The Hamiltonian of the Reeds-Shepp forward model has a quadratic structure, involving a non-symmetric first term related to the physical momentum  $\hat{\mathbf{x}}$ . For any point

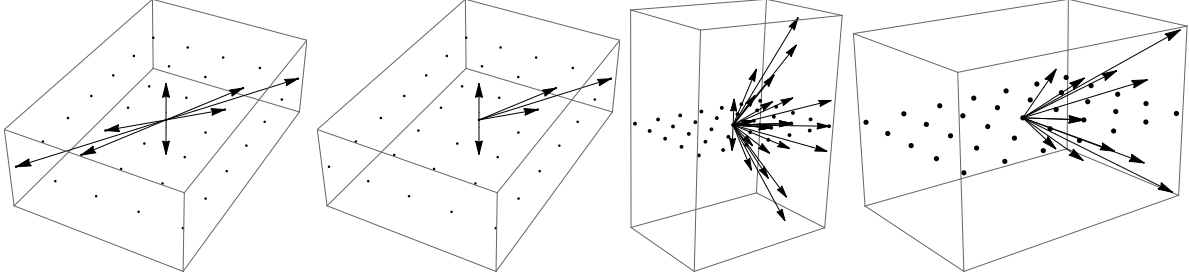


Figure 3.7 – Offsets of the finite differences used for the discretization of the Reeds-Shepp reversible, Reeds-Shepp forward, Euler-Mumford, and Dubins models. Note the sparseness and the anisotropy of the stencils. Model parameters:  $\xi = 0.2$ , current angular coordinate  $\theta = \pi/3$ . Discretization parameters:  $\varepsilon = 0.1$ , and for Euler-Mumford  $K = 5$ .

$(\mathbf{x}, \theta) \in \mathbb{M}$  of the state space, and any co-vector  $(\hat{\mathbf{x}}, \hat{\theta}) \in T_{(\mathbf{x}, \theta)}^* \mathbb{M}$ , one has

$$2\mathcal{H}_{(\mathbf{x}, \theta)}(\hat{\mathbf{x}}, \hat{\theta}) = \langle \hat{\mathbf{x}}, \mathbf{n}(\theta) \rangle_+^2 + |\hat{\theta}/\xi|^2, \quad (3.13)$$

where  $a_+ := \max\{a, 0\}$ . The following proposition is used to approximate the first term of this Hamiltonian.

**Proposition 3.2.3.** *Let  $d \in \{2, 3\}$ , let  $\hat{\mathbf{n}} \in \mathbb{R}^d$ , and let  $\varepsilon \in ]0, 1]$ . Then there exists non-negative weights  $\rho_{\hat{\mathbf{e}}}^\varepsilon(\hat{\mathbf{n}}) \geq 0$ , where  $\hat{\mathbf{e}} \in \mathbb{Z}^d$  is an integral offset, such that for all  $\hat{\mathbf{p}} \in \mathbb{R}^d$*

$$\langle \hat{\mathbf{p}}, \hat{\mathbf{n}} \rangle_+^2 \leq \sum_{\hat{\mathbf{e}} \in \mathbb{Z}^d} \rho_{\hat{\mathbf{e}}}^\varepsilon(\hat{\mathbf{n}}) \langle \hat{\mathbf{p}}, \hat{\mathbf{e}} \rangle_+^2 \leq \langle \hat{\mathbf{p}}, \hat{\mathbf{n}} \rangle_+^2 + \varepsilon^2 \|\hat{\mathbf{n}}\|^2 \|\hat{\mathbf{p}}\|^2.$$

Furthermore the support  $\{\hat{\mathbf{e}} \in \mathbb{Z}^d; \rho_{\hat{\mathbf{e}}}^\varepsilon(\hat{\mathbf{n}}) > 0\}$  has at most 3 elements in dimension  $d = 2$  (resp. 6 elements in dimension  $d = 3$ ), and is contained in a ball of radius  $C_{\text{WS}}/\varepsilon$ , where  $C_{\text{WS}}$  is an absolute constant. In addition  $\sum_{\hat{\mathbf{e}} \in \mathbb{Z}^d} \rho_{\hat{\mathbf{e}}}^\varepsilon(\hat{\mathbf{n}}) \|\hat{\mathbf{e}}\|^2 = \|\hat{\mathbf{n}}\|^2(1 + (d-1)\varepsilon^2)$ .

The proof is based on Voronoi's first reduction, and some additional geometrical discussions for the radius estimate  $r_\varepsilon : \mathcal{O}(\varepsilon^{-1})$ , see [Mir17b]. The latter point is non trivial, and is particularly relevant for our application, since convergence analysis requires that the scaled stencil radius  $hr_\varepsilon$  tends to zero, see Theorems 7.4.2 and 3.1.4.

Using proposition 3.2.3, we obtain a relaxation  $H^\varepsilon$  of the Hamiltonian (3.13), which is amenable to discretization.

$$2H_{(\mathbf{x}, \theta)}^\varepsilon(\hat{\mathbf{x}}, \hat{\theta}) = \sum_{\hat{\mathbf{e}} \in \mathbb{Z}^2} \rho_{\hat{\mathbf{e}}}^\varepsilon(\mathbf{n}(\theta)) \langle \hat{\mathbf{x}}, \hat{\mathbf{e}} \rangle_+^2 + |\hat{\theta}/\xi|^2.$$

Indeed, this expression is defined in terms of scalar products of the co-vector  $(\hat{\mathbf{x}}, \hat{\theta})$  with integral vectors, here of the form  $(\hat{\mathbf{e}}, 0)$  or  $(0, 1)$ . Proceeding as in (3.4), we obtain a monotone and causal finite differences scheme, denoted  $H_h^\varepsilon$ . For any  $U : \mathbb{M}_h \rightarrow \mathbb{R}$  and any  $(\mathbf{x}, \theta) \in \mathbb{M}_h$

$$2H_h^\varepsilon U(\mathbf{x}, \theta) := h^{-2} \sum_{\hat{\mathbf{e}} \in \mathbb{Z}^2} \rho_{\hat{\mathbf{e}}}^\varepsilon(\mathbf{n}(\theta)) (U(\mathbf{x}, \theta) - U(\mathbf{x} - h\hat{\mathbf{e}}, \theta))_+^2 \quad (3.14)$$

$$+ (\xi h)^{-2} \max\{0, U(\mathbf{x}, \theta) - U(\mathbf{x}, \theta - h), U(\mathbf{x}, \theta) - U(\mathbf{x}, \theta + h)\}^2.$$

The Reeds-Shepp forward model can be extended to dimension 3, using a singular metric on the 5-dimensional manifold  $\mathbb{R}^3 \times \mathbb{S}^2$ , see §4.1.4. The resulting 5-dimensional eikonal PDE is then discretized and solved using an approach similar to the one above, see [Mir17b].

### 3.2.2 The Euler-Mumford elastica model.

The Euler-Mumford elastica model benefits from a physical interpretation, as the bending energy of an elastic bar. Originally discovered by Euler, and later introduced by Mumford in the field of image processing [Mum94], it is regarded as one of the most natural energy models for image segmentation purposes. The Hamiltonian is (the half square of) the sum of a sub-Riemannian and of a linear term:

$$2\mathcal{H}_{(\mathbf{x},\theta)}(\hat{\mathbf{x}}, \hat{\theta}) = \frac{1}{4} \left( \langle \hat{\mathbf{x}}, \mathbf{n}(\theta) \rangle + \sqrt{\langle \hat{\mathbf{x}}, \mathbf{n}(\theta) \rangle^2 + |\hat{\theta}/\xi|^2} \right)^2.$$

One can recognize a degenerate instance of Rander Hamiltonian, see §3.1.3. Unfortunately, the FM-ASR numerical scheme introduced §2.2 is not applicable since model is three dimensional. The non-causal variant of the FM-VR1 designed for Rander metrics, see §3.1.3, is not directly applicable either because the metric is singular. We tried an approach based on relaxation but only obtained unsatisfying results. A different approach is thus developed, based on the following integral representation of the Hamiltonian: for any  $\mathbf{p} \in \mathbb{M}$ , with angular coordinate  $\theta \in \mathbb{S}^1$ , and any  $\hat{\mathbf{p}} \in T_{\mathbf{p}}\mathbb{M}$

$$2\mathcal{H}_{\mathbf{p}}(\hat{\mathbf{p}}) = \frac{3}{4} \int_{-\pi/2}^{\pi/2} \langle \hat{\mathbf{p}}, \dot{\mathbf{v}}(\theta, \varphi) \rangle_+^2 \cos(\varphi) \, d\varphi, \quad \text{where } \dot{\mathbf{v}}(\theta, \varphi) := (\mathbf{n}(\theta) \cos \varphi, \xi^{-1} \sin \varphi).$$

See [Mir17b] for a proof. Consider a quadrature rule on the interval  $[-\pi/2, \pi/2]$  with cosine weight, denoted  $(\alpha_k)_{k=0}^K$  in the following, which is non-negative and second order consistent. For instance the Clenshaw-Curtis or Fejer rules<sup>3</sup>. Using Proposition 3.2.3, we define a two parameter approximation of the Hamiltonian

$$2H_{\mathbf{p}}^{\varepsilon,K}(\hat{\mathbf{p}}) := \frac{3}{4} \sum_{0 \leq k \leq K} \alpha_k \sum_{\hat{\mathbf{e}} \in \mathbb{Z}^3} \rho_{\hat{\mathbf{e}}}^{\varepsilon}(\dot{\mathbf{v}}(\theta, \varphi)) \langle \hat{\mathbf{p}}, \hat{\mathbf{e}} \rangle_+^2.$$

A monotone and causal finite difference scheme is obtained, as for the Reeds-Shepp forward model (3.14), by replacing each term  $\langle \hat{\mathbf{p}}, \hat{\mathbf{e}} \rangle_+$  with the finite difference  $h^{-1}(U(\mathbf{p}) - U(\mathbf{p} - h\hat{\mathbf{e}}))_+$ .

### 3.2.3 The Dubins car model.

This model implements a hard constraint on the path turning radius, bounded below by the parameter  $\xi > 0$ , which is appropriate for applications in motion planning. The Hamiltonian is non-smooth, and is a maximum of two terms

$$2\mathcal{H}_{\mathbf{p}}(\hat{\mathbf{p}}) = \max \left\{ \langle \hat{\mathbf{p}}, \dot{\mathbf{v}}^+(\theta) \rangle_+^2, \langle \hat{\mathbf{p}}, \dot{\mathbf{v}}^-(\theta) \rangle_+^2 \right\}, \quad \text{where } \dot{\mathbf{v}}^{\pm}(\theta) := (\mathbf{n}(\theta), \pm\xi^{-1}).$$

<sup>3</sup>These are usually described as quadrature rules on the interval  $[-1, 1]$  with uniform weight, but this is equivalent since  $\int_{-1}^1 f(t) \, dt = \int_{-\pi/2}^{\pi/2} f(\sin \varphi) \cos \varphi \, d\varphi$  for any  $f \in L^1([-1, 1])$ .

Using Proposition 3.2.3 we obtain an approximation of this Hamiltonian, which is amenable to discretization, similarly to the two previous models

$$2H_{\mathbf{p}}^\varepsilon(\hat{\mathbf{p}}) := \max_{\sigma \in \{+, -\}} \sum_{\hat{\mathbf{e}} \in \mathbb{Z}^3} \rho_{\hat{\mathbf{e}}}^\varepsilon(\dot{\mathbf{v}}^\sigma(\theta, \varphi)) \langle \hat{\mathbf{p}}, \hat{\mathbf{e}} \rangle_+^2.$$

# Chapter 4

## Applications

### Contents

---

<b>4.1 Tubular structure segmentation . . . . .</b>	<b>78</b>
4.1.1 Historical approaches . . . . .	78
4.1.2 Data adaptive Riemannian metrics . . . . .	81
4.1.3 Curvature penalized planar paths. . . . .	84
4.1.4 Models in dimension $3 + 2$ . . . . .	86
<b>4.2 Region segmentation using Rander metrics . . . . .</b>	<b>88</b>
<b>4.3 Motion planning and surveillance . . . . .</b>	<b>91</b>
4.3.1 Mathematical background of trajectory optimization . . . . .	92
4.3.2 Reverse mode semi-automatic differentiation . . . . .	93
4.3.3 Numerical experiments . . . . .	94

---

### 4.1 Tubular structure segmentation

This subsection is devoted to variational methods for tubular structure segmentation, based on paths minimizing a data-driven energy. Historical approaches are first recalled, followed by the enhancements made possible by the anisotropic fast marching methods developed by the author.

#### 4.1.1 Historical approaches

Historical approaches to tubular structure segmentation can be divided into two groups, depending on the structure of the path energy that is minimized. The first group consists of methods based on complex energies, typically featuring second order terms, such as the snakes model, see Kass et al [KWT88] and (4.1) below. This approach suffers from reliability issues since in practice the energy can only be locally minimized. The second group consists of methods based on a basic conformal cost, locally proportional to Euclidean

path length, see Cohen and Kimmel [CK97] or (4.2). This type of functional can be globally minimized using the classical fast marching method [Tsi95], but only offers limited flexibility. The latter approach is often enhanced by dimension lifting, see Li and Yezzi [LY07], that is considering paths with an additional coordinate, in an abstract parameter space.

We describe these works in more detail in the following paragraphs. Note that the numerical methods presented in §3.2 and [Mir17b], fast marching with curvature penalization, attempt to combine the strong points of the three historical approaches: an energy featuring second order terms (as in the snake model), a guarantee of global optimality (as in the Cohen and Kimmel model), and an intrinsic dimension lifting in  $\mathbb{R}^2 \times \mathbb{S}^1$  (as in the Li and Yezzi model).

### The snake model

The segmentation of tubular structures is a natural and challenging task in medical image processing. Pioneer works by Kass et al [KWT88] suggested to extract these image features as paths  $\gamma : [0, 1] \rightarrow \Omega$  minimizing the following quantity, referred to as the snake model energy

$$\int_0^1 a \|\ddot{\gamma}(t)\|^2 + b \|\dot{\gamma}(t)\|^2 + c(\gamma(t)) dt. \quad (4.1)$$

This expression features a Sobolev-like part, weighted by coefficients  $a, b > 0$ , and a non-convex part encoded in a cost  $c : \Omega \rightarrow \mathbb{R}$ , that is usually data driven in applications. The endpoints of the path  $\gamma$  are prescribed, assumed to be at the extremities of the tubular structure of interest, provided by the user or detected by another algorithm. A similar approach can be used to extract the contours of two dimensional regions, by imposing a periodic boundary condition instead of fixed endpoints, see §4.2.

The heuristic behind the snakes model is that the data-driven cost  $c(\gamma(t))$ , data-driven and designed to be small in the neighborhood of the structures of interest, favors paths staying close them. The energy terms  $b|\dot{\gamma}(t)|^2$  and  $a|\ddot{\gamma}(t)|^2$ , which are of Sobolev type, control the regularity of the minimal paths and are loosely<sup>1</sup> related to the penalization of path length and path curvature. Path energies rigorously implementing a curvature cost are discussed in §3.2, and applied to tubular structure extraction in §4.1.3.

Numerical implementations of the snake model typically represent the path  $\gamma$  as a piecewise polynomial curve, and optimize the energy (4.1) by gradient descent, see the appendix of [KWT88]. This approach unfortunately suffers from deficiencies, which make it hard to use in practice, and are typical of numerical methods based on the local optimization of a non-convex functional. Such methods indeed have a tendency to get stuck at *local* minima of the functional of interest, here defined by (4.1), and are sensitive to the initial guess.

---

<sup>1</sup>It would rigorously be the case if the path was parametrized at unit Euclidean speed.

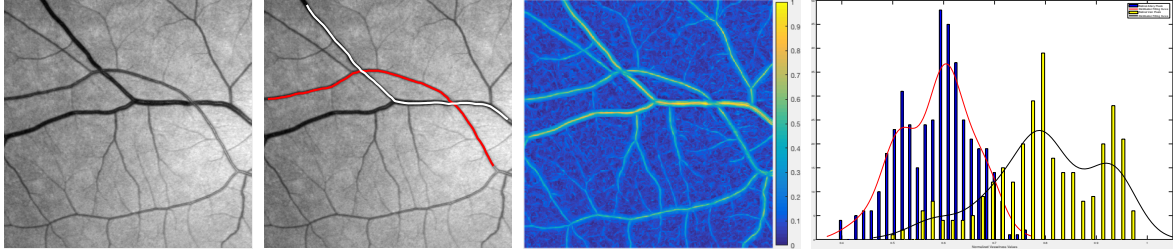


Figure 4.1 – **Column 1** A typical retinal image patch. **Column 2** White and red curves indicate a vein and an artery respectively. **Column 3** Visualization of the vesselness map. **Column 4** Normalized vesselness values distribution along the vein (light blue curve) and the artery (red curve) labeled in column 2. Work with Da Chen and L. Cohen.

### Globally optimal paths w.r.t. conformal metrics.

Cohen and Kimmel [CK97] suggested, as a remedy to the lack of reliability of the snake energy minimization procedure, to focus on simpler models for which global minimization is achievable. The considered energy is locally proportional to Euclidean path length, hence of the form

$$\int_0^1 c(\gamma(t)) \|\gamma'(t)\| dt. \quad (4.2)$$

We denote by  $c : \Omega \rightarrow \mathbb{R}$  a cost, continuous and bounded below, which is data-driven in applications and designed so as to favor paths staying close to the features of interest. In contrast with the snakes model, *global* minimizers for this path energy, with prescribed endpoints, can be computed efficiently by solving the standard eikonal equation  $\|du(\mathbf{x})\| = c(\mathbf{x})$  on the image domain, with appropriate boundary conditions. Numerically, this is done using the original isotropic fast marching algorithm [Tsi95, RT92], with quasi-linear complexity  $\mathcal{O}(N \ln N)$  w.r.t. the number of discretization points. The robustness of this approach, especially in comparison with the snakes model, enabled the design of a variety of image processing methods [PPK10]. Their development was eventually limited by the very rigid and specific form of the cost functions that could be addressed, see (4.2).

### Dimension lifting

We focus in this paragraph on the setting where the two dimensional input image displays a large number of intersecting tubular structures, this is for instance the case of retinal background images, which are actually the superposed projections of distinct vessels in a three dimensional volume. This overlay of structures unfortunately tends to fool segmentation methods based on the minimization of the two dimensional measure of path length (4.2). Indeed, these methods typically select paths going along the concatenation of several distinct biological vessels. The extracted path jumps from one vessel to another, when they cross or come nearby, an issue referred to as the shortcuts problem. These defective paths are typically only *piecewise* smooth, with angles at the (undesirable) transitions between distinct vessels, and the second order term appearing in the snakes model (which has its own defects) is precisely meant to eliminate them.

Li and Yezzi [LY07] proposed to introduce an artificial third dimension to the input

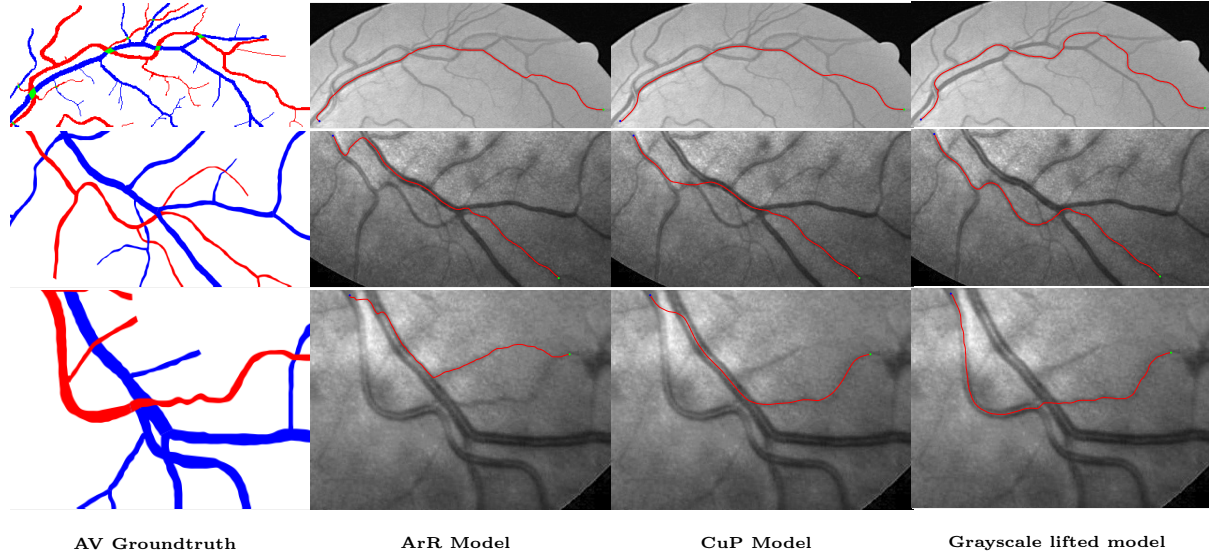


Figure 4.2 – Retinal vessel extraction examples. **Column 1** is the groundtruth. **Columns 2-4** are paths from the ArR (Anisotropic radius lifted Riemannian), CuP (Curvature Penalized) and another lifted model based on grayscale coherency proposed with Da Chen and L. Cohen, which gives here the best results.

image, in the attempt to separate the vessels, as they originally were in physical three dimensional space. Extracted paths  $\eta : [0, 1] \rightarrow \Omega \times A$  feature an additional coordinate  $\eta(t) = (\gamma(t), \alpha(t))$ , valued in an abstract parameter space. The cost function  $c(\mathbf{x}, a)$ , where  $(\mathbf{x}, a) \in \Omega \times A$ , accounts for the inverse likelihood that a vessel is present at position  $\mathbf{x}$  and has the feature  $a$ . In practice, the additional parameter  $a$  may account for the vessel radius [LY07], gray-level, or orientation [PKP09].

#### 4.1.2 Data adaptive Riemannian metrics

A natural enhancement of the Cohen and Kimmel model for tubular extraction [CK97], is to replace the conformal cost (4.2), which originally is locally proportional to the Euclidean metric, with a more general anisotropic Riemannian cost [BC10]. For that purpose, the local analysis of the image data, performed before the minimal path extraction, needs to be enhanced: a full Riemannian metric  $\mathcal{M} : \Omega \rightarrow S^{++}(\mathbb{E}_d)$  is assembled, instead of a scalar valued local cost  $c : \Omega \rightarrow \mathbb{R}_+^*$ . The Riemannian metric is chosen so as to favor paths which not only remain on tubular structures, but also go tangentially along them. As a side note, if it was possible to locally infer the direction of the blood flow in the vessels, in addition to the vessel orientation, then the above mentioned Riemannian metric could be advantageously replaced with an asymmetric Finsler metric.

#### Computational difficulties overcome

Computing minimal paths with respect to Riemannian metrics, by the corresponding eikonal equation, is a classical problem [SV03, BR06, AM11]. It happens however that the Riemannian metrics used for tubular extraction typically feature a large condition

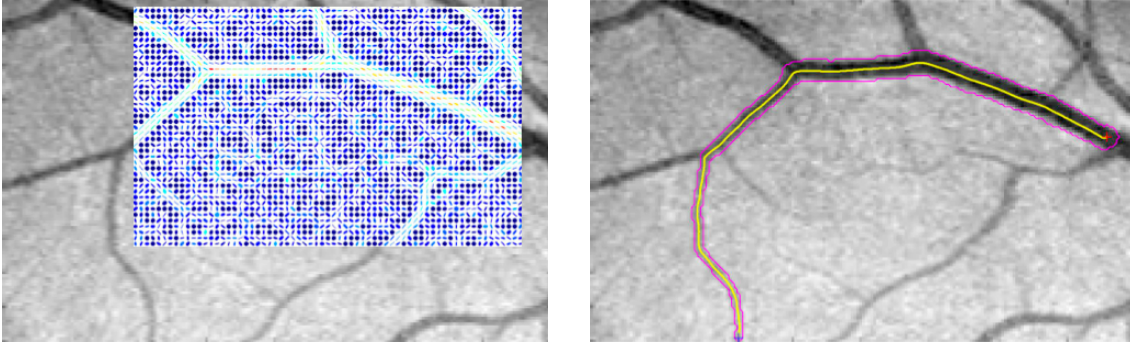


Figure 4.3 – Flow of minimal path based tubular structure segmentation. Left: A Riemannian metric is created. Right: minimal paths are extracted, between appropriate points. Credit: L. Cohen and F. Benmansour.

number and a large local contrast. In other words the metric  $(\mathbf{p}, \dot{\mathbf{p}}) \mapsto \mathcal{F}_{\mathbf{p}}(\dot{\mathbf{p}})$  varies strongly w.r.t. both the point  $\mathbf{p}$  and the vector  $\dot{\mathbf{p}}$ . A representative test case, originally proposed in [BC10], is illustrated on Figure 2.4 (right).

Classical causal methods [SV03, AM11] are sensitive to large condition numbers, which make them use very wide stencils, hence render them costly and inaccurate. Classical non-causal methods [BR06] are sensitive to both large contrast and large anisotropy, and as a result may take hundreds of iterations to converge [BC10]. This undesirable compromise ended with the FM-LBR numerical scheme, see [Mir14a] and §2.1, which is causal but nevertheless uses rather small stencils even for large anisotropies. The computational issue was essentially solved, reducing CPU time by up to four (!) orders of magnitude for a given accuracy in comparison with earlier state of the art in the above mentioned test case.

## Design of the metric

Constructing a Riemannian metric for tubular structure segmentation in medical images is a non-trivial task. There does not seem to be an universal solution, but rather application dependent models requiring substantial expert knowledge. This process may be streamlined in the future, by the adequate use of machine learning, but this is outside of the scope of this dissertation.

The first step is to construct a tensor field  $\mathcal{M}_0 : \Omega \rightarrow \mathbb{S}(\mathbb{E})$  which acts as a vessel detector, where  $\Omega \subseteq \mathbb{E}$  is the image domain, for instance the oriented flux tensor [LC08]. In other words, the presence of a vessel at a position  $\mathbf{x} \in \Omega$  implies that  $\mathcal{M}_0(\mathbf{x})$  has an eigenvector aligned with the vessel and associated with a small eigenvalue, and that the other eigenvalues are comparatively large.

The second step is to define the Riemannian metric  $\mathcal{M} : \Omega \rightarrow \mathbb{S}^{++}(\mathbb{E}_d)$  which, usually, has eigenvalues distinct from  $\mathcal{M}_0$  but shares the same eigenvectors. An eigenvalue  $\lambda$  of  $\mathcal{M}(\mathbf{x})$  is chosen small if the eigenvalue  $\lambda_0$  of  $\mathcal{M}_0(\mathbf{x})$  corresponding to the same eigenvector  $\mathbf{e}_0$  is small comparatively to the other eigenvalues of  $\mathcal{M}_0(\mathbf{x})$  (in other words, if a vessel is likely to be present at the position  $\mathbf{x}$  and with the orientation  $\mathbf{e}_0$ ). The other eigenvalues of  $\mathcal{M}(\mathbf{x})$  are chosen large. The specific form of the new eigenvalues, meant to enhance

paths alongside the vessels, is usually a complex recipe, see e.g. [BC10].

Data adaptive Riemannian metrics can be combined with the dimension lifting trick. The augmented space  $\Omega \times A$  has dimension  $d + d' > d$ ; typically  $d = 2$  and  $d' = 1$ . The Riemannian metric on this space is usually chosen block diagonal, with the  $d \times d$  block corresponding to the physical coordinates built as above [CCM14, CMC16c].

### Keypoint insertion methods: a definite improvement

In this paragraph, we discuss a vessel tree extraction algorithm based on keypoint insertion, which relies on the comparison of the Euclidean distance with a Riemannian distance defined w.r.t. a data adaptive metric. When first introduced, this algorithm relied on isotropic metrics [BC08]. Substantial improvements were obtained by upgrading those to anisotropic Riemannian metrics [CMC16c], for reasons that we discuss below.

Consider an image displaying a tubular structure shaped into a tree, and assume that a Riemannian metric  $\mathcal{M} : \bar{\Omega} \rightarrow \mathbb{S}^{++}(\mathbb{E})$  has been designed so that paths along the structure are particularly short. Let  $X_0 = \{\mathbf{x}_0\}$  be a singleton, containing the root  $\mathbf{x}_0 \in \Omega$  of the tree to be extracted. For each  $n \geq 0$  define inductively  $X_{n+1} := X_n \cup \{\mathbf{x}_{n+1}\}$  where  $\mathbf{x}_n$  is a minimizer to the following optimization problem:

$$\min_{\mathbf{x} \in \Omega} d_{\mathcal{M}}(\mathbf{x}, X_n) \quad \text{subject to} \quad d_0(\mathbf{x}, X_n) \geq \delta. \quad (4.3)$$

We denote by  $d_{\mathcal{M}}$  the distance w.r.t. the data-driven Riemannian metric, and by  $d_0$  the usual *Euclidean* distance. The distance to a set is defined as the minimal distance to the points of this set. This iterative procedure, defining a sequence of points  $(\mathbf{x}_n)_{n \geq 0}$ , is terminated after a finite number  $N$  of steps when an appropriate stopping criterion is met. The reconstructed tree is defined by the set  $X_N = \{\mathbf{x}_n\}_{n=0}^N$  of nodes, and the edges are the geodesics from  $\mathbf{x}_{n+1}$  to  $X_n$ , for all  $0 \leq n < N$ .

The scalar  $\delta > 0$  appearing in the keypoint definition (4.3) is a positive and fixed parameter. Choosing  $\delta$  excessively large leads to *leakage* and *shortcuts* problems: the geodesic from  $\mathbf{x}_{n+1}$  to  $X_n$  may leave the actual vessel tree, jumping to nearby vessels, which leads to an incorrect reconstruction. The smaller the scale  $\delta$ , the best these issues can be avoided. However,  $\delta$  also needs to be above a lower bound, for the keypoint insertion algorithm to work reliably in practice. It turns out that this lower bound for  $\delta$  is significantly smaller in the case of well designed anisotropic metrics (a few pixels) than for isotropic metrics (the vessel width), for reasons explained below. See also Figure 4.4.

Assume that the metric  $\mathcal{M}$  is Riemannian and anisotropic, designed so as to favor paths that remain tangent to the vessels. The keypoint insertion criterion (4.3) then works provided the Riemannian distance  $d_{\mathcal{M}}$  can be reliably estimated at Euclidean distance  $\delta$ . In other words,  $\delta$  must be larger than the size of the stencil used for the eikonal PDE discretization, which is typically a few pixels wide when using the FM-LBR algorithm with a reasonably anisotropic metric  $\mathcal{M}$ .

Assume now that the metric  $\mathcal{M}$  is isotropic,  $\mathcal{M}(x) = m(x)^2 \text{Id}$  where  $m : \bar{\Omega} \rightarrow ]0, \infty[$  is a data driven scalar cost. Then the data driven and the Euclidean distances are locally proportional:  $d_{\mathcal{M}}(\mathbf{x}, \mathbf{y}) \approx m(\mathbf{x})d_0(\mathbf{x}, \mathbf{y})$  for any  $\mathbf{x}, \mathbf{y} \in \Omega$  sufficiently close so that  $m$  can be regarded as constant at the scale  $\|\mathbf{x} - \mathbf{y}\|$ . Therefore, comparing  $d_{\mathcal{M}}(\mathbf{x}, \mathbf{y})$  with  $d_0(\mathbf{x}, \mathbf{y})$ , as done in the keypoint insertion procedure (4.3), only yields meaningful information

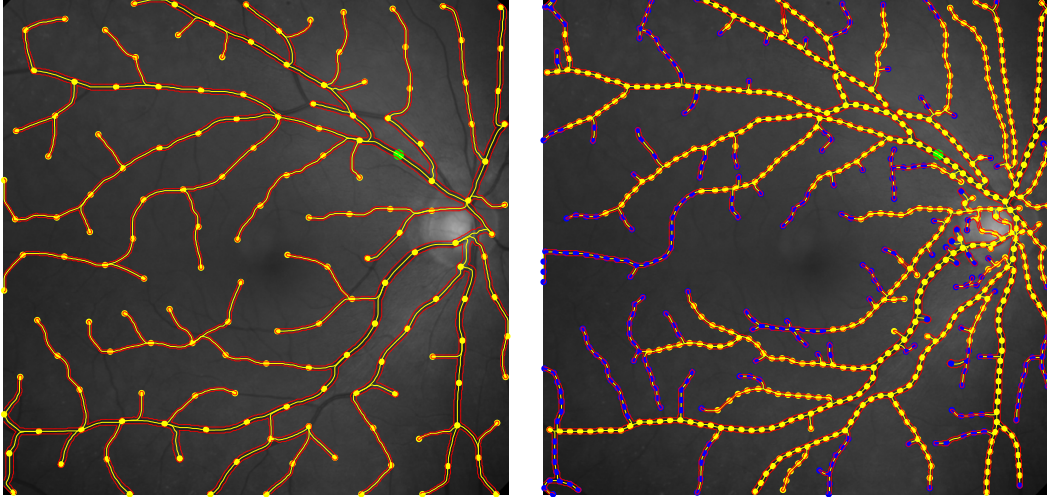


Figure 4.4 – Segmentation of the retina vessel tree. Left: Standard method. Right: Enhanced method, using an anisotropic metric and a small distance threshold  $\delta$ . Images from [CCM14], which contains more examples and comparisons.

(i.e. selects a point further along the tubular structure of interest) if  $\delta := d_0(\mathbf{x}, \mathbf{y})$  is significantly larger than the feature scale of the cost map  $m$ , which is here the radius of the vessels to be extracted in the input image.

### 4.1.3 Curvature penalized planar paths.

One of the main differences between the historical snakes model (4.1) [KWT88] and the conformal metric model considered by Cohen and Kimmel [CK97], is that the latter ignores the path acceleration. This simplification, from a second order model to a first order one, was motivated by computational considerations solely: for being able to compute globally minimal geodesic paths by solving a standard eikonal equation. From a modeling point of view, however, penalizing second order quantities such as path curvature is highly relevant. Indeed, it is one of the most natural and efficient approaches to avoid the shortcuts problem, which arises when extracting tubular structures from an image displaying a complex overlay of vessels. See the discussion in §4.1.1 related with the dimension lifting trick.

Fortunately, globally optimal paths with curvature penalization can now be computed using the methods of §3.2, with good accuracy and within a reasonable computation time. In fact, these methods allow for more variety in the choice of the second order term than the original snakes functional, which is limited to the basic  $H^2([0, 1])$  Sobolev type cost. Given an initial and final point and direction in  $\Omega \times \mathbb{S}^1$ , where  $\Omega \subseteq \mathbb{R}^2$  is the image domain, we can compute the path  $\mathbf{x} : [0, L] \rightarrow \Omega$  globally minimizing the energy

$$\int_0^L c(\mathbf{x}(t), \dot{\mathbf{x}}(t)) \mathcal{C}(|\ddot{\mathbf{x}}(t)|) dt. \quad (4.4)$$

The path is here assumed to be parametrized at unit speed, and its Euclidean length  $L \geq 0$  is a free parameter. The cost function  $c : \Omega \times \mathbb{S}^1 \rightarrow ]0, \infty[$  is usually data driven in

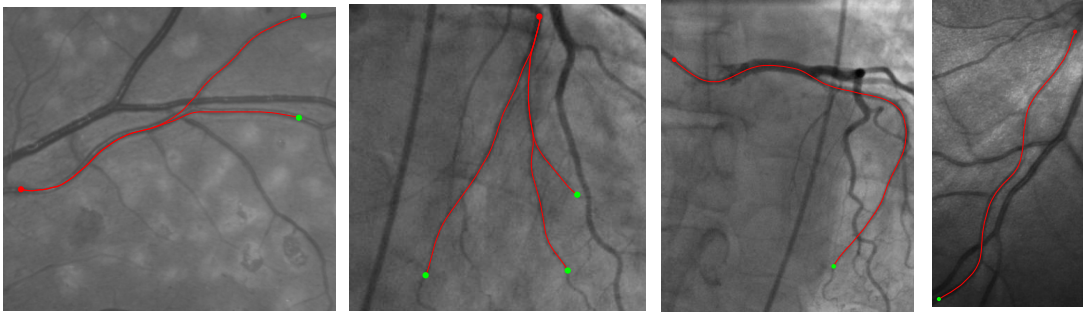


Figure 4.5 – Vessel extraction using the Euler-Mumford elastica model, see [CMC17].

applications, and  $c(\mathbf{x}, \mathbf{n})$  should be small when a vessel is likely to be present at the point  $\mathbf{x}$  and with the orientation  $\mathbf{n}$ . Note that curvature penalization implies, automatically, a dimension lifting. The design of the local cost  $c$  is usually a complex recipe, typically based on local correlations with oriented wavelets [DFGtHR07, DDHCG13], which is outside the scope of this paper, see e.g. [BDMS15]. This issue is also related with the Riemannian metric design evoked in §4.1.2

The curvature penalization  $\mathcal{C} : [0, \infty[ \rightarrow [0, \infty]$  must, in the present state of our numerical methods, be chosen among the three possibilities discussed in §3.2. Each is parametrized by a scalar  $\xi > 0$  which is homogeneous to a radius of curvature. The Reeds-Shepp model is defined by  $\mathcal{C}(\kappa) := \sqrt{1 + \xi^2 \kappa^2}$ , and may or may not be authorized to shift into reverse gear. The Euler elastica model obeys  $\mathcal{C}(\kappa) := 1 + \xi^2 \kappa^2$ . The Dubins model satisfies  $\mathcal{C}(\kappa) := 1$  if  $\xi \kappa \leq 1$ , and  $\mathcal{C}(\kappa) := \infty$  otherwise.

The Reeds-Shepp model with reverse gear, which has a sub-Riemannian structure, was first considered as it is the easiest to implement. A non-causal discretization is proposed in [BDMS15], and a causal one is introduced in [SBD<sup>+</sup>15]. Definite improvements are obtained over the first order models, but the presence of cusps, due to the ability to shift into reverse gear, yields annoying artifacts. The forward only Reeds-Shepp model solves the latter issue, see [DMMP16].

Among the four models, the Euler-Mumford elastica seems to deliver the best tubular segmentation results, see Figure 4.5. A non-causal discretization is proposed in [CMC17], where we also discuss region segmentation, see Figure 4.6. A causal one is finally obtained in [Mir17b], see §3.2. The improvement over the Reeds-Shepp forward model is striking when the cost function  $c : \Omega \times \mathbb{S}^1 \rightarrow ]0, \infty[$  is independent<sup>2</sup> of the direction  $\theta \in \mathbb{S}^1$ , see the synthetic test cases in [Mir17b]. The forward only Reeds-Shepp model does however deliver rather similar results when the cost function is well designed (dependent of both position and orientation), and it has the advantage of requiring up to 4 times less CPU time in practice, since it uses a stencil with less points, see Figure 3.7.

Finally, the bounded turning radius implemented in the Dubins model turns out to be more adequate for vehicle path planning than for vessel segmentation.

<sup>2</sup>This is a poor design choice in practice, only considered so as to exacerbate the differences between the curvature penalized models.

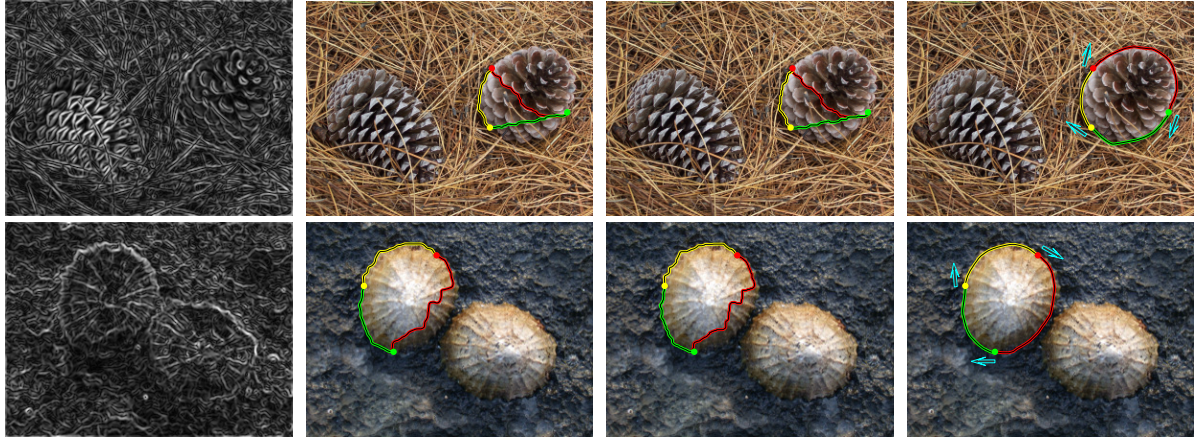


Figure 4.6 – Application of globally minimal Euler-Mumford elastica paths to region segmentation, see [CMC16a]. Contour detection results from different models. **Column 1** shows the edge maps, which determines the ground speed, here orientation independent:  $\alpha = \alpha(\mathbf{x})$ . **Columns 2-4** show the contour detection results from the Cohen-Kimmel model [CK97], the orientation lifted model [PKP09], and the model [CMC16a] based on Euler-Mumford elastica curves [Mum94].

#### 4.1.4 Models in dimension $3 + 2$ .

Extracting globally optimal curvature penalized paths in  $\mathbb{R}^d$  requires, with our dimension lifting approach, to solve a singular eikonal PDE on the on the  $(2d - 1)$ -dimensional product manifold  $\mathbb{M}_d := \mathbb{R}^d \times \mathbb{S}^{d-1}$ . Because of the curse of dimension, the case of three dimensional paths, lifted in dimension  $3 + 2 = 5$ , seems to be the limit. We describe here our results in this setting, which as of today are more experimental than in the planar case, see Figure 4.7 and [DMMP16, Mir17a, Mir17b]. This is due to the important numerical costs associated with solving 5-dimensional PDEs, and to the fact that the fundamental motivation for curvature penalization, coming from the overlaid two dimensional projection of three dimensional vessels in e.g. retinal background images, does not have a counterpart in three dimensional image data. The tractography of brain white matter fiber may raise issues of similar nature though [DMMP16], since groups of such fibers may cross each other.

We limited our attention to variants of the Reeds-Shepp model: the (classical) reversible instance, the forward only variant, and a dual<sup>3</sup> variant which does not exist in dimension  $d = 2$ . Indeed, their hamiltonian benefits from a separable structure, see (4.5) below, which simplifies their implementation: one can rely on Voronoi’s first reduction of three dimensional quadratic forms. More complex models, based on the Euler-Mumford and Dubins costs, will be the subject of future work. Regarding the Reeds-Shepp *forward* model, we refer to §3.2 (for planar paths) and [DMMP16], and we focus below on the *reversible* and *dual* variants.

The Reeds-Shepp reversible model selects paths of low curvature, but potentially with cusps. The dual model enhances paths embedded within a smooth hypersurface, but

<sup>3</sup>This term is here used informally, in view of the expressions (4.5) and (4.6).

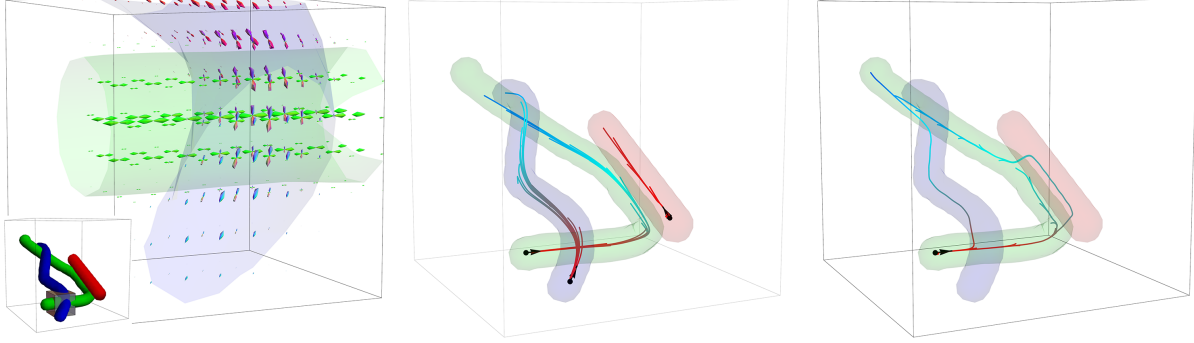


Figure 4.7 – Synthetic segmentation test of 3D tubular structures, using curvature penalization, from [DMMP16]. Left: 3D configuration of bundles and a visualization of part of the synthetic dMRI data. Middle: successful backtracking of geodesics in  $(\mathbb{M}, d_{\mathcal{F}_\epsilon})$  from several points inside the curves to end points of the bundle, using  $\epsilon = 0.1$ . Right: when using  $\epsilon = 1$  (isotropic metric), the dominant red bundle can cause the paths from the green bundle to deviate from the correct structure.

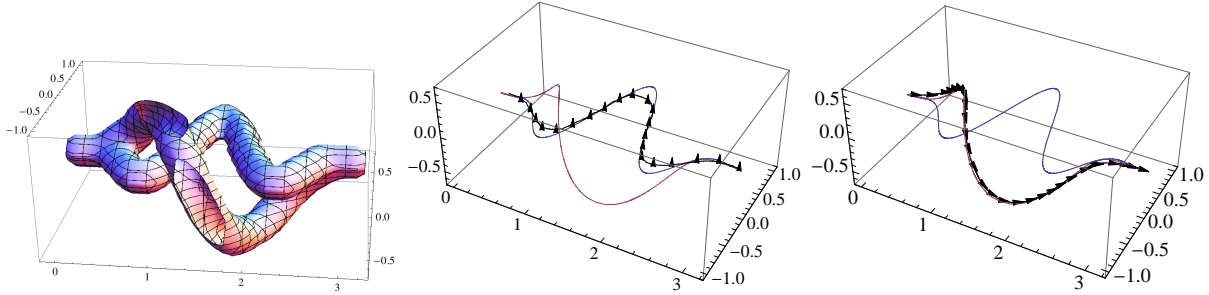


Figure 4.8 – Synthetic example. Left: The speed function  $\mathcal{S}(\mathbf{x}, \mathbf{n}) = \mathcal{S}(\mathbf{x})$  is small in the neighborhood of two curves, with respectively low curvature and low torsion. Center: Shortest path for the generalized Reeds-Shepp model (4.5) on  $\mathbb{R}^3 \times \mathbb{S}^2$ . Right: Shortest path for the dual model (4.6).

potentially with folds. These cusps and folds are a signature of sub-Riemannian geometry, and can only be avoided with more complex metrics as described in §3.2. We choose to describe these models by providing directly the corresponding families of approximating Riemannian metrics, denoted respectively  $(\mathcal{M}_\epsilon)_{\epsilon>0}$  and  $(\mathcal{M}'_\epsilon)_{\epsilon>0}$ . For any point  $(\mathbf{x}, \mathbf{n}) \in \mathbb{M}_d = \mathbb{R}^d \times \mathbb{S}^{d-1}$ , and any tangent vector  $(\dot{\mathbf{x}}, \dot{\mathbf{n}}) \in T_{(\mathbf{x}, \mathbf{n})}\mathbb{M}_d$

$$\|(\dot{\mathbf{x}}, \dot{\mathbf{n}})\|_{\mathcal{M}_\epsilon(\mathbf{x}, \mathbf{n})}^2 := \mathcal{S}(\mathbf{x}, \mathbf{n})^{-2} \left( \langle \mathbf{n}, \dot{\mathbf{x}} \rangle^2 + \epsilon^{-2} \|P_{\mathbf{n}}(\dot{\mathbf{x}})\|^2 + \xi^2 \|\dot{\mathbf{n}}\|^2 \right), \quad (4.5)$$

$$\|(\dot{\mathbf{x}}, \dot{\mathbf{n}})\|_{\mathcal{M}'_\epsilon(\mathbf{x}, \mathbf{n})}^2 := \mathcal{S}(\mathbf{x}, \mathbf{n})^{-2} \left( \epsilon^{-2} \langle \mathbf{n}, \dot{\mathbf{x}} \rangle^2 + \|P_{\mathbf{n}}(\dot{\mathbf{x}})\|^2 + \xi^2 \|\dot{\mathbf{n}}\|^2 \right). \quad (4.6)$$

We denoted by  $P_{\mathbf{n}}(\dot{\mathbf{x}}) := \dot{\mathbf{x}} - \langle \mathbf{n}, \dot{\mathbf{x}} \rangle \mathbf{n}$  the orthogonal projection of  $\dot{\mathbf{x}}$  onto the hyperplane orthogonal to  $\mathbf{n}$ . When  $\epsilon = 1$ , these two models coincide, and define a standard Riemannian metric on the manifold  $\mathbb{M}_d$ . The speed function  $\mathcal{S}$  is usually application dependent and data driven. The parameter  $\xi > 0$ , homogeneous to a radius of curvature, balances the relative cost of motion of the physical coordinate  $\mathbf{x}$  and of the angular coordinate  $\mathbf{n}$ .

As  $\epsilon \rightarrow 0$  some contributions explode, effectively enforcing constraints on vectors  $(\dot{\mathbf{x}}, \dot{\mathbf{n}})$

of bounded norm at the point  $(\mathbf{x}, \mathbf{n})$ . For the Reeds-Shepp model  $\mathcal{M}_0$ , this constraint is  $P_{\mathbf{n}}(\dot{\mathbf{x}}) = 0$ , in other words the physical speed  $\dot{\mathbf{x}}$  must be positively or negatively collinear with the angular direction  $\mathbf{n}$ . Since the motion of  $\mathbf{n}$  is also penalized, the model overall amounts to a penalization of path curvature, with here the possibility of cusps, see §3.2 for a discussion of similar ideas.

For the dual model  $\mathcal{M}'_0$  the enforced constraint is  $\langle \mathbf{n}, \dot{\mathbf{x}} \rangle = 0$ , in other words the physical speed  $\dot{\mathbf{x}}$  must remain orthogonal to the angular direction  $\mathbf{n}$ . This model selects paths which admit a smoothly varying normal, which is the case of paths embedded in manifolds of co-dimension 1, as well as of paths of low torsion. See Figure 4.8.

## 4.2 Region segmentation using Rander metrics

The segmentation of image regions is an image processing problem which is as much classical, if not more, as the segmentation of tubular structures discussed in §4.1. A number of models and of numerical methods have been considered, under the generic name of *active contours* [KWT88, CK97, CKS97, MPAT08], including the following recent works relying on our anisotropic fast marching methods [CMC16b, CMC17, CC17a, CC17b]. We limit our attention to two dimensional regions, which boundary is a one dimensional curve and can thus be extracted using minimal path methods. Two main differences distinguish region segmentation from tubular structure extraction.

- Absence of overlays. Region boundaries do not cross each other, except in the rare case where the input image represents a superposition of semi-transparent objects. In contrast, the overlay of tubular structures is frequent and is typically the major difficulty for segmentation. Regions do occlude each other, but this issue is usually addressed with different tools.
- Region boundaries are oriented, for instance counter-clockwise. The best minimal path models for region segmentation take this asymmetry into account, and are thus based on asymmetric Finsler metrics [MPAT08, ZSN09, CC17b].

In this section, we discuss how some variational models for region segmentation, usually implemented numerically using level set methods, can be reformulated into a minimal geodesic problem w.r.t. an asymmetric metric, and solved with unprecedented speed and reliability using the FM-ASR method §2.2. These results were presented in [CMC16b]. We focus for simplicity on the following energy functional

$$\mathcal{E}(U) := \int_U f + \int_{\partial U} g \tag{4.7}$$

where  $U \subseteq \Omega$  is the unknown region to be found by energy minimization, and the cost functions  $f, g : \Omega \rightarrow \mathbb{R}$  are given, with  $g$  being positive. The classical Chan-Vese energy [CSV00] can be written under the form (4.7) (up to an additive constant), and more complex energies may be locally linearized into this form.

Consider a region  $U$ , with a smooth boundary of signed curvature  $\kappa : \partial U \rightarrow \mathbb{R}$ , and a sufficiently small function  $\eta : \partial U \rightarrow \mathbb{R}$ . Defined a perturbed region  $U_\eta$  by moving, at each

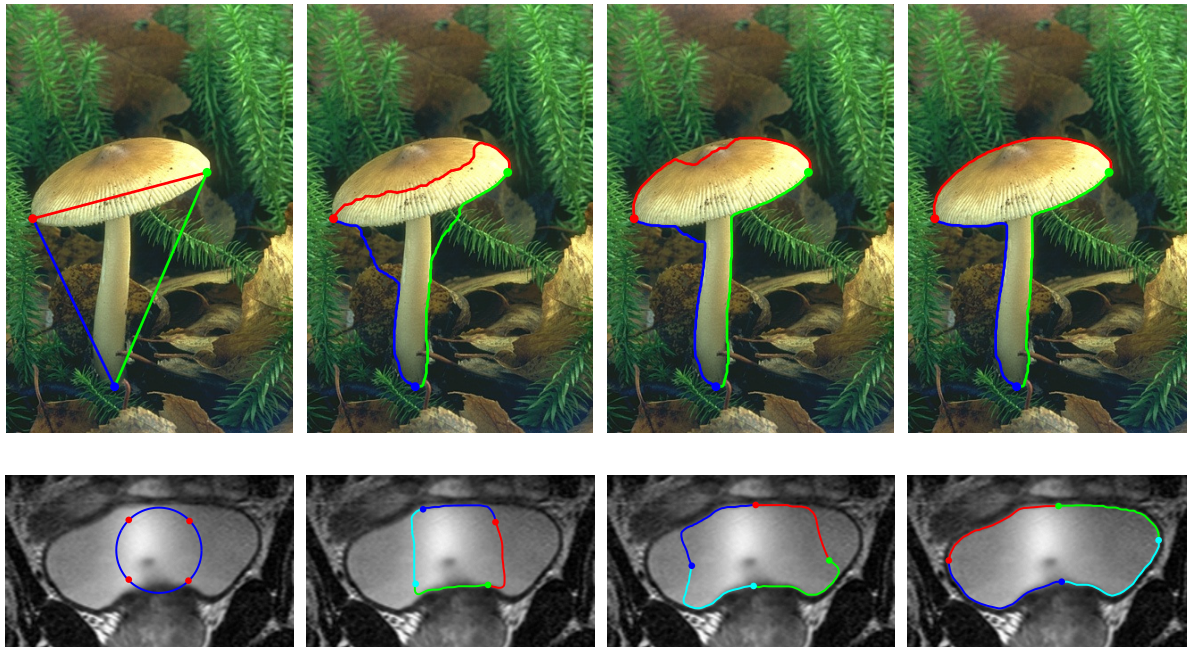


Figure 4.9 – Application of our method to image segmentation. Left: Initialization. Center left and right: Intermediate steps. Right: Final (and third) iteration. Images from [CMC16b].

point of  $\partial U$ , the boundary of  $U$  in the direction of its outward normal on the distance  $\eta$ . One easily obtains the following first order approximation, referred to as a shape gradient [ABFJB06]

$$\mathcal{E}(U_\eta) - \mathcal{E}(U) \approx \int_{\partial U} f\eta + g\kappa\eta.$$

The classical strategy for minimizing (4.7) is based on the linearization (4.2) combined with either a piecewise polynomial representation of the contour (as for the snake model [KWT88]), or an implicit representation of the region  $U$  using a level set function [CSV00]. In any case, the results tend to be quite sensitive to initialization, for at least two reasons. First, one is minimizing a non-convex functional using successive linearizations, which is known to be risky. Second, the data-driven region cost  $f : \Omega \rightarrow \mathbb{R}$  is usually non-smooth, since it is directly derived from the image, at least in the original Chan-Vese model [CSV00]. Hence restricting  $f$  to the one dimensional region boundary  $\partial U$  is unstable if not mathematically ill posed, if e.g.  $f \in L^p(\Omega)$  for some  $p < \infty$ . (The boundary weight  $g$  is usually smoother in contrast, if not identically constant.)

We propose an approach for globally minimizing the energy (4.7) can be globally minimized, in dimension  $d = 2$ , entirely distinct from the previous level set methods. We make at first a series of strong assumptions, but show in the end that they can be considerably weakened in practice. Denoting by  $U_*$  the optimal region, we assume that:

1. The optimal region  $U_*$  has the topology of a disk, and a neighborhood  $\Omega_*$  of  $\partial U_*$  is known, with the topology of a ring. In other words  $\Omega_*$  is homeomorphic to  $\{\mathbf{x} \in \mathbb{E}_2; 1/2 < |\mathbf{x}| < 2\}$ , and  $U_*$  to the unit ball.

2. A vector field  $\omega : \Omega_* \rightarrow \mathbb{E}_2$  is known, obeying pointwise on  $\Omega_*$

$$\operatorname{div} \omega = f, \quad \|\omega\| < g. \quad (4.8)$$

3. A point of the optimal region boundary is known, denoted  $\mathbf{x}_* \in \partial U_*$ .

Let  $U \subseteq \Omega$  be a region, which is sufficiently close to the optimal region  $U_*$  so that the symmetric difference  $(U \setminus U_*) \cup (U_* \setminus U)$  is contained in the neighborhood  $\Omega_*$  of  $\partial U_*$ . Let also  $\gamma : [0, 1] \rightarrow \Omega$  be a counter-clockwise parametrization of  $\partial U$ . Then using (4.8, left) and the divergence theorem one obtains [ABFJB06, CMC16b]

$$\mathcal{E}(U) = \int_0^1 (g(\gamma(t))\|\gamma'(t)\| + \langle \omega^\perp(\gamma(t)), \gamma'(t) \rangle) dt + \text{Cst}, \quad (4.9)$$

where the constant is independent of the region  $U$ , subject to the above assumptions. Crucially, the energy (4.9) is (up to the constant term) the length of the path  $\gamma$  measured with respect to the Rander metric  $\mathcal{F}_{\mathbf{p}}(\dot{\mathbf{p}}) := g(\mathbf{p})\|\dot{\mathbf{p}}\| + \langle \omega(\mathbf{p})^\perp, \dot{\mathbf{p}} \rangle$ . The compatibility condition (3.8) is satisfied in view of (4.8, right).

We have reformulated the region energy (4.7) as the geodesic length of its contour, with respect to a data driven, asymmetric Finsler metric. The contour of the optimal region  $U_*$  is therefore the shortest closed geodesic within the ring shaped domain  $\Omega_0$ . Since a point  $\mathbf{x}_0 \in \partial U_*$  is known by assumption, this geodesic can be extracted in a single pass by numerically solving an eikonal equation.

In the rest of this section, we discuss how the assumptions used to introduce our method can be weakened, and the scope of our approach extended to realistic use cases, as in [CMC16b]. The following discussion is only heuristic, and mathematical proofs of e.g. the convergence of the suggested iterative algorithms may be the object of future work.

1. The assumption that the optimal region  $U^*$  has the topology of a disk is not limiting, since the connected components of  $U^*$  can otherwise be extracted independently. If a connected component has holes, then these holes may be extracted using a similar approach. Actually, the fact that our numerical method has a topological guarantee (it returns a disc shaped region), is in our eyes a strength rather than a weakness.

The assumption that one knows a ring shaped neighborhood  $\Omega_*$  is however more limiting for applications, because this neighborhood needs to be rather *thin*, due to point 2. below. In practice, an iterative approach is used: an initial ring shaped subdomain  $\Omega_0$  is provided, which may not contain the boundary of the globally optimal region, and an optimal curve  $\gamma_0$  within  $\Omega_0$  computed. Then a new ring  $\Omega_1$  is defined as a tubular neighborhood of the curve  $\gamma_0$ , and the process is repeated until convergence. This procedure stabilizes rapidly in practice, and three iterations only are required to achieve convergence for the instances of Figure 4.9.

2. The co-vector field  $\omega$  obeying (4.9) does not actually need to be known a priori, of course. Instead, it is computed as a preprocessing step of our numerical method, by solving an elliptic equation. More precisely, we set  $\omega = \nabla u$ , where  $\Delta u = f$  on  $\Omega_*$

with suitable boundary conditions<sup>4</sup>. If  $f \in L_{\text{loc}}^{2+\varepsilon}$  for some  $\varepsilon > 0$ , and if the domain  $\Omega_*$  has sufficiently *small area*, then the smallness condition (4.9) is met [CMC16b]. This is the reason why  $\Omega_*$  needs to be a rather *thin* ring, see point 1.

3. The assumption that one knows a point lying exactly on the optimal region boundary does not seem realistic, but it can be eliminated as follows, see also Figure 4.9 (bottom). Consider an arbitrary point  $\mathbf{x}_0 \in \Omega$  (a possibly incorrect substitute for  $\mathbf{x}_* \in \partial U_*$ ), and observe that the proposed numerical method can extract the region  $U_0$  minimizing the energy (4.7), but subject to the *additional constraint* that  $\mathbf{x}_0 \in \partial U_0$ . In order to remove the latter constraint, an iterative strategy is appropriate: for each  $n \geq 0$ , select a point  $\mathbf{x}_{n+1} \in \partial U_n$ , as far as possible from  $\mathbf{x}_n$ , and define  $U_{n+1}$  as the region minimizing  $\mathcal{E}(U)$  subject to  $\mathbf{x}_{n+1} \in \partial U_{n+1}$ . We observe empirically that  $U_n$  converges to  $U_*$ .

Finally, we note that several generalizations of the method presented in this subsection were formulated and successfully implemented [Che16, CC17a], such as (i) constraining the region boundary to contain several given points, (ii) introducing a balloon force, (iii) replacing the linear region energy term  $\int_U f$  with a general functional, which is then locally linearized for optimization purposes.

### 4.3 Motion planning and surveillance

We present in this subsection a proof of concept numerical implementation of a two player game involving motion planning, whose results were presented in [MD17]. A first player selects, within an admissible class  $\Xi$ , an integral cost function on paths, which takes into account the path position, orientation, and possibly curvature. The second player selects a path, within an admissible class  $\Gamma$ , with prescribed endpoints and an intermediate keypoint. The players objective is respectively to maximize and minimize the path cost

$$\mathfrak{C}(\Xi, \Gamma) := \sup_{\xi \in \Xi} \inf_{\gamma \in \Gamma} \mathfrak{C}(\xi, \gamma), \quad \text{where } \mathfrak{C}(\xi, \gamma) := \int_0^{T(\gamma)} \mathcal{C}_\xi(\gamma(t), \gamma'(t), \gamma''(t)) dt, \quad (4.10)$$

where the path  $\gamma$  is parametrized at unit Euclidean speed, and the final time  $T(\gamma)$  is free. From a game theoretic point of view, this is a non-cooperative zero-sum game, where player  $\Xi$  has no information and player  $\Gamma$  has full information over the opponent's strategy.

The game (4.10) typically models a surveillance problem [Str11], in which  $\exp(-\mathfrak{C}(\Xi, \Gamma))$  is the probability for player  $\Gamma$  to visit a prescribed keypoint without being detected by player  $\Xi$ . For instance player  $\Xi$  is responsible for the installation of radar [BM00] or sonar detection systems [Str11], and would like to prevent vehicles sent by player  $\Gamma$  from spying on some objectives without being detected.

The dependence of the cost  $\mathcal{C}_\xi$  on the path tangent  $\gamma'(t)$  models the variation of a measure of how detectable the second player vehicle is (radar cross section, directivity

---

<sup>4</sup>Numerically we use Neumann boundary conditions, but the proof of smallness discussed in the next argument does require a distinct formulation, see [CMC16b].

index, etc.) w.r.t. the relative positions and orientations of the target and sensor. The dependence of  $\mathcal{C}_\xi$  on the path curvature  $\gamma''(t)$  models the vehicle maneuverability constraints, such as the need to slow down in tight turns [Mum94], or even a hard bound on the path curvature [Dub57].

Stroke [Str11] has shown the interplay of motion planning and game theory in a similar setting, on a multistatic sonar network use case, but using graph-based path planning. The same year, Barbaresco [Bar11] used fast-marching for computing threatening paths towards a single radar. In comparison with these earlier works, our contributions are (i) the use anisotropic and curvature penalized path models in this context, and (ii) an implementation of a reverse mode semi-automatic differentiation of the fast marching method, for efficiently (locally) optimizing w.r.t. parameter  $\xi \in \Xi$ .

### 4.3.1 Mathematical background of trajectory optimization

The objective of player  $\Gamma$  is to find a path of minimal energy within a planar domain, w.r.t. a cost  $\mathcal{C}_\xi(\mathbf{x}, \dot{\mathbf{x}}, \ddot{\mathbf{x}})$  featuring in particular a penalization of curvature. The path must start from the “home” of player  $\Gamma$ , visit a prescribed target, and then return back home. (We chose this setting over the simplified problem where the path does not need to return back home, so as to emphasize the role of curvature penalization, see 4.3.3.) In this paragraph, we describe the PDE formalism underlying this optimization problem, see also §3.2.

The second order path energy minimization problem of player  $\Gamma$  is first lifted into a shortest path problem within the three dimensional domain  $\mathbb{R}^2 \times \mathbb{S}^1$ , the state space of positions and orientations. We let  $\Omega, \Upsilon, \Theta \subseteq \mathbb{R}^2 \times \mathbb{S}^1$  be respectively the full accessible domain, the source of player  $\Gamma$ , and his target. We assume  $\Upsilon \subseteq \partial\Omega$ , and  $\Theta \subseteq \Omega$ . A singular metric  $\mathcal{F}^\xi : T\Omega \rightarrow [0, \infty]$  is also introduced, encoding similarly to (3.11) the curvature penalized cost  $\mathcal{C}_\xi$  into a first order model, dimension lifted and non-holonomic. More precisely, for any point  $\mathbf{p} = (\mathbf{x}, \theta) \in \Omega$  of the state space, and any tangent vector  $\dot{\mathbf{p}} = (\dot{\mathbf{x}}, \dot{\theta})$  such that  $\dot{\mathbf{x}} = (\cos \theta, \sin \theta)$  we let

$$\mathcal{F}_{\mathbf{p}}^\xi(\dot{\mathbf{p}}) = \mathcal{F}_{(\mathbf{x}, \theta)}^\xi(\dot{\mathbf{x}}, \dot{\theta}) := \mathcal{C}_\xi(\mathbf{x}, \theta, \dot{\theta}).$$

The metric is extended by positive 1-homogeneity,  $\mathcal{F}_{\mathbf{p}}^\xi(\lambda \dot{\mathbf{p}}) = \lambda \mathcal{F}_{\mathbf{p}}^\xi(\dot{\mathbf{p}})$  for all  $\lambda > 0$ , and set to  $+\infty$  whenever  $\dot{\mathbf{x}}$  is not positively collinear with  $(\cos \theta, \sin \theta)$ .

The minimal action map  $u_\xi : \Omega \rightarrow [0, \infty]$  is defined as the minimal cost  $u_\xi(\mathbf{p}) = \int_0^1 \mathcal{F}_{\eta(t)}^\xi(\dot{\eta}(t)) dt$  of a path  $\eta : [0, 1] \rightarrow \Omega$  ending at some given point  $\mathbf{p} = (\mathbf{x}, \theta) \in \Omega$  and starting from an arbitrary point  $\mathbf{q} = (\mathbf{y}, \varphi)$  of the source set  $\Upsilon$ . A closely related variant  $u_\xi^-(\mathbf{p})$  is defined likewise, except that the path endpoint orientations are reversed:  $(\mathbf{x}, -\theta)$  and  $(\mathbf{y}, -\varphi)$ . By construction, the minimal cost of a path from the source set  $\Upsilon$  to itself, passing through the target  $\Theta$ , is

$$\min_{\mathbf{p} \in \Theta} u_\xi(\mathbf{p}) + u_\xi^-(\mathbf{p}). \quad (4.11)$$

Numerically,  $u_\xi$  and  $u_\xi^-$  are computed by solving generalized eikonal equations. We focus on  $u_\xi$  for simplicity, and recall that under weak assumptions [BCD08] it is the viscosity solution to the following PDE, involving the Hamiltonian  $\mathcal{H}^\xi$  of the problem. For all

$\mathbf{p} \in \Omega$

$$\mathcal{H}_{\mathbf{p}}^{\xi}(du_{\xi}(\mathbf{p})) = 1/2, \quad \text{where } \mathcal{H}_{\mathbf{p}}^{\xi}(\hat{\mathbf{p}}) := \sup_{\dot{\mathbf{p}}} \langle \hat{\mathbf{p}}, \dot{\mathbf{p}} \rangle - \frac{1}{2} \mathcal{F}_{\mathbf{p}}^{\xi}(\dot{\mathbf{p}})^2, \quad (4.12)$$

with boundary condition  $u_{\xi}(\mathbf{p}) = 0$  on the source set  $\Upsilon$ , and  $u_{\xi} = +\infty$  on the rest of  $\partial\Omega$ .

### 4.3.2 Reverse mode semi-automatic differentiation

In this subsection, we describe how solutions to the parametric eikonal PDE (4.12) can be numerically computed and differentiated w.r.t. the opponent's strategy  $\xi \in \Xi$ . For that purpose we introduce discrete sets  $X, \partial X, Y \subseteq \mathbb{R}^2 \times \mathbb{S}^1$ , usually on a cartesian grid, acting as counterparts of the domain  $\Omega$ , boundary  $\partial\Omega$ , and source set  $\Upsilon$ . We then design a sum-of-squares representation of the Hamiltonian: for all  $(\mathbf{p}, \hat{\mathbf{p}}) \in T^*\Omega$

$$\mathcal{H}_{\mathbf{p}}^{\xi}(\hat{\mathbf{p}}) \approx h^{-2} \sum_{\mathbf{q} \in X} c_{\xi}^2(\mathbf{p}, \mathbf{q}) \langle \mathbf{p} - \mathbf{q}, \hat{\mathbf{p}} \rangle_+^2, \quad (4.13)$$

where  $c_{\xi} : X \times (X \cup \partial X) \rightarrow [0, \infty[$  is a family of weights, and where  $a_+ := \max\{0, a\}$ . Expression (4.13) is typical, although some models require a slight generalization, see §3.2 for details. The discretized PDE system reads: find  $U_{\xi} : X \rightarrow [0, \infty]$  obeying for all  $\mathbf{p} \in X$

$$\sum_{\mathbf{q} \in X} c_{\xi}^2(\mathbf{p}, \mathbf{q}) (U_{\xi}(\mathbf{p}) - U_{\xi}(\mathbf{q}))_+^2 = h^2/2, \quad (4.14)$$

with  $u = 0$  on the source set  $Y$ , and  $u = +\infty$  on the rest of  $\partial X$ . See §3.2 for the convergence analysis.

The minimal cost (4.11) for player  $\Gamma$  is determined by the values of  $u_{\xi}$  on the set  $\Theta \subseteq \Omega$ , which is typically small, e.g. of the form  $\{\mathbf{x}_*\} \times \mathbb{S}^1$ . Hence we are only interested in the values of  $U_{\xi}$  at a few points of  $X$ , say for simplicity a single point  $\mathbf{p}_*$ . We describe below how to numerically estimate the sensitivity of  $U_{\xi}(\mathbf{p}_*)$  w.r.t. variations of the parameter  $\xi$ , thus also in the weights  $c_{\xi}(\mathbf{p}, \mathbf{q})$ ,  $\mathbf{p}, \mathbf{q} \in X$ . For that purpose we differentiate the discretized PDE system (4.14) w.r.t.  $\xi$  at an arbitrary point  $\mathbf{p} \in X \setminus \Upsilon$ , and obtain

$$\sum_{\mathbf{q} \in X} \omega_{\xi}(\mathbf{p}, \mathbf{q}) \left( dU_{\xi}(\mathbf{p}) - dU_{\xi}(\mathbf{q}) + (U_{\xi}(\mathbf{p}) - U_{\xi}(\mathbf{q})) d \ln c_{\xi}(\mathbf{p}, \mathbf{q}) \right) = 0,$$

where  $\omega_{\xi}(\mathbf{p}, \mathbf{q}) := c_{\xi}^2(\mathbf{p}, \mathbf{q}) (U_{\xi}(\mathbf{p}) - U_{\xi}(\mathbf{q}))_+$ . Therefore

$$dU_{\xi}(\mathbf{p}) = \sum_{\mathbf{q} \in X} \alpha_{\xi}(\mathbf{p}, \mathbf{q}) dU_{\xi}(\mathbf{q}) + \sum_{\mathbf{q} \in X} \beta_{\xi}(\mathbf{p}, \mathbf{q}) dc_{\xi}(\mathbf{p}, \mathbf{q}), \quad (4.15)$$

where  $\alpha_{\xi}(\mathbf{p}, \mathbf{q}) := \omega_{\xi}(\mathbf{p}, \mathbf{q}) / \sum_{\mathbf{q}} \omega_{\xi}(\mathbf{p}, \mathbf{q})$ , and  $\beta_{\xi}(\mathbf{p}, \mathbf{q}) := \alpha_{\xi}(\mathbf{p}, \mathbf{q}) / c_{\xi}(\mathbf{p}, \mathbf{q})$ . We first choose  $\mathbf{p} = \mathbf{p}_*$  in (4.15), and then recursively eliminate the terms  $dU_{\xi}(\mathbf{q})$  by applying the same formula at these points, except for points in the source set  $\mathbf{q} \in Y$  for which one uses the explicit expression  $dU_{\xi}(\mathbf{q}) = 0$  (since  $U_{\xi}(\mathbf{q}) = 0$  is in this case independent of  $\xi$ ). This procedure terminates: indeed, whenever  $dU_{\xi}(\mathbf{p})$  depends on  $dU_{\xi}(\mathbf{q})$  in (4.15), one has  $\alpha_{\xi}(\mathbf{p}, \mathbf{q}) > 0$ , thus  $\omega(\mathbf{p}, \mathbf{q}) > 0$ , hence  $U_{\xi}(\mathbf{p}) > U_{\xi}(\mathbf{q})$ . It is closely related to automatic differentiation by reverse accumulation [GW08], and has the modest complexity  $\mathcal{O}(N)$  where  $N = \#(X)$ .

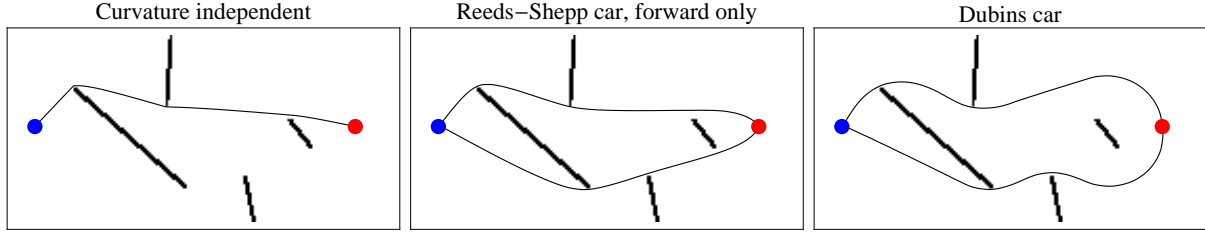


Figure 4.10 – Shortest path from the blue point (left) to the red keypoint (right) and back.

### 4.3.3 Numerical experiments

The chosen physical domain  $R$  is the rectangle  $[0, 2] \times [0, 1]$  minus some obstacles, as illustrated on Figure 4.10. The computational domain is thus  $\Omega = R$  for curvature independent models and  $\Omega = R \times \mathbb{S}^1$  for curvature dependent models, which is discretized on a  $180 \times 89$  or  $180 \times 89 \times 60$  grid respectively. We use a single physical source point  $(0.2, 0.5)$  and target keypoint  $(1.8, 0.5)$ , thus for curvature dependent models the source and target set both have the structure  $\{\mathbf{x}\} \times \mathbb{S}^1$ .

**No intervention from the first player.** We first consider a cost function  $\mathcal{C}_\xi(\mathbf{x}, \dot{\mathbf{x}}, \ddot{\mathbf{x}}) = \mathcal{C}_*(|\ddot{\mathbf{x}}|)$ , independent of the first player strategy  $\xi \in \Xi$ . The curvature cost  $\mathcal{C}_*(\kappa)$  is respectively 1 (curvature independent),  $\sqrt{1 + \rho^2 \kappa^2}$  (Reeds-Shepp, without reverse gear) and 1 iff  $\rho \kappa \leq 1$ , otherwise  $+\infty$  (Dubins car), with  $\rho := 0.3$ . The differences between the three models are apparent. The curvature independent model uses the same path forward and back. The Reeds-Shepp forward car spreads some curvature along the way but still makes an angle at the target point, due to the ability of this model to perform in-place rotations. The trajectory of the Dubins car is a succession of straight and circular segments of radius  $\rho$ . Note that following an optimal trajectory for the Dubins model might be dangerous in practice, since any small deviation is typically impossible to correct locally, and may drive into an obstacle; these trajectories are also easier to detect due to the large circular arc motions.

Next we study three games where player one aims to detect player two along its way from the source set  $\Upsilon$  to the target  $\Theta$  and back, using different means. If the first player does not intervene, see Figure 4.10, or if its strategy is not optimized, see Figure 4.12, then there is typically a unique optimal path (actually, an optimal loop in our setting) for player two. In contrast, an interesting qualitative property of the *optimal* strategy  $\xi \in \Xi$  for the first player is that it has a large number of optimal responses from player two, see Figure 4.13, in some cases even a continuum, see Figure 4.11 (bottom) and [BCPS10]. This is typical of two player games.

**Fresh paint based detection.** In this toy model, see Figure 4.11, the first player spreads some fresh paint over the domain, and the second player is regarded as detected if he comes back covered in paint from his visit to the keypoint. The cost function is  $\mathcal{C}_\xi(\mathbf{x}, \dot{\mathbf{x}}, \ddot{\mathbf{x}}) = \xi(\mathbf{x})\mathcal{C}_*(|\ddot{\mathbf{x}}|)$ , where  $\xi : R \rightarrow \mathbb{R}_+$  is the fresh paint density, decided by the first player, and  $\mathcal{C}_*(\kappa)$  is as above. For wellposedness, we impose upper and lower bounds on

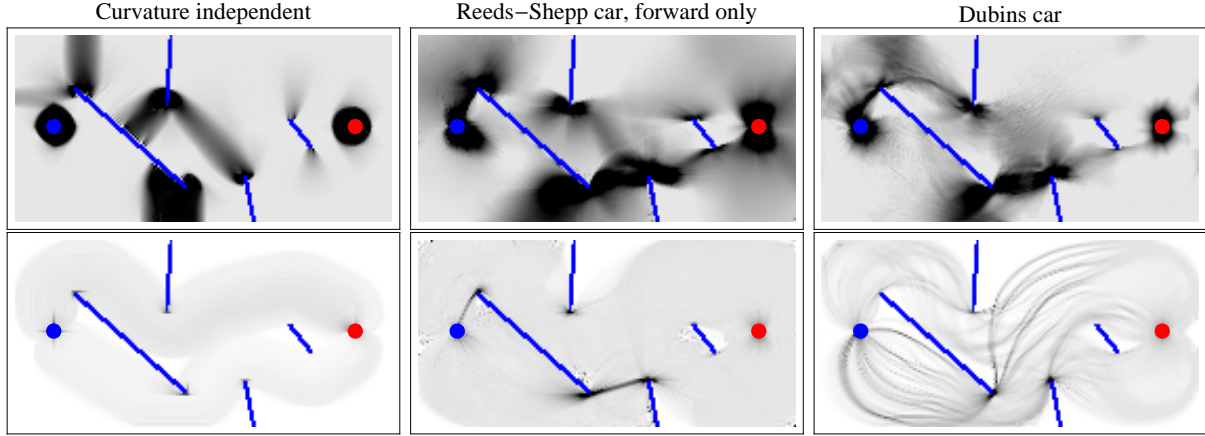


Figure 4.11 – Top: Optimal distribution of paint, to mark a path from the blue point (left) to the red keypoint (right) and back. Bottom: Geodesic density at the optimal paint distribution.

the paint density, namely  $0.1 \leq \xi(\mathbf{x}) \leq 1$ , and subtract the paint supply cost  $\int_R \xi(\mathbf{x}) d\mathbf{x}$  to (4.10). The main interest of this specific game, also considered in [BCPS10], is that the function  $\mathcal{C}(\xi, \Gamma)$  to be maximized is concave w.r.t.  $\xi \in \Xi$ . The observed optimal strategy for player  $\Xi$  is in the curvature independent case to make some “fences” of paint between close obstacles, and in the curvature penalized models to deposit paint at the edges of obstacles, as well as along specific circular arcs for the Dubins model.

**Visual detection.** The first player places some cameras, e.g. with a 360-degree field of view and mounted at the ceiling, which efficiency at detecting the second player decreases with distance and is blocked by obstacles, see Figure 4.12. The cost function is

$$\mathcal{C}_\xi(\mathbf{x}, \dot{\mathbf{x}}, \ddot{\mathbf{x}}) = \mathcal{C}_*(\kappa) \sum_{\substack{\mathbf{y} \in \xi \\ [\mathbf{x}, \mathbf{y}] \subseteq R}} \frac{1}{\|\mathbf{y} - \mathbf{x}\|^2}, \quad (4.16)$$

where  $\xi \in \Xi$  is a subset of  $R$  with prescribed cardinality, two in our experiments. The green arrows on Fig 4.12 originate from the current (non optimal) camera position, and point in the direction of greatest growth  $\nabla \mathcal{C}(\xi, \Gamma)$  for the first player objective function.

**Radar based detection.** The first player places some radars on the domain  $R = [0, 2] \times [0, 1]$ , here devoid of obstacles, and the second player has to fly by undetected. The cost function is

$$\mathcal{C}_\xi(\mathbf{x}, \dot{\mathbf{x}}, \ddot{\mathbf{x}}) = \mathcal{C}_*(|\ddot{\mathbf{x}}|) \sqrt{\sum_{\mathbf{y} \in \xi} \frac{\langle \dot{\mathbf{x}}, n_{\mathbf{x}\mathbf{y}} \rangle^2 + \delta^2 \langle \dot{\mathbf{x}}, n_{\mathbf{x}\mathbf{y}}^\perp \rangle}{\|\mathbf{x} - \mathbf{y}\|^4}} \quad (4.17)$$

where  $n_{\mathbf{x}\mathbf{y}} := (\mathbf{y} - \mathbf{x}) / \|\mathbf{y} - \mathbf{x}\|$ . The first player strategy  $\xi$  contains the positions of three radars, constrained to lie in the subdomain  $[0.4, 1.6] \times [0, 1]$ . The parameter  $\delta$  is set to 1 for an isotropic radar cross section (RCS), or to 0.2 for an anisotropic RCS. In the latter

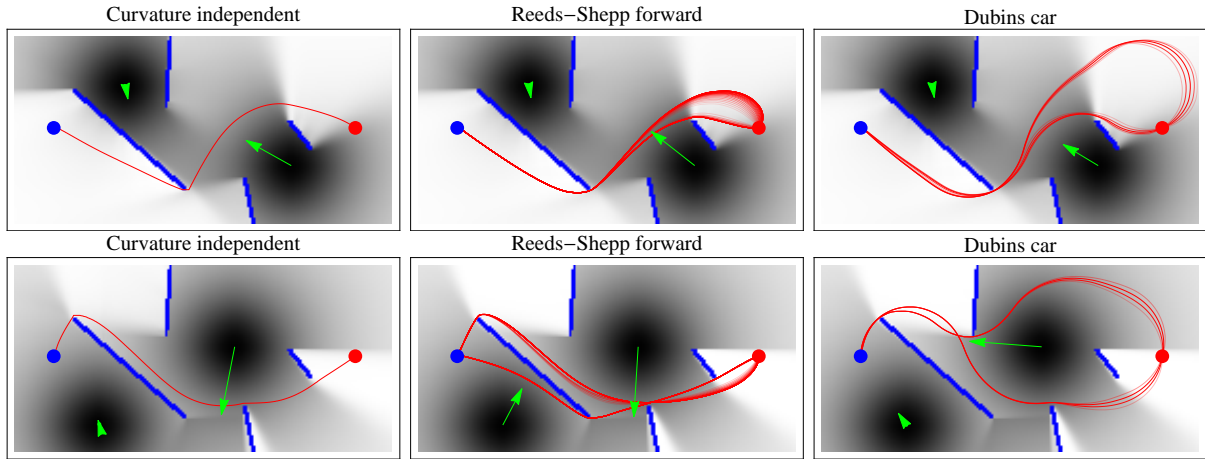


Figure 4.12 – Field of view of the cameras (black gradients), optimal furtive paths (red lines), local direction of improvement of the camera position (green arrows).

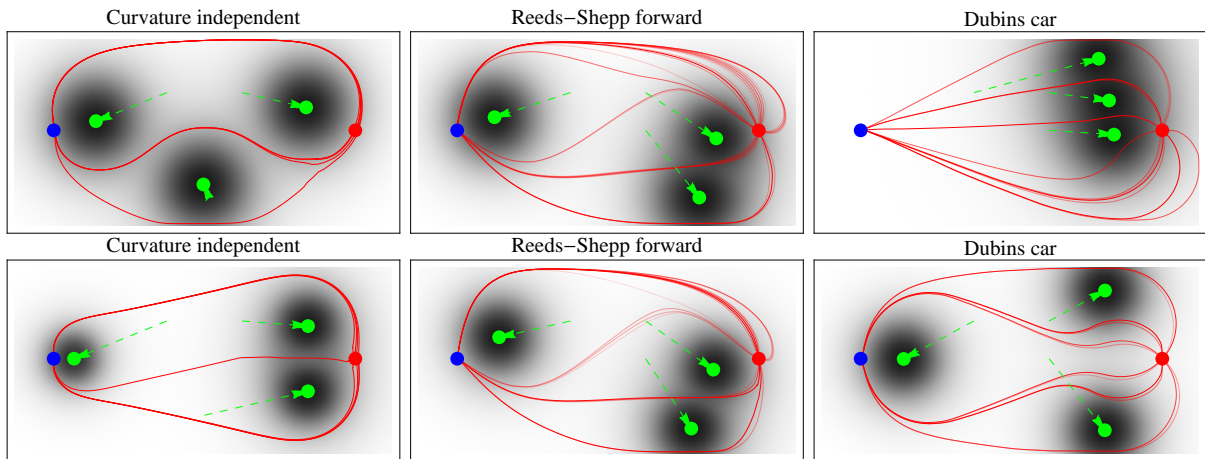


Figure 4.13 – Optimal radar placement with an isotropic (top) or anisotropic (bottom) radar cross section.

case a plane showing its side to radar is five times less likely to be detected than a plane showing its nose or back, at the same position. Green arrows on Figure 4.13 point from the original position to the (locally) optimized position for player  $\Xi$ . At this position, several paths are optimal for player  $\Gamma$ , shown in red on Fig 4.13.

**Discussion of the computational cost.** On a standard Laptop computer (2.7Ghz, 16GB ram), optimizing the second player objective, by solving a generalized eikonal equation, takes  $\approx 1s$  in the curvature dependent case, and  $\approx 60$  times less in the curvature independent case thanks to the absence of angular discretization of the domain. Optimizing the first player objective takes  $\approx 100$  *L-BFGS* iterations, each one taking at most 8s. For the stability of the minimization procedure, the considered problems were slightly regularized by the use of soft-minimum functions and by “blurring” the target keypoint over the  $3 \times 3$  box of adjacent pixels.

## Part II

# Second order equations

This part is devoted to numerical methods for a wide class of second order PDEs, relying on cartesian grid discretizations as in the rest of this dissertation. We discuss diffusion PDEs in §5, in divergence or non-divergence form, focusing on the difficulties related to (strongly) anisotropic tensor fields. We introduce a numerical scheme for Monge-Ampere equations in §6, which in principle can be generalized to the wider class of Pucci's extremal operators. Finally, we study the constraint of convexity in §7, which is of second order since it can be expressed as the non-negativity of the hessian matrix.

This second part features less *geometry* than the first, which was mostly devoted to the numerical computation of distance maps on manifolds. In order to alleviate notations, we thus rely on the euclidean structure on  $\mathbb{E}_d := \mathbb{R}^d$  to identify vectors with co-vectors, and do not use decorations such as  $\dot{\mathbf{x}}$  or  $\hat{\mathbf{x}}$ .

# Chapter 5

## Anisotropic diffusion

### Contents

---

<b>5.1 Non-Divergence form diffusion</b> . . . . .	<b>99</b>
<b>5.2 Divergence form diffusion</b> . . . . .	<b>102</b>

---

This chapter is devoted to Anisotropic Diffusion using Lattice Basis Reduction (AD-LBR), a numerical scheme applicable to diffusion PDEs in divergence or non-divergence form. This work was presented in [FM14, Mir16b, MFRT15], and is at the foundation of our numerical scheme for Monge-Ampere equations presented in §6. Our approach requires a cartesian discretization grid, and is based on Voronoi’s first reduction of quadratic forms.

### 5.1 Non-Divergence form diffusion

This section is devoted to non-divergence form diffusion, a PDE which appears (time reversed) in stochastic problems, and describes the evolution of an expectancy of gain attached to a brownian motion. It is one of the simplest second order anisotropic PDEs, and Voronoi’s first reduction is both natural and adequate for its discretization. We only say a few words on the modeling aspects, see last paragraph of this section, and emphasize instead the issues of numerical analysis and discretization. The numerical scheme presented below (5.2) can be regarded as a generalization, to arbitrary dimension, of the two dimensional method [BOZ04]. It has not been published elsewhere at the time of writing, in contrast with our work on divergence form diffusion presented in §5.2.

Consider a domain  $\Omega \subseteq \mathbb{R}^d$ , and a field  $\mathcal{D} : \bar{\Omega} \rightarrow \mathbb{S}^{++}(\mathbb{E}_d)$  of diffusion tensors. Non-divergence form diffusion takes the form

$$\partial_t u(\mathbf{x}, t) = \text{Tr}(\mathcal{D}(\mathbf{x}) \nabla^2 u(\mathbf{x}, t)). \tag{5.1}$$

Boundary conditions, e.g. of Dirichlet type for the model considered in the end of this section, are provided on  $\partial\Omega \times \mathbb{R}_+$ . An initial distribution at time  $t = 0$  completes the system.

The solution  $u$  of (5.1) can be regarded as an expectancy, see the last paragraph of this section, hence it obeys the maximum principle. More precisely, if initial distribution

and the boundary conditions are uniformly bounded by some constant, then so is  $u$ . We would like to guarantee this property at the discrete level since, in addition to be natural, it enables stable computations. The following class of discretization schemes is designed to achieve these properties. Recall that  $\mathbb{E}_d := \mathbb{R}^d$  and  $\mathbb{L}_d := \mathbb{Z}^d$ .

**Definition 5.1.1.** *A  $D$ -diffusion scheme, where  $D \in S^{++}(\mathbb{E}_d)$ , is the data of weights  $\rho_i \geq 0$  and offsets  $\mathbf{e}_i \in \mathbb{L}_d$ , where  $1 \leq i \leq d'$  and  $d'$  is an arbitrary integer, such that the following Taylor expansion is (second order) consistent as  $h \rightarrow 0$*

$$\mathrm{Tr}(D\nabla^2 u(\mathbf{x})) \approx \sum_{1 \leq i \leq d'} \rho_i \Delta_h^{\mathbf{e}_i} u(\mathbf{x}), \quad \text{with } \Delta_h^{\mathbf{e}_i} u(\mathbf{x}) := \frac{u(\mathbf{x} - h\mathbf{e}_i) - 2u(\mathbf{x}) + u(\mathbf{x} + h\mathbf{e}_i)}{h^2}. \quad (5.2)$$

This discretization of diffusion is qualified as monotone, because  $-\Delta_h^{\mathbf{e}_i} u(\mathbf{x})$  is a non-decreasing function of the finite differences  $(u(\mathbf{x}) - u(\mathbf{y}))_{\mathbf{y} \in X}$ , where  $X := \Omega \cap h\mathbb{L}_d$  is the cartesian discretization grid. For each  $\mathbf{x} \in X$  denote<sup>1</sup> by  $(\rho_i(\mathbf{x}), \mathbf{e}_i)_{i=1}^{d'}$  a  $\mathcal{D}(\mathbf{x})$ -diffusion scheme, where  $\mathcal{D} : \bar{\Omega} \rightarrow S^{++}(\mathbb{E}_d)$  is the given field of diffusion tensors. Non-divergence form diffusion (5.1) can then be numerically implemented using the following explicit scheme

$$U^{n+1}(\mathbf{x}) = \frac{\delta}{h^2} \sum_{1 \leq i \leq d'} \rho_i(\mathbf{x}) (U^n(\mathbf{x} - h\mathbf{e}_i) + U^n(\mathbf{x} + h\mathbf{e}_i)) + \left(1 - \frac{\delta}{h^2} \sum_{1 \leq i \leq d'} \rho_i(\mathbf{x})\right) U^n(\mathbf{x}), \quad (5.3)$$

where  $\delta > 0$  is the time step. The discrete function  $U^n : X \rightarrow \mathbb{R}$  is intended to approximate  $u(\cdot, n\delta)$ , and may need to be extended outside  $X$  using e.g. the provided Dirichlet boundary conditions. Assume that the time step  $\delta$  obeys the following Courant-Friedrichs-Levy [CFL28] condition: for each  $\mathbf{x} \in X$

$$\frac{\delta}{h^2} \sum_{1 \leq i \leq d'} \rho_i(\mathbf{x}) < 1. \quad \left(\text{Note that } \sum_{1 \leq i \leq d'} \rho_i(\mathbf{x}) \leq \sum_{1 \leq i \leq d'} \rho_i(\mathbf{x}) \|\mathbf{e}_i\|^2 = \mathrm{Tr}(\mathcal{D}(\mathbf{x})).\right) \quad (5.4)$$

Then  $U^{n+1}(\mathbf{x})$  is a positively weighted linear combination of the values of  $U^n$ , see (5.3), and as a result remains bounded above and below by the initial condition, as desired. Note that our focus is on the spatial discretization of the PDE (5.1) only, and we thus refer to [PHHR55, GWB10] for more subtle time discretizations than the explicit time step (5.3).

The property defining  $D$ -diffusion schemes is easily shown to be equivalent to

$$D = \sum_{1 \leq i \leq d'} \rho_i \mathbf{e}_i \otimes \mathbf{e}_i.$$

The design such decompositions is a natural objective, see [KT92, Wei98, BZ03, BC05]. Contrary to previous works, we rely for that purpose on Voronoi's first reduction, applied to the quadratic form defined by  $D$ , see §A.2.1 which yields  $d' = d(d+1)/2$ . In the

---

<sup>1</sup>The dependency of the offset  $\mathbf{e}_i = \mathbf{e}_i(\mathbf{x})$  on the reference point  $\mathbf{x}$  is omitted for readability.

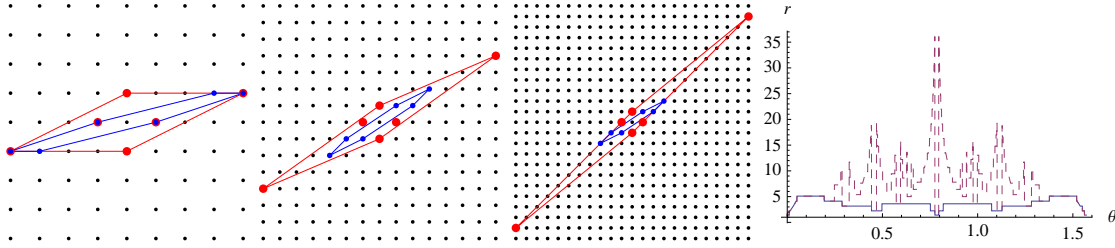


Figure 5.1 – Illustration of the AD-LBR stencils minimality, see Proposition 5.1.2. (I,II,III) Comparison of the AD-LBR diffusion stencil (blue), with another construction due to Weickert [Wei98, FM14], for some  $D \in S^{++}(\mathbb{E}_2^*)$  with  $\text{Cond}(D) = 10$  and various orientations  $\theta \in \mathbb{S}^1$  of the eigenvector associated with the small eigenvalue. (IV) Stencil radius as a function of  $\theta \in [0, \pi/2]$ , for the two constructions.

special case of the dimension  $d = 2$ , Bonnans et al [BOZ04] proposed an alternative but equivalent construction, based on the Stern-Brocot tree, defined in §A.1.3.

PDE discretization schemes based on small stencils are often preferred in applications, because they tend to be more robust, accurate, amenable to parallelization, and since the treatment of boundary conditions raises fewer issues. Our next result, proved in [Mir16b], shows that the  $D$ -diffusion stencils obtained by Voronoi’s first reduction are optimal in this regard, in two dimensions, in the strong sense of convex hull inclusion.

**Proposition 5.1.2.** *Let  $d = 2$ , and let  $D \in S^{++}(\mathbb{E}_2)$ . Let  $(\rho_i, \mathbf{e}_i)_{i=1}^n$  be the  $D$ -diffusion stencil defined by Voronoi’s first reduction, with  $\rho_i > 0$  for each  $1 \leq i \leq n$ , and let  $(\rho'_i, \mathbf{e}'_i)_{i=1}^{n'}$  be another  $D$ -diffusion stencil. Then*

$$\text{Hull}(\pm \mathbf{e}_i, 1 \leq i \leq n) \subseteq \text{Hull}(\pm \mathbf{e}'_i, 1 \leq i \leq n').$$

In addition to this qualitative result, one may want to bound the radius of a  $D$ -diffusion stencil in terms of the condition number  $\text{Cond}(D) := \sqrt{\|D\| \|D^{-1}\|}$  of the diffusion tensor. In dimension  $d = 2$ , a key observation is that the concepts of  $D$ -diffusion stencil and of  $M$ -acute stencil are equivalent [Mir16b], where  $M := D^{-1}$  and where the second concept is defined in §2.1 in the context of semi-Lagrangian fast marching schemes. As a result, applying Theorem 2.1.6, we obtain that the worst case bound on the stencil radius is  $\mathcal{O}(\text{Cond } D)$ , for the construction based on Voronoi’s first reduction. We also obtain sharp average bounds, for instance the quadratic mean of the stencil radius upon random rotations of the tensor is  $\mathcal{O}(\sqrt{\text{Cond}(D) \ln(\text{Cond } D)})$ .

**Elements of stochastic calculus.** In this paragraph, we briefly describe the modeling aspects underlying non-divergence form diffusion. For that purpose we need to introduce some elements stochastic calculus. Our objective is only to provide a short, elementary, informal, self contained motivation for the PDE studied, and we refer to classical textbooks such as [KS12] for more background on the subject. Note that, for reasons detailed below, this analysis leads to a *time reversed* variant of the PDE (5.1). In particular, the time variable is *negative* in this paragraph,  $t \in ]-\infty, 0]$ .

Consider a domain  $\Omega \subseteq \mathbb{R}^d$ , and a continuous field of diffusion tensors  $\mathcal{D} : \bar{\Omega} \rightarrow S^{++}(\mathbb{E}_d)$ . Let  $(X_t)_{t \leq 0}$  be a Brownian motion, without drift, with covariance tensors  $\mathcal{D}$ ,

which is frozen when it hits the boundary  $\partial\Omega$ . Thus for any  $\mathbf{x} \in \Omega$ , any  $t < 0$ , and any sufficiently small  $h > 0$ , one has denoting  $Z_h := X_{t+h} - \mathbf{x}$  the conditional expectancies

$$E[Z_h | X_t = \mathbf{x}] = o(h), \quad E[Z_h \otimes Z_h | X_t = \mathbf{x}] = h\mathcal{D}(\mathbf{x}) + o(h), \quad E[\|Z_h\|^3 | X_t = \mathbf{x}] = o(h). \quad (5.5)$$

Define for any  $t \leq 0$ , and any  $\mathbf{x} \in \bar{\Omega}$ , the conditional expectancy

$$u(t, \mathbf{x}) := E[u_0(X_0) | X_t = \mathbf{x}],$$

where  $u_0 : \bar{\Omega} \rightarrow \mathbb{R}$  is a given continuous map. The following boundary conditions are satisfied: At the terminal time  $u(0, \mathbf{x}) = u_0(\mathbf{x})$ , for any  $\mathbf{x} \in \Omega$ , since the Brownian motion has no time to move. On the domain boundary  $u(t, \mathbf{x}) = u_0(\mathbf{x})$ , for any  $\mathbf{x} \in \partial\Omega$  and any  $t \leq 0$ , since the Brownian motion is frozen.

On the domain interior, recalling that Brownian motions have no memory, one obtains the following self-consistency property. For any  $\mathbf{x} \in \Omega$  and any  $t < t + h < 0$

$$u(t, \mathbf{x}) := E[u(t + h, X_{t+h}) | X_t = \mathbf{x}]. \quad (5.6)$$

We next proceed to a formal Taylor expansion, conditionally to  $X_t = \mathbf{x}$  and denoting again  $Z_h := X_{t+h} - \mathbf{x}$ .

$$u(t + h, X_{t+h}) = u(t, \mathbf{x}) + h\partial_t u(t, \mathbf{x}) + \langle Z_h, \nabla u(t, \mathbf{x}) \rangle + \frac{1}{2} \langle Z_h, \nabla^2 u(t, \mathbf{x}) Z_h \rangle + \mathcal{O}(h^2 + \|Z_h\|^3).$$

Inserting this expression in (5.6), and using (5.5) to compute the expectancy, we obtain

$$u(t, \mathbf{x}) = u(t, \mathbf{x}) + h\partial_t u(t, \mathbf{x}) + 0 + \frac{1}{2}h \operatorname{Tr}(\mathcal{D}(\mathbf{x})\nabla^2 u(t, \mathbf{x})) + o(h).$$

We also used the identity  $\langle \mathbf{z}, M\mathbf{z} \rangle = \operatorname{Tr}(\mathbf{z} \otimes \mathbf{z} \cdot M)$  with  $\mathbf{z} := Z_h$  and  $M := \nabla^2 u(t, \mathbf{x})$ . The latest equation is equivalent to  $-\partial_t u = \frac{1}{2} \operatorname{Tr}(\mathcal{D}\nabla^2 u)$ , which is (5.1) as announced, up to the time reversal and the scaling factor  $1/2$ .

## 5.2 Divergence form diffusion

The physical interpretation of divergence form diffusion PDEs, as the gradient flow of an elliptic energy, is fundamentally distinct from the stochastic expectancy underlying non-divergence form diffusion. This energetic interpretation may explain the successes of divergence form diffusion in image processing applications [Wei98], and in particular denoising. The numerical scheme presented in this section also has applications outside of image processing. It has been used for the computation of gradient flows w.r.t. the Wasserstein metric [Pey15], and the approximation of distance maps using Varadhan's formula [YC17].

The anisotropic, divergence form diffusion PDE takes the following form

$$\partial_t u(\mathbf{x}, t) = \operatorname{div}(\mathcal{D}(\mathbf{x})\nabla u(\mathbf{x}, t)), \quad (5.7)$$

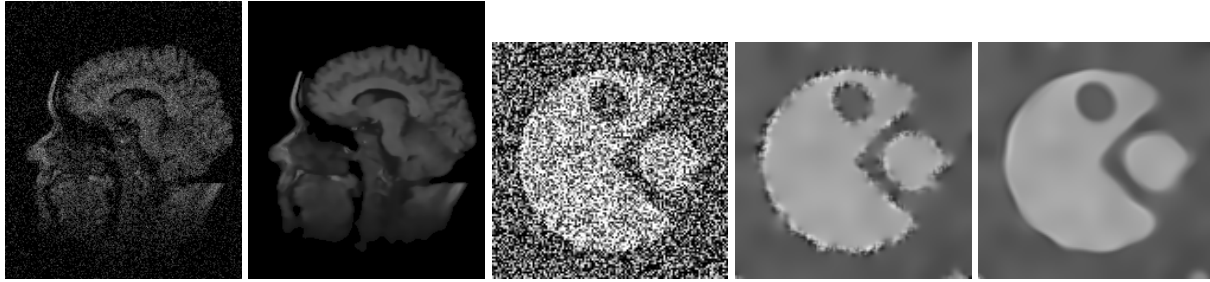


Figure 5.2 – *Left*. I: MRI scan, with artificially added noise. II: effect of Weickert’s Coherence Enhancing Diffusion PDE, implemented using the AD-LBR; this is a slice of Figure 1.10 right. *Right*. I: Noisy cartoon image. II: Effect of Perona and Malik’s nonlinear isotropic diffusion. (Object boundaries are not denoised) III: Effect Weickert’s Edge Enhancing Diffusion, implemented using the AD-LBR. (Object boundaries are denoised by tangential diffusion.)

on  $\Omega \times [0, \infty[$ , where  $\Omega \subseteq \mathbb{E}_d$  is the physical domain, and  $\mathcal{D} : \bar{\Omega} \rightarrow \mathbb{S}^{++}(\mathbb{E}_d)$  is a continuous field of diffusion tensors. With boundary conditions of Neumann type on  $\partial\Omega$ , the solution (5.7) follows as announced the steepest slope w.r.t. the  $L^2$  norm for an elliptic Lyapunov functional. More precisely, for any  $t \in [0, \infty[$ , denoting  $u(t) := u(\cdot, t) \in L^2(\Omega)$ , one has at first order as  $\delta \rightarrow 0$

$$u(t + \delta) \approx \operatorname{argmin}_{v: \Omega \rightarrow \mathbb{R}} \frac{1}{2\delta^2} \|v - u(t)\|_{L^2(\Omega)}^2 + \mathcal{E}(v), \quad \text{where } \mathcal{E}(u) := \int_{\Omega} \|\nabla u(\mathbf{x})\|_{\mathcal{D}(\mathbf{x})}^2 \, d\mathbf{x}. \quad (5.8)$$

Consider a positive tensor  $D \in \mathbb{S}^{++}(\mathbb{E}_d)$  and a  $D$ -diffusion stencil  $(\rho_i, \mathbf{e}_i)_{i=1}^{d'} \in (\mathbb{R}_+ \times \mathbb{L}_d)^{d'}$ , in the sense of Definition 5.1.1. Then using (5.1) one obtains the (first order) Taylor expansion

$$\|\nabla u(\mathbf{x})\|_D^2 \approx \sum_{1 \leq i \leq d'} \rho_i \frac{(u(\mathbf{x}) - u(\mathbf{x} - h\mathbf{e}_i))^2 + (u(\mathbf{x}) - u(\mathbf{x} + h\mathbf{e}_i))^2}{2h^2}, \quad (5.9)$$

which is reminiscent but also quite different from (5.2). Recall that  $\|\mathbf{x}\|_D := \sqrt{\langle \mathbf{x}, D\mathbf{x} \rangle}$ .

The integral energy  $\mathcal{E}$  defined in (5.8) can be approximated, on the cartesian grid  $X := \Omega \cap h\mathbb{L}_d$ , with the Riemann sum  $\mathcal{E}(u) \approx h^d \sum_{\mathbf{x} \in X} \|\nabla u(\mathbf{x})\|_{\mathcal{D}(\mathbf{x})}^2$ . Each term of the sum is in turn approximated using (5.9), but with weights  $\rho_i(\mathbf{x})$  and offsets  $\mathbf{e}_i = \mathbf{e}_i(\mathbf{x})$  adapted to the local tensor  $\mathcal{D}(\mathbf{x})$ . It is shown in [FM14], in dimension  $d = 2$ , that this finite differences based energy is asymptotically equivalent, as the grid scale is refined, to the finite element energy obtained using an adaptive Delaunay triangulation [LS03] of the point set  $X$  w.r.t. the Riemannian metric  $\mathcal{M} := \mathcal{D}^{-1}$ .

The fully discretized counterpart of the elliptic energy  $\mathcal{E}(u)$  takes the form  $U^T A U$ , where  $A$  is a positive semi-definite matrix and  $U : X \rightarrow \mathbb{R}$  is regarded as a vector. Divergence form diffusion can be implemented using explicit time discretization as  $U^{n+1} = U^n - (\delta/h^2) A U^n$ , where  $\delta > 0$  is the time step and  $U^n$  is intended to approximate  $u(\cdot, n\delta)$ . By construction (5.9), a structural property of the matrix  $A$  is that its diagonal terms are positive, and the off diagonal terms are non-positive. Therefore, the proposed explicit scheme preserves the non-negativity of  $(U^n)_{n \geq 0}$  through the iterations, provided the time

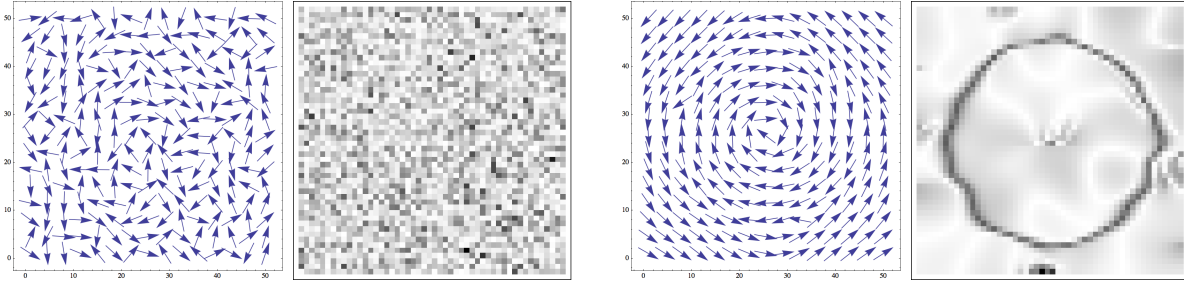


Figure 5.3 – Left: Directions and norms (black=0, white=1) of the vector field  $v(x) := \text{sign}(\|x\| - 1) x^\perp / \|x\|$  on  $[-1.3, 1.3]^2$ , degraded by gaussian noise of variance 2, on a  $50 \times 50$  grid. Right: Effect of cEED. Note that the streamlines are better reconstructed, and that the norms vanish along the (approximate) circle  $\|x\| = 1$  where  $v(x)$  changes sign so that there is a cancellation effect (and likewise close to the vector field singularity at the center). Images from [MFRT15].

step  $\delta$  is sufficiently small [FM14]. (The CFL condition is identical to the non-divergence form case (5.4), and more subtle schemes w.r.t. the time variable can again be implemented if needed [PHHR55, GWB10].)

This numerical scheme is implemented in the Insight Toolkit toolbox for medical image processing [MFRT15]. It is, straightforwardly, adapted to non-linear diffusion equations, whose tensors  $\mathcal{D}_u(\mathbf{x})$  depend on the current state of the function  $u$ , and to multi-channel images. Numerical experiments based on Weickert’s edge-enhancing and coherence-enhancing diffusion PDEs [Wei98] are presented on Figures 5.2 and 5.3. Note that our works are irrelevant for the simpler case of diffusion PDEs involving non-linear *isotropic* tensors, i.e. proportional to the identity matrix, such as in the Perona and Malik model [PM90].

# Chapter 6

## The Monge-Ampere operator

### Contents

---

6.1	Discretization of general Pucci operators . . . . .	106
6.2	The MA-LBR numerical scheme . . . . .	111

---

This chapter is devoted to Monge-Ampere using Lattice Basis Reduction (MA-LBR), a monotone and consistent discretization of the Monge-Ampere operator, on two dimensional cartesian grids, introduced by Benamou, Collino, and the author. In contrast with our original publication [BCM16], we do not motivate our approach by the geometrical interpretation of the Monge-Ampere operator [Gut01, OP89], but regard it as a generic instance within the larger class of Pucci extremal operators, which take the form

$$\inf_{D \in \mathfrak{D}} \text{Tr}(D \nabla^2 u(\mathbf{x})), \tag{6.1}$$

where  $\mathfrak{D} \subseteq S^{++}(\mathbb{E}_d^*)$  is an arbitrary set of matrices. Pucci extremal operators may also be defined using a supremum, instead of the infimum (6.1). These operators, thus in particular the Monge-Ampere operator, see (6.9), share a fundamental structural property: they are *monotone* operators [CIL92].

**Definition 6.0.1.** *A monotone PDE operator on a domain  $\Omega \subseteq \mathbb{E}_d$  takes the form*

$$F(\mathbf{x}, u(\mathbf{x}), \nabla u(\mathbf{x}), \nabla^2 u(\mathbf{x})), \tag{6.2}$$

where  $\mathbf{x} \in \Omega$  and  $u : \Omega \rightarrow \mathbb{R}$ . The function  $F : \Omega \times \mathbb{R} \times \mathbb{E}_d \times S(\mathbb{E}_d)$  must be non-decreasing w.r.t. the second variable “ $u(\mathbf{x})$ ”, and non-increasing w.r.t. the fourth variable “ $\nabla^2 u(\mathbf{x})$ ” for the usual partial order on symmetric matrices<sup>1</sup>.

“Degenerate ellipticity” is sometimes used as a synonym for “monotony” [Obe06]. Monotony implies comparison principles, which are typically used to prove convergence results upon perturbations of the PDE [CIL92]. It has a discrete counterpart, see the next definition, and monotone numerical schemes similarly benefit from comparison principles. When satisfied, this property is an essential tool for proving the numerical scheme

---

<sup>1</sup>For any  $A, B \in S(\mathbb{E}_d)$ , one has  $A \preceq B$  iff  $B - A \in S^+(\mathbb{E}_d)$ .

stability and establishing the convergence of its discrete solutions towards the continuous problem solution as the grid scale is refined, see [Obe06, FO11b]. The same technique is used in the context of first order equations in e.g. [BR06, SMK16] and the author’s works [Mir14a, Mir17a, Mir17b].

**Definition 6.0.2.** *A monotone numerical scheme on a finite set  $X$  takes the form*

$$F(\mathbf{x}, u(\mathbf{x}), (u(\mathbf{x}) - u(\mathbf{y}))_{\mathbf{y} \in X}), \tag{6.3}$$

where  $\mathbf{x} \in X$  and  $u : X \rightarrow \mathbb{R}$ . The function  $F : X \times \mathbb{R} \times \mathbb{R}^X$  must be non-decreasing w.r.t. the third variable  $(u(\mathbf{x}) - u(\mathbf{y}))_{\mathbf{y} \in X}$ , componentwise.

A natural objective is to design monotone discretizations of monotone PDE operators of interest [KT92, Fro15], yet naive approaches to this task unfortunately suffer from several flaws. Often the resulting numerical schemes may rely on very wide stencils, which increases the cost of the linear systems to be solved (by reducing their sparsity), and reduces the solution accuracy (by increasing the effective discretization scale). Another source of accuracy loss is the lack of consistency of a number of schemes, in the sense that (6.3) is not equal to (6.2), even for quadratic functions  $u$ , but only approximates it as some relaxation parameter tends to zero. A possible remedy is to use *filtered* schemes combining together a monotone but poorly accurate numerical scheme, and another non-monotone but accurate scheme [FO13], in the attempt to combine their strengths. We propose a different approach, which is the design of *monotone and consistent* schemes, based on *optimally small* stencils.

**Outline.** We describe in §6.1 the discretization of general Pucci operators, using Voronoi’s first reduction of quadratic forms, and its specialization to the Monge-Ampere operator. Further discussion of the MA-LBR numerical scheme is presented §6.2.

## 6.1 Discretization of general Pucci operators

The work presented in this section belongs to a line of research initiated by Trudinger and Kuo [KT92], devoted to the discretization of general second order Hamilton-Jacobi PDEs using *monotone* finite differences schemes, and which is still active today [BOZ04, Obe04, Obe05, FO11a, Fro15]. Our contribution, in comparison with earlier research, is that our schemes are *consistent* - instead of being asymptotically consistent as some relaxation parameter tends to zero -, and that their discretization stencils can be shown to be *optimally small* in a number of cases - see e.g. Proposition 5.1.2 or Theorem 1.9 in [BCM16]. Our approach is based on Voronoi’s first reduction of quadratic forms, see below, and thus requires a cartesian discretization grid. The reader solely interested in the properties of our MA-LBR numerical scheme for the Monge-Ampere operator may skip this part and jump to §6.2. The contributions of this section are original, and have not been published elsewhere.

Consider a Pucci extremal operator, defined as in (6.1) by taking the infimum of a family of non-divergence form linear operators with diffusion tensor  $D \in \mathfrak{D}$ , where  $\mathfrak{D} \subseteq S^{++}(\mathbb{E}_d^*)$  is a given fixed set. In the case where  $\mathfrak{D} = \{D\}$  is a singleton, one

obtains an usual non-divergence form diffusion operator:  $\text{Tr}(D\nabla^2 u(\mathbf{x}))$ . We discretize it using a  $D$ -diffusion stencil, see Definition 5.1.1, obtained as a byproduct of Voronoi's first reduction, see A.2.1 and below, which is chosen for its optimality, see Proposition 5.1.2.

A slightly more general case is the one of a finite set  $\mathfrak{D} = \{D_1, \dots, D_K\} \subseteq S^{++}(\mathbb{E}_d)$  of diffusion tensors. For any discrete map  $U : h\mathbb{L}_d \rightarrow \mathbb{R}$  we define

$$\Lambda U(\mathbf{x}) := \min_{1 \leq k \leq K} \sum_{1 \leq i \leq d'} \rho_i^k \Delta_h^{\mathbf{e}_i^k} U(\mathbf{x}), \quad \text{where } D_k = \sum_{1 \leq i \leq d'} \rho_i^k \mathbf{e}_i^k \otimes \mathbf{e}_i^k \quad (6.4)$$

for all  $1 \leq k \leq K$ . Again, Voronoi's first reduction is used to obtain this matrix decomposition. We denoted by  $\Delta_h^{\mathbf{e}} u(\mathbf{x}) := (u(\mathbf{x} - h\mathbf{e}) - 2u(\mathbf{x}) + u(\mathbf{x} + h\mathbf{e}))/h^2$  the second order centered finite difference on the cartesian grid  $h\mathbb{L}_d$ , at the position  $\mathbf{x}$  and in the direction  $\mathbf{e}$ , as in the previous section (5.2).

In the case of a general Pucci operator, and in particular of the Monge-Ampere operator see below, the set  $\mathfrak{D} \subseteq S^{++}(\mathbb{E}_d^*)$  of diffusion tensors is typically infinite. For discretization purposes, we partition these diffusion tensors into subsets determined by the support of the corresponding diffusion PDE schemes, e.g.  $\{\pm \mathbf{e}_i^k; 1 \leq i \leq d'\}$  for the tensor  $D_k$  in (6.4, right). In order to better describe this procedure, we recall the definition Voronoi's first reduction, see §A.2.1, denoted  $\text{VR} : S^{++}(\mathbb{E}_d^*) \rightarrow S^{++}(\mathbb{E}_d)$ . For any  $D \in S^{++}(\mathbb{E}_d^*)$ ,

$$\text{VR}(D) := \underset{M \in \mathfrak{M}}{\text{argmin}} \text{Tr}(DM), \quad \text{where } \mathfrak{M} := \{M \in S^{++}(\mathbb{E}_d); \forall \mathbf{e} \in \mathbb{L}_d \setminus \{0\}, \|\mathbf{e}\|_M \geq 1\}. \quad (6.5)$$

The set  $\mathfrak{M} \subseteq S(\mathbb{E}_d)$  is a polytope, since it can be defined in terms of the linear constraints  $\|\mathbf{e}\|_M^2 = \text{Tr}(M\mathbf{e} \otimes \mathbf{e}) \geq 1$  where  $\mathbf{e} \in \mathbb{L}_d \setminus \{0\}$  (the positive definiteness constraint is redundant). The vertices of  $\mathfrak{M}$  are called perfect forms, and we denote their collection by  $\mathfrak{M}_0$ . The linear problem defining  $\text{VR}(D)$  is well posed, and admits a single minimizer provided  $D$  is outside<sup>2</sup> of a set of co-dimension 1, which by construction is an extremal point of  $\mathfrak{M}$ , hence a perfect form.

Consider a fixed  $D \in S^{++}(\mathbb{E}_d^*)$  and denote by  $M := \text{VR}(D) \in \mathfrak{M}_0$  the corresponding perfect form. The Karush-Kuhn-Tucker conditions for this linear optimization problem can be written in the form of a matrix decomposition, that we have used several times already: denoting by  $\rho_{\mathbf{e}}^D \geq 0$  the Lagrange multipliers

$$D = \sum_{\mathbf{e} \in \mathbb{L}_d} \rho_{\mathbf{e}}^D \mathbf{e} \otimes \mathbf{e}. \quad (6.6)$$

By construction, the offsets  $\mathbf{e} \in \mathbb{L}_d$  such that  $\rho_{\mathbf{e}}^D > 0$  all belong to the following finite set  $\mathbb{L}_M \subseteq \mathbb{L}_d$  determined by the perfect form  $M = \text{VR}(D)$

$$\mathbb{L}_M := \{\mathbf{e} \in \mathbb{L}_d; \|\mathbf{e}\|_M = 1\}. \quad (6.7)$$

---

<sup>2</sup> In non-generic cases, this optimization problem admits a compact set of minimizers, of which one at least is a perfect form.

Indeed, these offsets correspond to *active* constraints in (6.5). Denoting by  $\mathfrak{D}_M := \{D \in \mathfrak{D}; \text{VR}(D) = M\}$  the collection of diffusion tensors which share a perfect form, we discretize the Pucci extremal operator (6.1) as follows. For any  $U : h\mathbb{L}_d \rightarrow \mathbb{R}$

$$\Lambda U(\mathbf{x}) := \min_{M \in \mathfrak{M}_0} \Lambda_M U(\mathbf{x}), \quad \text{where} \quad \Lambda_M U(\mathbf{x}) := \min_{D \in \mathfrak{D}_M} \sum_{\mathbf{e} \in \mathbb{L}_M} \rho_{\mathbf{e}}^D \Delta_h^{\mathbf{e}} U(\mathbf{x}). \quad (6.8)$$

Each of the sub-operators  $\Lambda_M$  associated with a perfect form  $M \in \mathfrak{M}_0$  is monotone, and is discretized using a bounded stencil only, namely  $\{\mathbf{x}\} \cup \{\mathbf{x} + h\mathbf{e}; \mathbf{e} \in \mathbb{L}_M\}$ . It is defined in terms of a finite dimensional optimization problem (6.8, right), which admits an explicit solution in some cases of interest, such as the Monge-Ampere operator discussed in the following paragraph.

If the condition number is bounded over the set  $\mathfrak{D}$  defining the operator (6.1) then, by wellposedness of Voronoi's first reduction, the Voronoi reductions of the tensors in  $\mathfrak{D}$  all belong to a finite subset of  $\mathfrak{M}_0$ . Hence the minimum (6.8, left) is over a finite subset of  $\mathfrak{M}_0$  only, which eases the numerical implementation. In some other cases, such as for the Monge-Ampere operator discussed next, the condition number is unbounded over  $\mathfrak{D}$ , but the Pucci operator associated with  $\mathfrak{D}' \supseteq \{D \in \mathfrak{D}; \text{Cond}(D) \leq \kappa\}$ , where  $\kappa \geq 1$  is sufficiently large, is equal to the original one provided the solution Hessian is not too degenerate. The latter property may be guaranteed by a-priori estimates, making it still feasible to design a consistent discretization.

As a final note, let us mention that it seems uneasy but not necessarily un-tractable to adapt the strategy (6.8) to define monotone and consistent discretizations of fully general second order HJB monotone operators, which (under mild assumptions [CIL92]) take the form

$$\sup_{\alpha \in A} \inf_{\beta \in B} \text{Tr}(D_{\alpha\beta} \nabla^2 u(\mathbf{x})),$$

where  $(D_{\alpha\beta})_{\alpha \in A}^{\beta \in B}$  is a two-parameter family in  $S^{++}(\mathbb{E}_d^*)$ . Similar strategies have been considered in the past [KT92, BOZ04], but our approach has added benefits which make it more effective, such as the consistency of the discretization and the smallness of the stencils.

## Specialization to the two dimensional Monge-Ampere operator.

In the rest of this section, we fully describe the discretization (6.8) of the Monge-Ampere operator, regarded as a Pucci operator. More precisely, we consider the following operator, defined for any smooth and convex  $u : \mathbb{E}_d \rightarrow \mathbb{R}$

$$d(\det \nabla^2 u(\mathbf{x}))^{\frac{1}{d}} = \inf_{\substack{\det D=1 \\ D>0}} \text{Tr}(\nabla^2 u(\mathbf{x})D). \quad (6.9)$$

In doing so, in dimension  $d = 2$ , we recover the MA-LBR numerical scheme [BCM16], which interestingly was not discovered using this systematic way, see §6.2.

In order to apply the discretization strategy (6.8), our first step is to describe the set  $\mathfrak{M}_0$  of perfect forms, and to characterize tensors  $D \in S^{++}(\mathbb{E}_2^*)$  which Voronoi reduction is a given perfect form  $M \in \mathfrak{M}_0$ . Perfect forms in dimension  $d \leq 3$  can be parametrized by a

family of (redundant) coordinate systems named *superbases*, see [CS92], or §4 of [Mir17b], or §A. A superbase of  $\mathbb{Z}^2$  is a triplet  $(\mathbf{e}, \mathbf{f}, \mathbf{g}) \in (\mathbb{Z}^2)^3$  obeying

$$\mathbf{e} + \mathbf{f} + \mathbf{g} = 0, \quad \text{and } |\det(\mathbf{f}, \mathbf{g})| = 1. \quad (6.10)$$

Define the corresponding perfect form by<sup>3</sup>  $M = \frac{1}{2}(\mathbf{e}^\perp \otimes \mathbf{e}^\perp + \mathbf{f}^\perp \otimes \mathbf{f}^\perp + \mathbf{g}^\perp \otimes \mathbf{g}^\perp) \in \mathfrak{M}_0$ , which support (6.7) is  $\mathbb{L}_M := \{\pm \mathbf{e}, \pm \mathbf{f}, \pm \mathbf{g}\}$ .

Let us fix the superbase  $(\mathbf{e}, \mathbf{f}, \mathbf{g})$  as well as  $M$  in the rest of this section. Matrices  $D \in S^{++}(\mathbb{E}_d^*)$  such that  $\text{VR}(D) = M$  can be parametrized by three scalars  $a, b, c \geq 0$ , taking the role of the Lagrange multipliers  $\rho_{\mathbf{e}}^D, \rho_{\mathbf{f}}^D, \rho_{\mathbf{g}}^D$  in (6.6) respectively. Thus

$$D = a \mathbf{e} \otimes \mathbf{e} + b \mathbf{f} \otimes \mathbf{f} + c \mathbf{g} \otimes \mathbf{g}, \quad \text{and } \det(D) = \det \begin{pmatrix} b+a & a \\ a & c+a \end{pmatrix} = ab + ac + bc.$$

The expression of  $\det(D)$  is obtained using a linear change of variables from  $(\mathbf{e}, \mathbf{f}, \mathbf{g})$  to the canonical superbase  $(-1, -1), (1, 0), (0, 1)$ . This change of variables has unit determinant in view of (6.10, right). We deduce, from above the parametrization of  $D$  and the expression of its determinant, a semi-explicit expression of the operator  $\Lambda_M$  appearing when discretizing the (6.9) in the form (6.8). For any  $U : h\mathbb{L}_d \rightarrow \mathbb{R}$

$$\Lambda_M U(\mathbf{x}) = G(\Delta_h^{\mathbf{e}} U(\mathbf{x}), \Delta_h^{\mathbf{f}} U(\mathbf{x}), \Delta_h^{\mathbf{g}} U(\mathbf{x})),$$

where we denoted, for any  $\alpha, \beta, \gamma \in \mathbb{R}$

$$G(\alpha, \beta, \gamma) := \min\{\alpha a + \beta b + \gamma c; a, b, c \geq 0, ab + bc + ca = 1\}. \quad (6.11)$$

The following proposition, un-published, concludes our discretization of the Monge-Ampere operator by explicitly solving the optimization problem (6.11).

**Proposition 6.1.1.** *For any  $\alpha, \beta, \gamma > 0$ , one has  $G(\alpha, \beta, \gamma) = 2\sqrt{H_0(\alpha, \beta, \gamma)}$ , where*

$$H_0(\alpha, \beta, \gamma) := \begin{cases} \beta\gamma & \text{if } \alpha \geq \beta + \gamma, \text{ and likewise permuting } \alpha, \beta, \gamma, \\ \frac{1}{2}(\alpha\beta + \beta\gamma + \gamma\alpha) - \frac{1}{4}(\alpha^2 + \beta^2 + \gamma^2) & \text{otherwise.} \end{cases} \quad (6.12)$$

*Proof.* The minimum defining (6.11) is attained at some  $(a, b, c) \in \mathbb{R}_+^3$ , fixed in the following, since the objective function  $(a, b, c) \mapsto \alpha a + \beta b + \gamma c$  is coercive on  $\mathbb{R}_+^3$ , and since the constraint  $ab + bc + ca = 1$  is closed. If  $c = 0$ , then the optimization problem becomes  $\min\{\alpha a + \beta/a; a > 0\}$ , by elimination of  $b = 1/a$ , which solution is  $2\sqrt{\alpha\beta}$  attained for  $a = \sqrt{\beta/\alpha}$ . Likewise if  $a = 0$  or  $b = 0$  instead of  $c = 0$ .

Consider now the case where all three of  $a, b, c$  are positive. Then by the KKT conditions for the optimization problem (6.11), there exists a Lagrange multiplier  $\lambda \geq 0$  such that  $(\alpha, \beta, \gamma) = (\lambda/2)(b + c, c + a, a + b)$ . Equivalently

$$\lambda(a, b, c) = (\beta + \gamma - \alpha, \gamma + \alpha - \beta, \alpha + \beta - \gamma). \quad (6.13)$$

---

<sup>3</sup> The opposite convention, namely  $M = \frac{1}{2}(\mathbf{e} \otimes \mathbf{e} + \mathbf{f} \otimes \mathbf{f} + \mathbf{g} \otimes \mathbf{g})$  and thus  $\mathbb{L}_M := \{\pm \mathbf{e}^\perp, \pm \mathbf{f}^\perp, \pm \mathbf{g}^\perp\}$ , is chosen in [Mir17b] for a better generalization to dimension  $d = 3$ .

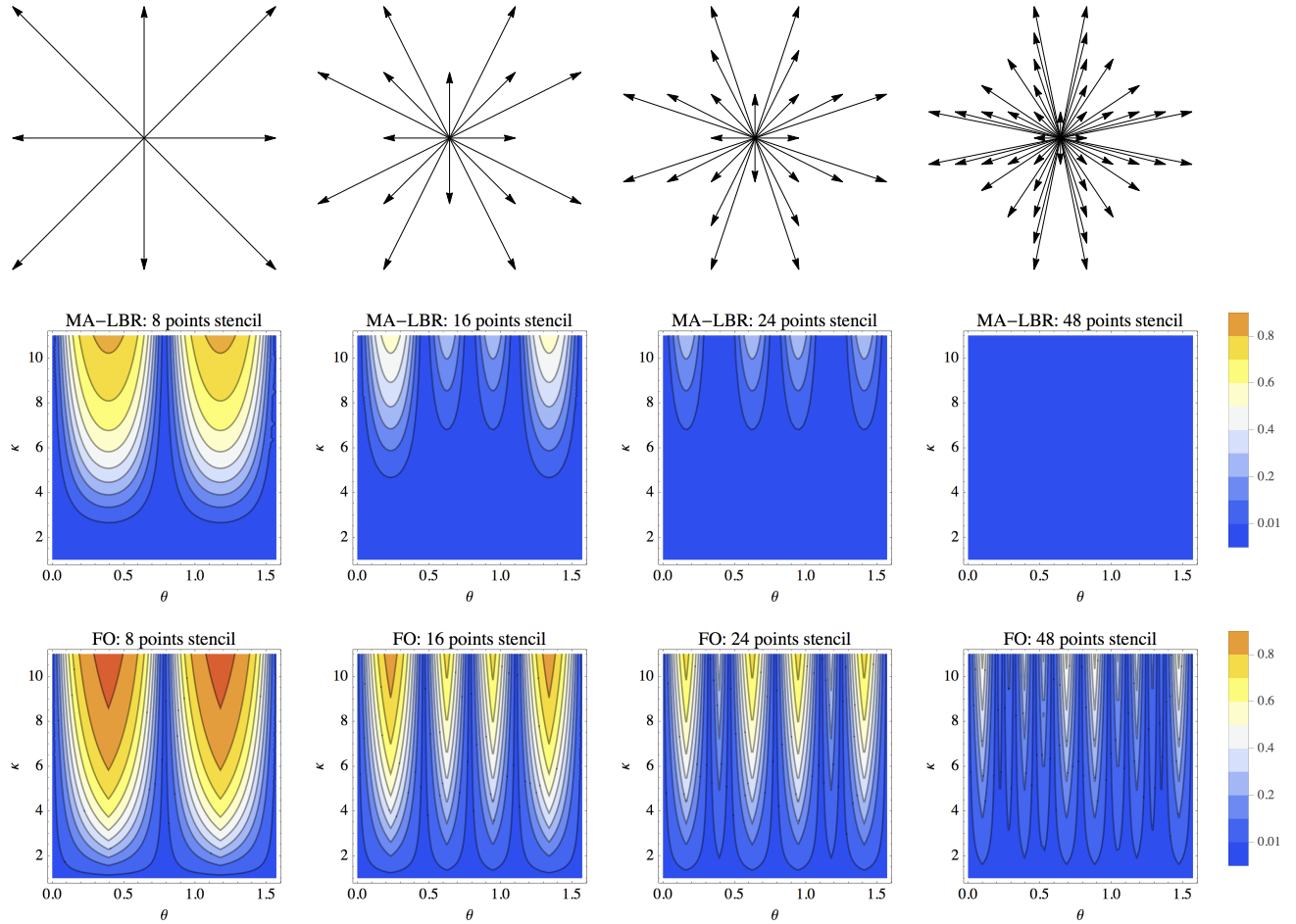


Figure 6.1 – Top: Finite differences stencil. Middle: Relative consistency error of the MA-LBR. Bottom: Relative consistency error of the Froese-Oberman [Fro12] wide stencil scheme. Matrix parametrization:  $M_\kappa(\theta) := \kappa^{-1}\mathbf{n}(\theta) \otimes \mathbf{n}(\theta) + \kappa\mathbf{n}(\theta)^\perp \otimes \mathbf{n}(\theta)^\perp$ , where  $\mathbf{n}(\theta) := (\cos\theta, \sin\theta)$ . Parameters  $\theta$  and  $\kappa$  are along the horizontal and vertical axes respectively. Note that the MA-LBR consistency error vanishes to zero *exactly*, for any given matrix, once the stencil size is sufficiently large.

In particular, we obtain that the positiveness of  $a$  and  $b$  and  $c$  cannot hold if  $\alpha \geq \beta + \gamma$ , or  $\beta \geq \gamma + \alpha$ , or  $\gamma \geq \alpha + \beta$ , as announced in the expression (6.12) of  $H_0$ . Replacing  $a, b, c$  with their expression in terms of  $\lambda$  and  $\alpha, \beta, \gamma$ , see (6.13), and doing straightforward simplifications, we obtain new expressions of the problem (6.11) objective and constraint

$$\alpha a + \beta b + \gamma c = \Delta/\lambda, \quad 1 = ab + bc + ca = \Delta/\lambda^2,$$

with  $\Delta := 2(\alpha\beta + \beta\gamma + \gamma\alpha) - (\alpha^2 + \beta^2 + \gamma^2)$ . The constraint yields  $\lambda = \sqrt{\Delta}$ , and the objective value is thus  $\Delta/\lambda = \sqrt{\Delta} = 2\sqrt{H_0(\alpha, \beta, \gamma)}$  as announced.  $\square$

## 6.2 The MA-LBR numerical scheme

In this section, we discuss some properties of the MA-LBR numerical scheme, a monotone and consistent discretization of the two dimensional Monge-Ampere operator, on cartesian grids [BCM16], defined as follows. For any  $U : h\mathbb{L}^2 \rightarrow \mathbb{R}$ , and any discretization point  $\mathbf{x} \in h\mathbb{L}_2$ , where  $h > 0$  is the grid scale

$$\Lambda U(\mathbf{x}) := \inf_{\substack{(\mathbf{e}, \mathbf{f}, \mathbf{g}) \\ \text{superbase}}} H(\Delta_h^{\mathbf{e}}U(\mathbf{x}), \Delta_h^{\mathbf{f}}U(\mathbf{x}), \Delta_h^{\mathbf{g}}U(\mathbf{x})). \quad (6.14)$$

A superbase is a discrete object, a triplet of vectors  $(\mathbf{e}, \mathbf{f}, \mathbf{g}) \in \mathbb{L}_2^3$  obeying the compatibility conditions (6.10), which naturally appears in lattice classification [CS92]. The function  $H : \mathbb{R}^3 \rightarrow \mathbb{R}$  is defined as  $H(a, b, c) := H_0(a_+, b_+, c_+)$ , where  $a_+ := \max\{a, 0\}$  and where  $H_0$  is defined by (6.12). This discretization is monotone since, as can easily be checked,  $H$  is a non-decreasing function of its arguments. Furthermore, if  $u : \mathbb{E}_2 \rightarrow \mathbb{R}$  is sufficiently smooth, and if the grid scale  $h$  is sufficiently small, then

$$\Lambda u(\mathbf{x}) \approx \det^+(\nabla^2 u(\mathbf{x})), \quad (6.15)$$

where  $\det^+(D) := \det(D)$  if  $D \in S^+(\mathbb{E}_d^*)$ , and  $\det^+(D) := 0$  otherwise.

Interestingly, the MA-LBR numerical scheme was not discovered in this systematic way, but was instead related to numerical approaches based on Pogorelov solutions of Monge-Ampere equations and on the computation of convex envelopes [OP89, AHA98, Mer11]. Indeed, each member of the infimum (6.14) can be interpreted as the subgradient measure  $|\partial u(\mathbf{x})|$  of a symmetrized interpolation of  $u$  on the local stencil  $\{\mathbf{x}, \mathbf{x} \pm \mathbf{e}, \mathbf{x} \pm \mathbf{f}, \mathbf{x} \pm \mathbf{g}\}$ , see Remark 1.8 in [BCM16].

Numerically, one can choose a finite collection  $\mathfrak{B}$  of superbases, and implements the operator  $\Lambda_{\mathfrak{B}}$  defined by restricting the minimum (6.14) to elements of  $\mathfrak{B}$ . This discretization is consistent in the following sense: for any compact set  $K \subseteq S^{++}(\mathbb{E}_d)$ , there exists a finite family  $\mathfrak{B}$  of superbases, such that *equality* holds in (6.15) for any quadratic function  $u(\mathbf{x}) = \frac{1}{2}\langle \mathbf{x}, M\mathbf{x} \rangle$ , where  $M \in K$ , see [BCM16]. The practical choice of the set  $\mathfrak{B}$  of superbases may be guided by a-priori estimates on the regularity of the addressed Monge-Ampere PDE.

A significant part of the publication [BCM16] is devoted to the design and proof of correctness of an adaptive strategy for the evaluation of the operator (6.14, right) associated to the infinite set of superbases - excluding only those for which the stencil support  $\{\mathbf{x} \pm h\mathbf{e}, \mathbf{x} \pm h\mathbf{f}, \mathbf{x} \pm h\mathbf{g}\}$  goes outside of the discretization domain. The algorithm is extremely cheap in practice, since it is able to a-priori discard all superbases except a few. It requires the assumption  $\Lambda U(\mathbf{x}) > 0$  (a property akin to discrete convexity), and is based on a hierarchical exploration of the Stern-Brocot tree structure, with a suitable termination criterion. We choose not to present the details of this approach here, and refer instead to the original publication [BCM16] and to §7 where ideas of similar nature are exposed.

A discretization of the three dimensional Monge-Ampere operator is proposed in [Mir15b], based on the sub-gradient interpretation of (6.14) rather than the general approach presented in §6.1. The global convergence of a damped Newton algorithm for

solving the discretized system of equations is proved in this context, see also [KMT16]. This is an interesting development since previous theoretical guarantees for numerical solvers of discretized Monge-Ampere equations were limited to much solver algorithms, based on e.g. coordinate wise increment [OP89], which are never used in practice. Finally, let us mention that the MA-LBR scheme was originally implemented with Dirichlet boundary conditions [BCM16], but that its adaptation to optimal transport type boundary conditions seems possible and is under investigation by Benamou and Duval.

# Chapter 7

## The constraint of convexity

### Contents

---

7.1	Discrete analogues of convexity. . . . .	114
7.2	Convexity constraints on the cartesian grid. . . . .	116
7.3	Hierarchical cones of discrete convex functions . . . . .	119
7.4	Cardinality of the minimal stencils . . . . .	121

---

This chapter is devoted to a numerical method for optimization problems posed on the set of convex functions, originally presented in [Mir16a]. Since the seminal work [CLM06], which established that the most natural discretization of the constraint of convexity is not consistent, a surprisingly diverse variety of strategies have been developed to address it [CLRM01, AM08, AM09, EMB10, Obe13, MO14, Wac17, Mir16a]. A first specificity of our approach is its *adaptive nature*: it is based on adaptive stencils, refined until a sufficient angular resolution is obtained in the directions along which the solution Hessian degenerates. Some may find it reminiscent of Adaptive Finite Element Methods [MN06], which increase the mesh spatial resolution around the solution singularities. A second specificity is that we require the discretization set to be a cartesian grid, and heavily rely on the Stern-Brocot tree structure to define our discretization and the refinement strategy. This structure is also used in §2.2 and [Mir14b, BCM16]. Our main result is an average case estimate of the behavior of our numerical scheme, under random orientations of the grid, see Theorem 7.4.2. This chapter is adapted rather directly<sup>1</sup> from the introduction of [Mir16a], because its subject is in large part independent from the other parts of the dissertation.

A number of mathematical problems can be formulated as the optimization of a convex functional over the *cone of convex functions* on a domain  $\Omega$ :

$$\text{Conv}(\Omega) := \{u : \Omega \rightarrow \mathbb{R}; u \text{ is convex}\}.$$

This includes optimal transport, as well as various geometrical conjectures such as Newton’s problem of the body of least resistance [LRO05, MO14, Wac14], Meissner’s problem on bodies of constant width [KW11], ... . We choose for concreteness to emphasize an

---

<sup>1</sup>The other chapters of this dissertation were in contrast entirely written from scratch.

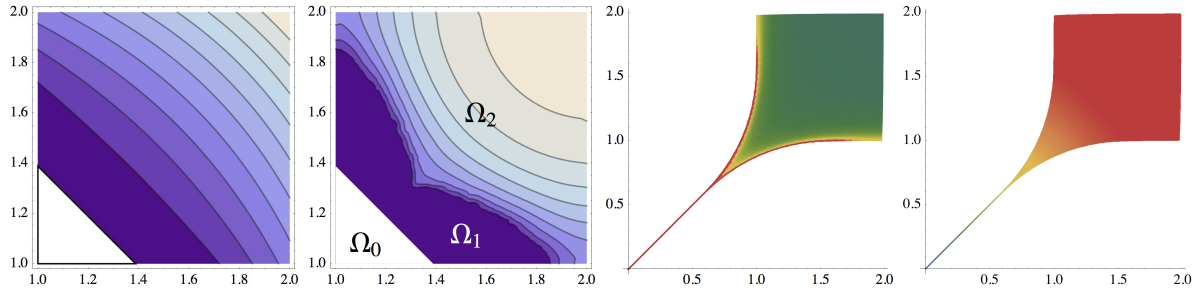


Figure 7.1 – Numerical approximation  $U$  of the solution of the classical Monopolist’s problem (7.1), computed on a  $50 \times 50$  grid. Left: level sets of  $U$ , with  $U = 0$  in white. Center left: level sets of  $\det(\nabla^2 U)$  (with again  $U = 0$  in white); note the degenerate region  $\Omega_1$  where  $\det(\nabla^2 U) = 0$  but  $U$  is non-constant. Center right: distribution of products sold by the monopolist. Right: profit margin of the monopolist for each type of product (margins are low on the one dimensional part of the product line, at the bottom left). Color scales on Figure 7.2.

economic application: the Monopolist (or Principal Agent) problem [RC98], in which the objective is to design an optimal product line, and an optimal pricing catalog, so as to maximize profit in a captive market. The following minimal instance is numerically studied in [AM08, EMB10, Obe13]. With  $\Omega = [1, 2]^2$

$$\min \{ \mathcal{E}(u); u \in \text{Conv}(\Omega), u \geq 0 \}, \quad \mathcal{E}(u) := \int_{\Omega} \left( \frac{1}{2} \|\nabla u(\mathbf{z})\|^2 - \langle \nabla u(\mathbf{z}), \mathbf{z} \rangle + u(\mathbf{z}) \right) d\mathbf{z} \quad (7.1)$$

We refer to [RC98] for the economic model details; let us only say here that the Monopolist’s optimal product line is  $\{\nabla U(z); z \in \Omega\}$ , and that the optimal prices are given by the Legendre-Fenchel dual of  $U$ . Denote by  $\nabla^2 U$  the Hessian of  $U$ , and consider the following three regions: for any  $k \in \{0, 1, 2\}$  (implicitly excluding points  $z \in \Omega$  at which  $U$  is not smooth)

$$\Omega_k := \{z \in \Omega; \text{Rank}(\nabla^2 u(z)) = k\}. \quad (7.2)$$

Strong empirical evidence suggests that these three regions have a non-empty interior, see Figure 7.1 (II), although no qualitative mathematical theory has yet been developed for these problems. The optimal product line observed numerically, see Figure 7.1 (III and IV), confirms a qualitative (and conjectural) prediction of the economic model [RC98] called “bunching”: low-end products are less diverse than high-end ones, down to the topological sense. The monopolist willingly limits the variety of cheap products, because they may compete with the more expensive ones, on which he has a higher margin.

## 7.1 Discrete analogues of convexity.

We propose an adaptive numerical scheme for the problem (7.1), on a two dimensional convex domain  $\Omega \subseteq \mathbb{R}^2$ , discretized on a cartesian grid. For that purpose, following [CLRM01], we consider restrictions of convex functions to a finite set of points, referred

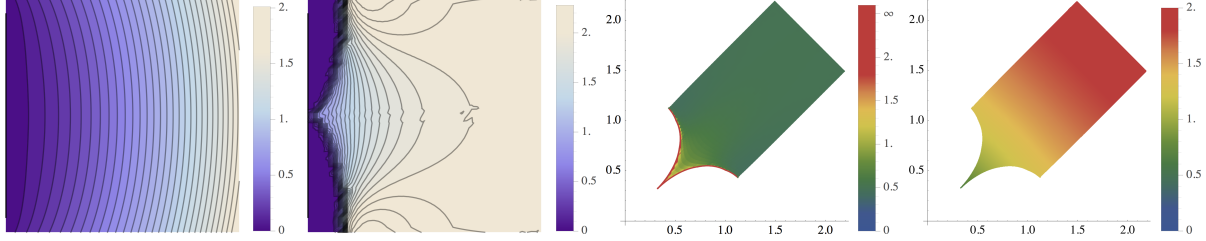


Figure 7.2 – Similar to Figure 7.1, but the domain  $[1, 2]^2$  is rotated by  $\pi/4$  around its center. See Figure 10 in [Mir16a] for more examples.

to as *discrete convex functions*<sup>2</sup>. We also consider piecewise linear convex functions on a triangulation  $\mathcal{T}$  of  $X$ , and denote by  $I_{\mathcal{T}}$  the interpolation operator. Their collections are denoted

$$\begin{aligned} \text{Conv}(X) &:= \{u : X \rightarrow \mathbb{R}; \exists \hat{u} \in \text{Conv}(\Omega), u = \hat{u}|_X\}, \\ \text{Conv}(\mathcal{T}) &:= \{u : X \rightarrow \mathbb{R}; I_{\mathcal{T}} u \in \text{Conv}(\Omega)\}. \end{aligned}$$

Let  $(\mathcal{T}_h)_{h>0}$  be a family of well shaped triangulations of  $\Omega$  of scale  $h > 0$ , and denote by  $X_h$  the collection of their vertices. Maury et al [CLRM01] showed that the solutions of the discretized problems

$$\min\{\mathcal{E}(I_{\mathcal{T}_h} u); u \in \text{Conv}(X_h)\} \quad (7.3)$$

converge uniformly as  $h \rightarrow 0$  to the solution of the continuous problem (7.1), see also the appendix of [Mir16a]. It is known, in contrast and quite surprisingly, that replacing  $\text{Conv}(X_h)$  with  $\text{Conv}(\mathcal{T}_h)$  in (7.3) yields a *non-convergent* discretization [CLM06].

We choose, similarly to [CLRM01], to numerically solve the optimization problem (7.3). For that purpose we enumerate the linear constraints characterizing  $\text{Conv}(X)$  when  $X$  is a cartesian grid, correcting an error of [CLRM01]. It turns out that their number is quadratic  $\mathcal{O}(N^2)$  w.r.t. the number of unknowns  $N := \#(X)$ . We thus propose an adaptive strategy to select only the active constraints, without even enumerating them all. Our approach is based on a hierarchical family of sub- and super-cones of  $\text{Conv}(X)$ , and by Theorem 7.4.2 below only  $\mathcal{O}(N \ln N)$  constraints need to be considered in average.

Before entering the details of our approach, we need to mention alternative strategies for discretizing the constraint of convexity.

- (Global constraint methods) The functional of interest, suitably discretized, is minimized over the cone  $\text{Conv}(X)$  of discrete convex functions [CLRM01], or alternatively [EMB10] on the augmented cone

$$\text{GradConv}(X) := \{(U|_X, \nabla U|_X); U \in \text{Conv}(\Omega)\}, \quad (7.4)$$

in which we refer by  $\nabla U$  to arbitrary elements of the subgradient of the convex map  $U$ .

Both  $\text{Conv}(X)$  and  $\text{GradConv}(X)$  are characterized by a family of long range linear inequalities, with domain wide supports, and of *quadratic*  $\mathcal{O}(N^2)$  cardinality, see

<sup>2</sup>Contrary to [FT07], we do not require our discrete convex functions to take integer values.

§7.2 and [EMB10]. Despite rather general convergence results, these two methods are limited by their expensive numerical cost, in terms of both computation time and memory.

- (Local constraints methods) Another cone  $\text{Conv}'(X)$  is introduced, usually satisfying neither  $\text{Conv}(X) \subseteq \text{Conv}'(X)$  nor  $\text{Conv}'(X) \subseteq \text{Conv}(X)$ , but typically characterized by relatively few constraints, with short range supports. Oberman et al. [OF11, Obe13] use  $\mathcal{O}(N)$  linear constraints. Merigot et al. [MO14] use slightly more linear constraints, but provide an efficient optimization algorithm based on proximal operators. Aguilera et al. [AM08, AM09] consider  $\mathcal{O}(N)$  constraints of semi-definite type.

The methods [AM08, AM09, MO14] benefit from convergence guarantees as  $N \rightarrow \infty$ . Those tested numerically [AM08, OF11, Obe13], however show a lesser accuracy, for a given grid scale, than methods based on global constraints, see the numerical experiments in [Mir16a].

Recently interior approximations using convex  $\mathbb{P}_2$  finite elements have been considered [Wac17]. This method requires the domain to be triangulated using a Delaunay mesh obeying a quantitative non-degeneracy property [BDG13]. While this approach is appealing from the theoretical standpoint, the numerical experiments resented in [Wac17] are somewhat puzzling: for instance, using adaptive meshes unexplicably degrades the solution accuracy, and the use of a Taylor made constrained optimization solver seems required for the method to work at its best.

- (Geometric methods) A polygonal convex set can be described as the convex hull of a finite set of points, or as an intersection of half-spaces. Geometric methods approximate a convex function  $U$  by representing its epigraph  $\{(z, t); z \in \Omega, t \geq U(z)\}$  under one of these forms. Energy minimization is done by adjusting the points position, or the coefficients of the affine forms defining the half-spaces, see [Wac14, LRO05].

Merigot and the author also considered implementing convexity by enforcing, through a logarithmic penalization term, the subgradient measures  $(|\partial_x u|)_{x \in X}$  to remain strictly positive, where  $u : X \rightarrow \mathbb{R}$ . Some (unpublished) results of these experiments are presented on Figures 7.3 and 7.4.

## 7.2 Convexity constraints on the cartesian grid.

In this paragraph, we describe the minimal collection of linear constraints characterizing the polytope  $\text{Conv}(X)$ , when  $X$  is a cartesian grid. The results presented here are proved in [Mir16a]. Given a compact and convex domain  $\Omega \subseteq \mathbb{R}^2$ , denote  $X$  the grid of integer points, by  $X_h$  the grid of scale  $h$ , and by  $X_h^{\theta, \xi}$  the scaled, rotated and offsetted grid defined as follows

$$X := \Omega \cap \mathbb{Z}^2, \quad X_h := \Omega \cap h\mathbb{Z}^2, \quad X_h^{\theta, \xi} := \Omega \cap hR_\theta(\xi + \mathbb{Z}^2).$$

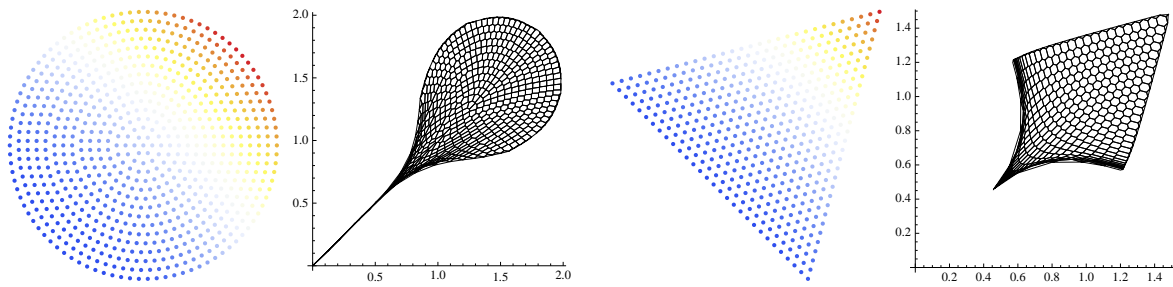


Figure 7.3 – Numerical experiments based on a distinct, geometrical method, with Q. Merigot. Solution to the principal agent problem, color coded, on a disk (I) or a triangular (III) domain, instead of a square as in Figure 7.1. Corresponding product line (II and IV), which is the gradient of the solution.

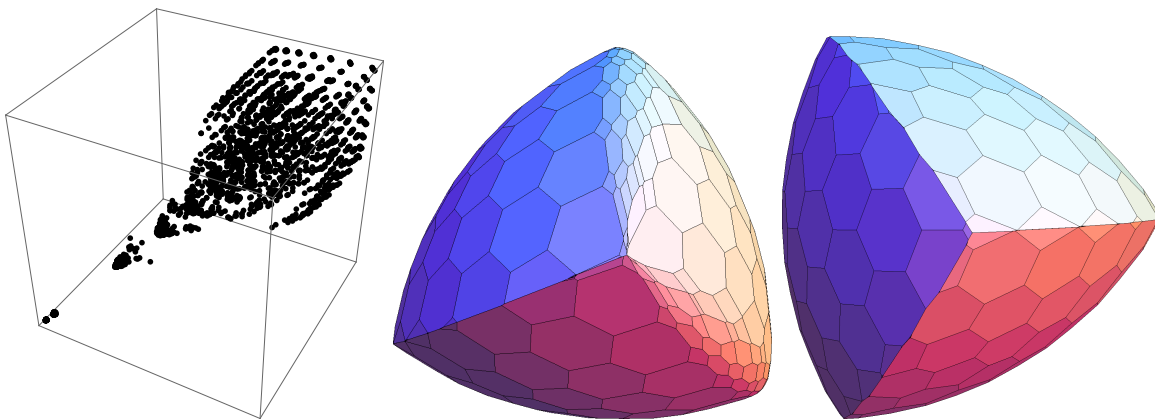


Figure 7.4 – Numerical experiments based on a distinct, geometrical method, with Q. Merigot. (I) Product line (gradient of the solution) for the principal agent problem posed on the three dimensional domain  $[1, 2]^3$ . (II and III) Numerical solutions to Meissner's problem [KW11]. The optimal shapes are conjectured to be tetrahedron-like bodies with some rounded and some angular edges.

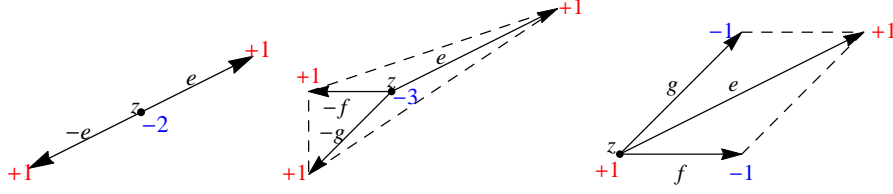


Figure 7.5 – The supports, and weights, of the different linear forms  $S_x^e$ ,  $T_x^e$ ,  $P_x^e$ .

In order to describe our results, we need to introduce an arithmetic structure related to the Stern-Brocot tree<sup>3</sup>, see §A.1.3 and [Bro62].

**Definition 7.2.1.** A basis  $(\mathbf{f}, \mathbf{g})$  of  $\mathbb{Z}^2$  is said *direct* iff  $\det(\mathbf{f}, \mathbf{g}) = 1$ , and *acute* iff  $\langle \mathbf{f}, \mathbf{g} \rangle \geq 0$ . A vector  $\mathbf{e} \in \mathbb{Z}^2$  is said *irreducible* iff its coordinates are co-prime.

**Proposition 7.2.2.** The map  $(\mathbf{f}, \mathbf{g}) \mapsto \mathbf{e} := \mathbf{f} + \mathbf{g}$  defines a bijection between direct acute bases  $(\mathbf{f}, \mathbf{g})$  of  $\mathbb{Z}^2$ , and irreducible elements  $\mathbf{e} \in \mathbb{Z}^2$  such that  $\|\mathbf{e}\| > 1$ . The elements  $\mathbf{f}, \mathbf{g}$  are called the *parents* of  $\mathbf{e}$ . (Unit vectors have no parents.)

We next introduce a family of linear constraints, illustrated in Figure 7.5, and applicable to functions defined on the grid  $\mathbb{Z}^2$ . The geometrical shape of their support is emphasized, since it plays an important role in our approach, see Figure 7.7.

**Definition 7.2.3.** For each  $\mathbf{x} \in \mathbb{Z}^2$  and  $u \in \mathbb{Z}^2 \rightarrow \mathbb{R}$  define

1. (Segments) For any irreducible  $\mathbf{e} \in \mathbb{Z}^2$ :

$$S_{\mathbf{x}}^{\mathbf{e}}(u) := u(\mathbf{x} + \mathbf{e}) - 2u(\mathbf{x}) + u(\mathbf{x} - \mathbf{e}).$$

2. (Triangles) For any irreducible  $\mathbf{e} \in \mathbb{Z}^2$ , with  $\|\mathbf{e}\| > 1$ , of parents  $\mathbf{f}, \mathbf{g}$ :

$$T_{\mathbf{x}}^{\mathbf{e}}(u) := u(\mathbf{x} + \mathbf{e}) + u(\mathbf{x} - \mathbf{f}) + u(\mathbf{x} - \mathbf{g}) - 3u(\mathbf{x}).$$

3. (Parallelograms) For any irreducible  $\mathbf{e} \in \mathbb{Z}^2$ , with  $\|\mathbf{e}\| > 1$ , of parents  $\mathbf{f}, \mathbf{g}$ :

$$P_{\mathbf{x}}^{\mathbf{e}}(u) := u(\mathbf{x} + \mathbf{e}) - u(\mathbf{x} + \mathbf{f}) - u(\mathbf{x} + \mathbf{g}) + u(\mathbf{x}).$$

A linear form  $L$  among the above can be regarded as a finite weighted sum of Dirac masses. In this sense we define the support  $\text{supp}(L) \subseteq \mathbb{Z}^2$ ,  $\#\text{supp}(L) \in \{3, 4\}$ . The linear form  $L$  is also applicable to any  $u : X \rightarrow \mathbb{R}$  such that  $\text{supp}(L) \subseteq X$ .

Correcting a result of [CLRM01], we obtain a minimal characterization of  $\text{Conv}(X)$  by linear inequalities. As announced, there are  $\mathcal{O}(N^2)$  such constraints, where  $N = \#(X)$ . This is because the irreducible vectors involved in their definition are not rare. In fact, they have positive density in  $\mathbb{Z}^2$

$$\frac{6}{\pi^2} = \lim_{n \rightarrow \infty} n^{-2} \# \{(i, j) \in \{1, \dots, n\}^2; \gcd(i, j) = 1\}.$$

This large number of constraints, quadratic in the number of unknowns, motivates the introduction of sub-cones of  $\text{Conv}(X)$  in the next section.

<sup>3</sup>In order to match the classical description [Niq07], associate to each irreducible vector  $\mathbf{e} = (\alpha, \beta) \in \mathbb{Z}_+^2$  the ratio  $\alpha/\beta \in \mathbb{Q}$ . In order to match the description of Proposition A.1.11, associate to  $\mathbf{e}$  the pair  $(\mathbf{f}, \mathbf{g})$  of its parents, see Proposition 7.2.2.

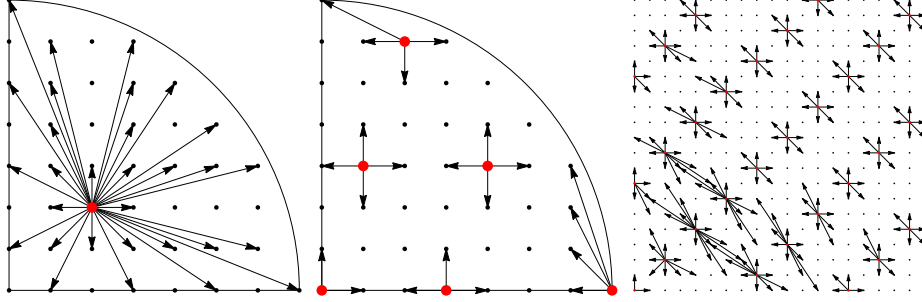


Figure 7.6 – Left: a maximal stencil at a point of a domain. Center: some minimal stencils. Right: some adaptively generated stencils used in the numerical resolution of (7.1).

**Theorem 7.2.4.** *The cone  $\text{Conv}(X)$ , where  $X := \Omega \cap \mathbb{Z}^2$ , is a convex polytope. Elements  $u \in \text{Conv}(X)$  are characterized by the following minimal<sup>4</sup> set of linear inequalities:  $S_{\mathbf{x}}^{\mathbf{e}}u \geq 0$  and  $T_{\mathbf{x}}^{\mathbf{e}}u \geq 0$  whenever these are supported on  $X$ , where  $\mathbf{x}, \mathbf{e} \in \mathbb{Z}^2$  are as in Definition 7.2.3.*

### 7.3 Hierarchical cones of discrete convex functions

We introduce in this section the notion of stencils  $\mathcal{V} = (\mathcal{V}(\mathbf{x}))_{\mathbf{x} \in X}$  on  $X$ , and discuss the properties (hierarchy, complexity) of cones  $\text{Conv}(\mathcal{V})$  attached to them. The following family  $\mathcal{V}_{\max}$  of sets is referred to as the “maximal stencils”: for all  $\mathbf{x} \in X$

$$\mathcal{V}_{\max}(\mathbf{x}) := \{\mathbf{e} \in \mathbb{Z}^2 \text{ irreducible}; \mathbf{x} + \mathbf{e} \in X\}. \quad (7.5)$$

The convex cone generated by a subset  $A$  of a vector space is denoted by  $\text{Cone}(A)$ , with the convention  $\text{Cone}(\emptyset) = \{0\}$ .

**Definition 7.3.1.** *A family  $\mathcal{V}$  of stencils on  $X$  (or just: “Stencils on  $X$ ”) is the data, for each  $\mathbf{x} \in X$  of a collection  $\mathcal{V}(\mathbf{x}) \subseteq \mathcal{V}_{\max}(\mathbf{x})$  (the stencil at  $\mathbf{x}$ ) of irreducible elements of  $\mathbb{Z}^2$ , satisfying the following properties:*

- (Stability) Any parent  $\mathbf{f} \in \mathcal{V}_{\max}(\mathbf{x})$ , of any  $\mathbf{e} \in \mathcal{V}(\mathbf{x})$ , satisfies  $\mathbf{f} \in \mathcal{V}(\mathbf{x})$ .
- (Visibility) One has  $\text{Cone}(\mathcal{V}(\mathbf{x})) = \text{Cone}(\mathcal{V}_{\max}(\mathbf{x}))$ .

The set of candidates for refinement  $\hat{\mathcal{V}}(\mathbf{x})$  consists of all elements  $\mathbf{e} \in \mathcal{V}_{\max}(\mathbf{x}) \setminus \mathcal{V}(\mathbf{x})$  which two parents  $\mathbf{f}, \mathbf{g}$  belong to  $\mathcal{V}(\mathbf{x})$ .

In other words, a stencil  $\mathcal{V}(\mathbf{x})$  at a point  $\mathbf{x} \in X$  contains the parents of its members whenever possible (Stability), and covers all possible directions (Visibility). By construction, these properties are still satisfied by the *refined stencil*  $\mathcal{V}(\mathbf{x}) \cup \{\mathbf{e}\}$ , for any candidate for refinement  $\mathbf{e} \in \hat{\mathcal{V}}(\mathbf{x})$ .

<sup>4</sup>Up to the duplicate constraints  $S_{\mathbf{x}}^{\mathbf{e}} = S_{\mathbf{x}}^{-\mathbf{e}}$ .

**Definition 7.3.2.** *To each family  $\mathcal{V}$  of stencils on  $X$  we associate a cone  $\text{Conv}(\mathcal{V}) \subseteq \mathcal{F}(X)$ , characterized by the non-negativity of the following linear forms: for all  $\mathbf{x} \in X$*

1.  $S_{\mathbf{x}}^{\mathbf{e}}$ , for all  $\mathbf{e} \in \mathcal{V}(\mathbf{x})$  such that  $\text{supp}(S_{\mathbf{x}}^{\mathbf{e}}) \subseteq X$ .
2.  $T_{\mathbf{x}}^{\mathbf{e}}$  for all  $\mathbf{e} \in \mathcal{V}(\mathbf{x})$ , with  $\|\mathbf{e}\| > 1$ , such that  $\text{supp}(T_{\mathbf{x}}^{\mathbf{e}}) \subseteq X$ .
3.  $P_{\mathbf{x}}^{\mathbf{e}}$  for all  $\mathbf{e} \in \hat{\mathcal{V}}(\mathbf{x})$  (by construction  $\text{supp}(P_{\mathbf{x}}^{\mathbf{e}}) \subseteq X$ ).

When discussing unions, intersections, and cardinalities, we (abusively) identify a family  $\mathcal{V}$  of stencils on  $X$  with a subset of  $X \times \mathbb{Z}^2$ :

$$\mathcal{V} \approx \{(\mathbf{x}, \mathbf{e}); \mathbf{x} \in X, \mathbf{e} \in \mathcal{V}(\mathbf{x})\}. \quad (7.6)$$

Note that the cone  $\text{Conv}(\mathcal{V})$  is defined by at most  $3\#\mathcal{V}$  linear inequalities. The sets  $\mathcal{V}_{\max}$  are clearly stencils on  $X$ , which are maximal for inclusion, and by Theorem 7.2.4 we have  $\text{Conv}(\mathcal{V}_{\max}) = \text{Conv}(X)$ . The cone  $\text{Conv}(\mathcal{V})$  always contains the quadratic function  $q(\mathbf{x}) := \frac{1}{2}\|\mathbf{x}\|^2$ , for any family  $\mathcal{V}$  of stencils. Indeed, the inequalities  $S_{\mathbf{x}}^{\mathbf{e}}(q) \geq 0$ ,  $\mathbf{x} \in X$ ,  $\mathbf{e} \in \mathcal{V}(\mathbf{x})$ , and  $T_{\mathbf{x}}^{\mathbf{e}}(q) \geq 0$ ,  $\|\mathbf{e}\| > 1$ , hold by convexity of  $q$ . In addition for all  $\mathbf{e} \in \hat{\mathcal{V}}(x)$ , of parents  $\mathbf{f}, \mathbf{g}$ , one has

$$P_{\mathbf{x}}^{\mathbf{e}}(q) = \frac{1}{2} (\|\mathbf{x} + \mathbf{f} + \mathbf{g}\|^2 - \|\mathbf{x} + \mathbf{f}\|^2 - \|\mathbf{x} + \mathbf{g}\|^2 + \|\mathbf{x}\|^2) = \langle \mathbf{f}, \mathbf{g} \rangle \geq 0,$$

since the basis  $(\mathbf{f}, \mathbf{g})$  of  $\mathbb{Z}^2$  is acute by definition, see Proposition 7.2.2. There is an elegant relation between cones of convex functions associated to our stencils  $\mathcal{V}$ , and to triangulations  $\mathcal{T}$ , see [Mir16a] for a proof. Whenever  $\text{Conv}(\mathcal{V})$  has non-empty interior,

$$\text{Conv}(\mathcal{V}) = \bigcup_{\mathcal{T} \subseteq \mathcal{V}} \text{Conv}(\mathcal{T}). \quad (7.7)$$

where the inclusion  $\mathcal{T} \subseteq \mathcal{V}$  is meant in the sense of graphs, i.e. any edge  $[\mathbf{x}, \mathbf{x} + \mathbf{e}]$  of  $\mathcal{T}$  satisfies  $\mathbf{e} \in \mathcal{V}(\mathbf{x})$ . Stencils can thus be regarded as a relaxation of triangulations. In light of (7.7), the following result is not surprising.

**Theorem 7.3.3** (Hierarchy). *The union  $\mathcal{V} \cup \mathcal{V}'$ , and the intersection  $\mathcal{V} \cap \mathcal{V}'$  of two families  $\mathcal{V}, \mathcal{V}'$  of stencils are also families of stencils on  $X$ . In addition*

$$\text{Conv}(\mathcal{V}) \cap \text{Conv}(\mathcal{V}') = \text{Conv}(\mathcal{V} \cap \mathcal{V}'), \quad (7.8)$$

$$\text{Conv}(\mathcal{V}) \cup \text{Conv}(\mathcal{V}') \subseteq \text{Conv}(\mathcal{V} \cup \mathcal{V}'). \quad (7.9)$$

As a result, if two families of stencils  $\mathcal{V}, \mathcal{V}'$  satisfy  $\mathcal{V} \subseteq \mathcal{V}'$ , then

$$\text{Conv}(\mathcal{V}) \subseteq \text{Conv}(\mathcal{V}') \subseteq \text{Conv}(X).$$

The left inclusion follows from (7.8), and the right inclusion from (7.9) applied to  $\mathcal{V}'$  and  $\mathcal{V}_{\max}$ . The intersection rule (7.8) also implies the existence of stencils  $\mathcal{V}_{\min}$  minimal for inclusion, which are illustrated on Figure 7.6. Elements of proof of Theorem 7.3.3 are illustrated on Figure 7.7.

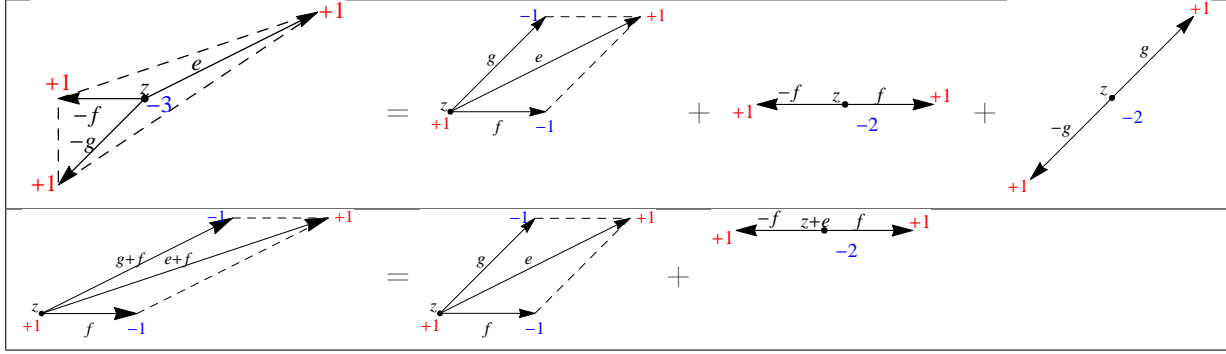


Figure 7.7 – The linear forms  $S_z^e$ ,  $T_z^e$  and  $P_z^e$  can be regarded as weighted sums of Diracs, located at grid points. The hierarchical properties presented in Theorem 7.3.3 follow from the ability to build long range constraints by combining together several short range constraints, as illustrated in the above figure.

**Remark 7.3.4** (Optimization strategy). *For any  $u \in \text{Conv}(X)$ , there exists by (7.8) a unique smallest (for inclusion) family of stencils  $\mathcal{V}$  such that  $u \in \text{Conv}(\mathcal{V})$ . If  $u$  is the minimizer of an energy  $\mathcal{E}$  on  $\text{Conv}(X)$ , then it can be recovered by minimizing  $\mathcal{E}$  on the smaller cone  $\text{Conv}(\mathcal{V})$ , defined by  $\mathcal{O}(\#\mathcal{V})$  linear constraints. Algorithms presented in [Mir16a], attempt to find these smallest stencils  $\mathcal{V}$  (or slightly larger ones), starting from  $\mathcal{V}_{\min}$  and successively incorporating refinement candidates.*

## 7.4 Cardinality of the minimal stencils

In this last section, we fix a grid scale  $h > 0$  and consider for all  $\theta \in \mathbb{R}$ , and all  $\xi \in \mathbb{R}^2$ , the grid

$$X_\theta^\xi := \Omega \cap hR_\theta(\xi + \mathbb{Z}^2). \quad (7.10)$$

The notions of stencils and of the related cones trivially extend to this setting. We denote by  $|\Omega|$  the domain area, and by  $\text{diam}(\Omega) := \max\{\|y - x\|; x, y \in \Omega\}$  its diameter. We also introduce rescaled variants, defined for  $h > 0$  by

$$|\Omega|_h := h^{-2}|\Omega|, \quad \text{diam}_h(\Omega) := h^{-1} \text{diam}(\Omega).$$

For any parameters  $\theta, \xi$ , one has denoting  $N := \#(X_\theta^\xi)$  (with underlying constants depending only on the shape of  $\Omega$ )

$$|\Omega|_h \approx N, \quad \text{diam}_h(\Omega) \approx \sqrt{N}. \quad (7.11)$$

**Proposition 7.4.1.** *Let  $X := X_\theta^\xi$ , for some grid position parameters  $\theta \in \mathbb{R}$ ,  $\xi \in \mathbb{R}^2$ , and let  $N := \#(X)$ . Let  $u \in \text{Conv}(X)$ , and let  $\mathcal{V}$  be the minimal stencils on  $X$  such that  $u \in \text{Conv}(\mathcal{V})$ . Then  $\#\mathcal{V} \leq CN \text{diam}_h(\Omega)$ , for some universal constant  $C$  (i.e. independent of  $\Omega, h, \theta, \xi, u$ ).*

Combining this result with (7.11) we see that an optimization strategy as described in Remark 7.3.4 should heuristically not require solving optimization problems subject to

more than  $N \text{diam}_h(\Omega) \approx N^{\frac{3}{2}}$  linear constraints. This is already a significant improvement over the  $\approx N^2$  linear constraints defining  $\text{Conv}(X)$ . The typical situation is however even more favorable: in average over randomized grid orientations  $\theta$  and offsets  $\xi$ , the restriction to  $X_\theta^\xi$  of a convex map  $U : \Omega \rightarrow \mathbb{R}$  (e.g. the global continuous solution of the problem (7.1) of interest) belongs to a cone  $\text{Conv}(\mathcal{V}_\theta^\xi)$  defined by a quasi-linear number  $\mathcal{O}(N \ln^2 N)$  of linear inequalities. See [Mir16a] for the proof, which is based on elements of convex analysis, and on the structure of the Stern-Brocot tree.

**Theorem 7.4.2.** *Let  $U \in \text{Conv}(\Omega)$ , and let  $\mathcal{V}_\theta^\xi$  be the minimal stencils on  $X_\theta^\xi$  such that  $U|_{X_\theta^\xi} \in \text{Conv}(\mathcal{V}_\theta^\xi)$ , for all  $\theta \in \mathbb{R}$ ,  $\xi \in \mathbb{R}^2$ . Assuming  $\text{diam}_h(\Omega) \geq 2$ , one has for some universal constant  $C$  (i.e. independent of  $h, \Omega, U$ ):*

$$\int_{[0,1]^2} \int_0^{\pi/2} \#(\mathcal{V}_\theta^\xi) d\theta d\xi \leq C |\Omega|_h (\ln \text{diam}_h(\Omega))^2. \quad (7.12)$$

Finally, we briefly discuss algorithmic geometry concepts known as the edge flipping procedure, and regular/generalized Delaunay triangulations. Consider  $U \in \text{Conv}(\Omega)$ , and a finite point set  $X \subseteq \Omega$ . Generically, there exists a unique triangulation  $\mathcal{T}(U)$  such that the interpolation  $I_{\mathcal{T}(U)} U$  is convex. Such triangulations are referred to as regular triangulations in CGAL $\text{\textcircled{R}}$ , and are at the foundation of the so-called semi-discrete methods for Monge-Ampere equations and optimal transport [OP89, AHA98, Mer11]. They generalize Delaunay triangulations, which corresponds to the special case  $U(\mathbf{x}) := \frac{1}{2} \|\mathbf{x}\|^2$ .

Edge flipping is a local modification of a triangulation, in which the common side of two triangles forming a convex quadrilateral  $Q$  is removed from the triangulation, and replaced with the other diagonal of  $Q$ . For any two triangulations of a common point set, there exists a sequence of edge flips which transforms one into the other, and the minimal length of such a chain is called the edge flipping distance between the triangulations. Edge flipping is a common procedure in mesh generation, used in diverse domains such as fluid dynamics simulations [DF08], or GPU accelerated image vectorization [QCT13]. Little is known however on its complexity from the theoretical standpoint, apart from some conservative worst case estimates [HNU99].

We show in [Mir16a] that the edge flipping distance from the usual Delaunay triangulation of  $X$  to any regular triangulation  $\mathcal{T}(U)$  is at most the stencil cardinality  $\#(\mathcal{V}(U))$ . Proposition 7.4.1 and Theorem 7.4.2 can thus be regarded as respectively a worst case and an average case complexity estimate of mesh generation by edge flipping, in the particular case of regular triangulations and of cartesian grids. The mean estimate  $\mathcal{O}(N \ln^2 N)$ , under rotations and translations of the grid, is the first of its kind for this algorithm. Recall that  $N$  is the discrete domain cardinality, and note that the worst case complexity is  $\mathcal{O}(N^{\frac{3}{2}})$ .

Part III  
Appendix

# Appendix A

## Geometry of lattices

### Contents

---

<b>A.1</b>	<b>Basis reduction methods</b>	<b>125</b>
A.1.1	Minkowski reduction	125
A.1.2	Selling's algorithm	127
A.1.3	The Stern-Brocot tree	128
<b>A.2</b>	<b>Voronoi reductions of quadratic forms</b>	<b>129</b>
A.2.1	Perfect forms and the first reduction	130
A.2.2	Voronoi diagrams and the second reduction	131

---

This appendix is devoted to the description of a series of tools from discrete geometry, which are at the foundation of the numerical schemes presented in this dissertation. More precisely, these tools come from the field of low dimensional lattice geometry, and are described in particular in [Sch09, CS92, NS04]. Two contributions of the author are also presented, see Theorem A.1.5 and Proposition A.2.2.

A lattice is a discrete subgroup of a vector space, which linearly spans the vector space. Up to a linear transformation, the lattice and the vector space can be identified with  $\mathbb{L}_d := \mathbb{Z}^d$  and  $\mathbb{E}_d := \mathbb{R}^d$ . A matrix  $M \in S^{++}(\mathbb{E}_d)$  is fixed throughout this appendix and defines a scalar product  $\langle M \cdot, \cdot \rangle$  and a norm  $\|\cdot\|_M$ . The distortion of this norm w.r.t. the usual euclidean norm on the vector space  $\mathbb{E}_d$  is measured by the condition number  $\text{Cond}(M) := \sqrt{\|M\| \|M^{-1}\|}$ .

The first section §A.1 of this appendix is devoted to the characterization and design of preferred coordinate systems in lattices of low dimension, using a variety of concepts such as Minkowski reduction, Selling's algorithm, and the Stern-Brocot tree. The second section A.2 describes the two Voronoi reductions of quadratic forms, which are maps from the set of positive definite tensors  $S^{++}(\mathbb{E}_d)$  to a suitable discrete set, and are designed to be compatible with the action of the linear group  $\text{GL}(\mathbb{L}_d)$ . All the tools described have substantial applications in several parts of the dissertation, to which pointers are provided.

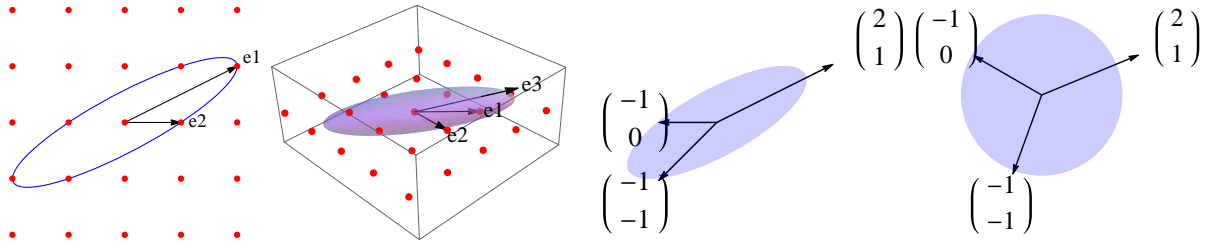


Figure A.1 – Left:  $M$ -Minkowski reduced bases of  $\mathbb{Z}^2$  and  $\mathbb{Z}^3$ , w.r.t. some  $M \in \mathbb{S}^{++}(\mathbb{E}_d)$  whose unit ball is presented. Right:  $M$ -obtuse superbase of  $\mathbb{Z}^2$ , see §A.1.2, before and after change of variables by  $M^{\frac{1}{2}}$ .

## A.1 Basis reduction methods

Lattice basis reduction is study of coordinate systems, in additive lattices within a normed vector space, obeying preferred geometrical properties. Some of the most iconic applications of this field are related to high dimensional lattices and the celebrated LLL algorithm [LLL82]. It has applications in number theory, cryptography, operational research, etc [NV09].

In view of our applications to PDE discretizations, we focus in contrast on low-dimensional basis reduction. Indeed, the dimension  $d$  of the lattice is also the dimension of the PDE domain, which is typically  $d \in \{2, 3\}$  and in the worst case  $d = 5$  for our applications. Cartesian grids are not regarded as adequate for PDE discretizations in higher dimensions, due to the *curse of dimension*.

We discuss Minkowski reduced bases, which are built of small vectors w.r.t. the norm  $\|\cdot\|_M$ , in §A.1.1. Obtuse superbases, and the related algorithm of Selling, are presented in §A.1.2. The Stern-Brocot tree, discussed in §A.1.3, places a hierarchical structure on bases of  $\mathbb{Z}^2$ .

### A.1.1 Minkowski reduction

A basis of a  $d$ -dimensional lattice is a  $d$ -plet of lattice vectors which determinant is non-zero and minimal in absolute value. Formally, and limiting our attention to the integer lattice.

**Definition A.1.1.** A basis of  $\mathbb{L}_d$  is a  $d$ -plet  $(\mathbf{e}_1, \dots, \mathbf{e}_d) \in \mathbb{L}_d^d$  s.t.  $|\det(\mathbf{e}_1, \dots, \mathbf{e}_d)| = 1$ .

Any lattice of dimension  $d \geq 2$  admits countably infinitely many bases. Geometrical problems posed on lattices are usually defined w.r.t. a given norm - for instance computing the shortest non-zero lattice vector, or the closest lattice vector to a given point. In order to solve these, a natural first step is to select a lattice basis which is “reduced” w.r.t. the norm, in the sense that its vectors are small, and/or are close to being orthogonal to each other. Formally, a number of notions of reductions have been introduced, by several authors and over more than a century: Hermite (1850), Minkowski (1896), Hermite-Korkine-Zolotarev (1905), Venkov (1972), Lenstra-Lenstra-Lovász (1982), etc. See [NS04] and references therein. We limit here our attention to Minkowski reduction.

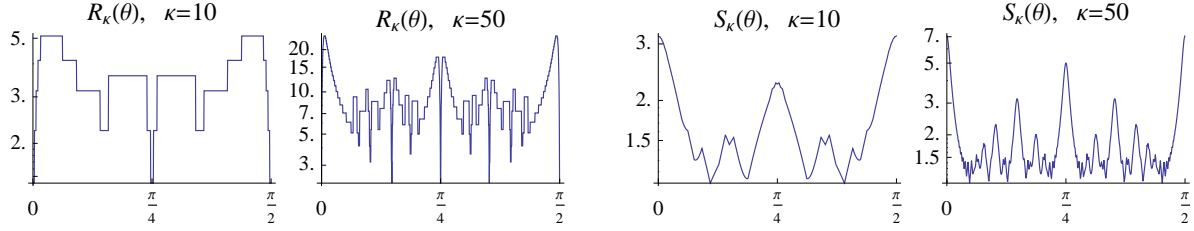


Figure A.2 – Plots of  $R_\kappa(\theta)$  (left) and  $S_\kappa(\theta)$  (right), for  $\kappa \in \{10, 50\}$ , as a function of  $\theta \in [0, \pi/2]$ , see Definition A.1.4. Logarithmic scale.

**Definition A.1.2.** Let  $M \in S^{++}(\mathbb{E}_d)$  be fixed. A basis  $(\mathbf{e}_1, \dots, \mathbf{e}_d)$  of  $\mathbb{L}_d$  is said  $M$ -Minkowski reduced iff the vector  $(\|\mathbf{e}_1\|_M, \dots, \|\mathbf{e}_d\|_M)$  is minimal, among all bases of  $\mathbb{L}_d$ , w.r.t. lexicographic ordering.

For instance, if  $(\mathbf{e}_1, \dots, \mathbf{e}_d)$  is  $M$ -Minkowski reduced, then  $\|\mathbf{e}_1\|_M \leq \dots \leq \|\mathbf{e}_d\|_M$ , and  $\mathbf{e}_1$  is the shortest non-zero vector of  $\mathbb{L}_d$  w.r.t.  $\|\cdot\|_M$ . See also Figure A.1.

Algorithmically, an  $M$ -Minkowski reduced basis can be computed in dimension  $d = 2$  using Lagrange’s algorithm [Lag75], which has logarithmic complexity  $\mathcal{O}(\ln(\text{Cond}(M)))$  and can be regarded as a the transposition to vectors of Euclid’s gcd algorithm. This algorithm is extended in [NS04] to compute Minkowski-reduced bases of three and four dimensional lattices, still with logarithmic complexity. Note that we benefit here from the favorable properties of low-dimensional lattices, since computing even the first vector of a Minkowski-reduced basis (i.e. the shortest lattice non-zero vector), is in contrast a NP-hard problem in high dimensions [Ajt98], to the point that it is used at the foundation of some cryptographic protocols [Pei09].

The author’s contribution has been to determine, in dimension  $d = 2$ , the average radius of  $M$ -Minkowski reduced bases, when  $M$  is a random rotation of a given symmetric positive definite matrix, see Theorem A.1.5 below which is proved in [Mir16b]. Our motivation was to estimate how compact are the stencils used in our PDE schemes, in average, assuming that the preferred directions of the differential operators (encoded for instance in a Riemannian metric) are independent of those of the cartesian grid used for discretization. These results apply to the FM-LBR and the AD-LBR numerical schemes, devoted respectively to Riemannian eikonal PDEs and anisotropic diffusion PDEs, and described in §2.1 and §5 respectively.

**Definition A.1.3.** Let  $M \in S^{++}(\mathbb{E}_d)$ , and let  $(\mathbf{e}_1, \dots, \mathbf{e}_d)$  be an  $M$ -Minkowski reduced basis. We denote  $R(M) := \|\mathbf{e}_1\|_M$  and  $S(M) := \|\mathbf{e}_d\|_M$ .

Let  $\mathbf{n}(\theta) := (\cos \theta, \sin \theta)$ , for any  $\theta \in \mathbb{R}$ , and let  $\mathbf{e}^\perp := (-b, a)$  if  $\mathbf{e} = (a, b) \in \mathbb{E}_2$ .

**Definition A.1.4.** In dimension  $d = 2$  we let  $R_\kappa(\theta)$  and  $S_\kappa(\theta)$ , where  $\kappa \geq 1$  and  $\theta \in \mathbb{R}$  be the quantities of Definition A.1.3 attached to the matrix  $M_\kappa(\theta) \in S^{++}(\mathbb{E}_2)$  defined by

$$M_\kappa(\theta) := \kappa^{-1} \mathbf{n}(\theta) \otimes \mathbf{n}(\theta) + \kappa \mathbf{n}(\theta)^\perp \otimes \mathbf{n}(\theta)^\perp.$$

Our main result, presented below, is illustrated on Figures A.2 and A.3. We write  $A(\kappa) \approx B(\kappa)$  iff the ratio  $A(\kappa)/B(\kappa)$  is bounded independently of  $\kappa$ .

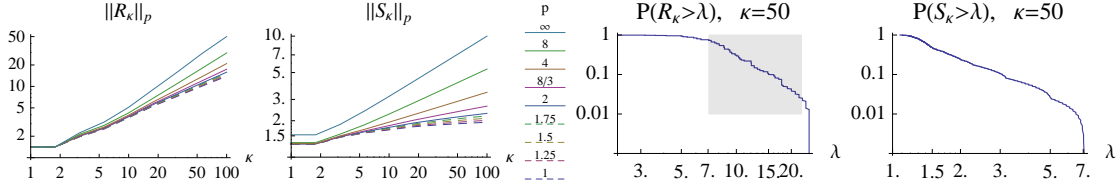


Figure A.3 – Left:  $L^p([0, \pi[)$  norms of  $R_\kappa$  and  $S_\kappa$ , as a function of  $\kappa \in [1, 100]$  for different exponents  $p \in [1, \infty]$ . The behavior for  $p < 2$  (dashed) and  $p > 2$  is significantly different, see Theorem A.1.5. Right: Tail distribution of  $R_\kappa$  and  $S_\kappa$ . Log-log scale.

**Theorem A.1.5.** *For any  $p \in [1, \infty]$  one has uniformly w.r.t.  $\kappa \in [2, \infty[$*

$$\|R_\kappa\|_{L^p} \approx \|S_\kappa\|_{L^p}, \quad \|S_\kappa\|_{L^p} \approx \begin{cases} \kappa^{\frac{1}{2}-\frac{1}{p}} & \text{if } p > 2, \\ (\ln \kappa)^{\frac{1}{2}} & \text{if } p = 2, \\ 1 & \text{if } p < 2, \end{cases}$$

where the  $L^p$  norms are over the interval  $[0, \pi]$ .

## A.1.2 Selling's algorithm

We discuss superbases, which are slightly redundant coordinate systems in a lattice, and Selling's algorithm, used in dimension  $d \leq 3$  to generate superbases obeying preferred geometrical properties. Superbases can be obtained by the adjunction of an initial vector  $\mathbf{e}_0 = -(\mathbf{e}_1 + \dots + \mathbf{e}_d)$  to a basis, see Definition A.1.1.

**Definition A.1.6.** *A superbase of  $\mathbb{L}_d$  is a  $(d+1)$ -plet  $(\mathbf{e}_0, \dots, \mathbf{e}_d) \in \mathbb{L}_d^{d+1}$  such that  $\mathbf{e}_0 + \dots + \mathbf{e}_d = 0$  and  $|\det(\mathbf{e}_1, \dots, \mathbf{e}_d)| = 1$ .*

In contrast with the numerous concepts of reduced basis of a lattice, see the previous subsection, there is a consensus on what a good superbase is [CS92]. See also Figure A.1.

**Definition A.1.7.** *A superbase  $(\mathbf{e}_0, \dots, \mathbf{e}_d)$  of  $\mathbb{L}_d$  is said  $M$ -obtuse iff  $\langle M\mathbf{e}_i, \mathbf{e}_j \rangle \leq 0$  for all  $0 \leq i < j \leq d$ .*

Obtuse superbases have exceptional properties. The fundamental bricks of our discretization schemes, Voronoi's first and second reduction of a matrix  $M$  are easily constructed from an  $M$ -obtuse superbase, see §A.2. For this reason, our numerical codes implementing the FM-LBR, FM-VR1, and AD-LBR schemes for eikonal equations and anisotropic diffusion, see §2.1, §3.1, and §5 respectively, compute as a preliminary step an obtuse superbase with respect to the tensor attached to each pixel. However, for reasons detailed in the next paragraph, this strategy is only appropriate in dimension  $d \leq 3$ .

A lattice equipped with a scalar product, such as  $(\mathbb{L}_d, M)$ , is said of Voronoi's first kind iff there exists an  $M$ -obtuse superbase of  $\mathbb{L}_d$ . This property does systematically hold in dimension  $d \leq 3$ , but fails for some lattices of dimension  $d = 4$  and higher [NS04]. The proof of existence in dimension  $d \leq 3$  is constructive and due to Selling [Sel74], see

also [Mir17b]. It is based on the decrease of the following energy, defined w.r.t. a matrix  $M \in S^{++}(\mathbb{E}_d)$  and attached to any superbase  $b = (\mathbf{e}_0, \dots, \mathbf{e}_d)$

$$\mathcal{E}_M(b) := \frac{1}{2^d} \sum_{I \subseteq \llbracket 0, d \rrbracket} \|\mathbf{e}_I\|_M^2, \quad \text{where } \mathbf{e}_I := \sum_{i \in I} \mathbf{e}_i.$$

**Proposition A.1.8** (Selling’s algorithm). *Let  $M \in S^{++}(\mathbb{E}_d)$ , where  $d \in \{2, 3\}$ , and let  $b = (\mathbf{e}_0, \dots, \mathbf{e}_d)$  be a superbase of  $\mathbb{L}^d$ . Define a second superbase  $b'$  of  $\mathbb{L}_d$  by:*

$$\text{Case } d = 2 : b' := (-\mathbf{e}_0, \mathbf{e}_1, \mathbf{e}_0 - \mathbf{e}_1). \quad \text{Case } d = 3 : b' := (-\mathbf{e}_0, \mathbf{e}_1, \mathbf{e}_0 + \mathbf{e}_2, \mathbf{e}_0 + \mathbf{e}_3).$$

*Then  $\mathcal{E}_M(b) - \mathcal{E}_M(b') = 2^{2-d} \langle \mathbf{e}_0, \mathbf{e}_1 \rangle_M$ . Selling’s algorithm consists in iteratively, and until  $b$  is an  $M$ -obtuse superbase: (a) reordering the superbase  $b$  so that  $\langle \mathbf{e}_0, \mathbf{e}_1 \rangle_M > 0$ , and (b) applying the transformation  $b \leftarrow b'$ .*

*This algorithm terminates, and in particular there exists an  $M$ -obtuse superbase of  $\mathbb{L}_d$ .*

Selling’s algorithm can also be regarded as a specialization of the simplex algorithm to the linear program defining Voronoi’s first reduction, see §A.2.1 and [Mir17b]. It is straightforward to implement, and sufficient for the moderate condition numbers  $\text{Cond}(M)$  encountered in PDE discretizations. Alternatively, in dimension  $d \leq 3$ , an  $M$ -obtuse superbase of  $\mathbb{L}_d$  can be obtained in a single step from an  $M$ -Minkowski reduced basis, see e.g. Proposition 1 in [FM14]. The complexity  $\mathcal{O}(\ln \text{Cond}(M))$  of this second approach makes it preferable in applications involving tensors of huge condition number, such as integer programming.

### A.1.3 The Stern-Brocot tree

A third type of coordinate system is considered in this subsection: *direct* and *acute* bases of the two dimensional lattice  $\mathbb{L}_2$ . We regard them as delimiting *angular sectors* originating from 0, by integral vectors. A refinement procedure allows to split these angular sectors into two (unequal) parts, in a way that is compatible with the underlying grid structure.

This process is appropriate for discretizing two-dimensional anisotropic PDEs on cartesian grids, and was initially proposed for anisotropic diffusion in [BOZ04]. It is also used within the FM-ASR numerical scheme for Finslerian eikonal equations §2.2, and the implementations of the Monge-Ampere operator and of the constraint of convexity §6 and §7.

**Definition A.1.9.** *A basis  $(\mathbf{e}_1, \mathbf{e}_2)$  of  $\mathbb{L}_2$  is said direct iff  $\det(\mathbf{e}_1, \mathbf{e}_2) = 1$ . It is said acute iff  $\langle \mathbf{e}_1, \mathbf{e}_2 \rangle \geq 0$ .*

**Definition A.1.10.** *The children of a direct and acute basis  $(\mathbf{e}_1, \mathbf{e}_2)$  are  $(\mathbf{e}_1, \mathbf{e}_1 + \mathbf{e}_2)$  and  $(\mathbf{e}_1 + \mathbf{e}_2, \mathbf{e}_2)$ . They are also direct and acute bases.*

The Stern-Brocot tree, described in the next proposition, organises direct and acute bases into a hierarchical structure, using the relation of the latest definition.

**Proposition A.1.11.** *Let  $\mathfrak{T}$  be the collection of all direct and acute bases of  $\mathbb{L}_2$ , and let  $\mathfrak{T}_+$  be the subset of those which coordinates are non-negative. Then  $\mathfrak{T}_+$  is a complete infinite binary tree, referred to as the Stern-Brocot tree, whose root is the canonical basis  $(\mathbf{e}_1, \mathbf{e}_2)$  where  $\mathbf{e}_1 = (1, 0)$  and  $\mathbf{e}_2 = (0, 1)$ .*

*In addition  $\mathfrak{T}$  consists of four disconnected infinite binary trees, whose roots are  $(\mathbf{e}_1, \mathbf{e}_2)$ ,  $(\mathbf{e}_2, -\mathbf{e}_1)$ ,  $(-\mathbf{e}_1, -\mathbf{e}_2)$  and  $(-\mathbf{e}_2, \mathbf{e}_1)$  respectively.*

Our description of the Stern-Brocot tree is slightly unorthodox, since it is classically described as a tree of rational numbers [Niq07]. To match this convention one should map each basis  $b = (\mathbf{e}_1, \mathbf{e}_2) = ((a, b), (a', b')) \in \mathfrak{T}_+$  to the rational number  $(a + a')/(b + b')$ . See Figure 1.3.

## A.2 Voronoi reductions of quadratic forms

This section is devoted to the description of Voronoi’s first and second reduction, see §A.2.1 and §A.2.2 respectively. We use these constructions in many of our numerical schemes: the first reduction is used for Riemannian eikonal equations and generalizations (FM-VR1) §3.2, anisotropic diffusion (AD-LBR) §5, and non-linear second order equations (MA-LBR) §6; the second reduction in a semi-Lagrangian scheme for Riemannian eikonal equations (FM-LBR) §2.1. It can be argued however, that we use only by-products of Voronoi’s constructions. The rest of this introduction briefly explains the original intentions of Voronoi, as far as we understand them, and the meaning of the word *reduction*, see §[Sch09] for more details. The impatient reader may directly jump to §A.2.1.

The arithmetic properties of quadratic forms have long fascinated mathematicians: consider for instance Lagrange’s celebrated four squares theorem, which expresses that any integer  $n \geq 0$  can be written under the form  $a^2 + b^2 + c^2 + d^2$ . There are infinitely many distinct quadratic forms, but many of them share the same arithmetic properties. For instance Lagrange proved that any positive quadratic form of determinant 1 with integer coefficients is equivalent to  $(a, b) \mapsto a^2 + b^2$ , up to an invertible linear change of variables with integer coefficients as well, and thus takes the integer values described in Fermat’s two squares theorem.

Lagrange similarly classified the two dimensional positive definite quadratic forms with integer coefficients and determinant below 17, see [Lag75]. For that purpose he relied on Lagrange’s algorithm<sup>1</sup>, which provides an algorithmic method for computing a canonical basis of a two-dimensional lattice, that we now describe as Minkowski-reduced see §A.1.1. This approach could later be extended to dimension up to 4, see [Sem01, NS04] but it does not seem appropriate beyond [Sch09].

Voronoi’s reductions help with this classification effort [Sch09], by providing a canonical way to *reduce* an arbitrary  $M \in S^{++}(\mathbb{E}_d)$  quadratic form to a *fundamental domain*, see Definition A.2.1 below, under the following action of linear changes of coordinates with integer coefficients. For any  $M \in S^{++}(\mathbb{E}_d)$  and any  $A \in GL(\mathbb{L}_d)$

$$A \cdot M := AMA^T. \tag{A.1}$$

---

<sup>1</sup>Often incorrectly called Gauss’s algorithm, see [NS04].

**Definition A.2.1.** Let  $G$  be a group acting on a set  $X$ . Consider the relation on  $X$  defined by  $x \sim x'$  iff there exists  $g \in G$  such that  $x' = g \cdot x$ . A fundamental domain, for the action of  $G$  on  $X$ , is a subset  $A \subseteq X$  containing exactly one element of each equivalence class.

In order to compute such fundamental domains, Voronoi introduces mappings from  $S^{++}(\mathbb{E}_d)$  into some discrete spaces, which are compatible with the action of  $GL(\mathbb{L}_d)$ . These spaces consist of countable families, *perfect forms* or *Delaunay triangulations* defined below, and have a finitely many equivalence classes under the action of  $GL(\mathbb{L}_d)$ . In other words, a suitably chosen finite set defines a fundamental domain for the target space. Taking the pre-image we obtain a (superset of a) fundamental domain for the action of  $GL(\mathbb{L}_d)$  on  $S^{++}(\mathbb{E}_d)$ .

### A.2.1 Perfect forms and the first reduction

Consider the set of quadratic forms with value at least 1 on each non-zero vector with integer coordinates

$$\mathfrak{M} := \{M \in S^{++}(\mathbb{E}_d); \forall \mathbf{e} \in \mathbb{L}_d \setminus \{0\}, \|\mathbf{e}\|_M \geq 1\}.$$

Observing that  $\|\mathbf{e}\|_M^2 = \langle M\mathbf{e}, \mathbf{e} \rangle = \text{Tr}(M\mathbf{e} \otimes \mathbf{e})$  is a linear function of  $M$ , and that the positive-definiteness constraint is redundant, we obtain that  $\mathfrak{M}$  is a polytope of the  $d(d+1)/2$ -dimensional space  $S^{++}(\mathbb{E}_d)$ . Voronoi calls *perfect forms* the vertices of  $\mathfrak{M}$ , and proves that there are only finitely many distinct classes of perfect forms under the action of  $GL(\mathbb{E}_d)$ . The exact number of equivalence classes is 1, 1, 2, 3, 7, 33, 10916 in dimension two to eight, where the known classification ends [Sch09]. Voronoi associates to each  $D \in S^{++}(\mathbb{E}_d)$  a perfect form defined as the minimizer to the linear program

$$\min_{M \in \mathfrak{M}} \text{Tr}(MD). \tag{A.2}$$

This optimization problem is well posed in the sense that it has a compact set of minimizers, which is generically a single vertex of  $\mathfrak{M}$ , hence a perfect form [Sch09]. Denoting this minimizer by  $\text{VR}(D)$ , one easily checks compatibility with the group action:  $\text{VR}(A \cdot D) = (A^{-1})^T \cdot \text{VR}(D)$ , for any  $A \in GL(\mathbb{L}_d)$ , using the notation (A.1). See Figure A.4 for a partition of the collection of two-dimensional positive definite quadratic forms according to VR. Interestingly, Voronoi's first reduction (A.2) is one of the first non-trivial linear programs ever studied [Vor08], in arbitrary dimension and with infinitely many constraints. In particular, it precedes by three decades Kantorovich's linear relaxation of the optimal transport problem [Kan42].

The Karush-Kuhn-Tucker conditions for the linear program (A.2) state that the objective function  $M \mapsto \text{Tr}(MD)$  is a non-negatively weighted linear combination of the active constraints  $M \mapsto \text{Tr}(M\mathbf{e} \otimes \mathbf{e})$ . Hence there exists weights and offsets  $(\rho_i, \mathbf{e}_i)_{i=1}^{d'} \in (\mathbb{R}_+ \times \mathbb{L}_d)^{d'}$ , obeying  $\|\mathbf{e}_i\|_M = 1$  and where  $d' = \dim(S(\mathbb{E}_d)) = d(d+1)/2$ , such that

$$D = \sum_{1 \leq i \leq d'} \rho_i \mathbf{e}_i \otimes \mathbf{e}_i,$$

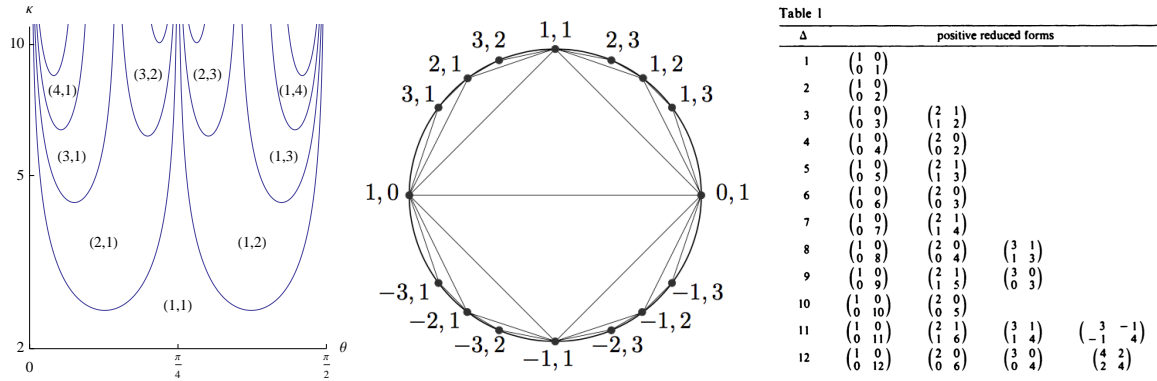


Figure A.4 – I-II. Matrices  $M \in S^{++}(\mathbb{R}^2)$  such that  $\det(M) = 1$  partitioned according to Voronoi’s first reduction. I: Parametrization by condition number  $\kappa$  and eigenvector’s orientation  $\theta$ , see Definition A.1.4. II: Natural parametrization by Poincaré’s disk [Sch09]. III: Classification of two dimensional positive quadratic forms with integer entries, by Lagrange [Lag75].

as announced in the general introduction of the dissertation. The following result estimates the size of the vectors  $\mathbf{e}_i \in \mathbb{L}_d$ , which dictates the size of the stencil of our PDE discretization schemes. It scales linearly with the condition number of  $D$ , in dimension  $d \leq 3$ . In two dimensions, the average case estimates of Theorem A.1.5 also apply, because one can turn a Minkowski reduced basis into an obtuse superbase, and then into a solution to Voronoi’s first reduction, see the end of this subsection.

**Proposition A.2.2.** *The offsets  $(\mathbf{e}_i)_{i=1}^{d'}$  associated with the active constraints for Voronoi’s first reduction (A.2) of  $D \in S^{++}(\mathbb{E}_d)$  obey  $\|\mathbf{e}_i\| \leq C \text{Cond}(D)^{d-1}$ , where  $C$  is an absolute constant. In dimension  $d = 3$  one can show the improved estimate  $\|\mathbf{e}_i\| \leq C \text{Cond}(D)$ .*

The first estimate of Proposition A.2.2 follows from the finiteness of equivalence classes of perfect forms, see [Mir17a]. It is sub-optimal for  $d = 3$ , and presumably also for  $d > 3$ . The second estimate, which proof is more involved, is an original result of the author, to our knowledge, presented in [Mir17b].

We end this subsection by outlining the connection of Voronoi’s first reduction with the concept of obtuse superbase, defined in §A.1.2. More precisely, if  $(\mathbf{e}_0, \dots, \mathbf{e}_d)$  is a  $D$ -obtuse superbase, then the minimizer  $M$  to (A.2) and the KKT conditions are respectively

$$M = \frac{1}{2^d} \sum_{I \subseteq [0,d]} \mathbf{e}_I \otimes \mathbf{e}_I, \quad D = \sum_{0 \leq i < j \leq d} \lambda_{ij} \mathbf{v}_{ij} \otimes \mathbf{v}_{ij}, \quad (\text{A.3})$$

where  $\mathbf{e}_I := \sum_{i \in I} \mathbf{e}_i$ ,  $\lambda_{ij} := -\langle \mathbf{e}_i, D\mathbf{e}_j \rangle$ , and the offsets are defined by the linear relations  $\langle \mathbf{v}_{ij}, \mathbf{e}_k \rangle = \delta_{ik} - \delta_{jk}$ . See [Mir17b] for a proof, and [CS92] or Appendix B of [BK10] for more discussion.

## A.2.2 Voronoi diagrams and the second reduction

The Voronoi diagram, of a discrete set  $Z \subseteq \mathbb{E}_d$  of sites, collects the region closest to each given site. We measure distances using the  $\|\cdot\|_M$  norm, where  $M \in S^{++}(\mathbb{E}_d)$  is a given

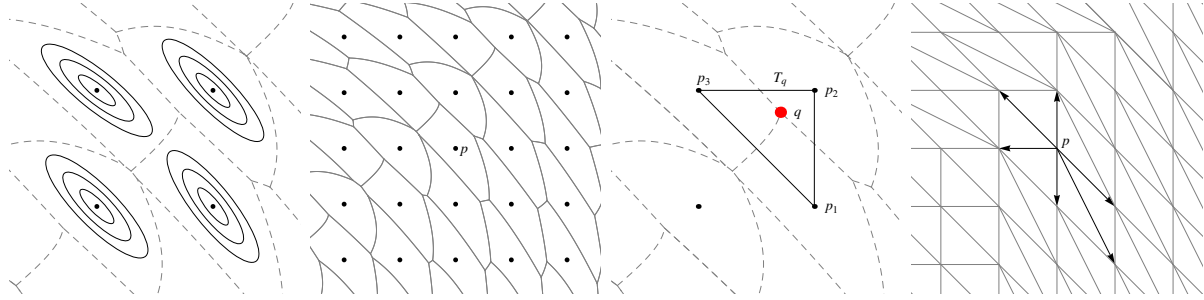


Figure A.5 – Illustration of the concept of Voronoi diagram (left), and dual Delaunay triangulation (right). (The presented diagram generalized in the sense of [LS03]. In contrast, region boundaries are straight for a standard Voronoi diagram.) Images from [FM14].

matrix. For all  $\mathbf{p} \in Z$ ,

$$\text{Vor}_M^Z(\mathbf{p}) := \{\mathbf{x} \in \mathbb{E}_d; \mathbf{p} \in \underset{\mathbf{q} \in Z}{\text{argmin}} \|\mathbf{x} - \mathbf{q}\|_M^2\}.$$

Note that one may assume  $M = \text{Id}$ , as is commonly done, up to a linear change of coordinates. Voronoi diagrams have numerous generalizations, and many more uses [ES86]. Generalized Voronoi diagrams include Laguerre diagrams (used in so-called semi-discrete numerical schemes for Monge-Ampere equations and optimal transport [OP89, AHA98]), Apollonius diagrams, Riemannian diagrams (used for anisotropic mesh generation [LS03, BPC09]), etc. See also Figure A.5.

The Delaunay triangulation  $\text{Del}_M^Z$  contains all simplices, of arbitrary dimension  $k$ , which Voronoi regions intersect

$$\{\mathbf{p}_0, \dots, \mathbf{p}_k\} \in \text{Del}_M^Z \quad \Leftrightarrow \quad \text{Vor}_M^Z(\mathbf{p}_0) \cap \dots \cap \text{Vor}_M^Z(\mathbf{p}_k) \neq \emptyset.$$

Under generic assumptions, e.g. that no  $k + 1$  points of  $X$  belong to a common  $k - 1$  dimensional affine space, the Delaunay triangulation is a valid triangulation of  $\text{Hull}(Z)$ . This triangulation is, again, a fundamental tool in discrete geometry, with numerous generalizations which are the subject of ongoing research, see e.g. [LS03, BWY15].

Voronoi's second reduction associates to each  $M \in S^{++}(\mathbb{E}_d)$  the Delaunay triangulation  $\text{Del}(M) := \text{Del}_M^{\mathbb{L}_d}$  of the periodic point set  $\mathbb{L}_d$ , computed with respect to the metric  $\|\cdot\|_M$ . This triangulation is well defined for almost every  $M \in S^{++}(\mathbb{E}_d)$ , and it has specific geometrical properties that make it suitable for the discretization of semi-Lagrangian Riemannian equations, see Lemma 2.1.2 in §2.1. One easily checks the co-variance property  $\text{Del}(A \cdot M) = (A^{-1})^T \cdot \text{Del}(M)$ , where  $A \in \text{GL}_d(M)$ . The linear group here acts by congruence (A.1) on  $S^{++}(\mathbb{E}_d)$ , and by linear change of coordinates on the triangulation.

Voronoi proved that there are only finitely many distinct classes of triangulations  $\text{Del}(M)$  up to linear changes of coordinates in  $\text{GL}(\mathbb{L}_d)$ . In fact, there is only one such class in dimension  $d \leq 3$ . (There are also 3 classes in dimension 4, and 222 classes in dimension 5, and the known classification stops there at the time of writing [Sch09].)

Finally, the knowledge of an  $M$ -obtuse superbase  $(\mathbf{e}_0, \dots, \mathbf{e}_d)$  of  $\mathbb{L}_d$  (if one exists), allows to construct the related Delaunay triangulation in a simple and efficient manner,

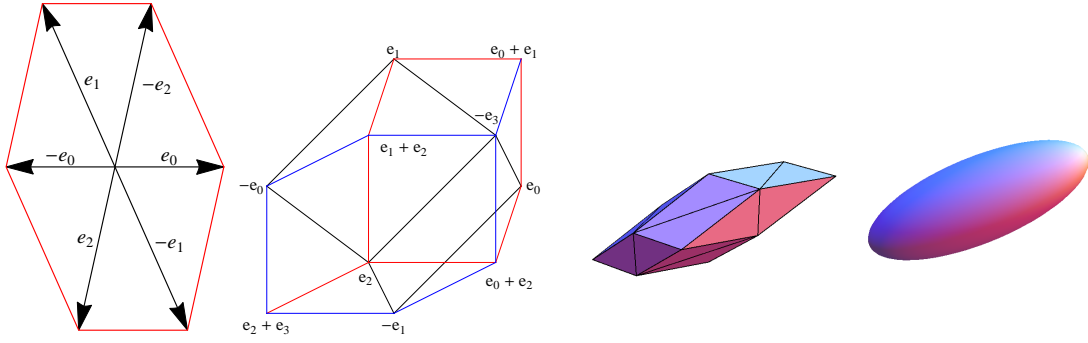


Figure A.6 – Left: Construction of the Delaunay triangulation  $\text{Del}(M)$  from an  $M$ -obtuse superbase  $(\mathbf{e}_0, \dots, \mathbf{e}_d)$ , where  $M \in S^{++}(\mathbb{E}_d)$ , in dimension  $d = 2$  and  $d = 3$  (simplices containing the origin shown). Right: Unit ball  $\{\mathbf{x} \in \mathbb{E}_3; \|\mathbf{e}\|_M \leq 1\}$  and neighborhood of the origin in  $\text{Del}(M)$ , for some  $M \in S^{++}(\mathbb{E}_3)$ .

see [CS92] and Figure A.6. For instance, the  $(d + 1)!$  simplices of  $\text{Del}(M)$  containing the origin are

$$\{\mathbf{v}_0^\varphi, \dots, \mathbf{v}_d^\varphi\}, \quad \text{where } \mathbf{v}_i^\varphi := \sum_{0 \leq j < i} \mathbf{e}_{\varphi(j)},$$

and where  $\varphi$  is an arbitrary permutation of  $\llbracket 0, d \rrbracket$ . This construction is used in our numerical implementation [Mir15a] of the FM-LBR numerical scheme in dimension  $d \leq 3$ , see §2.1. The superbase itself is obtained via Selling’s algorithm, see §A.1.2.

# Appendix B

## The fast marching algorithm

### Contents

---

<b>B.1</b>	<b>Fixed point formulation . . . . .</b>	<b>136</b>
<b>B.2</b>	<b>Systems of equations . . . . .</b>	<b>137</b>

---

This appendix describes the Fast-Marching algorithm [Tsi95, RT92], which can be regarded as a generalization of Dijkstra’s algorithm [Dij71]. This algorithm is far from new, but it has several formulations and generalizations that we choose to put in light in this appendix, in view of the applications in §2 and §3. We also discuss in this introduction the limitations of this method, and its possible alternatives. The results presented in this appendix are reformulations and sometimes generalizations of the literature. Proofs are provided for completeness.

We make a distinction between two formulations of the fast marching algorithm, designed to solve fixed point problems and systems of equations respectively. They are naturally encountered in semi-Lagrangian discretizations of eikonal PDEs, see (2.2) in §2, and Eulerian discretizations, see (3.4) in §3, respectively. The discretized systems read

$$\Lambda U = U, \qquad \text{(resp. } \mathfrak{F}U = 0\text{)}. \qquad \text{(B.1)}$$

The unknown is a map  $U : X \rightarrow \mathbb{R}$ , defined on a finite set  $X$ , and the operator  $\Lambda : \mathbb{R}^X \rightarrow \mathbb{R}^X$  (resp.  $\mathfrak{F}$ ) is given. The fast marching algorithm efficiently solves either form of the system (B.1) in a single pass, with typically a quasi-linear complexity  $\mathcal{O}(N \ln N)$  in the discrete domain cardinality  $N := \#(X)$ . For that purpose, it reconstructs at run-time the ordering  $U(\mathbf{x}_1) \leq U(\mathbf{x}_2) \leq \dots \leq U(\mathbf{x}_N)$  of the solution values, relying on a property of the operator  $\Lambda$  (resp.  $\mathfrak{F}$ ) referred to as causality. See also Figure B.1. Before focusing entirely on the Fast-Marching algorithm, we review its two main limitations, and the alternative equation solvers that have been proposed to address them.

- (Obeying the causality property.) As a fundamental assumption, the fast marching algorithm requires the operator  $\lambda$  (resp.  $\mathfrak{F}$ ) to obey the strong structural property of *causality*, see Definitions B.1.1 and B.2.1 below respectively. Designing such a discretization scheme, with reasonably small stencils, is highly non-trivial, see §2 and §3 or [SV03, Alt10]. It remains an open question in a number of cases of

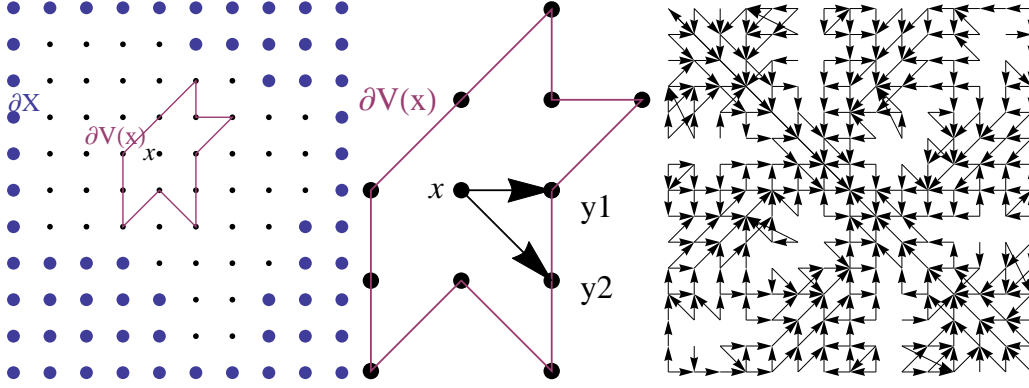


Figure B.1 – Illustration of the causality principle, in a semi-Lagrangian scheme. (Left) The value  $\Lambda U(\mathbf{p})$  is defined in terms of a number of neighbors. (Center) Those “active” obey  $U(\mathbf{q}) < U(\mathbf{p})$ . (Right) Global dependency graph, obeying  $U(\mathbf{p}) > U(\mathbf{q})$  whenever  $U(\mathbf{p})$  depends on  $U(\mathbf{q})$  (denoted  $\mathbf{p} \rightarrow \mathbf{q}$ ). The Fast-Marching algorithm reconstructs the ordering  $U(\mathbf{p}_0) \leq \dots U(\mathbf{p}_N)$  at run-time.

interest, such as e.g. Riemannian metrics on three dimensional meshed domains, or Finslerian metrics on three dimensional cartesian grids, see §3.1.3.

Numerical methods such as Fast-Sweeping [TCO04], or Adaptive Gauss-Siedel Iteration [BR06], do not require the operator to be causal. They are generalizations of Bellman-Ford’s algorithm on graphs, instead of Dijkstra’s algorithm, and they do not attempt to reconstruct on the fly the ordering of the solution values. Their complexity is reportedly  $\mathcal{O}(N^{1+\frac{1}{d}})$ , see [BR06], which is good enough for many applications. The hidden constant however depends on the geometry of the specific problem instance, and is severely unfavorable in applications to image segmentation, see §4.1.2.

- (Serial enumeration of the domain points.) A defining feature of the Fast-Marching algorithm is that it iterates over the discrete domain according to the ordering of the solution values, which is reconstructed at run time. This procedure is serial in nature, which is a major limitation in the era of parallel computing. The issue of parallelization was studied from the start [Tsi95], but remains an active subject of research [CV15, Tug08], in particular for GPU architectures [WDB<sup>+</sup>08, JW08].

**Notations.** A finite set  $X$  is fixed in this appendix, and we denote  $\mathcal{U} := ]-\infty, \infty]^X$ . Given  $U, V \in \mathcal{U}$ , we write  $U \leq V$  iff  $U(\mathbf{x}) \leq V(\mathbf{x})$  for all  $\mathbf{x} \in X$ . For any  $U \in \mathcal{U}$ , for any threshold  $\lambda$  and any subset  $A \subseteq X$ , we let  $U^{<\lambda}, U^{\setminus A} \in \mathcal{U}$  be defined by

$$U^{<\lambda}(\mathbf{x}) := \begin{cases} U(\mathbf{x}) & \text{if } U(\mathbf{x}) < \lambda, \\ +\infty & \text{otherwise.} \end{cases} \quad U^{\setminus A}(\mathbf{x}) := \begin{cases} U(\mathbf{x}) & \text{if } \mathbf{x} \in A, \\ +\infty & \text{otherwise.} \end{cases}, \quad (\text{B.2})$$

for all  $\mathbf{p} \in X$ . We define  $U^{\leq\lambda} \in \mathcal{U}$  likewise.

## B.1 Fixed point formulation

This section describes the fast marching algorithm, as applied to semi-Lagrangian discretizations of optimal control problems, see §2. In this context, it acts as a solver of fixed point systems  $\Lambda U = U$ , where  $U \in \mathcal{U} := ]-\infty, \infty]^X$  is the unknown and  $\Lambda$  is a given operator which mimics Bellman's optimality principle (2.2). The quantity  $\Lambda U(\mathbf{x})$ , where  $\mathbf{x} \in X$ , should be regarded as the estimated arrival time of a front at the point  $\mathbf{x} \in X$ , knowing the arrival times  $U(\mathbf{y})$  at its neighbors  $\mathbf{y} \in X \setminus \{\mathbf{x}\}$ .

**Definition B.1.1.** *An operator on a finite set  $X$  is a map  $\Lambda : \mathcal{U} \rightarrow \mathcal{U}$ , where  $\mathcal{U} := ]-\infty, \infty]^X$ . The operator is said*

- Monotone if for all  $U, V \in \mathcal{U}$  one has:  $U \leq V \Rightarrow \Lambda U \leq \Lambda V$ .
- Causal if for all  $U, V \in \mathcal{U}$  and all  $\lambda \in ]-\infty, \infty]$  one has:

$$U^{<\lambda} = V^{<\lambda} \quad \Rightarrow \quad (\Lambda U)^{\leq\lambda} = (\Lambda V)^{\leq\lambda}.$$

Monotony alone, plus mild assumptions, is sufficient to establish the existence of fixed points of the operator  $\Lambda$ , which can be computed by sufficiently iterating  $\Lambda$ , see the next proposition. There exists more efficient alternative solvers of the equation  $\Lambda U = U$  using monotony only [BR06, Zha05].

**Proposition B.1.2** (Gauss-Siedel iteration). *Let  $\Lambda$  be a monotone operator on a finite set  $X$ , which has a continuous restriction to  $\mathbb{R}^X$ . Assume that there exists  $U^-, U^+ \in \mathbb{R}^X$  such that  $U^- \leq U^+$ ,  $\Lambda U^- \geq U^-$  and  $\Lambda U^+ \leq U^+$ . Then  $\Lambda^n U^+$  converges as  $n \rightarrow \infty$  to a limit  $U \in \mathbb{R}^X$  such that  $U^- \leq U \leq U^+$  and  $\Lambda U = U$ . (Likewise for  $\Lambda^n U^-$ .)*

*Proof.* By monotony one has  $\Lambda U^- \leq \Lambda U^+$ , hence  $U^- \leq \Lambda U^- \leq \Lambda U^+ \leq U^+$ . By induction  $\Lambda^n U^- \leq \Lambda^{n+1} U^- \leq \Lambda^{n+1} U^+ \leq \Lambda^n U^+$  for all  $n \geq 0$ . The sequences  $(\Lambda^n U^-(\mathbf{x}))_{n \geq 0}$  and  $(\Lambda^n U^+(\mathbf{x}))_{n \geq 0}$  are thus monotone and bounded, for any  $\mathbf{x} \in X$ , hence converging to limits denoted  $U_\infty^-(\mathbf{x})$  and  $U_\infty^+(\mathbf{x})$  respectively. Then  $U^- \leq U_\infty^- \leq U_\infty^+ \leq U^+$  by the above inequalities, and as announced  $U_\infty^+ = \lim_{n \rightarrow \infty} \Lambda^{n+1} U^+ = \Lambda(\lim_{n \rightarrow \infty} \Lambda^n U^+) = \Lambda U_\infty^+$  by continuity of  $\Lambda$  (likewise for  $U_\infty^-$ ).  $\square$

The next proposition presents an algorithm which, depending on the choice of operator  $\Lambda$ , may be called Dijkstra's algorithm, or the Fast Marching algorithm, or the Dynamic programming principle. In terms of efficiency, it greatly improves upon Gauss-Siedel iteration, but it requires in addition the operator to be causal.

**Proposition B.1.3** (Fast marching). *Let  $\Lambda$  be a monotone and causal operator, on a finite set  $X$  of cardinality  $N$ . Let  $A_0 := \emptyset$ , and  $U_0 := \infty$  identically on  $X$ . For each  $1 \leq i \leq N$ :*

(a) *Define  $U_i := \Lambda U_{i-1}^{A_{i-1}}$ . (This notation is defined in (B.2).)*

(b) *Define  $A_i := A_{i-1} \cup \{\mathbf{x}_i\}$ , where  $\mathbf{x}_i$  is an arbitrary minimizer of  $U_i$  on  $X \setminus A_{i-1}$ .*

*Then  $\Lambda U_N = U_N$ . In addition  $U_{i+1}^{A_i} = U_i^{A_i}$  for each  $0 \leq i \leq N$ .*

*Proof.* Define  $\lambda_0 := -\infty$ , and  $\lambda_i := U_i(\mathbf{x}_i)$  for each  $1 \leq i \leq N$ . Our first objective is to establish by induction the property  $\mathbb{P}_i$ : “ $U_{i+1}^{\leq \lambda_i} = U_i^{\leq \lambda_i}$  and  $\lambda_i \leq \lambda_{i+1}$ ”, for each  $0 \leq i \leq N$ . Induction basis: both  $U_1^{\lambda_0}$  and  $U_0^{\lambda_0}$  are identically equal to  $+\infty$ , and  $\lambda_0 = -\infty$  can only be less or equal than  $\lambda_1$ , hence  $\mathbb{P}_0$  holds.

For the induction, namely the proof of  $\mathbb{P}_{i+1}$ , assuming  $\mathbb{P}_j$  for all  $j \leq i$ , our first step is to show that  $(U_i^{A_i})^{< \lambda_i} = (U_{i-1}^{A_{i-1}})^{< \lambda_i}$ . For that purpose, we consider  $\mathbf{x} \in X$ , and distinguish two cases:

- If  $\mathbf{x} \in A_{i-1}$ , then  $\mathbf{x} = \mathbf{x}_j$  for some  $j \leq i-1$ , hence  $U_j(\mathbf{x}) = U_j(\mathbf{x}_j) = \lambda_j$ . By induction one has  $\lambda_j \leq \lambda_{i-1}$ , hence also  $U_j^{\leq \lambda_j} = \dots = U_{i-1}^{\leq \lambda_j} = U_i^{\leq \lambda_j}$ . Thus  $U_{i-1}(\mathbf{x}) = U_i(\mathbf{x}) = \lambda_j$ , and therefore  $(U_i^{A_i})^{< \lambda_i}(\mathbf{x}) = (U_{i-1}^{A_{i-1}})^{< \lambda_i}(\mathbf{x})$  equals  $\lambda_j$  if  $\lambda_j < \lambda_i$ , or  $+\infty$  if  $\lambda_j = \lambda_i$ .
- If  $\mathbf{x} \notin A_{i-1}$ , then  $U_i(\mathbf{x}) \geq \lambda_i$  by definition of  $\lambda_i$ , thus  $(U_i^{A_i})^{< \lambda_i}(\mathbf{x}) = \infty = (U_{i-1}^{A_{i-1}})^{< \lambda_i}(\mathbf{x})$ .

Having shown that  $(U_i^{A_i})^{< \lambda_i} = (U_{i-1}^{A_{i-1}})^{< \lambda_i}$  we obtain  $U_{i+1}^{\leq \lambda_i} = U_i^{\leq \lambda_i}$ , by step (a) of the algorithm and causality of the operator  $\Lambda$ , as announced. Finally assuming for contradiction that  $\lambda_{i+1} < \lambda_i$ , we obtain  $U_i(\mathbf{x}_{i+1}) = U_i^{\leq \lambda_i}(\mathbf{x}_{i+1}) = U_{i+1}^{\leq \lambda_i}(\mathbf{x}_{i+1}) = \lambda_{i+1} < \lambda_i$ . This contradicts the definition of  $\mathbf{x}_i$ , as the minimizer of  $U_i$  on  $X \setminus A_{i-1} \subseteq X \setminus A_i \ni \mathbf{x}_{i+1}$ , hence concludes the proof of  $\mathbb{P}_{i+1}$  and the induction argument.

The above argument implies that  $U_i$  takes on  $A_i$  the values  $\{\lambda_1 \leq \dots \leq \lambda_i\}$ . Hence  $U_{i+1}^{A_i} = U_i^{A_i}$  follows from  $U_{i+1}^{\leq \lambda_i} = U_i^{\leq \lambda_i}$ . Choosing  $i = N$  and observing that  $A_N = X$  yields  $U_N = U_{N+1} = \Lambda U_N$ .  $\square$

In summary, the fast marching algorithm finds an exact fixed point by applying the operator  $\Lambda$  finitely many times, namely  $N$  times where  $N := \#(X)$ . The operator  $\Lambda$  is applied successively to discrete maps  $U_{i-1}^{A_{i-1}}$  and  $U_i^{A_i}$  which only differ at a single point  $\mathbf{x}_i$  of the domain. In other words, the operator value  $\Lambda U(\mathbf{y})$  thus has to be recomputed (for a cost regarded as unit) and inserted into a sorted list, for each point  $\mathbf{y} \in X \setminus A_i$  such that  $\Lambda U(\mathbf{y})$  depends on  $U(\mathbf{x}_i)$ . Overall, the complexity of this algorithm is thus  $\mathcal{O}(M \ln N)$  using a standard heap structure for the sorted list ( $\mathcal{O}(M+N \ln N)$  using a Fibonacci heap), where  $M$  is the cardinality of the dependency graph  $\{(\mathbf{x}, \mathbf{y}); \Lambda U(\mathbf{y}) \text{ depends on } U(\mathbf{x})\}$ .

## B.2 Systems of equations

This section describes the Fast-Marching algorithm, as applied to eulerian discretizations of eikonal equations, which take the form of a system of coupled and non-linear equations  $\mathfrak{F}U = 0$ . Similarly to the semi-Lagrangian case, the operator  $\mathfrak{F}$  needs to obey two structural assumptions.

**Definition B.2.1.** *A (finite differences) scheme on a finite set  $X$  is a continuous map  $\mathfrak{F} : X \times \mathbb{R} \times \mathbb{R}^X \rightarrow \mathbb{R}$ . The scheme is said:*

- *Monotone, iff  $\mathfrak{F}$  is non-decreasing w.r.t. the second and (each of the) third variables.*

- Causal, iff  $\mathfrak{F}$  only depends on the positive part of the third variable.

To the scheme is associated a function  $\mathbb{R}^X \rightarrow \mathbb{R}^X$  still (abusively) denoted by  $\mathfrak{F}$ , and defined for all  $\mathbf{x} \in X$  and all  $U \in \mathbb{R}^X$  by

$$(\mathfrak{F}U)(\mathbf{x}) := \mathfrak{F}(\mathbf{x}, U(\mathbf{x}), (U(\mathbf{x}) - U(\mathbf{y}))_{\mathbf{y} \in X}).$$

In order to solve the system  $\mathfrak{F}U = 0$ , we reformulate it as a fixed point problem  $\Lambda U = U$ , and rely on the method of the previous section, see Proposition B.1.3. More precisely, we associate to each scheme  $\mathfrak{F}$  an operator  $\Lambda : \mathcal{U} \rightarrow \mathcal{U}$  defined for all  $U \in \mathcal{U} := ]-\infty, \infty]^X$  and all  $\mathbf{x} \in X$  by

$$\Lambda U(\mathbf{x}) := \sup\{V(\mathbf{x}); V \in \mathbb{R}^X, \mathfrak{F}V(\mathbf{x}) \leq 0, V \leq U \text{ on } X \setminus \{\mathbf{x}\}\}. \quad (\text{B.3})$$

For the numerical schemes  $\mathfrak{F}$  considered in this report, see §3, computing (B.3) amounts to solving a (small number of) univariate quadratic equations.

Let us emphasize that the concepts of *monotony* and *causality* have different meanings for the operator  $\Lambda$  and the scheme  $\mathfrak{F}$ , see Definitions B.1.1 and B.2.1 respectively. These meanings are related by the following lemma.

**Lemma B.2.2.** *Let  $\mathfrak{F}$  be a scheme on a finite set  $X$ , in the sense of Definition B.2.1, and let  $\Lambda$  be the associated operator, defined by (B.3). Then  $\Lambda$  is by construction monotone. In addition*

1. *If  $\mathfrak{F}$  is monotone then  $(\Lambda U = U \Rightarrow \mathfrak{F}U = 0)$ , for any  $U \in \mathbb{R}^X$ .*
2. *If  $\mathfrak{F}$  is causal then  $\Lambda$  is causal.*

*Proof. Monotony of  $\Lambda$ :* If  $U_1 \leq U_2$  then  $(V \leq U_1 \Rightarrow V \leq U_2)$  for any  $V \in \mathbb{R}^X$ , hence  $\Lambda U_1 \leq \Lambda U_2$  by definition (B.3). *Proof of point 1:* The result easily follows from the continuity of  $\mathfrak{F}$  and the observation that: for any  $\mathbf{x} \in X$ , the supremum defining  $\Lambda U(\mathbf{x})$  is attained for some  $V \in \mathbb{R}^X$  obeying  $V = U$  on  $X \setminus \{\mathbf{x}\}$ , by monotony of  $\mathfrak{F}$ . *Proof of point 2:* Let  $\mathfrak{F}$  be a causal scheme, and let  $U \in \mathcal{U}$ ,  $\mathbf{x} \in X$ ,  $\lambda \in \mathbb{R}$ . One easily checks that

$$(\Lambda U(\mathbf{x}))^{\leq \lambda} = \sup\{V^{\leq \lambda}(\mathbf{x}); V \in \mathbb{R}^X, \mathfrak{F}V(\mathbf{x}) \leq 0, V \leq U^{\leq \lambda} \text{ on } X \setminus \{\mathbf{x}\}\}.$$

Thus  $(\Lambda U)^{\leq \lambda}$  only depends on  $U^{\leq \lambda}$ , as announced, which concludes the proof.  $\square$

# Bibliography

- [ABFJB06] Gilles Aubert, Michel Barlaud, Olivier Faugeras, and Stéphanie Jehan-Besson. Image Segmentation Using Active Contours: Calculus of Variations or Shape Gradients? *SIAM Journal on Applied Mathematics*, 63(6):2128–2154, July 2006.
- [AHA98] F Aurenhammer, F Hoffmann, and B Aronov. Minkowski-Type Theorems and Least-Squares Clustering. *Algorithmica*, 20(1):61–76, January 1998.
- [Ajt98] Miklós Ajtai. The shortest vector problem in L2 is NP-hard for randomized reductions. In *Proceedings of the thirtieth annual ACM symposium on Theory of computing*, pages 10–19, New York, New York, USA, May 1998. ACM.
- [Alt10] K Alton. *Dijkstra-like ordered upwind methods for solving static Hamilton-Jacobi equations*. PhD thesis, University of British Columbia, 2010.
- [AM08] Nestor E Aguilera and Pedro Morin. Approximating optimization problems over convex functions. *Numerische Mathematik*, 111(1):1–34, 2008.
- [AM09] Nestor E Aguilera and Pedro Morin. On Convex Functions and the Finite Element Method. *SIAM Journal on Numerical Analysis*, 47(4):3139–3157, January 2009.
- [AM11] Ken Alton and Ian M Mitchell. An Ordered Upwind Method with Precomputed Stencil and Monotone Node Acceptance for Solving Static Convex Hamilton-Jacobi Equations. *Journal of Scientific Computing*, 51(2):313–348, July 2011.
- [Arn66] Vladimir Arnold. Sur la géométrie différentielle des groupes de Lie de dimension infinie et ses applications à l’hydrodynamique des fluides parfaits. *Annales de l’institut Fourier*, 16(1):319–361, 1966.
- [Bar11] F Barbaresco. Computation of most threatening radar trajectories areas and corridors based on fast-marching & Level Sets. In *IEEE Symposium On Computational Intelligence For Security And Defence Applications*, pages 51–58. IEEE, 2011.

- [BC05] Christophe Buet and Stéphane Cordier. On the non existence of monotone linear schema for some linear parabolic equations. *Comptes Rendus Mathematiques*, 340(5):399–404, March 2005.
- [BC08] Fethallah Benmansour and Laurent D. Cohen. Fast Object Segmentation by Growing Minimal Paths from a Single Point on 2D or 3D Images. *Journal of Mathematical Imaging and Vision*, 33(2):209–221, December 2008.
- [BC10] Fethallah Benmansour and Laurent D. Cohen. Tubular Structure Segmentation Based on Minimal Path Method and Anisotropic Enhancement. *International Journal of Computer Vision*, 92(2):192–210, March 2010.
- [BCC<sup>+</sup>15] Jean-David Benamou, Guillaume Carlier, Marco Cuturi, Luca Nenna, and Gabriel Peyré. Iterative Bregman Projections for Regularized Transportation Problems. *SIAM Journal on Scientific Computing*, 37(2):A1111–A1138, January 2015.
- [BCD08] Martino Bardi and Italo Capuzzo-Dolcetta. *Optimal control and viscosity solutions of Hamilton-Jacobi-Bellman equations*. Springer Science & Business Media, 2008.
- [BCD<sup>+</sup>16] Jérémy Bleyer, Guillaume Carlier, Vincent Duval, Jean-Marie Mirebeau, and Gabriel Peyré. A  $\Gamma$ -Convergence Result for the Upper Bound Limit Analysis of Plates. *ESAIM: Mathematical Modelling and Numerical Analysis*, 50(1):215–235, 2016.
- [BCM16] Jean-David Benamou, Francis Collino, and Jean-Marie Mirebeau. Monotone and Consistent discretization of the Monge-Ampere operator. *Mathematics of computation*, 85(302):2743–2775, 2016.
- [BCP17] Erik J Bekkers, Da Chen, and Jorg M Portegies. Nilpotent Approximations of Sub-Riemannian Distances for Fast Perceptual Grouping of Blood Vessels in 2D and 3D. *arXiv preprint arXiv:1707.02811*, 2017.
- [BCPS10] F Benmansour, G Carlier, G Peyré, and F Santambrogio. Derivatives with respect to metrics and applications: subgradient marching algorithm. *Numerische Mathematik*, 116(3):357–381, May 2010.
- [BDG13] Jean-Daniel Boissonnat, Ramsay Dyer, and Arijit Ghosh. The stability of Delaunay triangulations. *International Journal of Computational Geometry and Applications*, 23(04n05):303–333, August 2013.
- [BDMS15] Erik J Bekkers, Remco Duits, Alexey Mashtakov, and Gonzalo R Sanguinetti. A PDE approach to data-driven sub-Riemannian geodesics in SE (2). *SIAM Journal on Imaging Sciences*, 8(4):2740–2770, 2015.
- [BE84] M Bardi and L C Evans. On Hopf’s formulas for solutions of Hamilton-Jacobi equations. *Nonlinear Analysis. Theory, Methods and Applications*.

*An International Multidisciplinary Journal. Series A: Theory and Methods*, 8(11):1373–1381, 1984.

- [BGM97] H Borouchaki, P L George, and B Mohammadi. Finite Elements in Analysis and Design - Delaunay mesh generation governed by metric specifications Part II. Applications. *Finite Elements in Analysis and Design*, 1997.
- [BK10] Jean-Benoît Bost and Klaus Künnemann. Hermitian vector bundles and extension groups on arithmetic schemes. I. Geometry of numbers. *Advances in Mathematics*, 223(3):987–1106, February 2010.
- [BM00] F Barbaresco and B Mounier. Minimal geodesics bundles by active contours: Radar application for computation of most threatening trajectories areas & corridors. In *Signal Processing Conference*, 2000.
- [BOZ04] J Frederic Bonnans, Elisabeth Ottenwaelter, and Housnaa Zidani. A fast algorithm for the two dimensional HJB equation of stochastic control. *ESAIM: Mathematical Modelling and Numerical Analysis*, 38(4):723–735, 2004.
- [BPC09] Sébastien Bogleux, Gabriel Peyré, and Laurent Cohen. Compression d’images par triangulation géodésique anisotrope. In *Gretsi*, 2009.
- [BR06] Folkmar Bornemann and Christian Rasch. Finite-element Discretization of Static Hamilton-Jacobi Equations based on a Local Variational Principle. *Computing and Visualization in Science*, 9(2):57–69, June 2006.
- [Bre89] Yann Brenier. The least action principle and the related concept of generalized flows for incompressible perfect fluids. *Journal of the American Mathematical Society*, 2(2):225–255, 1989.
- [Bre08] Y Brenier. Generalized solutions and hydrostatic approximation of the Euler equations. *Physica D: Nonlinear Phenomena*, 2008.
- [Bro62] Achille Brocot. *Calcul des rouages par approximation, nouvelle méthode*. 1862.
- [BWY15] Jean-Daniel Boissonnat, Camille Wormser, and Mariette Yvinec. Anisotropic Delaunay Mesh Generation. *SIAM Journal on Computing*, 44(2):467–512, March 2015.
- [BZ03] J Frederic Bonnans and Housnaa Zidani. Consistency of Generalized Finite Difference Schemes for the Stochastic HJB Equation. *SIAM Journal on Numerical Analysis*, 41(3):1008–1021, January 2003.
- [CC17a] Da Chen and Laurent Cohen. Anisotropic Edge-based Balloon Eikonal Active Contours. In *Geometrical Science of Information*, 2017.
- [CC17b] Da Chen and Laurent D. Cohen. Fast Asymmetric Fronts Propagation for Image Segmentation. *arXiv.org*, July 2017.

- [CCM14] Da Chen, Laurent D. Cohen, and Jean-Marie Mirebeau. Vessel extraction using anisotropic minimal paths and path score. In *2014 IEEE International Conference on Image Processing (ICIP)*, pages 1570–1574, paris, France, 2014. IEEE.
- [CFL28] R Courant, K Friedrichs, and H Lewy. On the Partial Difference Equations of Mathematical Physics. *Mathematische Annalen*, 1928.
- [Che16] Da Chen. *New Minimal Path Models for Tubular Structure Extraction and Image Segmentation*. PhD thesis, University Paris-Dauphine, September 2016.
- [CHK13] Marcel Campen, Martin Heistermann, and Leif Kobbelt. Practical Anisotropic Geodesy. *Computer Graphics Forum*, 32(5):63–71, August 2013.
- [CIL92] Michael G Crandall, Hitoshi Ishii, and Pierre-Louis Lions. User’s guide to viscosity solutions of second order partial differential equations. *Bulletin of the American Mathematical Society*, 27(1):1–67, 1992.
- [CK97] Laurent D Cohen and R Kimmel. Global minimum for active contour models: A minimal path approach. *International Journal of Computer Vision*, 24(1):57–78, 1997.
- [CKS97] Vicent Caselles, Ron Kimmel, and Guillermo Sapiro. Geodesic Active Contours. *International Journal of Computer Vision*, 22(1):61–79, 1997.
- [CLM06] Philippe Choné and Hervé V J Le Meur. Non-convergence result for conformal approximation of variational problems subject to a convexity constraint. *Numerical Functional analysis and Optimization*, 22(5-6):529–547, August 2006.
- [CLRM01] Guillaume Carlier, Thomas Lachand-Robert, and Bertrand Maury. A numerical approach to variational problems subject to convexity constraint. *Numerische Mathematik*, 2001.
- [CMC16a] Da Chen, Jean-Marie Mirebeau, and Laurent D. Cohen. A New Finsler Minimal Path Model With Curvature Penalization for Image Segmentation and Closed Contour Detection. *Computer Vision and Pattern Recognition (CVPR)*, pages 355–363, June 2016.
- [CMC16b] Da Chen, Jean-Marie Mirebeau, and Laurent D Cohen. Finsler Geodesics Evolution Model for Region based Active Contours. *BMVC*, 2016.
- [CMC16c] Da Chen, Jean-Marie Mirebeau, and Laurent D. Cohen. Vessel tree extraction using radius-lifted keypoints searching scheme and anisotropic fast marching method. *Journal of Algorithms & Computational Technology*, 10(4):224–234, July 2016.

- [CMC17] Da Chen, Jean-Marie Mirebeau, and Laurent D. Cohen. Global Minimum for a Finsler Elastica Minimal Path Approach. *International Journal of Computer Vision*, 122(3):458–483, 2017.
- [CS88] J H Conway and N J A Sloane. Low-Dimensional Lattices. III. Perfect Forms. *Proceedings of the Royal Society of London A: Mathematical, Physical and Engineering Sciences*, 418(1854):43–80, July 1988.
- [CS92] J H Conway and N J A Sloane. Low-Dimensional Lattices. VI. Voronoi Reduction of Three-Dimensional Lattices. *Proceedings of the Royal Society A: Mathematical, Physical and Engineering Sciences*, 436(1896):55–68, January 1992.
- [CSV00] Tony F Chan, B Yezriev Sandberg, and Luminita A Vese. Active Contours without Edges for Vector-Valued Images. *Journal of Visual Communication and Image Representation*, 11(2):130–141, June 2000.
- [CV01] T F Chan and L A Vese. Active contours without edges. *IEEE Transactions on Image Processing*, 10(2):266–277, 2001.
- [CV15] Adam Chacon and Alexander Vladimirovsky. A Parallel Two-Scale Method for Eikonal Equations. *SIAM Journal on Scientific Computing*, 37(1):A156–A180, January 2015.
- [CWW12] Keenan Crane, Clarisse Weischedel, and Max Wardetzky. Geodesics in Heat. *arXiv.org*, April 2012.
- [DDHCG13] Remco Duits, Tom Dela Haije, Eric Creusen, and Arpan Ghosh. Morphological and linear scale spaces for fiber enhancement in DW-MRI. *Journal of Mathematical Imaging and Vision*, 46(3):326–368, 2013.
- [DF08] C Dobrzynski and P Frey. Anisotropic Delaunay Mesh Adaptation for Unsteady Simulations. In *Proceedings of the 17th international Meshing Roundtable*, pages 177–194. Springer Berlin Heidelberg, Berlin, Heidelberg, 2008.
- [DFGtHR07] Remco Duits, Michael Felsberg, Gösta Granlund, and Bart ter Haar Romeny. Image Analysis and Reconstruction using a Wavelet Transform Constructed from a Reducible Representation of the Euclidean Motion Group. *International Journal of Computer Vision*, 72(1):79–102, 2007.
- [dGWH<sup>+</sup>15] F de Goes, C Wallez, J Huang, U Zhejiang, and D Pavlov. Power Particles: An incompressible fluid solver based on power diagrams. *geometry.caltech.edu*, 2015.
- [Dij71] Edsger Wybe Dijkstra. *A short introduction to the art of programming*, volume 4. Technische Hogeschool Eindhoven Eindhoven, 1971.

- [DMMP16] Remco Duits, Stephan P L Meesters, Jean-Marie Mirebeau, and Jorg M Portegies. Optimal Paths for Variants of the 2D and 3D Reeds-Shepp Car with Applications in Image Analysis. *arXiv.org*, December 2016.
- [Dub57] L E Dubins. On curves of minimal length with a constraint on average curvature, and with prescribed initial and terminal positions and tangents. *American Journal of Mathematics*, 79:497–516, 1957.
- [EMB10] Ivar Ekeland and Santiago Moreno-Bromberg. An algorithm for computing solutions of variational problems with global convexity constraints. *Numerische Mathematik*, 2010.
- [ES86] Herbert Edelsbrunner and Raimund Seidel. Voronoi diagrams and arrangements. *Discrete and Computational Geometry*, 1(1):25–44, 1986.
- [Eva10] Lawrence C Evans. *Partial Differential Equations*. American Mathematical Soc., 2010.
- [FM06] Jérôme Fehrenbach and Mohamed Masmoudi. *Coupling topological gradient and Gauss-Newton methods*, volume 137 of *Solid Mechanics and Its Applications*. Springer Netherlands, 2006.
- [FM14] Jérôme Fehrenbach and Jean-Marie Mirebeau. Sparse non-negative stencils for anisotropic diffusion. *Journal of Mathematical Imaging and Vision*, 49(1):123–147, 2014.
- [FO11a] B D Froese and A M Oberman. Fast finite difference solvers for singular solutions of the elliptic Monge–Ampère equation. *Journal of Computational Physics*, 230(3):818–834, February 2011.
- [FO11b] Brittany D Froese and A M Oberman. Convergent Finite Difference Solvers for Viscosity Solutions of the Elliptic Monge–Ampère Equation in Dimensions Two and Higher. *SIAM Journal on Numerical Analysis*, 49(4):1692–1714, January 2011.
- [FO13] Brittany D Froese and A M Oberman. Convergent Filtered Schemes for the Monge–Ampère Partial Differential Equation. *SIAM Journal on Numerical Analysis*, 51(1):423–444, January 2013.
- [Fro12] Brittany Dawn Froese. *Numerical methods for the elliptic Monge-Ampere equation and optimal transport*. PhD thesis, June 2012.
- [Fro15] Brittany D Froese. Meshfree finite difference approximations for functions of the eigenvalues of the Hessian. *Numerische Mathematik*, 35(3):1–25, 2015.
- [FT07] Satoru Fujishige and Akihisa Tamura. A Two-Sided Discrete-Concave Market with Possibly Bounded Side Payments: An Approach by Discrete Convex Analysis. *Mathematics of Operations Research*, 32(1):136–155, February 2007.

- [GM16] Thomas Gallouët and Quentin Merigot. A Lagrangian scheme for the incompressible Euler equation using optimal transport. *arXiv.org*, May 2016.
- [Gut01] C E Gutiérrez. *The Monge-Ampère Equation*. Springer, 2001.
- [GV16] Thomas Gallouët and François Xavier Vialard. From unbalanced optimal transport to the Camassa-Holm equation. *arXiv.org*, September 2016.
- [GW08] Andreas Griewank and Andrea Walther. *Evaluating Derivatives*. Principles and Techniques of Algorithmic Differentiation. Society for Industrial and Applied Mathematics, 2008.
- [GWB10] Sven Grewenig, Joachim Weickert, and Andrés Bruhn. *From Box Filtering to Fast Explicit Diffusion*, volume 6376. Springer Berlin Heidelberg, Berlin, Heidelberg, 2010.
- [HNU99] F Hurtado, M Noy, and J Urrutia. Flipping Edges in Triangulations. *Discrete and Computational Geometry*, 22(3):333–346, October 1999.
- [HOS96] S Hanke, T Ottmann, and S Schuierer. The edge-flipping distance of triangulations. Technical report, 1996.
- [JW08] Won-Ki Jeong and Ross T Whitaker. A Fast Iterative Method for Eikonal Equations. *SIAM Journal on Scientific Computing*, 30(5):2512–2534, July 2008.
- [Kan42] L V Kantorovich. *Kantorovich: On the transfer of masses*. Dokl. Akad. Nauk. SSSR, 1942.
- [KMT16] Jun Kitagawa, Quentin Merigot, and Boris Thibert. Convergence of a Newton algorithm for semi-discrete optimal transport. *arXiv.org*, March 2016.
- [KR04] Reinhard Klette and Azriel Rosenfeld. *Digital geometry: Geometric methods for digital picture analysis*. Elsevier, 2004.
- [KS98] R Kimmel and J. A. Sethian. Computing geodesic paths on manifolds. *Proceedings of the National Academy of Sciences*, 95(15):8431–8435, July 1998.
- [KS12] Ioannis Karatzas and Steven Shreve. *Brownian motion and stochastic calculus*, volume 113. Springer Science and Business Media, 2012.
- [KT92] Hung-Ju Kuo and Neil S Trudinger. Discrete Methods for Fully Nonlinear Elliptic Equations. *SIAM Journal on Numerical Analysis*, 29(1):123–135, February 1992.
- [KW11] Bernd Kawohl and Christof Weber. Meissner’s Mysterious Bodies. *The Mathematical Intelligencer*, 33(3):94–101, July 2011.

- [KWT88] Michael Kass, Andrew Witkin, and Demetri Terzopoulos. Snakes: Active contour models. *International Journal of Computer Vision*, 1(4):321–331, January 1988.
- [Lag75] J L Lagrange. *Recherches d’arithmétique*. C.F. Voss, 1775.
- [LC08] Max W K Law and Albert C S Chung. Three Dimensional Curvilinear Structure Detection Using Optimally Oriented Flux. *Computer Vision-ECCV 2008. Springer Berlin Heidelberg*, pages 368–382, 2008.
- [LLL82] A K Lenstra, H W Lenstra, and L Lovász. Factoring polynomials with rational coefficients. *Mathematische Annalen*, 261(4):515–534, 1982.
- [LRO05] Thomas Lachand-Robert and Edouard Oudet. Minimizing within Convex Bodies Using a Convex Hull Method. *SIAM Journal on Optimization*, 16(2):368–379, January 2005.
- [LS80] D T Lee and B J Schachter. Two algorithms for constructing a Delaunay triangulation. *International Journal of Computer & Information Sciences*, 9(3):219–242, 1980.
- [LS03] François Labelle and Jonathan Richard Shewchuk. Anisotropic voronoi diagrams and guaranteed-quality anisotropic mesh generation. pages 191–200, 2003.
- [LY07] H Li and A Yezzi. Vessels as 4-D curves: Global minimal 4-D paths to extract 3-D tubular surfaces and centrelines. *IEEE Transactions on Medical Imaging*, 26(9):1213–1223, 2007.
- [MD17] Jean-Marie Mirebeau and Johann Dreo. Automatic differentiation of non-holonomic fast marching for computing most threatening trajectories under sensors surveillance. In *Geometrical Science of Information*, April 2017.
- [Mer11] Quentin Merigot. A Multiscale Approach to Optimal Transport. *Computer Graphics Forum*, 30(5):1583–1592, August 2011.
- [MFRT15] Jean-Marie Mirebeau, Jérôme Fehrenbach, Laurent Risser, and Shaza Tobji. Anisotropic Diffusion in ITK. *The Insight Journal*, March 2015.
- [Mir11] Jean-Marie Mirebeau. *Adaptive and anisotropic finite element approximation : Theory and algorithms*. PhD thesis, January 2011.
- [Mir14a] Jean-Marie Mirebeau. Anisotropic Fast-Marching on cartesian grids using Lattice Basis Reduction. *SIAM Journal on Numerical Analysis*, 52(4):1573–1599, January 2014.
- [Mir14b] Jean-Marie Mirebeau. Efficient fast marching with Finsler metrics. *Numerische Mathematik*, 126(3):515–557, 2014.

- [Mir15a] Jean-Marie Mirebeau. Anisotropic Fast Marching in ITK. *The Insight Journal*, June 2015.
- [Mir15b] Jean-Marie Mirebeau. Discretization of the 3D Monge-Ampere operator, between wide stencils and power diagrams. *M2AN. Mathematical Modelling and Numerical Analysis*, 49(5):1511–1523, 2015.
- [Mir16a] Jean-Marie Mirebeau. Adaptive, anisotropic and hierarchical cones of discrete convex functions. *Numerische Mathematik*, 132(4):807–853, 2016.
- [Mir16b] Jean-Marie Mirebeau. Minimal stencils for discretizations of anisotropic PDEs preserving causality or the maximum principle. *SIAM Journal on Numerical Analysis*, 54(3):1582–1611, 2016.
- [Mir17a] Jean-Marie Mirebeau. Anisotropic fast-marching on cartesian grids using Voronoi’s first reduction of quadratic forms. *HAL (Preprint)*, April 2017.
- [Mir17b] Jean-Marie Mirebeau. Fast Marching methods for Curvature Penalized Shortest Paths. *HAL (Preprint)*, June 2017.
- [MM16] Quentin Merigot and Jean-Marie Mirebeau. Minimal Geodesics Along Volume-Preserving Maps, Through Semidiscrete Optimal Transport. *SIAM Journal on Numerical Analysis*, 54(6):3465–3492, 2016.
- [MN06] Khamron Mekchay and Ricardo H Nochetto. Convergence of Adaptive Finite Element Methods for General Second Order Linear Elliptic PDEs. *SIAM Journal on Numerical Analysis*, 43(5):1803–1827, July 2006.
- [MO14] Quentin Merigot and Edouard Oudet. Handling convexity-like constraints in variational problems. *SIAM Journal on Numerical Analysis*, 52(5):2466–2487, 2014.
- [Mon06] Richard Montgomery. *A Tour of Subriemannian Geometries, Their Geodesics and Applications*. American Mathematical Soc., August 2006.
- [MP15] Bertrand Maury and Anthony Preux. Pressureless Euler equations with maximal density constraint : a time-splitting scheme. October 2015.
- [MPAT08] J Melonakos, E Pichon, S Angenent, and A Tannenbaum. Finsler Active Contours. *IEEE Transactions on Pattern Analysis and Machine Intelligence*, 30(3):412–423, 2008.
- [MTW05] Xi-Nan Ma, Neil S Trudinger, and Xu-Jia Wang. Regularity of Potential Functions of the Optimal Transportation Problem. *Archive for rational mechanics and analysis*, 177(2):151–183, 2005.
- [Mum94] David Mumford. Elastica and computer vision. In *Algebraic geometry and its applications*, pages 491–506. Springer, 1994.

- [Niq07] Milad Niqui. Exact arithmetic on the Stern–Brocot tree. *Journal of Discrete Algorithms*, 5(2):356–379, June 2007.
- [NS04] Phong Q. Nguyen and Damien Stehlé. Low-dimensional lattice basis reduction revisited. In *ANTS*, pages 338–357. Springer, 2004.
- [NV09] Phong Q. Nguyen and Brigitte Vallée, editors. *The LLL Algorithm*. Springer Berlin Heidelberg, Berlin, Heidelberg, October 2009.
- [Obe04] A M Oberman. A convergent monotone difference scheme for motion of level sets by mean curvature. *Numerische Mathematik*, 99(2):365–379, 2004.
- [Obe05] Adam Oberman. A convergent difference scheme for the infinity Laplacian: construction of absolutely minimizing Lipschitz extensions. *Mathematics of computation*, 74(251):1217–1230, 2005.
- [Obe06] A M Oberman. Convergent Difference Schemes for Degenerate Elliptic and Parabolic Equations: Hamilton–Jacobi Equations and Free Boundary Problems. *SIAM Journal on Numerical Analysis*, 44(2):879–895, January 2006.
- [Obe13] A M Oberman. A Numerical Method for Variational Problems with Convexity Constraints. *SIAM Journal on Scientific Computing*, 35(1):A378–A396, January 2013.
- [OF11] A M Oberman and Michael P Friedlander. A numerical method for variational problems over the cone of convex functions (Preprint). *arXiv.org*, July 2011.
- [OP89] V I Oliker and L D Prussner. On the numerical solution of the equation  $\frac{\partial^2 z}{\partial x^2} \frac{\partial^2 z}{\partial y^2} - \left(\frac{\partial^2 z}{\partial x \partial y}\right)^2 = f$  and its discretizations, I. *Numerische Mathematik*, 54(3):271–293, May 1989.
- [Pei09] Chris Peikert. *Public-key cryptosystems from the worst-case shortest vector problem*. extended abstract. ACM, New York, New York, USA, May 2009.
- [Pey15] Gabriel Peyré. Entropic approximation of Wasserstein gradient flows. *SIAM Journal on Imaging Sciences*, 8(4):2323–2351, 2015.
- [PHHR55] D W Peaceman and Jr H H Rachford. The Numerical Solution of Parabolic and Elliptic Differential Equations. *Journal of the Society for Industrial and Applied Mathematics*, 3(1):28–41, March 1955.
- [PKP09] M Pechaud, R Keriven, and G Peyré. Extraction of tubular structures over an orientation domain. In *2009 IEEE Computer Society Conference on Computer Vision and Pattern Recognition Workshops (CVPR Workshops)*, pages 336–342. IEEE, 2009.

- [PM90] P Perona and J Malik. Scale-space and edge detection using anisotropic diffusion. *IEEE Transactions on Pattern Analysis and Machine Intelligence*, 12(7):629–639, July 1990.
- [PPK10] G Peyré, M Pechaud, and R Keriven. Geodesic methods in computer vision and graphics. *Foundations and Trends® in Computer Graphics and Vision*, 5(3-4):197–397, 2010.
- [QCT13] Meng Qi, Thanh-Tung Cao, and Tiow-Seng Tan. Computing 2D constrained Delaunay triangulation using the GPU. *IEEE Transactions on Visualization and Computer Graphics*, 19(5):736–748, 2013.
- [Ran41] Gunnar Randers. On an Asymmetrical Metric in the Four-Space of General Relativity. *Physical Review*, 59(2):195–199, January 1941.
- [RC98] J C Rochet and P Choné. Ironing, Sweeping, and Multidimensional Screening. *Econometrica*, 1998.
- [RL16] Mael Rouxel-Labbé. *Génération de maillages anisotropes*. PhD thesis, Université Côte d’Azur, December 2016.
- [RS90] J A Reeds and L A Shepp. Optimal paths for a car that goes both forwards and backwards. *Pacific Journal of Mathematics*, 145(2):367–393, 1990.
- [RT92] Elisabeth Rouy and Agnès Tourin. A Viscosity Solutions Approach to Shape-From-Shading. *SIAM Journal on Numerical Analysis*, 29(3):867–884, July 1992.
- [SBD<sup>+</sup>15] Gonzalo Sanguinetti, Erik Bekkers, Remco Duits, Michiel HJ Janssen, Alexey Mashtakov, and Jean-Marie Mirebeau. Sub-Riemannian fast marching in SE (2). In *Iberoamerican Congress on Pattern Recognition*, pages 366–374. Springer, Springer, Cham, 2015.
- [Sch09] Achill Schürmann. Computational geometry of positive definite quadratic forms. *University Lecture Series*, 49, 2009.
- [Sel74] Eduard Selling. Ueber die binären und ternären quadratischen Formen. *Journal für die Reine und Angewandte Mathematik*, 77:143–229, 1874.
- [Sem01] Igor Semaev. A 3-Dimensional Lattice Reduction Algorithm. In *Cryptography and Lattices*, pages 181–193. Springer, Berlin, Heidelberg, Berlin, Heidelberg, 2001.
- [Set96] James A Sethian. A fast marching level set method for monotonically advancing fronts. *Proceedings of the National Academy of Sciences*, 93(4):1591–1595, 1996.
- [Set99] J. A. Sethian. *Level Set Methods and Fast Marching Methods: Evolving Interfaces in Computational Geometry, Fluid Mechanics, Computer Vision, and Materials Science*. Cambridge University Press, 1999.

- [SK04] Alon Spira and Ron Kimmel. An efficient solution to the eikonal equation on parametric manifolds. *Interfaces and Free Boundaries. Mathematical Modelling, Analysis and Computation*, 6(3):315–327, 2004.
- [SMK16] A Shum, K Morris, and A Khajepour. Convergence rate for the ordered upwind method. *Journal of Scientific Computing*, 68(3):889–913, 2016.
- [Str11] Christopher Strobe. Optimising multistatic sensor locations using path planning and game theory. In *IEEE Symposium On Computational Intelligence For Security And Defence Applications*, pages 9–16. IEEE, 2011.
- [SV03] James A. Sethian and Alexander Vladimirsky. Ordered upwind methods for static Hamilton-Jacobi equations: theory and algorithms. *SIAM Journal on Numerical Analysis*, 41(1):325–363, 2003.
- [TCO04] YHR Tsai, LT Cheng, and S Osher. Fast sweeping algorithms for a class of Hamilton-Jacobi equations. *SIAM Journal on Numerical Analysis*, 2004.
- [Tsi95] J.N. Tsitsiklis. Efficient algorithms for globally optimal trajectories. *IEEE transactions on Automatic Control*, 40(9):1528–1538, September 1995.
- [Tug08] Maria Cristina Tugurlan. *Fast Marching Methods - Parallel Implementation and Analysis*. PhD thesis, Louisiana State University, September 2008.
- [Var67] S R S Varadhan. On the behavior of the fundamental solution of the heat equation with variable coefficients. *Communications on Pure and Applied Mathematics*, 20(2):431–455, May 1967.
- [Vla08] Alexander Vladimirsky. Label-setting methods for Multimode Stochastic Shortest Path problems on graphs. *Mathematics of Operations Research*, 33(4):821–838, 2008.
- [Vor08] G Voronoi. *Sur quelques propriétés des formes quadratiques positives parfaites*. J. reine angew. Math, 1908.
- [Wac14] Gerd Wachsmuth. The numerical solution of Newton’s problem of least resistance. *Mathematical Programming*, 147(1-2):331–350, 2014.
- [Wac17] Gerd Wachsmuth. Conforming approximation of convex functions with the finite element method. *Numerische Mathematik*, 47(4):1–32, 2017.
- [WDB<sup>+</sup>08] Ofir Weber, Yohai S Devir, Alexander M Bronstein, Michael M Bronstein, and Ron Kimmel. Parallel algorithms for approximation of distance maps on parametric surfaces. *ACM Transactions on Graphics (TOG)*, 27(4):104–16, October 2008.
- [Wei98] Joachim Weickert. *Anisotropic diffusion in image processing*, volume 1. Teubner Stuttgart, 1998.

- [YC17] Fang Yang and Laurent D. Cohen. Tubular Structure Segmentation Based on Heat Diffusion. In *International Conference on Scale Space and Variational Methods in Computer Vision*, pages 54–65. Springer, 2017.
- [Zha05] H Zhao. A fast sweeping method for eikonal equations. *Mathematics of computation*, 2005.
- [ZSN09] Christopher Zach, Liang Shan, and Marc Niethammer. Globally Optimal Finsler Active Contours. In David Hutchison, Takeo Kanade, Josef Kittler, Jon M Kleinberg, Friedemann Mattern, John C Mitchell, Moni Naor, Oscar Nierstrasz, C Pandu Rangan, Bernhard Steffen, Madhu Sudan, Demetri Terzopoulos, Doug Tygar, Moshe Y Vardi, Gerhard Weikum, Joachim Denzler, Gunther Notni, and Herbert Süße, editors, *DAGM-Symposium*, pages 552–561. Springer, 2009.